Robust and Adaptive TVC Control Design Approaches for the VEGA Launcher

by

Diego Navarro Tapia

Department of Aerospace Engineering
University of Bristol

A dissertation submitted to the University of Bristol in accordance with the requirements for award of the degree of Doctor of Philosophy in the Faculty of Engineering.

April 2019

Supervisors:

Dr. Andrés Marcos
University of Bristol, UK

Dr. Samir Bennani
European Space Agency, The Netherlands

PhD defence:

Date
14 May 2019

Internal examiner
Dr. Branislav Titurus
University of Bristol, UK

External examiner
Dr. Matthew Turner
University of Leicester, UK

Independent chair
Dr. Guido Herrmann
University of Bristol, UK

Abstract

This thesis addresses the design of the atmospheric control system of a launch vehicle. During the ascent-flight phase, the launch vehicle is heavily impacted by wind-induced structural loads and generally exhibits a flexible behaviour characterised by several resonant modes that can generate large oscillations and lead to instability. In this challenging scenario, the control system must ensure stability to guidance commands while satisfying very demanding and tight performance requirements in the presence of parameter dispersions.

Based on the above, the atmospheric ascent-flight of a launch vehicle represents a challenging control problem, which is traditionally addressed using a classical design approach. Although there is a rich heritage and experience in applying classical control solutions to the launcher problem, several practical limitations are recognised. With the current industrial state-of-practice it is hard to achieve stability and performance robustness characteristics along the atmospheric phase. In addition, this strategy results in a very time-consuming design, tuning and validation process.

Considering the above limitations and also the increasingly competitive launch service market, more methodological synthesis techniques must be proposed to extend the actual control system capabilities as well as to facilitate the control design task. In this context, this thesis proposes a synthesis framework based on robust control techniques. In particular, the capabilities of the structured $\mathcal{H}_\infty$ and Linear Parameter Varying (LPV) synthesis techniques are explored for the design of the atmospheric control system of the European VEGA launcher. It is shown that these robust control approaches can provide a direct trade-off between robustness versus performance, reduce tuning effort across launch missions and has the capability to simultaneously handle multiple performance requirements and also to explicitly include system uncertainties in the design.

This thesis also explores adaptive features for the atmospheric VEGA control system with the aim to evaluate its performance and robustness properties. The main goals of the proposed adaptive scheme are to improve the performance in dispersed conditions and to provide recovery and prevent the loss of the vehicle in extreme off-nominal conditions. Finally, a comparison between the proposed structured $\mathcal{H}_\infty$, LPV and adaptive controllers are provided.

Dedication and acknowledgements

First and foremost, I would like to thank my supervisor Dr. Andrés Marcos for giving me a golden ticket to this four year roller-coaster ride called PhD research. I am extremely thankful for his sincere dedication and time, and for his guidance, not only in technical matters but also in personal skills. Thanks to his support I enjoyed every single loop of this roller-coaster. Also, I would like to explicitly acknowledge his enthusiasm and initiative proposing conferences, workshops, extra-curricular activities and also delightful socials.

Secondly, I would like to thank my co-supervisor Dr. Samir Bennani. Many thanks for opening the doors of your office to me during my stay at ESA-ESTEC in The Netherlands. I am deeply grateful for his technical support and indeed for his positive and inspiring attitude. Also thanks for highlighting everyday that science, philosophy and music can be placed in the same sentence.

I am also grateful to Dr. Tom Richardson for his constructive and useful feedback during the PhD annual reviews. I would also like to acknowledge the examiners Dr. Matthew Turner and Dr. Branislav Titurus. Their feedback and suggestions have helped to improve the quality of the final version of this PhD thesis.

I would like to dedicate some words to those subtle yet significant things that cannot be engineered. And here, I am talking about friendship. Many thanks to all the cave dwellers and farmers for creating such a nice environment. Although our twice-a-day coffee breaks may seem ephemeral as time goes by, I would like to state for the record that they were a bottomless source of inspiration, humour and epic conversations. And because of that, I take off my hat to you: Pedro, Andrea, Erwin, Duanqi, Sam, Kaiqiang, Henri, Alison, Yingbo, Sérgio, Dave, Yi, Siming, Yi-Yuan, Tim and Robert. I would like to devote some words to Pedro and Andrea, with whom I shared many trips, adventures, ping-pong sessions and technical discussions; to Erwin not only for his classic randomness but also for being such an extraordinary cicerone and coffee connoisseur; to Kaiqiang for his kindness and for his traditional lab Chinese wine tasting; to Sérgio for setting an example as a proper PostDoc; and to one of the founders of the *Cave*, Robert, for his spontaneity and also his traditional Christmas cards.

Many thanks to the ESA-ESTEC AOCS and GNC Division for their hospitality. I have very good memories of my research stay at ESTEC. In particular, thanks to Francesco, Giordana, Marina and Özgün, who shared many unforgettable moments in a place called *the bubble*. Indeed, ticking-off with nice people is twice as good.

I would also like to extend my gratitude to all the people I have encountered over the last four years. Thanks to the University of Bristol Symphonia orchestra for cheering up my Wednesdays with music. Special mention to my musicians friends Tim, Alasdair, Gareth, George and Rebekah with whom I have shared not only rehearsals and concerts but also memorable moments.

Special thanks to Isa for letting me stay in the atmosphere. Thanks for your many artistic advices, but more importantly for your true support and affection. And despite the distance, I am deeply grateful to you for colouring everyday my ship's log.

And last but not least, I would like to express my personal thanks to my family. This thesis is dedicated to you. I owe you more than words.

Author's declaration

I declare that the work in this dissertation was carried out in accordance with the requirements of the University's Regulations and Code of Practice for Research Degree Programmes and that it has not been submitted for any other academic award. Except where indicated by specific reference in the text, the work is the candidate's own work. Work done in collaboration with, or with the assistance of, others, is indicated as such. Any views expressed in the dissertation are those of the author.

SIGNED: ..... DATE: .....

Table of Contents

List of Tables

List of Figures

Figure **Page**

List of Acronyms

AVUM Attitude and Vernier Upper Module;

BM Bending Mode;

BMI Bilinear Matrix Inequality;

CG Center of Gravity;

CNES National Centre for Space Studies;

CP Center of Pressure;

DM Delay Margin;

DoF Degree of Freedom;

ELV European Launch Vehicle;

EMA Electro-Mechanical Actuator;

EPSRC Engineering and Physical Sciences Research Council;

ESA European Space Agency;

FEM Finite Element Method;

GM Gain Margin;

GNC Guidance, Navigation and Control;

GS Gain Scheduling;

GSLV Geosynchronous Satellite Launch Vehicle;

HF-GM High-Frequency Gain Margin;

HWIL Hardware-In-the-Loop;

ICBMs Intercontinental Ballistic Missiles;

IM Internal Model;

IMC Internal Model Control;

IMP Internal Model Principle;

INS Inertial Navigation System;

IQC Integral Quadratic Constraint;

ISRO Indian Space Research Organisation;

ISS International Space Station;

JAXA Japan Aerospace Exploration Agency;

LB Lower Bound;

LEO Low Earth Orbit;

LF-GM Low-Frequency Gain Margin;

LFT Linear Fractional Transformation;

LMI Linear Matrix Inequality;

LoV Loss of Vehicle;

LPV Linear Parameter Varying;

LQG Linear Quadratic Gaussian;

LQR Linear Quadratic Regulator;

LTI Linear Time Invariant;

LTV Linear Time Varying;

MC Monte Carlo;

MIMO Multiple-Input Multiple-Output;

NASA National Aeronautics and Space Administration;

NGA Non-Gravitational Acceleration;

NGV Non-Gravitational Velocity;

NP Nominal Performance;

PID Proportional-Integral-Derivative;

PM Phase Margin;

PVP Pivot Point;

RACS Roll Attitude Control System;

RC Resistor-Capacitor;

RCT Reaction Control Thruster;

RP Robust Performance;

RS Robust Stability;

SISO Single-Input Single-Output;

SLS Space Launch System;

SSO Sun Synchronous Orbit;

SWIL Software-In-the-Loop;

TVC Thrust Vector Control;

TWD Tail-Wag-Dog;

UB Upper Bound;

US United States;

USSR Union of Soviet Socialist Republics;

V&V Verification & Validation;

WWII World War II;

Nomenclature

Launch vehicle parameters

α	Angle of attack	(rad)
β	Thrust vector control actuator deflection	(rad)
γ	Drift angle	(rad)
$\mathrm{I_N}$	Moment of inertia of the nozzle engine about the nozzle pivot point	$(\mathrm{kg \cdot m^2})$
$\mathrm{I_o}$	Moment of inertia of the nozzle engine about the nozzle center of gravity	$(\mathrm{kg \cdot m^2})$
$\mathrm{I_{yy}}$	Lateral moment of inertia	$(\mathrm{kg \cdot m^2})$
ψ	Yaw angle	(rad)
ρ_a	Air density	$(\mathrm{kg/m^3})$
τ	Time delay	(s)
θ	Pitch angle	(rad)
a_6	Rotational aerodynamic instability parameter	$(\mathrm{s^{-2}})$
$C_{N\alpha}$	Lift coefficient gradient with respect to α	(-)
D	Aerodynamic drag force	(N)
F_ψ	Total yaw force	(N)
h	Altitude	(m)
k_1	Rotational control efficient parameter	$(\mathrm{s^{-2}})$
l_{CG}	Distance from the center of gravity to the nozzle pivot point	(m)
l_{CP}	Distance from the center of gravity to the aerodynamic center of pressure	(m)
l_{INS}	Distance from the center of gravity to the inertial navigation system location	(m)

l_N	Distance from the nozzle center of gravity to the nozzle pivot point	(m)
m	Launch vehicle mass	(kg)
M_ψ	Total yaw moment	(N · m)
m_N	Nozzle mass	(kg)
N	Normal force	(N)
Q	Dynamic pressure	(Pa)
q_i	State of the i^{th} bending mode	(-)
S_{ref}	Launcher reference area	(m^2)
T	Thrust force	(N)
t	Flight time	(s)
V	Vehicle speed	(m/s)
v_w	Wind speed	(m/s)
y	Lateral drift with respect to the reference trajectory in the pitch plane	(m)
z	Lateral drift with respect to the reference trajectory in the yaw plane	(m)
ω_{q_i}	Natural frequency of the i^{th} bending mode	(rad/s)
ζ_{q_i}	Damping ratio of the i^{th} bending mode	(-)
$\Psi'_{\#_i}$	Rotational length of the i^{th} bending mode at # location node	(rad)
$\Psi_{\#_i}$	Translational length of the i^{th} bending mode at # location node	(m)

Wind model parameters

σ_h	Turbulence standard deviation	(m/s)
A	Gust amplitude	(m/s)
H_f	Total length of the wind speed profile envelope	(m)
H_l	Leading edge length of the wind speed profile envelope	(m)
H_u	Trailing edge length of the wind speed profile envelope	(m)
L_h	Turbulence length scale	(m)

v_{wp}	Wind speed profile envelope	(m/s)

Robust control

$\Delta_{\#}$	Uncertainty matrix of system #
$\delta_{\#}$	Parametric uncertainty of variable #
$\mathcal{F}_l(X,Y)$	Lower linear fractional transformation of X with Y
$\mathcal{F}_u(X,Y)$	Upper linear fractional transformation of X with Y
$\mathcal{T}_{yx}$	Transfer function from input signal x to output y
$\mu_\Delta(X)$	Structured singular value of matrix X with respect to the uncertainty structure Δ
$\overline{\sigma}(X)$	Maximum singular value of matrix X
$P(s)$	Generalised plant

Subscripts

τ	Relative to delay
c	Relative to command signals
e	Relative to error signals
F	Relative to the launcher flexible-body dynamics
HP	Relative to High Pass filter
LP	Relative to Low Pass filter
N	Relative to the launcher nozzle dynamics
n	Relative to noise signals
R	Relative to the launcher rigid-body dynamics
TVC	Relative to Thrust Vector Control actuator
w	Relative to wind disturbance signal

CHAPTER 1

Introduction

1.1 Motivation

The design of the atmospheric ascent-flight control system of a launch vehicle is a very challenging task that requires careful consideration of different aspects. First, most of the launch vehicles are aerodynamically unstable due to the vehicle's design characteristics (the center of gravity lies below the center of pressure). Second, any launch vehicle undergoes a very high dynamic pressure during the atmospheric flight and is heavily impacted by several undesired effects such as wind-induced structural loads, which all combined cause a significant performance degradation and may even cause the Loss of Vehicle (LoV). Third, launch vehicles typically exhibit a flexible behaviour characterised by several resonant modes, also called bending modes, which generally present low damping. Thus, if these bending modes are excited by the control system, large oscillations can be produced and lead to instability. To avoid this problem, the control system must account for these flexible-body structure interactions and stabilise the bending modes. In particular, this task is highly complex due to the proximity of the first bending mode frequency and the rigid-body control bandwidth. Fourth, there is a wide variation of the flight parameters during the atmospheric phase due to the fast propellant consumption and the rapid launcher dynamics changes. In addition, further issues are introduced by non-linearities in the actuator, the nozzle dynamics as well as parameter dispersions.

The control of the atmospheric stage is typically performed using a Thrust Vector Control (TVC) system for the pitch and yaw axes. Based on the measurements from the Inertial Navigation System (INS), the launcher TVC flight control system computes the necessary engine nozzle deflections to ensure stability and follow the guidance commands while satisfying very demanding and tight performance requirements in the face of all the

aforementioned adverse effects. During the atmospheric phase, the guidance is performed in open-loop configuration following a pre-programmed trajectory. This flight strategy leads to deviations from the nominal trajectory, which are corrected in upper phases. On the other hand, the roll axis is generally controlled by a Roll Attitude Control System (RACS) using engine thrusters.

As demonstrated by the current state-of-practice, there is a rich heritage and experience in applying classical control solutions to the launcher problem. This is the design approach used by the small European VEGA launcher (see Figure 1.1), which uses a classical (proportional-derivative plus bending filters) controller for the TVC system [2]. This strategy has been proven successful in all of the VEGA missions performed so far, but several practical limitations are recognised. Classical control techniques are oriented to Single-Input Single-Output (SISO) systems, nevertheless, the TVC launcher control design generally results in a multivariable control problem when the aforementioned issues and multiple design objectives are considered. This aspect makes the design task more complex since every channel/requirement has to be iteratively addressed in a single-loop fashion. In addition, with the classical state-of-practice design approach, the control system design is performed for nominal conditions and robustness is only considered in an implicit fashion via stability margin requirements to guarantee stability under dispersed conditions. As a consequence, the launcher Verification & Validation (V&V) process must rely in an extensive analysis coverage after design. The synthesis has to be performed in several iterative phases because the designed controller may not satisfy all the requirements after V&V and may need to be redesigned. This results in an overall expensive (in terms of both cost and time) synthesis process, in which it is very difficult to achieve uniform stability and performance robustness throughout the entire flight.

Figure 1.1: VEGA launch vehicle [Courtesy of ESA - J. Huart]

Unfortunately, due to the wide range of mission configurations, different payloads and trajectories, the TVC control laws need to be updated and tailored for each mission. Thus, in the face of an increasingly competitive launch service market, it is necessary to develop a control synthesis framework which allows to improve and extend the actual Guidance, Navigation and Control (GNC) capabilities as well as facilitate the control design task. In this sense, robust and adaptive control synthesis techniques are of interest for the development of the future launch vehicles. The demonstration of the methodological and formal capabilities of these techniques for launcher control design is the main topic of this PhD thesis. In particular, unlike the state-of-practice, robust control techniques allow considering uncertainties in the design and are more oriented to multivariable control problems than classical techniques. Robust control theory also permits to analytically evaluate the robustness of the design, providing relevant insights on the stability and performance degradation due to model uncertainties. Moreover, robust control techniques can provide a more systematic design process approach with respect to the traditional state-of-practice, as well as reduced tuning and design effort across launch missions. On the other hand, adaptive GNC functionalities will allow the control system to provide recovery and prevent the loss of the vehicle in extreme off-nominal conditions.

1.2 State-of-the-art in launcher control design

The current state-of-practice in launcher control design has significant heritage from the Cold War between the United States (US) and the Union of Soviet Socialist Republics (USSR). After World War II (WWII), both countries started corresponding programs to develop Intercontinental Ballistic Missiles (ICBMs) for military purposes. This missile development also led to the so-called Space Race, where both nations showcased their technological progress in a series of space missions.

The first launch vehicles were developed based on the German V-2 rocket [3], which was widely used during the end of WWII against the Allies, mainly in London (United Kingdom) and Antwerp (Belgium). In a span of just few years, this frenetic technological race led to the development of many families of launch vehicles such as the Soviet R-7, Soyuz and Proton and the US Redstone, Atlas, Titan, Delta and Saturn rockets. Indeed, the Space Race meant a significant boost for the evolution of launch vehicle technology and specially for the necessary GNC architecture and algorithms to provide reliable performance and proper TVC attitude control. In fact, the actual state-of-the-art in TVC system design leverages a great body of knowledge from these rocket development programs.

The traditional TVC control system architecture consists of two main parts. First, a rigid-body controller which is based on a Proportional-Integral-Derivative (PID) controller in attitude to provide stabilisation for both pitch and yaw axes. The rigid-body controller also typically includes different measurement feedbacks based on the available on-board sensors (i.e. drift, drift-rate, acceleration, angle-of-attack) to minimise the structural loads suffered by

the launch vehicle. And second, a set of bending filters are incorporated to stabilise the flexible-body launch vehicle.

A good example [4, 5] is the Saturn V rocket used on the Apollo missions, which implemented a control law based on attitude and attitude-rate plus acceleration signals feedback for load alleviation and a set of bending filters formed by passive Resistor-Capacitor (RC) filtering networks. The same architecture was also successfully employed by the Space Shuttle [6] and the Japanese H-IIA launch vehicle [7]. Based on this heritage, other launch vehicles were also developed using this classical control configuration, i.e. the US Ares-I flight control system used an attitude PID controller in parallel with an anti-drift/load-relief algorithm to minimise lateral deviations and structural loads plus a set of attitude and rate bending filters [8], or the Brazilian VLS launcher which employed a PID controller in attitude plus notch filters for the stabilisation of the bending modes [9].

Most launch vehicles present axial symmetry along the roll axis. This characteristic allows to simplify the design and analysis of the TVC control system in a single plane, either the pitch or the yaw axis. The reason is that assuming a low roll rate, then the pitch and yaw axes can be considered decoupled and more importantly identical, and thus, the same controller can be applied to both axes.

The atmospheric TVC control problem is traditionally decomposed into a number of linear designs merged into an overall control design by using classical Gain Scheduling (GS) [10]. This design strategy not only allows to deal with the rapid time variation of the flight conditions during the atmospheric phase, but it also exploits the benefits of linear control theory, which offers a well-consolidated framework for synthesis and analysis (i.e. pole-placement, root locus, Bode diagrams, Nichols and Nyquist charts). Using the GS approach, the launch vehicle dynamics are linearised about several representative points along the flight and a controller is designed at each point. These linear controllers are then interpolated ad-hoc based on a measurable system parameter (e.g. time or non-gravitational velocity). Finally, the stability, performance and robustness of the resulting scheduled controller is verified and validated using a high-fidelity non-linear simulator and different uncertainty configurations are tested via Monte Carlo (MC) and vertex cases simulations [11, 12].

The synthesis of each linear controller consists in turn of several sequential and iterative steps [13, 14]. First, a rigid-body controller is initially designed to stabilise the rigid launch vehicle and satisfy the atmospheric flight specifications. Then, the flexible dynamics are added and a set of bending filters is designed to prevent the excitation of the flexible modes. Finally, both rigid-body controller and bending filters are manually tuned in an ad-hoc manual integration process until all the system requirements are met. These two steps are detailed next.

1.2.1 Rigid-body control design

In the first place, the design of the rigid-body control system has two main tasks: to achieve stability and to obtain an optimal performance along the atmospheric flight. In addition, the control system must fulfil these two tasks in a robust manner to ensure that the required stability and performance objectives are met in the presence of parametric uncertainties and disturbances.

As aforementioned, classical control design techniques do not implicitly consider uncertainties during the design process. The stability robustness is rather enforced through stability margin requirements, i.e. 6 dB gain margin and 30 deg phase margin are traditionally considered to avoid any instability case under dispersed conditions. In addition, the second rigid-body design task makes the control problem especially challenging because the control engineer must address two levels of trade-offs to optimize the atmospheric-flight design. First, the achievable performance of the launch vehicle is limited by the classic trade-off between stability robustness and performance. And second, the control system must deal with different competing requirements. In particular, the launcher control problem must fulfil the following (competing) strategies, some with higher priority over the others depending the flight phase:

- *Tracking performance:* the control system will minimise the attitude deviations from the guidance commands. However, this approach leads to lateral deviations from the trajectory and it does not account for wind-induced structural loads.
- *Drift performance:* this design scheme aims at minimising the lateral deviations of the vehicle. In this case, the control system will attempt to generate an attitude response so that the normal forces are cancelled out. The drawbacks of this approach are attitude deviations and, as in the previous case, high structural loads.
- *Load performance:* the main objective of this approach is to minimise the wind-induced structural loads. To that end, the vehicle will turn into the wind to reduce the angle of attack leading to attitude deviations and also translational dispersions with respect to the pre-programmed trajectory.

This performance trade-off problem is generally oriented towards minimising the performance degradation due to the wind disturbance contribution. In fact, the main traditional control strategies considered in the literature for launch vehicle control synthesis aim to cancel out the steady-state values of each of the previous three performance metrics from the wind disturbance input, leading to different control modes: i.e. attitude-error-minimum, drift-minimum and load-minimum [15, 16, 17]. These control modes are combined throughout the atmospheric flight to achieve a trade-off balance for the best global performance. In particular, a load-relief control mode is generally employed around the maximum dynamic pressure region. And for the rest of linear design points, the design is

normally focused on minimising the tracking error while keeping the lateral deviations bounded within specifications. After the design process, the wind disturbance rejection is normally evaluated using a thorough nonlinear simulation analysis using a wide set of different wind profiles.

From classical to optimal and robust control

Despite the successful application of classical methods for the design of launcher's TVC systems, the classical synthesis framework suffers from some practical limitations such as highly time-consuming synthesis process, difficulties to address multivariable problems and lack of robustness. These shortcomings led to the use of the linear optimal control theory, mainly based on two control techniques: Linear Quadratic Regulator (LQR) and Linear Quadratic Gaussian (LQG). Examples of these techniques are the Brazilian VLS launch vehicle, which uses the LQR method for the atmospheric control tuning [18] and the TVC flight system of the Ariane 5 launch vehicle which was initially designed using the LQG approach [19]. In addition, other research studies were conducted by the Indian Space Research Organisation (ISRO) to apply LQG to the Indian Geosynchronous Satellite Launch Vehicle (GSLV) [20].

These two optimal methods are oriented to multivariable control problems and allow to formulate the performance trade-off as an optimisation problem, reducing the complexity of the synthesis task and improving the optimality of the design. Nevertheless, the LQG approach does not provide any guaranteed stability robustness against parametric uncertainties and unmodelled dynamics [21, 22]. Furthermore, this synthesis approach also presents limitations in tackling the disturbance control problem, since it assumes that the disturbance signals are described by a white noise stochastic process.

The limitations of LQG control encouraged the development of the $\mathcal{H}_\infty$ theory for robust control in the 1980's [23, 24, 25]. As opposed to classical control techniques where the control objectives are expressed in the time domain, the $\mathcal{H}_\infty$ approach uses frequency-dependent weighting functions to describe the control design objectives. The $\mathcal{H}_\infty$ optimisation is based on the minimisation of the $\mathcal{H}_\infty$ norm of the weighted system. This norm represents the maximum singular value of the system, which is the generalisation of the eigenvalue for multivariable systems and can also be interpreted as the maximum gain or amplification of energy from the system inputs to the outputs to be controlled. In addition, this robust control theory allows to explicitly consider non-parametric uncertainties, resulting in control designs with enhanced robustness capabilities.

The $\mathcal{H}_\infty$ technique received widespread attention in many industrial control applications and also in the launcher industry [26, 27, 28]. In [27], the $\mathcal{H}_\infty$ approach was applied to the design of the atmospheric rigid-body control system of the Ariane 5 launch vehicle and compared with the LQG baseline controller. In this benchmark, the $\mathcal{H}_\infty$ design resulted in better rigid-body stability robustness, less TVC consumption and more systematic tuning process. These benefits motivated the change from LQG to $\mathcal{H}_\infty$ control for the evolution of the Ariane 5 launcher [29].

The $\mathcal{H}_\infty$ control theory was also employed for the first-stage attitude control design of the Japanese M-V launch vehicle [30] as well as for its evolution the Epsilon launcher [31]. In these works, the design is performed in two steps to facilitate the $\mathcal{H}_\infty$ optimisation: the unstable launch vehicle plant is first stabilised using a classical output feedback and then the $\mathcal{H}_\infty$ approach is applied to optimise performance.

Subsequently, the second stage of the M-V rocket was redesigned after the third flight, and the Japan Aerospace Exploration Agency (JAXA) decided to use structured singular value μ approach instead of $\mathcal{H}_\infty$ to improve the tracking performance robustness during the second phase of the flight [32]. The μ synthesis technique allows to consider parametric uncertainties explicitly and also provides good stability and performance robustness characteristics. The main principle of μ control is that the maximum singular value can be reduced by using D scales and a more robust controller K can be designed than using the $\mathcal{H}_\infty$ approach when the D scales are incorporated in the synthesis stage. This defines an iterative design procedure, also called D-K iteration, which sequentially fixes the D scales and then the K controller while optimising the other.

Despite the potentialities of μ synthesis and the availability of powerful tools such as the $\mu-$analysis and synthesis Matlab toolbox [33], the μ technique has not had an extensive acceptance in Space industry and only a few research studies can be found in the literature for launcher control design [34, 35]. One of the main issues is that there are no guarantees that the D-K iteration will converge. In this sense, the order of the system and the number of parametric uncertainties and its repetitions affect significantly the effectiveness of the optimisation.

From full-order techniques to structured $\mathcal{H}_\infty$

As stated before, the need to provide higher stability and performance robustness as well as that of reducing the control tuning effort prior to each mission led to investigate and adopt optimal and robust control techniques. In this journey towards robustness, the rigid-body controller architecture evolved from the classical structured configuration (PID plus measurement feedback for load alleviation) to an unstructured scheme. LQG, $\mathcal{H}_\infty$ and μ-synthesis provide full-order controllers whose order equals the size of the weighted design interconnection. This generally results in high-order controllers without a defined structure. This is an important drawback in aerospace applications where the computational power is limited, but also because the lack of structure complicates the understanding and tuning of the controller. Moreover, in most cases, the order of the controller is reduced by simplifying the system dynamics or by applying ad-hoc controller order reduction techniques –which may degrade the effectiveness of the controller.

In the last decade, two new approaches based on the $\mathcal{H}_\infty$ theory have been developed to address the aforementioned problems: the HIFOO approach, which allows to synthesize controllers with a desired order [36], and the structured $\mathcal{H}_\infty$ technique, which allows to fix the order and/or structure of the controller [37]. These features are important for industrial

applications where a good understanding of the controller structure is appreciated. Moreover, these techniques allow to reconcile the know-how of classical control architectures within a robust control design and analysis framework.

The main drawback of these robust structured techniques is that they are based on a non-smooth and non-convex optimisation. This implies that the design can be drastically affected by the choice of the controller structure as well as the number of tunable parameters and their initial guesses or initialisations. This problem can be mitigated by performing multiple optimisations from a set of random initialisations but it raises the problem of non-repeatability and that of understanding (i.e. how changes by the designer affect the controller synthesis).

Despite the non-smooth nature of the optimisation, the structured $\mathcal{H}_\infty$ technique has received special attention in the past few years, resulting in relevant Space flown missions such as the ESA Rosetta's orbit controller tuning [38], the design of the attitude and acceleration control of the French National Centre for Space Studies (CNES) microsatellite MICROSCOPE [39] and also recent piloted flight tests [40]. In addition, this newly developed technique has also been successfully applied to launch vehicle control design in several research studies [41, 42, 43] and more importantly, the structured $\mathcal{H}_\infty$ approach is being currently considered by industry as a design framework capable of simplifying the launch vehicle control design process [44].

In addition to the capability of configuring the size and architecture of the tunable controller, the structured $\mathcal{H}_\infty$ approach also offers many other interesting design capabilities such as explicit consideration of parametric uncertainties, multi-plant design and good stability/performance robustness trade-off objectives.

From gain-scheduling to Linear Parameter Varying control

The use of optimal control and subsequently robust control techniques significantly improved the stability and performance robustness properties of the linear rigid-body designs. As mentioned before, the atmospheric TVC problem has been traditionally addressed using the GS approach, which is a standard practice in industry to deal with systems with a wide dynamic variation. This means that a number of linear designs must be performed along the atmospheric flight envelope at distinct operational points (e.g. every 10 seconds for the VEGA launcher) and then a scheduled global controller is obtained by interpolating the different linear designs.

The main drawback of the GS methodology is that the stability and performance robustness achieved at the linear design points are no longer guaranteed for the flight instants between the design points. This issue is generally overcome by first analysing the linear stability of the system using a finer grid of analysis points (e.g. every second) and also by an extensive analysis coverage using a non-linear, high-fidelity 6 Degree of Freedom (DoF) simulator.

In this sense, the Linear Parameter Varying (LPV) control theory extends the GS approach guaranteeing robustness not only for the Linear Time Invariant (LTI) design points but for the full LPV model (which can capture the full trajectory based on a selected parameter, if properly modeled). This information is used by the LPV design optimiser to generate in a single step a scheduled controller based on the chosen parameter. In addition, this synthesis methodology can lead to a reduction of the design effort across missions as well as a simplification of the V&V process.

Despite those potential benefits, the introduction of the LPV approach in launch vehicle control design has been very scarce [45, 46]. The main reasons are the lack of reliable tools for LPV modelling, synthesis and analysis and the need of an adequate transfer of this technology to the Space industry. Nonetheless, LPV control is receiving increased attention in the past few years thanks to the development of LPV software tools such as LPVTools [47] and also some recent studies on different applications such as flutter suppression [48], load reduction of wind turbines [49] and microvibration control for flexible satellites [50].

Adaptive control

Different from the previously mentioned control design strategies, the US National Aeronautics and Space Administration (NASA) is advancing on the study of adaptive control functionalities for the development of the Space Launch System (SLS) rocket. The SLS flight control system relies on a classically designed baseline controller which is composed of a gain-scheduled PID controller in attitude plus a load-relief algorithm. The novelty of the SLS architecture is that the baseline controller is augmented by an adaptive control law, which provides minimal adaptation under nominal conditions but results in recovery actions for off-nominal conditions. This adaptive augmenting control strategy improves robustness to launch vehicle failures and provides extended safety envelope capabilities [51, 52, 53].

This adaptive strategy has successfully been demonstrated in flight tests on a F/A-18 aircraft [54]. Nevertheless, due to the adaptive behaviour of the system and to the nonlinear characteristics of the adaptive control law, there are no formal techniques capable of resulting on an equivalent analysis to the classical linear stability margins used by industry to verify and validate the designs. This topic has raised the attention of the control research community in recent years. Most of the works looking at this important issue rely on simulation-based nonlinear stability techniques [55, 56, 57].

1.2.2 Bending filter control design

In addition to stability and performance, the TVC system must also ensure that the bending modes related to the flexible structure of the launch vehicle are not excited. This is traditionally performed using a set of filters, also known as bending filters, that minimise these flexible-body structure interactions with the control system.

As aforementioned, the industrial standard practice is to design the rigid-body controller and bending filters separately in a sequential and iterative fashion. The main control objective of the bending filters is to stabilise the bending modes without altering the stability and performance achieved by the rigid-body controller. This control problem can become very complex when, due to vehicle's design aspects, the frequency of the first bending mode is low and close to the rigid-body control system bandwidth. Indeed, regardless of the rigid-body design approach used, the introduction of the bending filters generally results in degradation of the rigid-body stability margins and performance. Moreover, further complications are introduced by the fact that the main properties of the bending modes (i.e. frequency, damping factor, translational and rotational lengths) vary in time during the flight and are difficult to characterise, normally involving exhaustive 3D Finite Element Method (FEM) analyses. This can cause notable discrepancies between the launch vehicle model used for design and analysis and the real system, and thus, it is paramount to design the bending filters considering a wide range of uncertainties.

There are two main ways to stabilise the bending modes [13, 14]: gain stabilisation, in which the bending mode is attenuated so it does not cause any instability; and phase stabilisation, which implies a filter design where the phase of the bending mode is shaped to guarantee that the phase margin specifications are met. The latter is generally used for the first bending mode stabilisation in order to preserve the rigid-body stability margins and performance, whereas the upper bending modes are normally gain stabilised.

The classical approach is to use passive filtering with low-pass and notch configurations [13]. For example, the Saturn V rocket employed a network of manually-designed RC lag filters [4], whereas for the Space Shuttle digital design approaches were employed [6]. Similarly as for the rigid-body case, the methodology and techniques employed for the bending filter design problem have also evolved with the aim of providing more robustness and improving the easiness of design.

Although the literature for bending filter design is not as extensive as for the rigid-body case, different synthesis approaches have been investigated in the last decade. The bending filters of the NASA's Ares-I launch vehicle were designed using a constrained numerical optimization [58] providing minimal degradation to the rigid-body stability margins. The same technique was also applied to the design of the hold control system of the International Space Station (ISS) during Orbiter Repair Maneuver operations [59]. In both references, the filters are designed in continuous-time domain and then discretised using a bilinear transformation, while in [60], the same numerical optimization is directly employed in the discrete-time domain. In addition, the synthesis of time-varying and adaptive notch filters have also been studied for mode stabilisation [61, 62].

1.3 Objectives

The objective of this PhD activity is to advance the design and development of control systems for launchers, using the VEGA launcher as the industrial benchmark to demonstrate the developed approaches. The main aim is to study robust and adaptive control laws that can provide extended launch vehicle missions and safety envelope capabilities. The new designs will target to: 1) formalise the design approach into a more systematic methodology; 2) reduce the need for intensive mission dependent control design loops before each flight; 3) increase the overall GNC performance with better load drift trade-offs to meet safety corridor requirements; 4) improve the GNC stability robustness against plant uncertainties and degradations; 5) reduce the missionisation time.

The specific technical objectives of the activity can be listed as follows:

O1 - Study structured $\mathcal{H}_\infty$ and parameter optimisation control methods to enhance the overall system performance while keeping the same control architecture within a predefined structure and complexity. The aim is to provide a clear and methodological assessment of the potential of the techniques and of the axis of improvement for the current VEGA GNC system.

O2 - Study robust and LPV control concepts, which when relying on on-line acquired scheduling can increase the operational perimeter of the GNC system.

O3 - Develop modular prototypes of the control system designs so that they can be used as augmentation kits to the existing autopilot loop. The advantage of such an augmentation is to avoid the inner loop control re-qualification while allowing for a clear demarcation to measure the improvements.

O4 - Explore adaptive features of the GNC functions. These features will permit to augment the current VEGA GNC architecture with additional adaptive layers to cope with launcher degradations and adverse weather conditions.

1.4 Funding

This work was funded by the ESA through the Networking/Partnering Initiative contract No. 4000114460/15/NL/MH/ats. Mr. Diego Navarro-Tapia was also the recipient of a Doctoral Training Partnership award No. 1609551 by the Engineering and Physical Sciences Research Council (EPSRC).

1.5 Thesis Outline

The outline of this thesis is illustrated in Figure 1.2. This thesis contains 9 chapters organised in four main parts. Note that each chapter is shaded in color according to the synthesis technique used (i.e. structured $\mathcal{H}_\infty$ in cyan, LPV in green and adaptive control in purple). Chapters 3-8 address the objectives listed before in Section 1.3. Specifically, Objective O1 is addressed in Part I (i.e. Chapters 3-5), O2 in Chapter 6, O3 in Chapter 7 and finally, Objective O4 is covered in Chapter 8.

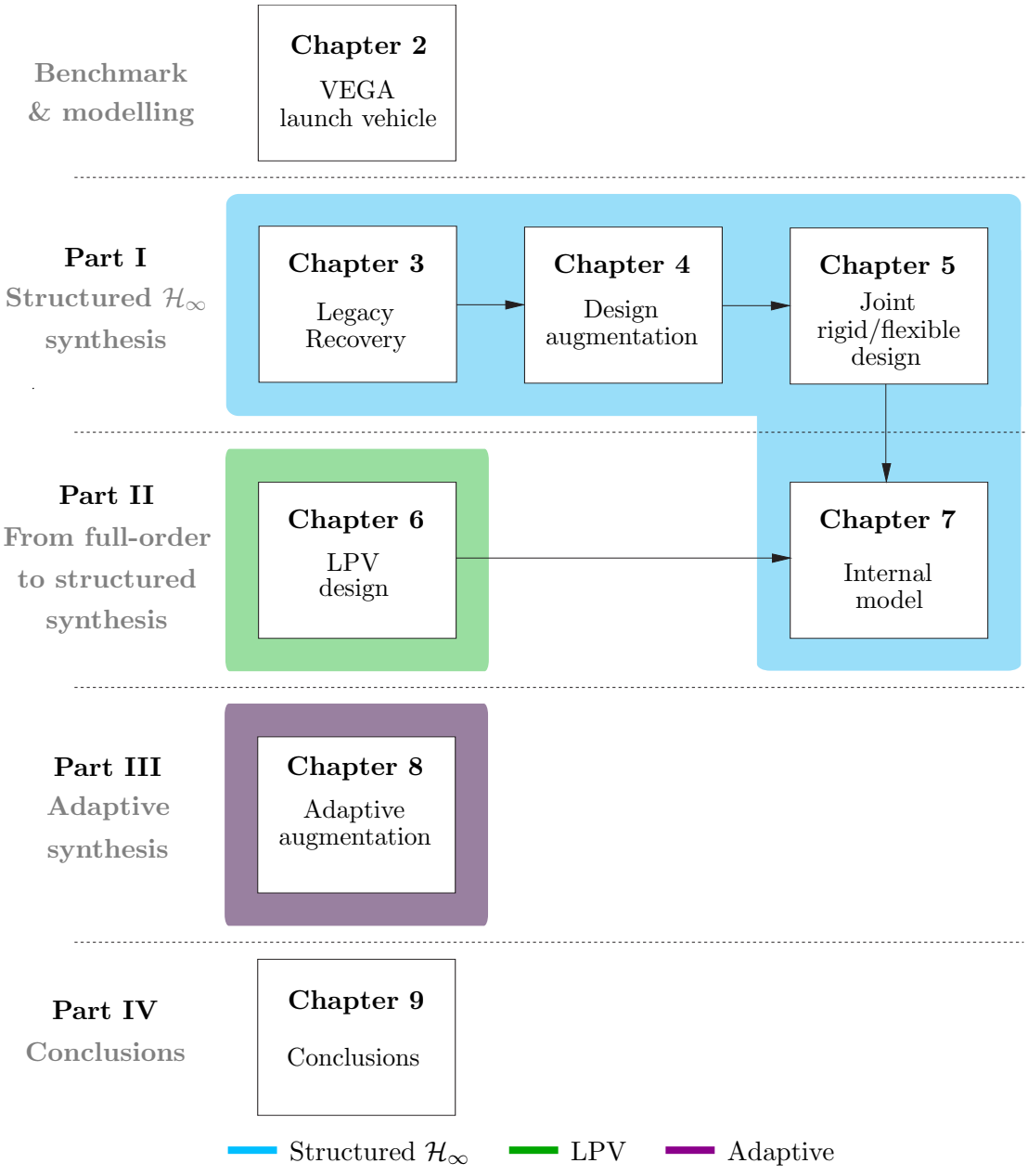

Figure 1.2: PhD thesis layout

Chapter 2 describes the VEGA launch vehicle and its GNC atmospheric phase architecture. The equations of motion of the launch vehicle are derived and expressed in a state-space representation. In addition, the Linear Fractional Transformation (LFT) formulation and modelling approach used to capture system uncertainties is presented. Finally, this chapter also describes the main requirements for the first phase of the VEGA mission and the high-fidelity, nonlinear simulator employed in this thesis for V&V purposes.

Part I proposes a systematic robust control synthesis framework based on the structured $\mathcal{H}_\infty$ approach for the design of the atmospheric TVC system of the VEGA launcher. Part I comprises Chapters 3, 4 and 5, which are described next.

In Chapter 3, the structured $\mathcal{H}_\infty$ approach is presented and applied to the actual VEGA VV05 mission data to recover the baseline rigid-body mission controller. This chapter provides key guidelines to formulate the atmospheric-phase TVC control synthesis as a robust control problem. The VEGA legacy control recovery is exemplified in a linear design point and then validated using the high-fidelity, nonlinear simulator described in Chapter 2.

Chapter 4 explores the potential for improvement offered by the structured $\mathcal{H}_\infty$ design framework over the classical design techniques to design the atmospheric-phase TVC rigid-body controller of a launch vehicle. The design interconnection is first augmented by including a wind turbulence model and subsequently by incorporating system parametric uncertainties. These two augmenting design capabilities are exemplified via representative design examples.

In Chapter 5 the flexible-body dynamics of the launcher are also considered to jointly address the design of the TVC rigid-body controller and the bending filters. This chapter describes how to formulate the structured $\mathcal{H}_\infty$ approach to perform this joint design.

Part II presents the capabilities of the LPV synthesis technique for launch vehicle control design. In addition, this part also shows how to augment the current VEGA TVC architecture based on the knowledge from a full-order LPV design. This part is organised in two chapters.

Chapter 6 presents an LPV control synthesis for the VEGA atmospheric-phase TVC system. A cursory introduction to LPV modelling and synthesis is given. Then, the LPV modelling approach employed for the VEGA launcher is described and a grid-based LPV synthesis technique is applied for the joint design of the TVC rigid-body controller and the bending filters of the VEGA launcher.

In Chapter 7 an indirect method is presented to characterise a wind disturbance internal model that enhances the nominal and robust wind rejection performance capabilities of the current VEGA control system. This internal model can be used as a modular augmentation of the actual VEGA TVC architecture. This process is based on the internal model principle and makes use of the knowledge from the full-order LPV design presented in Chapter 6, which implicitly encapsulates the internal model by design.

Part III explores adaptive features for the VEGA control system (Chapter 8). In particular, an adaptive augmentation control architecture is used to extend the safety envelope capabilities and increase the performance under extreme off-nominal conditions. The adaptive controller is compared to the joint rigid/flexible structured $\mathcal{H}_\infty$ design presented in Chapter 5 and the LPV controller from Chapter 6.

Finally, **Part IV** (Chapter 9) provides the conclusions of this thesis.

1.6 Author's list of publications

During the PhD several journal and conference publications have been achieved. They are listed below. In addition, the connection between these papers and the chapters of this thesis is provided.

Journals

International Journal of Robust and Nonlinear Control, 2019
(**Chapters 3 and 4**)
D. Navarro-Tapia, A. Marcos, P. Simplício, S. Bennani and C. Roux, "Legacy Recovery and Robust Augmentation Structured Design for the VEGA Launcher". *International Journal of Robust and Nonlinear Control.* (Accepted for publication in March 2019).

Conferences

IEEE Conference on Control Applications, September 2016 (**Chapter 3**)
D. Navarro-Tapia, A. Marcos, S. Bennani and C. Roux, "Structured $\mathcal{H}_\infty$ Control Based on Classical Control Parameters for the VEGA Launch Vehicle", in *Proceedings of the IEEE Conference on Control Applications.*

ESA-GNC conference, May 2017 (**Chapter 3**)
D. Navarro-Tapia, A. Marcos, S. Bennani and C. Roux, "Structured $\mathcal{H}_\infty$ Control Design for the VEGA Launch Vehicle: Recovery of the Legacy Control Behaviour", in *Proceedings of the* 10^{th} *International ESA Conference on Guidance, Navigation and Control Systems.*

EUCASS conference, July 2017
D. Navarro-Tapia, A. Marcos, S. Bennani and C. Roux, "Structured $\mathcal{H}_\infty$ and Linear Parameter Varying Control Design for the VEGA Launch Vehicle", in *Proceedings of the* 7^{th} *European Conference for Aeronautics and Space Sciences.*

Joint ROCOND and LPVS conference, September 2018 (**Chapter 6**)
D. Navarro-Tapia, A. Marcos, S. Bennani and C. Roux, "Linear Parameter Varying Control Synthesis for the atmospheric phase VEGA Launcher", in *Proceedings of the Joint* 9^{th} *IFAC Symposium on Robust Control Design and* 2^{nd} *IFAC Workshop on Linear Parameter Varying Systems.*

IAC conference, October 2018 (Chapter 5)
D. Navarro-Tapia, A. Marcos, S. Bennani and C. Roux, "Structured $\mathcal{H}_\infty$ Control Design for the VEGA Launcher Robust Control Design Augmentation", in *Proceedings of the* 69^{th} *International Astronautical Congress.*

ICSC conference, October 2018 (Chapter 7)
D. Navarro-Tapia, A. Marcos, S. Bennani and C. Roux, "Reconciling Full-Order LPV Design and Augmented Structured $\mathcal{H}_\infty$ via Internal Model Principle: a Launch Vehicle Application", in *Proceedings of the* 7^{th} *International Conference on Systems and Control.*

AIAA SciTech Forum conference, January 2019 (Chapter 8)
D. Navarro-Tapia, A. Marcos, S. Bennani and C. Roux, "Robust-Control-Based Design and Comparison of an Adaptive Controller for the VEGA Launcher", in *Proceedings of the 2018 AIAA Guidance, Navigation and Control Conference, AIAA SciTech Forum.*

EUCASS conference, July 2019
D. Navarro-Tapia, A. Marcos, S. Bennani and C. Roux, "Performance and robustness trade-off capabilities for the VEGA launcher TVC system", in *Proceedings of the* 8^{th} *European Conference for Aeronautics and Space Sciences.*

Furthermore, the following publications were achieved from collaborative work performed during the PhD, but not included in this thesis (since it was part of the knowledge acquisition training and not of the specific PhD project).

IFAC conference, July 2017
D. Navarro-Tapia, P. Simplício, A. Iannelli and A. Marcos, "Robust Flare Control Design Using Structured $\mathcal{H}_\infty$ Synthesis: a Civilian Aircraft Landing Challenge", in *Proceedings of the* 20^{th} *World Congress Congress of the International Federation of Automatic Control.*

IFAC conference, July 2017
A. Iannelli, P. Simplício, **D. Navarro-Tapia** and A. Marcos, "LFT Modeling and μ Analysis of the Aircraft Landing Benchmark", in *Proceedings of the* 20^{th} *World Congress Congress of the International Federation of Automatic Control.*

Joint ROCOND and LPVS conference, September 2018
P. Simplício, **D. Navarro-Tapia**, A. Iannelli and A. Marcos, "From Standard to Structured Robust Control Design: Application to Aircraft Automatic Glide-slope Approach", in *Proceedings of the Joint* 9^{th} *IFAC Symposium on Robust Control Design and* 2^{nd} *IFAC Workshop on Linear Parameter Varying Systems.*

CHAPTER 2

VEGA launch vehicle description

This chapter is organised in two main sections. The first section is devoted to introduce the VEGA launcher benchmark. First, the VEGA launch vehicle, its GNC atmospheric phase architecture and the industrial VEGA V&V test plan are described. In addition, the main characteristics of the high-fidelity, nonlinear simulator employed in this thesis are described and the atmospheric requirements for the VEGA mission are presented.

Section 2.2 provides the necessary background on launch vehicle modelling to obtain a physically meaningful representation of the system for analysis and design purposes. The equations of motion of the launch vehicle are first derived and expressed in a state-space representation. Then, the Linear Fractional Transformation (LFT) formulation and modelling approach used to capture system uncertainties is presented. Finally, the verification campaign used in this thesis to analyse TVC systems is described.

2.1 VEGA launcher

2.1.1 Launch vehicle and mission

VEGA (*Vettore Europeo di Generazione Avanzata*) is the new European small launch vehicle developed under the responsibility of ESA and European Launch Vehicle (ELV)/AVIO as prime contractor. The launcher has successfully performed thirteen launches since its maiden flight on 13^{th} February 2012.

VEGA is the smallest European launcher with approximately 30 m in height and a diameter of 3 m. This launch vehicle was developed to address the small and mini-satellites market, covering payloads from 300 kg to 2500 kg. VEGA performs a wide range of missions for Earth observation satellites and many specific purposes using mainly Sun Synchronous Orbits (SSOs) and Low Earth Orbits (LEOs). The VEGA launch site is located in the Guiana Space Centre in Kourou (French Guiana, France).

VEGA is a single-body launcher that follows a four-stage approach (see Figure 2.1). The three first stages are formed by three solid propellant motors (P80, Zefiro 23 and Zefiro 9), whereas the 4^{th} stage, also known as Attitude and Vernier Upper Module (AVUM), is composed of a bi-propellant liquid engine that provides fine attitude control capability and accurate payload orbital insertion. The liquid motor of the AVUM stage can be re-ignited and perform several boosts providing the capability to place multiple payloads into orbit as well as a de-orbiting boost.

All stages are controlled using a TVC system. Each stage is equipped with two orthogonal Electro-Mechanical Actuators (EMAs) that move the nozzle to provide attitude control for pitch and yaw axes [63]. On the other hand, the roll axis is controlled by a RACS, which consists of six on/off Reaction Control Thrusters (RCTs) located at the 4^{th} stage. Moreover, the RACS also perform a fine three-axis attitude control during the AVUM phase.

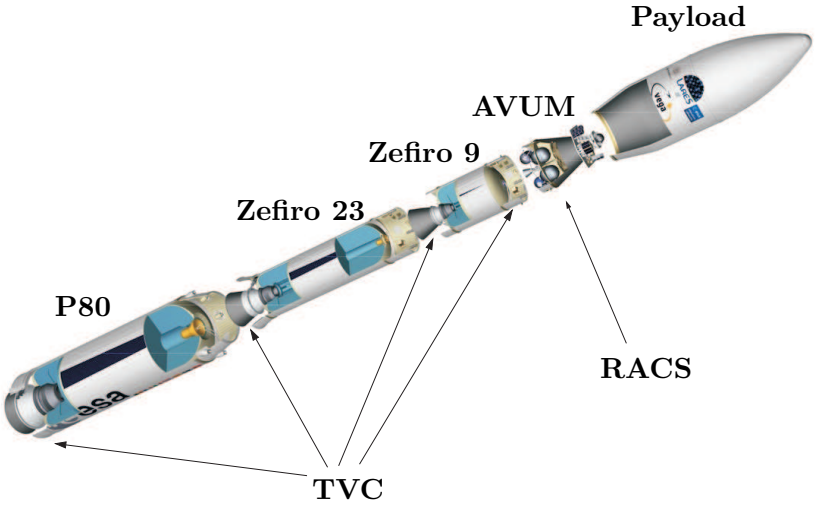

Figure 2.1: VEGA launcher stage configuration [1]

Atmospheric phase

The present study is focused on the atmospheric flight (first stage) of the VEGA launcher. The other stages are comparatively simpler from a control point of view, since only minor external perturbations disturb the vehicle. In particular, all the simulations and designs in this thesis are performed using the actual VEGA 5^{th} flight mission (VV05) data [64]. The payload of this mission was the Sentinel-2A satellite, part of the European Copernicus Earth observation program.

The VEGA atmospheric flight consists of different manoeuvres or events [2]. First, the P80 engine is ignited and the vehicle begins to lift-off. During this event, the main control task is to avoid possible collisions with the launch pad. After four seconds of vertical flight, the launch vehicle initiates a pitch over manoeuvre, also known as gravity turn, that pursues a zero angle of attack trajectory to minimise the aerodynamic loads applied on the vehicle.

During the atmospheric flight, the launch vehicle is heavily impacted by structural loads coming from the high dynamic pressure and changes in the angle of attack due to strong wind gusts. These structural loads are particularly critical between the flight instants t=50 s and t=60 s because during this region the dynamic pressure Q reaches its peak value. Indeed, the dynamic pressure strongly influences the launch vehicle dynamics and also the design of the TVC system. Figure 2.2a shows the evolution of this flight parameter that evolves as $Q = \frac{1}{2}\rho_a V^2$. It increases with the square of the velocity V, but at a certain altitude it starts decreasing once the low air density ρ_a has a predominant effect. Thus, after the maximum dynamic pressure region, the structural loads decrease significantly.

The launch vehicle reaches its maximum acceleration around t=90 s and subsequently when the acceleration reaches a certain level, the thrust is rapidly cut down in the so-called tail-off phase. Finally, the first stage is separated around t=110 s.

Figure 2.2 shows some flight parameters corresponding to the VEGA VV05 mission. It can be seen that these flight parameters have a high time variation during the atmospheric phase, i.e. in less than two minutes, the launch vehicle reaches Mach 5 and approximately 50 km of altitude (see Figure 2.2b).

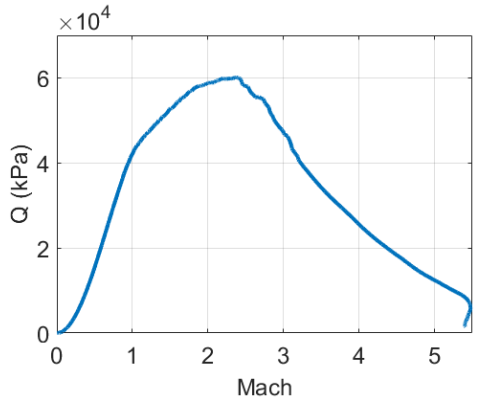

(a) Dynamic pressure versus Mach

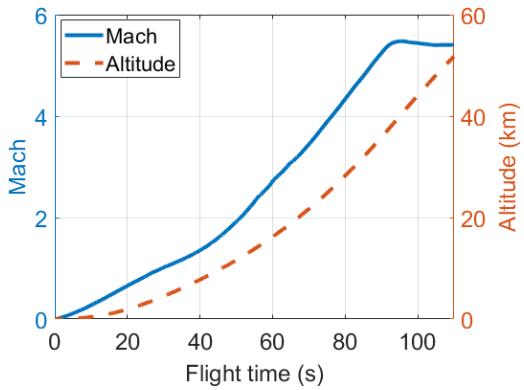

(b) Mach and altitude versus time

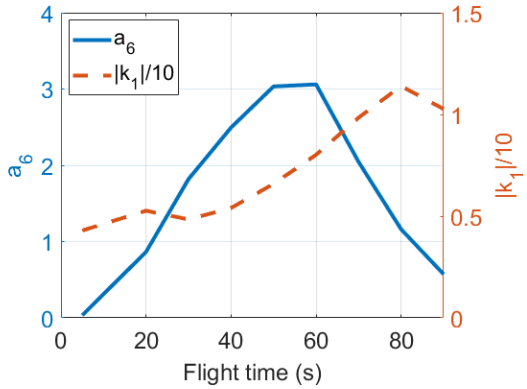

(c) Rigid-body rotational parameters

Figure 2.2: VEGA VV05 mission parameters

Furthermore, Figure 2.2c illustrates the time evolution of two critical parameters in launcher control design, i.e. the aerodynamic instability coefficient a_6 and the control efficiency parameter k_1. These two parameters determine the main rotational rigid-body motion dynamics between the yaw attitude angle ψ and the nozzle deflection angle β_ψ through the relation $\ddot{\psi} = a_6\psi + k_1\beta_\psi$, resulting in the following second order transfer function:

$$G_{LV_{a_6/k_1}}(s) = \frac{\psi(s)}{\beta_\psi(s)} = \frac{k_1}{s^2 - a_6} \tag{2.1}$$

The above model is simple yet significant. Indeed, it is standard in industrial launcher design to start with this rotational relation [2, 18].

2.1.2 GNC architecture

The GNC algorithms of the VEGA launcher are executed by the on-board flight computer, which is located in the avionics bay at the AVUM. The GNC system functions are described in Figure 2.3. First, the navigation system calculates the attitude, position, velocity and acceleration of the launch vehicle based on the measurements from the INS. Then using the outputs of the navigation function, the control system computes the necessary TVC nozzle deflections and RCT activations to follow the attitude commands delivered by the guidance system. For VEGA, this GNC procedure is executed by the flight program software with a sampling period of 40 ms.

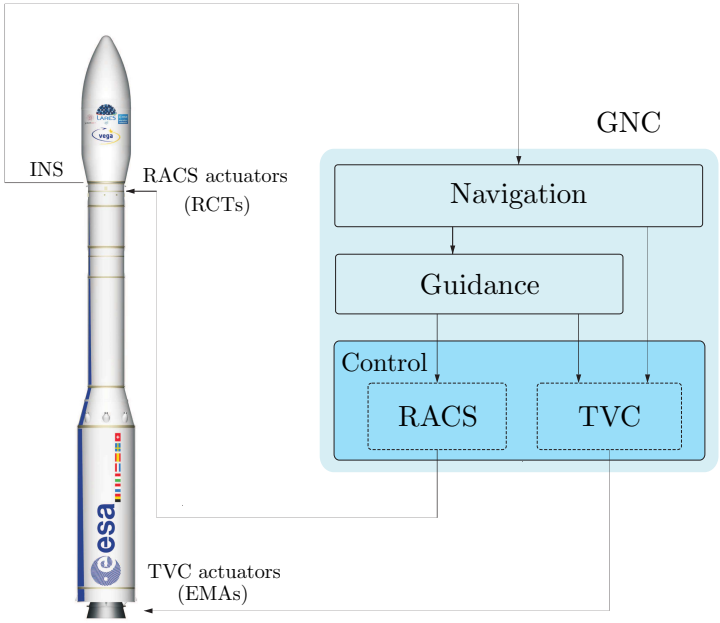

Figure 2.3: VEGA launcher GNC architecture

During the atmospheric phase, the guidance is performed in open-loop following a pre-programmed trajectory based on attitude tables versus a schedule variable (i.e. time or velocity). It is important to remark that a closed-loop guidance configuration would be in conflict with one of the main control tasks of the first stage, which is the load alleviation. In order to limit the structural loads, the control system must keep the angle of attack low in the presence of wind disturbances, which naturally leads to deviations from the reference trajectory. Thus, using guidance in open-loop, the GNC system focuses on controlling the launch vehicle drift for load alleviation purposes. Any final resulting deviations from the nominal trajectory are subsequently corrected during the upper stages using closed-loop guidance.

In addition, it should be remarked that the RACS only limits the maximum roll rate during the first stage. The main reason is that the RCT actuators are not strong enough to set the roll rate to zero due to the high moment of inertia that the launch vehicle exhibits during the atmospheric flight. As a solution, the roll rate is only bounded, which means that the RACS will only act if the roll rate is over a certain threshold. In fact, the telemetry from real flights shows that there are typically no RCT activations during the first stage. For all these reasons, the aim of this research focuses on the design of the VEGA TVC system.

Figure 2.4 describes the atmospheric-flight TVC control architecture for the VEGA launcher in the yaw channel, which results in a 26^{th} order controller. This controller receives as inputs the yaw attitude error ψ_e and the lateral deviations (both in position z_e and velocity $\dot{z}_e$) with respect to the reference trajectory and calculates the required yaw nozzle deflection $\beta_{\psi c}$ to follow the guidance commands. The control law is based on a classical structure formed by:

- PD controller on attitude ($K_{\psi p}$ and $K_{\psi d}$) to stabilise and control the launch vehicle;
- Lateral control feedback composed of a PD controller on drift (K_z and $K_{\dot{z}}$) to limit the lateral deviations of the vehicle and minimise the angle of attack for loads alleviation;
- Set of filters with different purposes: $H_1(s)$ is added to improve the rigid-body stability margins; $H_2(s)$ performs a derivative action to compute the attitude rate error signal $\dot{\psi}_e$; $H_3(s)$ notches the first bending mode and attenuates the upper bending modes; and $H_4(s)$ is a low-pass filter that reinforces the high-frequency attenuation on the drift channels.

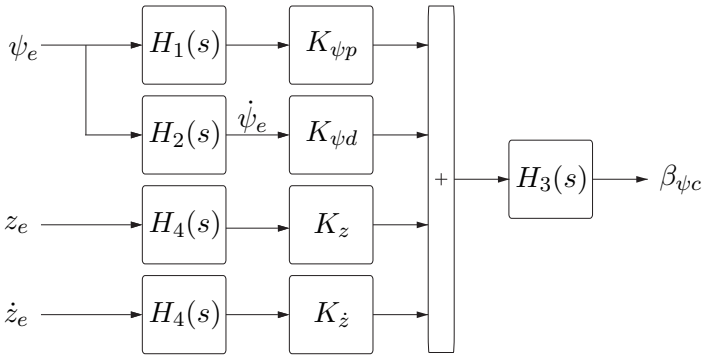

Figure 2.4: VEGA TVC control architecture

As mentioned before, the TVC system provides control for pitch and yaw axes. Due to axial symmetry of the VEGA launcher about the roll axis, pitch and yaw axes can be considered decoupled and more importantly identical. Thus, the same TVC controller described above is also applied to the pitch axis resulting in a pitch nozzle deflection command $\beta_{\theta c}$. Both nozzle angle commands ($\beta_{\psi c}$ and $\beta_{\theta c}$) are finally transformed into EMA elongations and contractions for TVC actuation. Note that this decoupling strategy is only valid if the roll rate is considered negligible, which is a standard assumption in launch vehicle TVC designs. The existing coupling between pitch and yaw axes due to roll rate is typically considered as a disturbance and subsequently examined ad hoc [65].

In order to cope with the large dynamical system variations, different controllers must be designed along the atmospheric trajectory at distinct operational design points. In particular, the VEGA launcher uses 12 linear design sets at approximately every 10 s except at lift- and tail-off phases. The VEGA design interval is a good trade-off to address the fast-changing characteristics of the system while featuring a reasonable complexity for design. Recall that the design of each of the linear controllers is a highly time-consuming task, and thus, more design points would significantly increase the complexity of the every GNC mission development. Finally, all the controller gains and filters are discretised and scheduled versus the non-gravitational velocity.

2.1.3 VEGA launcher verification and validation

The TVC and RACS control designs are all tested prior each mission in an extensive analysis coverage to verify and validate that the GNC algorithms work as expected and also that all the control mission requirements are met.

This V&V phase involves analyses in both the time and frequency domain. On the one hand, time-domain simulations are well suited to evaluate performance metrics. This is normally carried out using high-fidelity, 6 DoF, nonlinear models which are highly representative of the real launcher system. On the other hand, frequency-domain approaches are generally employed to analyse the stability of the launch vehicle using LTI models. Although the stability can also be assessed in the time domain, the frequency domain provides very valuable information on how close the system is to instability via the well-known stability margins. In addition, it allows to analyse the stability of the system with respect to different effects in the frequency spectrum of the launch vehicle (i.e. aerodynamics, TVC actuator, bending modes, etc).

The GNC V&V test plan for the VEGA launcher [2, 12, 66] is traditionally performed in several steps:

1. For each stage, the stability of the vehicle is evaluated using frequency-domain approaches. For instance, for the atmospheric stage the stability analysis is performed every 1 second;

2. If the stability requirements are met, then the control performance requirements are evaluated in the time domain for each stage separately and subsequently by simulating all the stages together;
3. In a third step, if stability and performance specifications are satisfied, Software-In-the-Loop (SWIL) and Hardware-In-the-Loop (HWIL) campaigns are carried out to test that the GNC algorithms run properly and that the level of performance using the real on-board equipment (computers, buses, actuators) is the adequate.

2.1.4 VEGA high-fidelity, nonlinear simulator

The high-fidelity, nonlinear 6 DoF simulator used in this work for V&V purposes is called VEGACONTROL. It is implemented in Matlab/Simulink using protected blocks and compiled code due to proprietary reasons (see Figure 2.5). This nonlinear simulator was developed by ELV based on the official simulator used in the VEGA program to verify and validate the GNC designs and algorithms of each mission. It is tailored to only simulate the VEGA launcher atmospheric phase and is prepared for accelerated-time simulations. Nonetheless, it is important to highlight that the provided simulator was found [67] to be highly representative of the real launch system during the atmospheric flight.

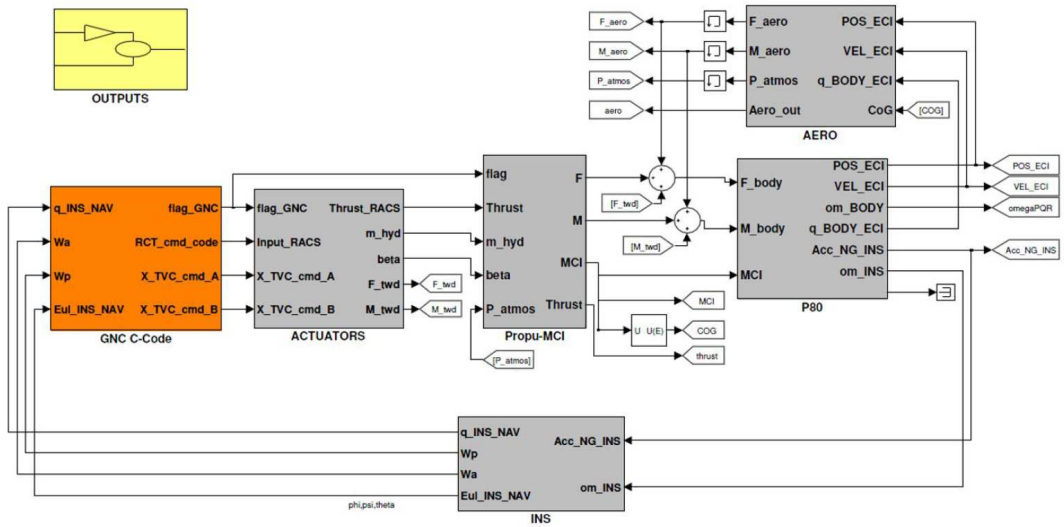

Figure 2.5: VEGACONTROL Simulink implementation

The nonlinear simulator allows to scatter more than 125 different operational parameters by means of normalised flags with the range $[-1, 1]$. Among these parameters are mass-center-inertia and aerodynamics parameters, INS mounting, thrust offset and misalignment scatterings and also bending mode properties. In addition, this analysis tool allows to perform simulations with different wind profiles (such as those shown later in Figure 2.8).

The high-level architecture of this simulator is composed of four main model blocks, see Figure 2.6.

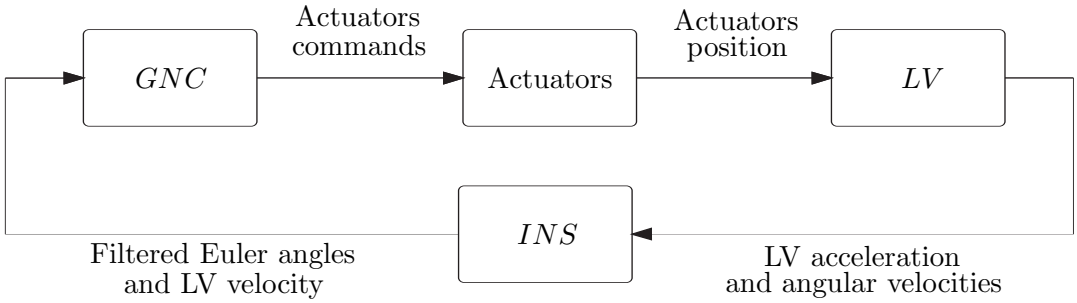

Figure 2.6: Simplified diagram block of VEGACONTROL simulator

The launch vehicle (LV) model contains the 6 DoF motion of the vehicle, which includes:

- 6 DoF rigid-body model, accounting for the rotational and translational dynamics of the vehicle;
- Elastic and sloshing modes;
- Tail-wag-dog effect, including the inertia forces and moments created by the motion of the gimbaled engines;
- Full external environment (rotating Earth, atmosphere and wind);
- Nonlinear aerodynamics (including aero-elastic effects);
- Disturbances (bias, offsets).

The INS block includes a detailed model of the measurement unit (calibration and mounting errors, quantisation and noise on measured velocity and angles) while the GNC model comprises a full representative code implementing the actual VEGA GNC and flight management algorithms. This block uses the measurements from the INS to compute the necessary nozzle deflections to follow the attitude commands from the guidance function. It is important to highlight that the GNC model (see orange block in Figure 2.5) is accessible and can be used to implement other controllers. Finally, the actuators block incorporates a detailed model of the nonlinear TVC actuators (with saturations in deflection and rate, backlash, delays and bias) and also of the RACS with thermal and thrust dynamics.

2.1.5 Atmospheric-phase VEGA TVC requirements

The TVC system must ensure stability to guidance commands while satisfying very demanding and tight performance requirements in the presence of external disturbances and parametric uncertainty. The most relevant specifications for the atmospheric phase are listed in Table 2.1.

Table 2.1: Main VEGA stability and performance requirements for the atmospheric phase

	Requirements	Metrics		Bounds
Stability	Rigid-body margins	LF-GM	Nominal	$\geq 6\,\text{dB}$
			Dispersed	$\geq 0.5\,\text{dB}$
		DM	Nominal	$\geq 100\,\text{ms}$
			Dispersed	$\geq 40\,\text{ms}$
		HF-GM	Nominal	$\leq$ -6 dB
			Dispersed	$\leq$ -3 dB
	Flexible-body margins	GM_f	Nominal	$\leq$ -3 dB
			Dispersed	
		DM_f	Nominal	$\geq 50\,\text{ms}$
			Dispersed	$\geq 20\,\text{ms}$
Performance	Load performance	Q_α		$< Q_\alpha$ envelope
	Lateral control performance	Position (y, z)		$< 500\,\text{m}$
		Velocity $(\dot{y},\dot{z})$		$< 15\,\text{m/s}$
	Actuation performance	β		$< 6.5°$
		Integrated angle		$< 250°$

Stability requirements

The V&V VEGA program defines stability requirements for both nominal and scattered conditions. Three rigid-body margins are considered: Low-Frequency Gain Margin (LF-GM), Delay Margin (DM) and High-Frequency Gain Margin (HF-GM). In addition, a gain margin (GM_f) and a delay margin (DM_f) are defined for gain- and phase-stabilised bending modes respectively. Note that due to industrial heritage from the Ariane launch vehicle program, Phase Margins (PMs) are expressed as the equivalent delay at the frequency ω at which the margin is computed $\big($i.e. DM $= \frac{\pi}{180}$ PM$/\omega$ with DM in s, PM in deg and ω in rad/s$\big)$.

The stability of the VEGA TVC system is traditionally analysed in the frequency domain in terms of the classical stability margins described above. Figure 2.7 illustrates the stability margin requirements for the VEGA launcher using a Nichols chart (the most common frequency visualisation plot used in launcher control design [8]). It can be seen that the margin specifications are defined for each crossing frequency around the critical instability points (indicated in the Nichols chart as red crosses).

It is important to remark that the stability specifications presented in Table 2.1 are to be verified considering a low roll rate assumption, and thus, this stability test can be performed in either the pitch or the yaw axis. The V&V VEGA program [2, 12, 66] also determines margins for a Multiple-Input Multiple-Output (MIMO) case in which pitch and yaw axes are coupled by a constant roll rate. The latter MIMO analysis is be covered in this thesis.

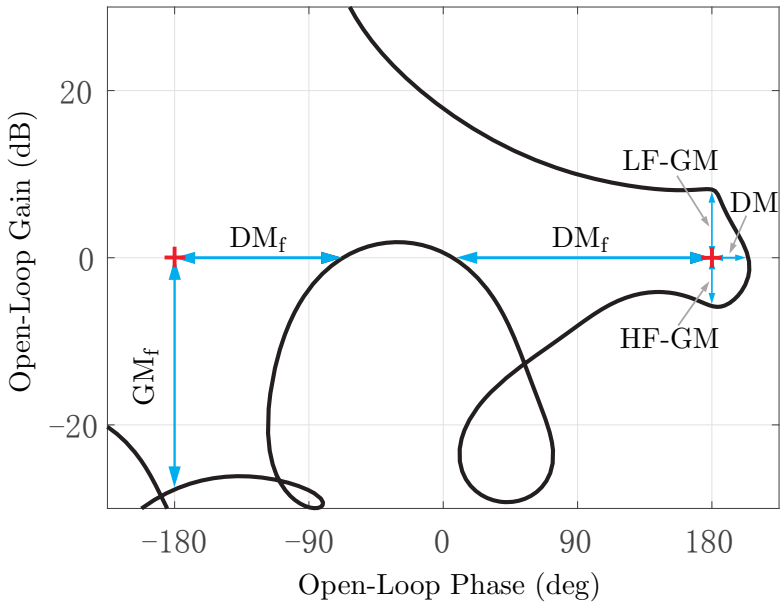

Figure 2.7: VEGA stability margin specifications

Performance requirements

Performance requirements are verified via time-domain MC simulations using a nonlinear, high-fidelity 6 DoF simulator. The different performance metrics shown in Table 2.1 must remain below given bounds in the face of parameter dispersion and disturbances such as noise and wind.

One of the main tasks of the atmospheric-flight TVC system is to keep the structural loads within a given envelope defined based on Mach number. This load requirement is expressed as a function of $Q\alpha$, which is the product of the dynamic pressure Q and the angle of attack α. In fact, due to its dependency on the angle of attack, $Q\alpha$ is evidently sensitive to wind disturbances as it can be seen in Figure 2.8. This plot shows the $Q\alpha$ responses corresponding to the same mission data and trajectory (the 5^{th} VEGA flight, VV05) but using different wind profiles (as measured at the launch site in French Guiana in the date indicated in the figure legend). Therefore, the control system must be particularly robust against moderate and strong wind gusts at different altitudes.

Furthermore, since the guidance is in open loop, the TVC system must also limit the drift with respect to the reference trajectory in both position (y, z) and velocity $(\dot{y}, \dot{z})$. It is also important to limit the actuation effort to avoid the saturation of the actuators and also reduce TVC consumption.

Although not covered in this thesis, the TVC validation plan also includes requirements for the lift off to avoid a collision with the launch tower and also for the tail off to ensure an adequate stage separation. In addition, there are also control requirements for the RACS, which validate its control accuracy and general functioning (i.e. consumption, maximum number of RCT activations).

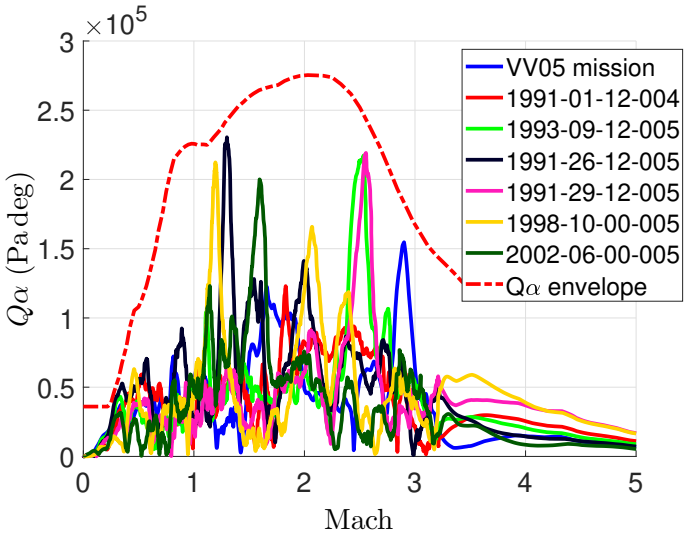

Figure 2.8: Effect of wind disturbance on the structural load requirement $Q\alpha$

2.2 VEGA launcher models and verification campaign

2.2.1 VEGA launch vehicle model

The motion of the vehicle is described by the standard 6 DoF equations of motion, which account for the translational and rotational dynamics of the launch vehicle. The derivation of the equations of motion of a generic launch vehicle can be found in reference [68].

The VEGA launch vehicle model is derived assuming that pitch and yaw axes are decoupled. In this section, the launcher model will be examined in the yaw plane, see Figure 2.9. The dynamics of the vehicle are described using a body-fixed frame (X_b, Z_b) with respect to a trajectory reference frame (X_T, Z_T) with X_T tangent to the ascent trajectory. Note that both reference frames are centred at the Center of Gravity (CG) of the vehicle. It is also important to remark that the trajectory reference frame can be considered an Earth-centred inertial frame because the Earth's rotation is negligible for the duration of the atmospheric flight [68, 69, 43].

The equations of motions are derived using two assumptions which are standard practice in launcher control design. First, it is considered that the vehicle will follow a gravity turn manoeuvre throughout the atmospheric flight. This manoeuvre uses a commanded pitch programme that equalises the gravitational acceleration with the inertial centripetal acceleration, and thus, the gravity term mg (see Figure 2.9) can be disregarded. A complete analytical demonstration of this assumption can be found in reference [43]. Second, the longitudinal dynamics are traditionally neglected because they are scarcely affected by small perturbations [68, 70]. This allows to simplify the model to a 2 DoF problem, described by Equations 2.2 and 2.3, which accounts for the translation in the Z_T axis and the rotation in the yaw plane.

Both translational and rotational dynamics are expressed as the sum of forces and moments from rigid-body (F_R, M_R), flexible-body (F_F, M_F) and nozzle motion dynamics (F_N, M_N). The latter is also known as the Tail-Wag-Dog (TWD) effect in the launcher field. In addition, other contributions such as wind disturbances are included via the corresponding forces and moments. Note that the forces and moments generated by the propellant sloshing modes are not included in the model due to their negligible impact on the vehicle during the atmospheric phase.

$$m\ddot{z} = \Sigma F_\psi = F_R + F_F + F_N \tag{2.2}$$

$$\mathrm{I_{yy}}\ddot{\psi} = \Sigma M_\psi = M_R + M_F + M_N \tag{2.3}$$

where m is the vehicle mass, $\mathrm{I_{yy}}$ is the lateral moment of inertia, $\ddot{z}$ is the linear drift acceleration and $\ddot{\psi}$ the yaw attitude acceleration.

2.2.1.1 Rigid-body dynamics

The rigid-body model describes the launch vehicle motion due to thrust and aerodynamics. The yaw-plane rigid-body model is illustrated in Figure 2.9.

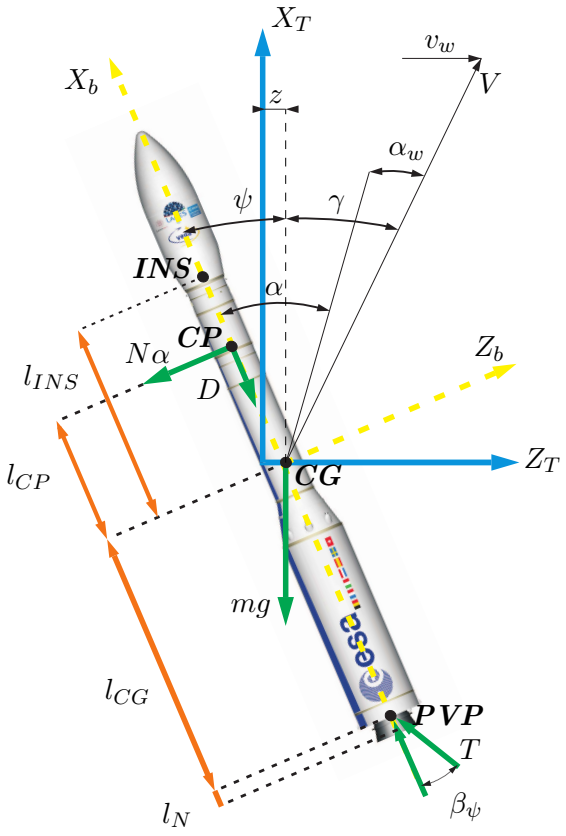

Figure 2.9: Rigid-body diagram

Using small-angle approximations and a gravity turn assumption, the rigid-body motion forces F_R and moments M_R in the inertial coordinate frame are given by:

$$F_R = -(T-D)\psi - N\alpha - T\beta_\psi \tag{2.4}$$

$$M_R = N\alpha l_{CP} - T\beta_\psi l_{CG} \tag{2.5}$$

where T is the gimbaled thrust force, D the aerodynamic drag force and $N\alpha$ the force gradient with respect to the angle of attack α. The latter is formed by $N = QS_{ref}C_{N\alpha}$, where Q is the dynamic pressure, S_{ref} is the launcher reference area and $C_{N\alpha}$ is the lift coefficient gradient with respect to α. The distance from the CG x-coordinate x_{CG} to the aerodynamic Center of Pressure (CP) x-coordinate x_{CP} is given by l_{CP} while l_{CG} is the distance from CG to the nozzle Pivot Point (PVP).

The main angles in this dynamic model are the yaw attitude angle ψ, the actuator deflection in the yaw plane β_ψ and the angle of attack α. Note that the latter is described by a component with respect to the ground ($\alpha_{ground} = \psi + \dot{z}/V$) and a wind induced term ($\alpha_w = v_w/V$) as follows:

$$\alpha = \alpha_{ground} - \alpha_w = \psi + \frac{\dot{z}}{V} - \frac{v_w}{V} \tag{2.6}$$

where $\dot{z}/V$ is the drift angle γ, V the vehicle velocity with respect to the ground and v_w the wind velocity.

2.2.1.2 Flexible-body dynamics

The flexible-body model represents the elastic behaviour of the launch vehicle, which is described in Figure 2.10.

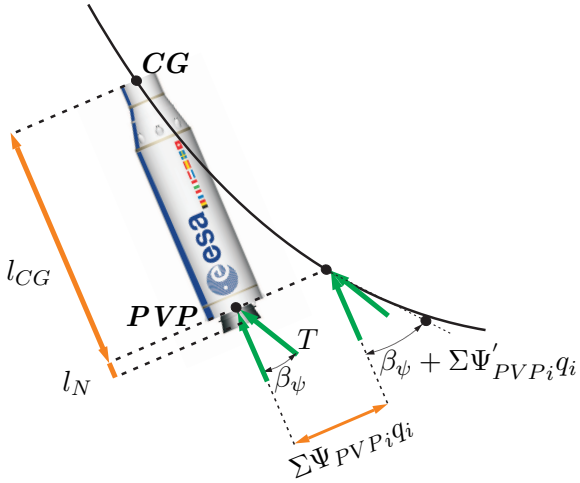

Figure 2.10: Flexible-body diagram

The flexible behaviour of the launch vehicle is characterised by several resonant modes. The dynamics of the i^{th} bending mode is represented by the following 2^{nd} order model with natural frequency ω_{q_i} and damping ratio ζ_{q_i} [69, 71]:

$$\ddot{q}_i + 2\zeta_{q_i}\omega_{q_i}\dot{q}_i + \omega_{q_i}^2 q_i = -T\Psi_{PVPi}\beta_\psi - \left(m_N l_N \Psi_{PVPi} - \mathrm{I_N}\Psi'_{PVPi}\right)\ddot{\beta}_\psi \tag{2.7}$$

where q_i is the state of the i^{th} bending mode, and Ψ'_{PVPi} and Ψ_{PVPi} are the rotational and translational lengths of the i^{th} bending mode at PVP respectively. Moreover, $\ddot{\beta}_\psi$ is the acceleration of the actuator in the yaw plane, m_N is the nozzle mass and l_N is the distance from the nozzle center of gravity to the PVP. Finally, $\mathrm{I_N}$ is the moment of inertia of the nozzle engine about the PVP and is given by $\mathrm{I_N} = \mathrm{I_o} + m_N l_N^2$, with $\mathrm{I_o}$ the moment of inertia of the nozzle engine about its center of gravity.

The bending modes produce additional lateral forces and create a local rotation added to the commanded gimbaled angle β_ψ. The inertial-frame flexible-body motion forces (F_F) and moments (M_F) considering k bending modes are given by:

$$F_F = T \sum_{i=1}^{k} \Psi'_{PVPi} q_i \tag{2.8}$$

$$M_F = -T\Big(l_{CG} \sum_{i=1}^{k} \Psi'_{PVPi} q_i + \sum_{i=1}^{k} \Psi_{PVPi} q_i\Big) \tag{2.9}$$

2.2.1.3 Nozzle dynamics

The motion of the gimbaled engines creates inertia forces and torques (the aforementioned TWD effect), which must be taken into account. The lateral force F_N and moment M_N due to nozzle dynamics are given by:

$$F_N = -m_N l_N \ddot{\beta}_\psi \tag{2.10}$$

$$M_N = -(m_N l_N l_{CG} + \mathrm{I_N})\ddot{\beta}_\psi \tag{2.11}$$

2.2.1.4 Sensors characterisation

The sensed values are defined at the node location of the INS, which is installed in the upper stage at a distance l_{INS} from CG (see Figure 2.9). In addition, the influence of the flexible-body motion at the sensor location must also be considered. The sensed attitude, drift and their derivatives are given by:

$$\psi_{INS} = \psi - \sum_{i=1}^{k} \Psi'_{INSi} q_i \tag{2.12}$$

$$\dot{\psi}_{INS} = \dot{\psi} - \sum_{i=1}^{k} \Psi'_{INSi} \dot{q}_i \tag{2.13}$$

$$z_{INS} = z - l_{INS}\psi + \sum_{i=1}^{k} \Psi_{INSi} q_i \tag{2.14}$$

$$\dot{z}_{INS} = \dot{z} - l_{INS}\dot{\psi} + \sum_{i=1}^{k} \Psi_{INSi} \dot{q}_i \tag{2.15}$$

where Ψ'_{INSi} and Ψ_{INSi} are the rotational and translational lengths of the i^{th} bending mode at INS respectively.

2.2.1.5 State-space representation

The equations of motion and sensors dynamics are typically expressed as a state-space form, which is a suitable representation for analysis and design. Thus, following the procedure described in reference [69], all the relevant dynamics are formulated using the state-space representation shown in Equation 2.16, where the rigid and flexible-body contributions are expressed separately.

$$\underbrace{\begin{aligned}\begin{bmatrix}\dot{\mathbf{x_R}}\\ \dot{\mathbf{x_F}}\end{bmatrix} &= \left[\begin{array}{c|c} A_R & A_{RF} \\ \hline A_{FR} & A_F \end{array}\right]\begin{bmatrix}\mathbf{x_R}\\ \mathbf{x_F}\end{bmatrix} + \begin{bmatrix}B_R\\ B_F\end{bmatrix}\mathbf{u_{LV}} \\ \mathbf{y_{LV}} &= \left[\begin{array}{c|c} C_R & C_F \end{array}\right]\begin{bmatrix}\mathbf{x_R}\\ \mathbf{x_F}\end{bmatrix} + D_R\ \mathbf{u_{LV}}\end{aligned}}_{G_{LV_{RF}}(s)} \tag{2.16}$$

The launch vehicle model $G_{LV_{RF}}(s)$ uses four rigid-body states given by the drift z, yaw attitude angle ψ and their derivatives $\left(\mathbf{x_R} = \begin{bmatrix} z & \dot{z} & \psi & \dot{\psi}\end{bmatrix}^T\right)$; $2k$ flexible-body states accounting for k bending modes $\left(\mathbf{x_F} = \begin{bmatrix}\mathbf{q} & \dot{\mathbf{q}}\end{bmatrix}^T \text{ with } \mathbf{q} = \begin{bmatrix}q_1 \cdots q_k\end{bmatrix} \text{ and } \dot{\mathbf{q}} = \begin{bmatrix}\dot{q}_1 \cdots \dot{q}_k\end{bmatrix}\right)$; five outputs $\left(\mathbf{y_{LV}} = \begin{bmatrix}Q\alpha & \psi_{INS} & \dot{\psi}_{INS} & z_{INS} & \dot{z}_{INS}\end{bmatrix}^T\right)$, which include the load performance indicator $Q\alpha$ and the measurements at INS node location for the four rigid-body states; and three inputs $\left(\mathbf{u_{LV}} = \begin{bmatrix}\beta_\psi & \ddot{\beta}_\psi & v_w\end{bmatrix}^T\right)$. Note that the acceleration of the actual nozzle deflection (i.e. $\ddot{\beta}_\psi$) is considered as an input system to account for the aforementioned TWD effect.

The matrices of the state-space model are given as follows:

$$\begin{bmatrix}\dot{z}\\ \ddot{z}\\ \dot{\psi}\\ \ddot{\psi}\\ \hline \dot{\mathbf{q}}\\ \ddot{\mathbf{q}}\end{bmatrix} = \left[\begin{array}{cccc|cc} 0 & 1 & 0 & 0 & \mathbf{0_{1k}} & \mathbf{0_{1k}} \\ 0 & a_1 & a_3 & a_2 & \mathbf{a_{zq}} & \mathbf{0_{1k}} \\ 0 & 0 & 0 & 1 & \mathbf{0_{1k}} & \mathbf{0_{1k}} \\ 0 & a_4 & a_6 & a_5 & \mathbf{a_{\psi q}} & \mathbf{0_{1k}} \\ \hline \mathbf{0_{k1}} & \mathbf{0_{k1}} & \mathbf{0_{k1}} & \mathbf{0_{k1}} & \mathbf{0_{kk}} & \mathbf{I_k} \\ \mathbf{0_{k1}} & \mathbf{0_{k1}} & \mathbf{0_{k1}} & \mathbf{0_{k1}} & \mathbf{a_{qq}} & \mathbf{a_{q\dot{q}}} \end{array}\right]\begin{bmatrix}z\\ \dot{z}\\ \psi\\ \dot{\psi}\\ \hline \mathbf{q}\\ \dot{\mathbf{q}}\end{bmatrix} + \left[\begin{array}{ccc} 0 & 0 & 0 \\ a_p & k_2 & -a_1 \\ 0 & 0 & 0 \\ k_1 & k_3 & -a_4 \\ \hline \mathbf{0_{k1}} & \mathbf{0_{k1}} & \mathbf{0_{k1}} \\ \mathbf{a_{q\beta}} & \mathbf{a_{q\ddot{\beta}}} & \mathbf{0_{k1}} \end{array}\right]\begin{bmatrix}\beta_\psi\\ \ddot{\beta}_\psi\\ v_w\end{bmatrix} \tag{2.17}$$

$$\begin{bmatrix}Q\alpha\\ \psi_{INS}\\ \dot{\psi}_{INS}\\ z_{INS}\\ \dot{z}_{INS}\end{bmatrix} = \left[\begin{array}{cccc|cc} 0 & Q/V & Q & 0 & \mathbf{0_{1k}} & \mathbf{0_{1k}} \\ 0 & 0 & 1 & 0 & -\mathbf{a_{\Psi' q}} & \mathbf{0_{1k}} \\ 0 & 0 & 0 & 1 & \mathbf{0_{1k}} & -\mathbf{a_{\Psi' q}} \\ 1 & 0 & -l_{INS} & 0 & \mathbf{a_{\Psi q}} & \mathbf{0_{1k}} \\ 0 & 1 & 0 & -l_{INS} & \mathbf{0_{1k}} & \mathbf{a_{\Psi q}} \end{array}\right]\begin{bmatrix}z\\ \dot{z}\\ \psi\\ \dot{\psi}\\ \hline \mathbf{q}\\ \dot{\mathbf{q}}\end{bmatrix} + \begin{bmatrix} 0 & 0 & -Q/V \\ 0 & 0 & 0 \\ 0 & 0 & 0 \\ 0 & 0 & 0 \\ 0 & 0 & 0 \end{bmatrix}\begin{bmatrix}\beta_\psi\\ \ddot{\beta}_\psi\\ v_w\end{bmatrix}$$

where $\mathbf{0_{ij}}$ is an $i \times j$ matrix filled with zeros and $\mathbf{I_i}$ is the identity matrix of size i. The rigid-body and flexible-body matrix coefficients are defined in terms of the physical parameters given in Equations 2.18 and 2.19 respectively.

$$
\begin{array}{lll}
a_1 = \frac{-N}{mV}; & a_2 = -a_1 l_{CP}; & a_3 = -acc + a_1 V; \\
a_p = -\frac{T}{m}; & k_2 = \frac{m_N}{m} l_N; & acc = \frac{T-D}{m}; \\
a_4 = \frac{N}{\mathrm{I_{yy}} V} l_{CP}; & a_5 = -a_4 l_{CP}; & a_6 = a_4 V; \\
k_1 = -\frac{T}{\mathrm{I_{yy}}} l_{CG}; & k_3 = \frac{1}{\mathrm{I_{yy}}}(m_N l_N l_{CG} - \mathrm{I_N}); &
\end{array}
\tag{2.18}
$$

$$
\begin{array}{ll}
\mathbf{a_{zq}} = \left[a_{zq_1} \cdots a_{zq_k} \right] & \text{with } a_{zq_k} = \dfrac{T}{m} \Psi'_{PVPk}; \\
\mathbf{a_{\psi q}} = \left[a_{\psi q_1} \cdots a_{\psi q_k} \right] & \text{with } a_{\psi q_k} = \dfrac{T}{\mathrm{I_{yy}}} (\Psi'_{PVPk} l_{CG} + \Psi_{PVPk}); \\
\mathbf{a_{q\beta}} = \left[a_{q\beta_1} \cdots a_{q\beta_k} \right]^T & \text{with } a_{q\beta_k} = -T \Psi_{PVPk}; \\
\mathbf{a_{q\ddot{\beta}}} = \left[a_{q\ddot{\beta}_1} \cdots a_{q\ddot{\beta}_k} \right]^T & \text{with } a_{q\ddot{\beta}_k} = \mathrm{I_N} \Psi'_{PVPk} - m_N l_N \Psi_{PVPk}; \\
\mathbf{a_{qq}} = diag\left(a_{qq_1} \cdots a_{qq_k} \right) & \text{with } a_{qq_k} = -\omega_{q_k}^2; \\
\mathbf{a_{q\dot{q}}} = diag\left(a_{q\dot{q}_1} \cdots a_{q\dot{q}_k} \right) & \text{with } a_{q\dot{q}_k} = -2\zeta_{q_k}\omega_{q_k}; \\
\mathbf{a_{\Psi q}} = \left[\Psi_{INS1} \cdots \Psi_{INSk} \right]; & \\
\mathbf{a_{\Psi' q}} = \left[\Psi'_{INS1} \cdots \Psi'_{INSk} \right]; &
\end{array}
\tag{2.19}
$$

For design and analysis purposes, the launch vehicle state-space model of Equation 2.17 is used to derive nominal LTI models at different operating points along the atmospheric phase considering that the parameters are frozen in time.

As mentioned in Section 2.1.1, all physical parameters vary greatly during the atmospheric phase. To illustrate this, the frequency responses of the nominal launch vehicle model at different flight instants are shown in Figure 2.11a. It can be seen in Figure 2.11a that the magnitude evolves with time presenting different characteristics throughout the atmospheric phase. This is clearly seen for the rigid-body dynamics in the low frequency region [0.001 10] rad/s and also for the flexible-body dynamics in the high frequency region. This plot also shows that the frequency of each bending mode peak increases with time. Note that only the first two bending modes are modelled, since they are the most relevant for TVC system design.

The behaviour described above is also confirmed looking at the pole migration map shown in Figure 2.11b. The launch vehicle model presents eight poles, four rigid-body and four flexible-body poles accounting for the two bending modes. It should be remarked that, as typical for launcher systems in open-loop, two of the rigid-body poles are unstable. The main stabilisation control problem comes from the larger unstable pole, which is mainly governed by the rotational motion of the vehicle and it is approximately placed at $s = \sqrt{a_6}$ (recall Equation 2.1). This pole highly varies with time and since a_6 is proportional to Q (see Figure 2.2) it reaches its maximum value around the maximum dynamic pressure region ($t = 50 - 60s$). Besides the stabilisation issue, the control problem is also very challenging from a performance point of view because the launch vehicle encounters the highest aerodynamic loads around this region. This demands more control actuation in order to counteract the torque generated by the structural loads. With respect to the second unstable pole, which is closer to the origin, it is mainly caused by the translational motion of the vehicle and it requires less control effort to stabilise due to its slow dynamics behaviour.

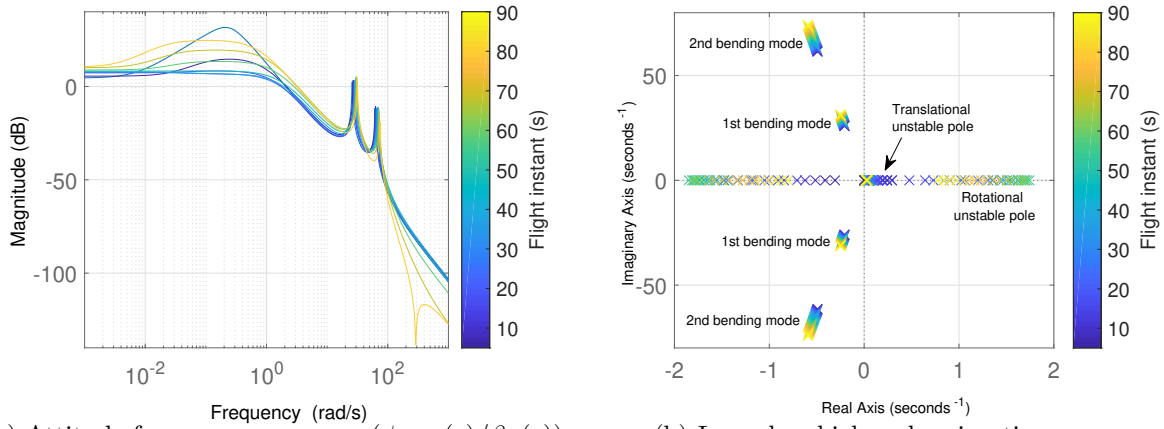

(a) Attitude frequency responses ($\psi_{INS}(s)/\beta_{\psi}(s)$) (b) Launch vehicle pole migration map

Figure 2.11: Launch vehicle open-loop time-varying properties

2.2.2 LFT modelling

The launch vehicle model presented in the previous section can be augmented to incorporate plant uncertainties using Linear Fractional Transformation (LFT) theory [72, 73]. The LFT formulation is a well-established and suitable approach to model the known unknowns of a system, allowing to account for parametric uncertainties according to the expected dispersions of each parameter along the flight. This uncertainty modelling offers a more realistic description of the launch vehicle, which is inherently uncertain and it certainly provides an additional level of insight at the design stage to provide good robustness against system uncertainties.

In this section, the formal and general LFT representation is briefly introduced and then, based on references [74, 71], the LFT modelling approach followed to model the launch vehicle and the actuation chain models is described.

2.2.2.1 LFT background

The LFT representation is defined by a feedback interconnection of two matrix operators $M \in \mathbb{C}^{(n_d+n_u)\times(n_e+n_y)}$ and $\Delta \in \mathbb{C}^{n_y \times n_u}$, where M is traditionally partitioned into four submatrices: $M = [M_{11}\ M_{12}; M_{21}\ M_{22}]$. There are two types of LFT interconnections, lower and upper LFT, which are both illustrated in Figure 2.12.

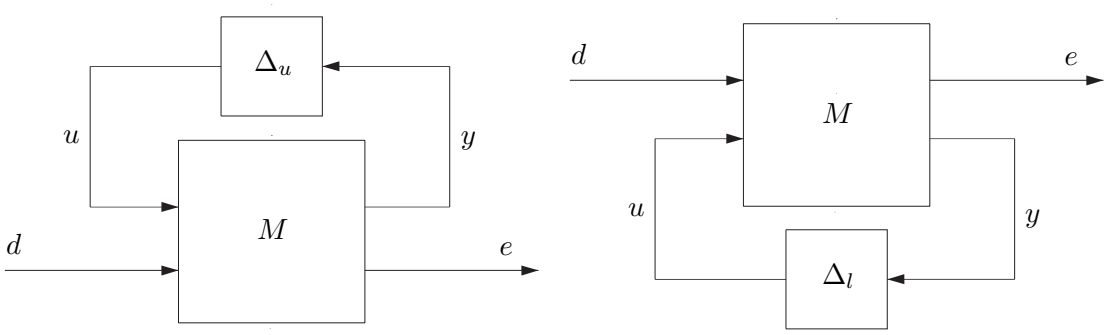

(a) Upper LFT interconnection (b) Lower LFT interconnection

Figure 2.12: LFT representations

The upper LFT shown in Figure 2.12a describes the relation between M and Δ_u. This connection can be represented by the operator $\mathcal{F}_u$, which defines the closed-loop from the input signal d to the output e as follows:

$$\mathcal{F}_u(M, \Delta_u) = \mathcal{T}_{de} = M_{22} + M_{21}\Delta_u(I - M_{11}\Delta_u)^{-1}M_{12} \tag{2.20}$$

The previous representation is widely used in the robust control community because it can be used to model plants subject to uncertainties. In this case, M_{22} represents the nominal plant while M_{12}, M_{21} and M_{11} describe how the nominal plant is affected by a perturbation Δ_u.

Similarly, the lower LFT describes the relation between M and Δ_l using the configuration shown in Figure 2.12b. This interconnection is defined by the operator $\mathcal{F}_l$ as follows:

$$\mathcal{F}_l(M, \Delta_l) = \mathcal{T}_{de} = M_{11} + M_{12}\Delta_l(I - M_{22}\Delta_l)^{-1}M_{21} \tag{2.21}$$

2.2.2.2 Uncertain launch vehicle model

The LFT model of the VEGA launcher is derived by augmenting the LTI nominal model presented in Section 2.2.1 with additive parametric uncertainties. This type of uncertainty is generally defined as $x = x^0 + \sigma_x\delta_x$, where x^0 represents the nominal value of parameter x, σ_x is the level of uncertainty and δ_x is a norm-bounded uncertainty flag $\left(||\delta_x||_\infty \leq 1\right)$.

Standard LFT modelling approaches generally define a different uncertainty flag for each variable of the model [71]. This strategy generally results in highly accurate LFT models but also of high complexity (in terms of number of uncertain parameters used and their repetitions). While this might be valid for some systems and some type of analyses, for robust control design and advanced analytical robust analyses (i.e. structured singular value, Integral Quadratic Constraint (IQC)), it is sometimes desirable to employ LFT models with low complexity.

In this thesis, the modelling approach proposed in reference [74] is employed. In that reference, the LFT models are derived using a reduced set of uncertainty flags which allows to reduce the complexity of the model while capturing the variability of the system parameters with respect to the nominal flight.

To identify the subset of uncertainty flags, different system scattering flags are examined through a time-domain sensitivity analysis using the high-fidelity, nonlinear 6 DoF simulator presented in Section 2.1.4. For each scattering flag, nine different time-domain simulations are evaluated, where the uncertainty flag to be examined is set iteratively to its minimum, nominal and maximum value (i.e. $\delta_{\#}$ = [-1, 0, 1]), while the other remaining system flags are fixed iteratively to [-1, 0, 1]. This analysis allows to study the impact of different uncertainty flags (one at a time) on the main physical parameters (e.g. dynamic pressure, velocity, mass, thrust) and determine the uncertainty dependencies of the system. A more detailed description of this sensitivity analysis can be found in reference [74]. The scattering flags with more impact on the system are described in Table 2.2, which lists the flags corresponding to rigid- and flexible-body motion separately.

Table 2.2: List of uncertain flags for the VEGA launch vehicle LFT model.

	Scattering flags description		
Rigid body	δ_{dTc}	–	combustion time
	δ_{ρ}	–	atmospheric density
	δ_{dispCN}	–	dispersions for the normal aerodynamic coefficient
	δ_{uncCN}	–	uncertainties for the normal aerodynamic coefficient
	$\delta_{dispX_{CP}}$	–	dispersions for the center of pressure x-coordinate
	$\delta_{uncX_{CP}}$	–	uncertainties the center of pressure x-coordinate
Flexible body	δ_{ω_q}	–	bending frequency
	$\delta_{\Psi_{PVP}}$	–	bending mode's translational length at PVP location node
	$\delta_{\Psi'_{PVP}}$	–	bending mode's rotational length at PVP location node
	$\delta_{\Psi_{INS}}$	–	bending mode's translational length at INS location node
	$\delta_{\Psi'_{INS}}$	–	bending mode's rotational length at INS location node

Based on the outcome and the recognised trends of the aforementioned sensitivity analysis, the uncertainty configurations were chosen to be modelled by linear ($x = x^0 + \sigma_x^{\#}\delta_{\#}$) and bilinear ($x = x^0 + \sigma_x^{\#}\delta_{\#} + \sigma_x^{\flat}\delta_{\flat}$) dependencies, in which the level of uncertainty $\sigma_x^{\bullet}$ can be associated to more than one flag. The selected parametric set is shown in Table 2.3.

Table 2.3: List of uncertain parameters for the VEGA launch vehicle LFT model.

Rigid-body uncertain parameters	Flexible-body uncertain parameters
$m = m^0 + \sigma_m^{dTc}\delta_{dTc}$	$\omega_{q_i} = \omega_{q_i}^{\ 0} + \sigma_{\omega_{q_i}}^{\omega_q}\delta_{\omega_q}$
$x_{CG} = x_{CG}^0 + \sigma_{X_{CG}}^{dTc}\delta_{dTc}$	$\Psi_{PVPi} = \Psi_{PVP_i}^{\ 0} + \sigma_{\Psi_{PVPi}}^{\Psi_{PVP}}\delta_{\Psi_{PVP}}$
$\mathrm{I}_{yy} = \mathrm{I}_{yy}^0 + \sigma_{\mathrm{I}_{yy}}^{dTc}\delta_{dTc}$	$\Psi'_{PVPi} = \Psi'^{\ 0}_{PVP_i} + \sigma_{\Psi'_{PVPi}}^{\Psi'_{PVP}}\delta_{\Psi'_{PVP}}$
$CN = CN^0 + \sigma_{CN}^{dispCN}\delta_{dispCN} + \sigma_{CN}^{uncCN}\delta_{uncCN}$	$\Psi_{INSi} = \Psi_{INS_i}^{\ 0} + \sigma_{\Psi_{INSi}}^{\Psi_{INS}}\delta_{\Psi_{INS}}$
$x_{CP} = x_{CP}^0 + \sigma_{CN}^{dispXcp}\delta_{dispX_{CP}} + \sigma_{X_{CP}}^{uncX_{CP}}\delta_{uncX_{CP}}$	$\Psi'_{INSi} = \Psi'^{\ 0}_{INS_i} + \sigma_{\Psi'_{INSi}}^{\Psi'_{INS}}\delta_{\Psi'_{INS}}$
$T = T^0 + \sigma_T^{dTc}\delta_{dTc}$	
$V = V^0 + \sigma_V^{dTc}\delta_{dTc}$	with $i = 1...k$
$Q = Q^0 + \sigma_Q^{dTc}\delta_{dTc} + \sigma_Q^{\rho}\delta_{\rho}$	
$acc = acc^0 + \sigma_{acc}^{dTc}\delta_{dTc} + \sigma_{acc}^{\rho}\delta_{\rho}$	

The nominal values x^0 and uncertainty levels $\sigma_x^{\#}$ of each rigid-body parameter x are computed as the mean and the standard deviation of the time-domain simulations obtained with the associated uncertainty flag $\delta_{\#}$ taking its minimum, nominal and maximum value. Differently, the corresponding values for the flexible-body parameters are directly extracted from the mission data used by the nonlinear simulator.

The VEGA LFT model is built using the state-space representation presented in Section 2.2.1 but employing the uncertain parameters listed in Table 2.3 instead of nominal values. Note that the uncertain parameters are defined using the Matlab Robust Control Toolbox [75]. The resulting VEGA LFT model has dimension 95 (counting number of parameters and their repetitions). It should be remarked that prior to the design and analysis stages, the model is simplified using LFT reduction methods and finally results in a smaller LFT dimension of 41.

This model can be also represented as an upper LFT interconnection as shown in Figure 2.13, where $G_{LV}(s)$ describes the known part of the launch vehicle model and $\Delta_{LV_{RF}}$ represents the model uncertainties. Note that the latter is a diagonal block, $\Delta_{LV_{RF}} = \mathrm{diag}(\Delta_{LV_R}, \Delta_{LV_F})$, that gathers all the uncertainties from rigid-body Δ_{LV_R} and flexible-body dynamics Δ_{LV_F}. These rigid and flexible uncertainties are defined in Equations 2.22 and 2.23, where $\mathrm{I}_{\bullet}$ is the identity matrix of size $\bullet$, and represents the number of repetitions of each uncertain parameter. Therefore, any uncertainty $\Delta_{LV_{RF}}$ belongs to the uncertainty set defined by $\boldsymbol{\Delta_{LV_{RF}}} = \mathrm{diag}(\boldsymbol{\Delta_{LV_R}}, \boldsymbol{\Delta_{LV_F}})$.

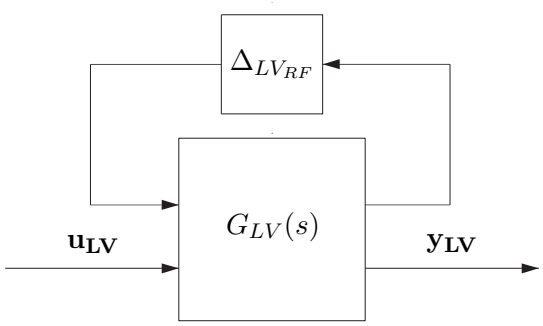

Figure 2.13: Full rigid/flexible VEGA LFT representation

$$\Delta_{LV_R} \in \boldsymbol{\Delta_{LV_R}} = \Big\{ \mathrm{diag}\big(\delta_{dTC}\mathrm{I}_{14}, \delta_{\rho}\mathrm{I}_3, \delta_{dispCN}\mathrm{I}_2, \delta_{uncCN}\mathrm{I}_2, \delta_{dispX_{CP}}\mathrm{I}_3, \delta_{uncX_{CP}}\mathrm{I}_3\big); \\ \delta_{\#} \in \mathbb{R}; ||\delta_{\#}||_{\infty} \leq 1 \Big\} \tag{2.22}$$

$$\Delta_{LV_F} \in \boldsymbol{\Delta_{LV_F}} = \Big\{ \mathrm{diag}\big(\delta_{\omega_q}\mathrm{I}_4, \delta_{\Psi_{PVP}}\mathrm{I}_3, \delta_{\Psi'_{PVP}}\mathrm{I}_3, \delta_{\Psi_{INS}}\mathrm{I}_2, \delta_{\Psi'_{INS}}\mathrm{I}_2\big); \delta_{\#} \in \mathbb{R}; ||\delta_{\#}||_{\infty} \leq 1 \Big\} \tag{2.23}$$

To illustrate the effect of model perturbations on the launch vehicle model, the frequency response of the nominal VEGA attitude channel at t=50 s (in red) and 1000 random scattered responses are shown in Figure 2.14a. This plot clearly shows the level of uncertainties defined for the flexible-body dynamics (high-frequency range). As for the dispersions for the rigid-body dynamics (low-frequency range), Figure 2.14b has been zoomed in for better visualisation.

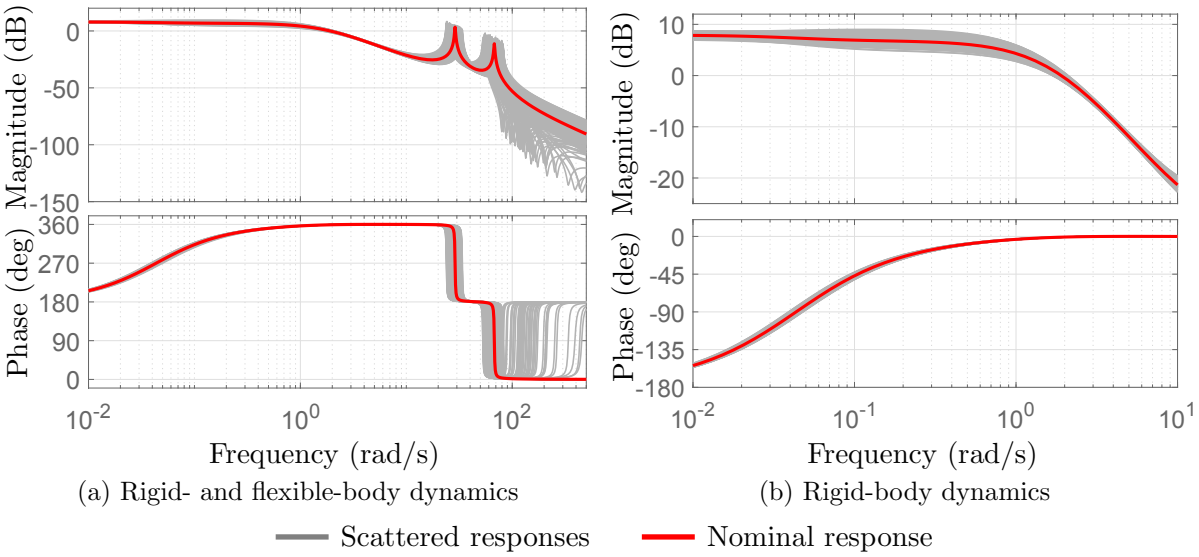

(a) Rigid- and flexible-body dynamics

(b) Rigid-body dynamics

Figure 2.14: Bode plot of the LFT VEGA model $\left(\psi_{INS}(s)/\beta_{\psi}(s)\right)$ at t=50 s

2.2.2.3 Uncertain TVC actuator model

The TVC actuator model characterises the dynamics of the TVC actuators obtained from HWIL simulations. This model is also described as an upper LFT interconnection $\mathcal{F}_u\big(G_{TVC}(s), \Delta_{TVC}\big)$, where $\Delta_{TVC} \in \boldsymbol{\Delta_{TVC}}$. This LFT model is obtained from reference [71]. The reader is referred to that reference for a detailed description of the model. The bode plot presenting the nominal frequency response and the LFT coverage is illustrated in Figure 2.15.

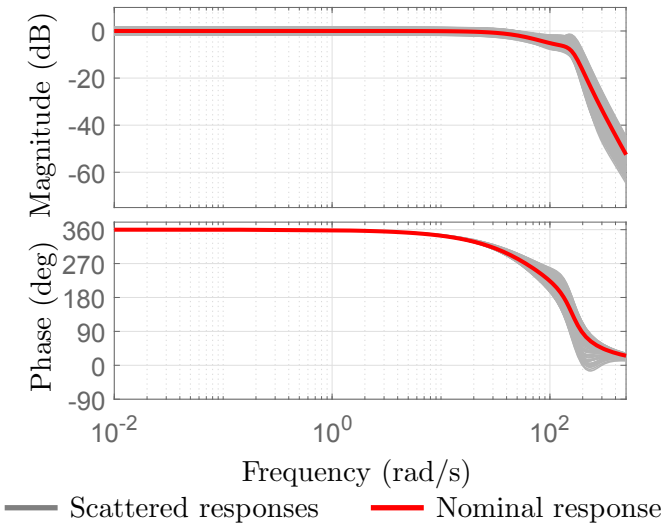

Figure 2.15: Bode plot of the LFT TVC actuator model $\big(\beta_\psi(s)/\beta_{c\tau}(s)\big)$

2.2.2.4 Uncertain delay model

This LFT model characterises the delays originated by the digital processing of the on-board computers (12 ms), sensors (12 ms) and TVC actuators (15 ms). All those contributors are modelled through a 2^{nd} order Padé approximation using an uncertain delay defined as $\tau = \tau^0 + \sigma_\tau \delta_\tau$ (with τ^0 =39 ms and σ_τ =10 ms). Similarly, this model can be expressed as an upper LFT interconnection $\mathcal{F}_u\big(G_\tau(s), \Delta_\tau\big)$, where $G_\tau(s)$ is described in Equation 2.24 and $\Delta_\tau \in \boldsymbol{\Delta_\tau}$ with $\boldsymbol{\Delta_\tau} = \big\{\delta_\tau \mathrm{I}_2; \delta_\tau \in \mathbb{R}; ||\delta_\tau||_\infty \leq 1\big\}$.

$$G_\tau(s) = \frac{s^2\tau^2 - s6\tau + 12}{s^2\tau^2 + s6\tau + 12} \tag{2.24}$$

The bode diagram with the nominal and dispersed responses is shown in Figure 2.16. This delay approximation provides a good convergence with respect to a pure time delay within the frequency range of interest for analysis and design, which for launcher systems generally covers until the second bending mode $\big([0.01\ 100]$ rad/s$\big)$.

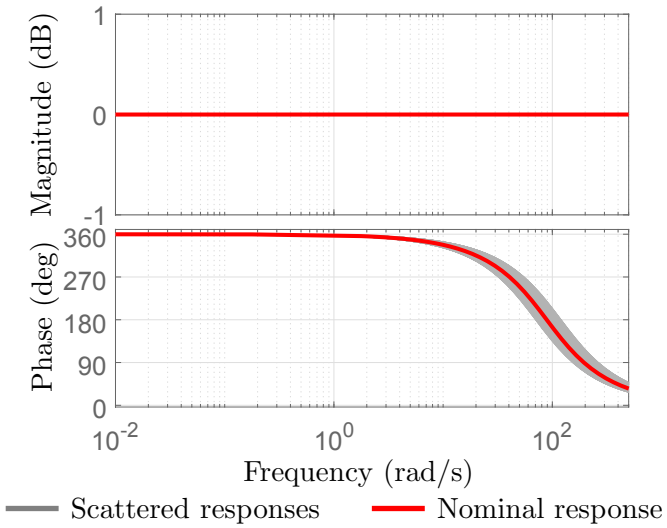

Figure 2.16: Bode plot of the LFT delay model $\left(\beta_{c\tau}(s)/\beta_c(s)\right)$

2.2.3 Analysis and verification process

The analysis and verification campaign employed in this thesis is based on the actual VEGA V&V test plan presented in Section 2.1.3. In particular, all the TVC designs presented will be analysed in two steps:

1. First, each linear design point will be evaluated in terms of the stability requirements presented in Table 2.1. In addition, the traditional stability validation analysis is complemented using an analytical robust technique (structured singular value μ) to evaluate the robustness of the design due to model uncertainties;

2. Second, the main TVC performance requirements (see Table 2.1) are evaluated for the P80 flight phase using nonlinear time-domain MC campaigns with different wind profiles.

It is highlighted that the verification campaign described above is not as intensive as the industrial V&V test plan described in Section 2.1.3. For instance, in this thesis the stability requirements are only evaluated at each linear design point (i.e. every 10 s for VEGA), while the current VEGA V&V framework defines a sampling of 1 second for the atmospheric phase. In addition, as aforementioned, control performance indicators for the lift- and tail-off phases or related to the RACS are not covered. Nonetheless, this analysis and verification campaign offers a very exhaustive assessment for launcher TVC systems.

Part I

Structured $\mathcal{H}_\infty$ control design

CHAPTER 3

VEGA controller legacy recovery

In this chapter, the structured $\mathcal{H}_\infty$ synthesis technique is applied to the actual VEGA VV05 mission data with the objective of recovering the same performance and robustness using the same controller architecture as the VEGA rigid-body controller [1]. The aim is to show that the same controller can be obtained but using a more methodological and efficient technique than the classical, loop-at-a-time approach currently used by VEGA. The resulting design interconnection will be used throughout the reminder of the thesis to serve as the first step for the development of a launcher robust design framework. In addition, this recovery also facilitates the transfer of technology to industry as it allows to build exactly from their architecture, and arrive to the same result, strongly building confidence on the process.

A preliminary recovery of the VEGA launcher controller was presented in reference [76], for a rotational a_6/k_1 launch vehicle model, and in reference [77] for a full rigid-body model of the launcher. In these two references, the main closed-loop transfer functions are analysed analytically to give an understanding on the constraints imposed by the controller structure and facilitate the weighting function selection.

This chapter outline is as follows. Section 3.1 gives a cursory introduction to the structured $\mathcal{H}_\infty$ synthesis approach. In Section 3.2, the atmospheric VEGA rigid-body TVC system design is formulated in a robust control synthesis framework. Then, Section 3.4 provides key guidelines on the weighting function selection. The VEGA legacy control recovery is exemplified in a linear design point in Section 3.5 and validated for the atmospheric phase using a nonlinear, high-fidelity simulator in Section 3.6. Finally, Section 3.7 ends with the conclusions.

[1] Initially, the main goal was to recover as close as possible the performance and robustness properties of the original baseline controller, but as it will be shown in this chapter by combining the optimisation process of the structured $\mathcal{H}_\infty$ technique with the analytical understanding of the launcher flight mechanics via the main transfer functions it was possible to recover exactly the original controller (without using the knowledge of its gains).

3.1 Structured $\mathcal{H}_\infty$ design approach

The structured $\mathcal{H}_\infty$ design approach allows to solve the $\mathcal{H}_\infty$ control problem while enforcing a defined controller structure and/or state order. These synthesis capabilities allow overcoming one of the main limitations of the standard $\mathcal{H}_\infty$, which is the lack of physical insight on the controller structure. Indeed, the standard $\mathcal{H}_\infty$ synthesis [24, 25] results in full-order controllers with no defined structure, generally of high order and sometimes with very high-frequency poles. These characteristics typically motivate the use of ad hoc controller reduction algorithms to facilitate its implementation, but they normally result in loss of performance.

The capability of defining the controller structure for design is a valuable feature for industrial applications, where it is important to have a good understanding of the role of each element of the controller. This also makes the scheduling and controller implementation simpler (i.e. no high-frequency poles and no need to apply controller reduction methods). Furthermore, it also facilitates the re-tuning of the controller if needed. A significant example of this was demonstrated during ESA's Rosetta mission, where the attitude control system had to be re-tuned due to a thruster anomaly. For that mission, the structured $\mathcal{H}_\infty$ technique was employed to refine the controllers, which were subsequently uploaded to the space probe before the final comet insertion manoeuvres [38].

A cursory description of this synthesis technique follows. The reader is referred to reference [78] for a comprehensive survey on the structured $\mathcal{H}_\infty$ control problem.

Standard $\mathcal{H}_\infty$ problem

As mentioned before, the structured $\mathcal{H}_\infty$ technique is based on $\mathcal{H}_\infty$ theory. The $\mathcal{H}_\infty$ control problem is traditionally formulated using the diagram shown in Figure 3.1, where the closed-loop of the system is represented by a lower LFT interconnection defined by $\mathcal{T}_{ed}(s) = \mathcal{F}_l\big(P(s), K(s)\big)$.

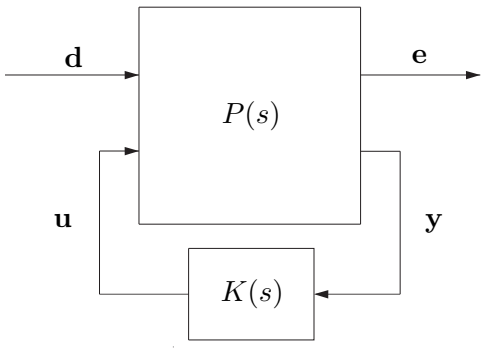

Figure 3.1: Standard $\mathcal{H}_\infty$ interconnection

$P(s)$ is called the generalised plant and it can be represented as:

$$\begin{bmatrix} \dot{\mathbf{x}} \\ \mathbf{e} \\ \mathbf{y} \end{bmatrix} = \underbrace{\begin{bmatrix} A & B_1 & B_2 \\ C_1 & D_{11} & D_{12} \\ C_2 & D_{21} & D_{22} \end{bmatrix}}_{P(s)} \begin{bmatrix} \mathbf{x} \\ \mathbf{d} \\ \mathbf{u} \end{bmatrix} \tag{3.1}$$

where $\mathbf{x}$ is the state vector of $P(s)$; $\mathbf{d}$ represents the exogenous inputs of the system (commands, disturbances) and $\mathbf{e}$ the regulated outputs to be controlled; finally, $\mathbf{u}$ and $\mathbf{y}$ define the input and output vectors of the controller $K(s)$.

The $\mathcal{H}_\infty$ control problem consists of finding a stabilising controller $K^*(s)$ that minimises the $\mathcal{H}_\infty$ norm of the closed-loop performance channel $\mathcal{T}_{ed}(s)$ as follows:

$$\min_{K(s)} ||\mathcal{T}_{ed}(s)||_\infty = \min_{K(s)} \max_{\omega \in \mathbb{R}} \overline{\sigma}\big(\mathcal{T}_{ed}(j\omega)\big) \tag{3.2}$$

where the $\mathcal{H}_\infty$ norm of a system $M(s)$ is formally defined as the maximum singular value $\overline{\sigma}\big(M(s)\big)$ [73].

In practice, the above control problem is computationally very demanding. The standard $\mathcal{H}_\infty$ problem is traditionally formulated to obtain a sub-optimal controller. Let $\gamma*$ be the optimal value of $||\mathcal{T}_{ed}(s)||_\infty$, the control problem is to find a controller such that $||\mathcal{T}_{ed}(s)||_\infty < \gamma$, with $\gamma \geq \gamma*$.

This problem has received widespread attention in the control community because robustness is guaranteed by design. Indeed, the $\mathcal{H}_\infty$ norm can be interpreted as a worst-case norm which represents the maximum amplification of energy from an input d with bounded energy $||d||_2^2$ to the output e:

$$||\mathcal{T}_{ed}||_\infty = \sup_{d \neq 0} \frac{||e||_2}{||d||_2} < \gamma \tag{3.3}$$

The lower LFT interconnection of Figure 3.1 is typically augmented using frequency-domain weighting functions at the input side $W_i(s)$ and at the output side $W_o(s)$ as shown in Figure 3.2. The total augmented system is defined by $\mathcal{T}_{e'd'}(s)$ as shown in Equation 3.4. The weighting functions are selected to normalise the problem and to impose the desired closed-loop performance of the system in the frequency domain. Hence, if there is a controller $K^*(s)$ that fulfils all the requirements defined by the weighting functions, then $||\mathcal{T}_{e'd'}(s)||_\infty < 1$.

$$\mathbf{e}' = \underbrace{W_o \, \mathcal{F}_l(P, K) \, W_i}_{\mathcal{T}_{e'd'}(s)} \; \mathbf{d}' \tag{3.4}$$

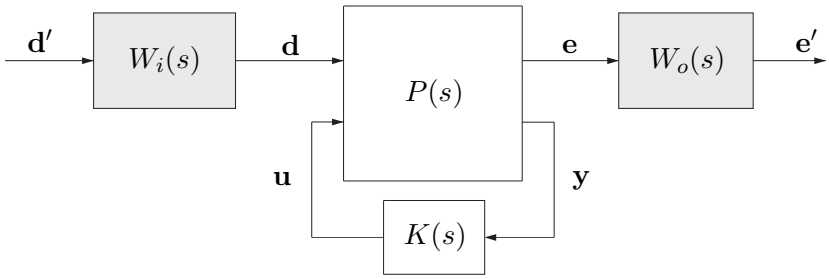

Figure 3.2: Augmented standard $\mathcal{H}_\infty$ interconnection

The $\mathcal{H}_\infty$ problem was first solved in reference [25] for the so-called full-order controller space $\mathcal{K}_{\mathbf{full}}$, which comprises the set of controllers with the same number of inputs and outputs as defined by the vectors $\mathbf{y}$ and $\mathbf{u}$, and same dimension as $\mathcal{T}_{e'd'}(s)$. Using this controller space, the problem is convex and can be solved via two algebraic Riccati equations [25] or as subsequently proposed in reference [79] via Linear Matrix Inequalities (LMIs).

Formal statement of the structured $\mathcal{H}_\infty$ problem

Unfortunately, if the controller space is constrained to an arbitrary structure (i.e. $\mathcal{K}_{\mathbf{struc}}$), the synthesis problem requires the solution of Bilinear Matrix Inequalities (BMIs), which results in non-convexity. The structured $\mathcal{H}_\infty$ control problem was first discussed in reference [80] using non-smooth local optimisation algorithms. The use of local-minima optimisation techniques may be seen as a weak point of this technique because it is possible that the design converges to a local minimum with poor performance. Moreover, the optimisation can be drastically affected by the choice of the controller structure as well as the initial guesses or initialisations. To mitigate these problems, it is recommended to perform multiple optimisations from a set of random initialisations [37]. However, it is important to remark that this solution also raises the problem of non-repeatability, which is a concern in industry.

This non-convex, non-smooth optimisation approach was further developed by the original authors and subsequently included in 2010 in Matlab's Robust Control Toolbox as the *hinfstruct* function [37]. In preparation for the structured $\mathcal{H}_\infty$ design, the controller architecture is parametrised using predefined Matlab control design blocks such as tunable gains, tunable PID controllers, fixed-order state-space models and fixed-order transfer functions. These building blocks allow to define which controller coefficients are to be tuned and which ones are to be fixed for the optimisation. All tunable parameters can be initialised by a given value and moreover, it is possible to constraint the optimisation by defining maximum and minimum allowable values for each tunable coefficient.

The *hinfstruct* function internally formulates the problem as the so-called *standard form*, which uses the same interconnection shown in Figure 3.2. But differently, this structured *standard form* defines a generalised plant $\tilde{P}(s)$ that absorbs the non-tunable part of the controller structure and a controller $\tilde{K}(s)$, which is defined by a diagonal block formed by the tunable coefficients of $K(s)$ $\left(\tilde{K}(s) = diag(a_1, ..., a_{n_k})\right)$. In addition, this function also formulates the $\mathcal{H}_\infty$ problem as a sub-optimal control problem to find an structured stabilising controller such that $||\mathcal{T}_{e'd'}(s)||_\infty < \gamma$.

Furthermore, the *hinfstruct* function allows to perform multi-model structured $\mathcal{H}_\infty$ synthesis, also known as multidisk problem [81]. This design configuration consists of finding a single controller $K^*(s)$ with a certain structure defined in the set $\mathcal{K}_{\mathbf{struc}}$ that stabilises a range of n_p different plants $P_j(s)$ and minimises the following cost function:

$$\min_{K(s)} \max_{j=1,\ldots,n_p} ||\mathcal{T}_{e'd'_j}(s)||_\infty < \gamma; \qquad \text{subject to } K(s) \in \mathcal{K}_{\mathbf{struc}} \tag{3.5}$$

In a similar fashion, the control problem can be posed to design self-scheduled structured controllers [42, 82, 83]. This synthesis scheme embeds the Gain-Scheduling (GS) interpolation by parametrising the tunable controller as a function of a scheduling variable ρ for a set of design points covering the operating range of the system.

Two years later, the same authors released a Matlab-based tool called *systune* [84], which extends the capabilities of *hinfstruct* to cope with multiple design requirements. This new Matlab function defines two set of control goals: soft and hard requirements. In essence, the optimisation is performed giving priority to meet the hard requirements, and if possible, also comply with the soft objectives. This formulation allows to perform mixed structured $\mathcal{H}_2/\mathcal{H}_\infty$ synthesis [85, 86] and also augment the structured $\mathcal{H}_\infty$ optimisation with extra design goals such as time-domain requirements (e.g. desired step response, maximum overshoot, maximum settling time) [87] and constraints on the closed-loop pole locations. Nonetheless, care should be taken in using this multi-objective approach because the different control objectives may overconstrain the optimisation and result in unsatisfactory designs.

More recently, *hinfstruct* and *systune* functions were upgraded to account for real parametric uncertainties during the design [88]. This problem is illustrated in Figure 3.3, where all the uncertainties of the system are pulled out in a diagonal block Δ that belongs to the real uncertainty set $\mathbf{\Delta}_\mathbb{R}$. Then, the robust structured $\mathcal{H}_\infty$ problem is defined as follows:

$$\min_{K(s)} \max_{\Delta \in \mathbf{\Delta}_\mathbb{R}} ||\mathcal{T}_{e'd'}(s, \Delta)||_\infty < \gamma; \qquad \text{subject to } K(s) \in \mathcal{K}_{\mathbf{struc}} \tag{3.6}$$

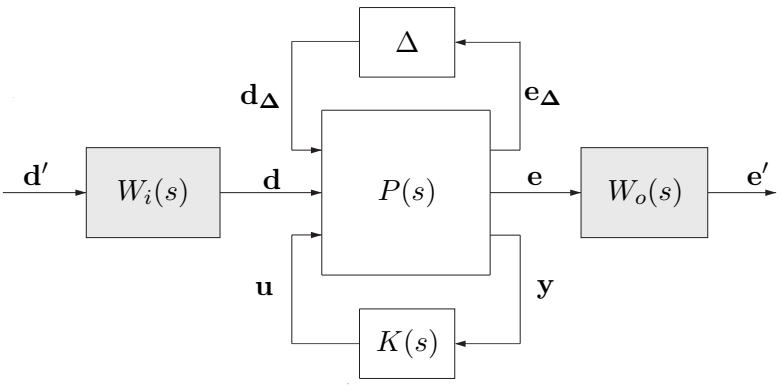

Figure 3.3: Augmented robust standard $\mathcal{H}_\infty$ interconnection

Note that the structured $\mathcal{H}_\infty$ problem using mixed uncertainties (i.e. real and complex uncertainties) is not yet available in Matlab's Robust Control Toolbox but it has recently been discussed in reference [89].

Despite its recent development (less than a decade), the structured $\mathcal{H}_\infty$ synthesis technique has proven to be a fast and reliable synthesis technique in a wide range of applications. Indeed, this technique has been successfully deployed operationally for aerospace systems [38, 39, 90], piloted flight tests [40], experimental platform set-ups [91], active control of broadband noise in vehicles [92] and also numerous studies in aircraft control design such as anti-windup control [93] or the design of a civil aircraft autoland control system [94, 95, 96].

There are also some research studies applying the structured $\mathcal{H}_\infty$ to launch vehicle control design [41, 42, 43, 97], and more importantly this newly developed technique is being currently considered by industry as a design framework capable of simplifying the launch vehicle control design process [44].

3.2 VEGA launcher structured $\mathcal{H}_\infty$ control problem formulation

In this section, the atmospheric VEGA rigid-body TVC system design is formulated as a robust control problem. As mentioned before, the main aim here is to recover the classically-designed VEGA rigid-body controller using the structured $\mathcal{H}_\infty$ optimisation approach. In particular, the control problem is posed to reproduce the classical design framework, and hence the synthesis is performed for nominal conditions (i.e. no uncertainties).

The closed-loop diagram used for design is depicted in Figure 3.4. This interconnection diagram is composed of four main blocks: the controller K_R and three nominal models representing the total delay of the system $G_\tau(s)$, the TVC actuator dynamics $G_{TVC}(s)$ and the rigid-body launch vehicle dynamics $G_{LV_R}(s)$.

The controller K_R represents the actual actual VEGA TVC architecture described in Section 2.1.2, except that the set of filters $H(s)$ are not implemented. This means that they are not re-optimised in this design, although they will be added for the time-domain validation stage. This controller structure is composed of four tunable rigid-body gains $\left(K_{\psi p}, K_{\psi d}, K_z, K_{\dot{z}}\right)$ and defines the following controller space $\mathcal{K}_{VEGA_R}$:

$$\mathcal{K}_{\mathbf{VEGA_R}} = \left\{ K : K = \begin{bmatrix} K_{\psi p} & K_{\psi d} & K_z & K_{\dot{z}} \end{bmatrix}^T \;\; with \;\; K \in \mathbb{R}^4 \right\} \tag{3.7}$$

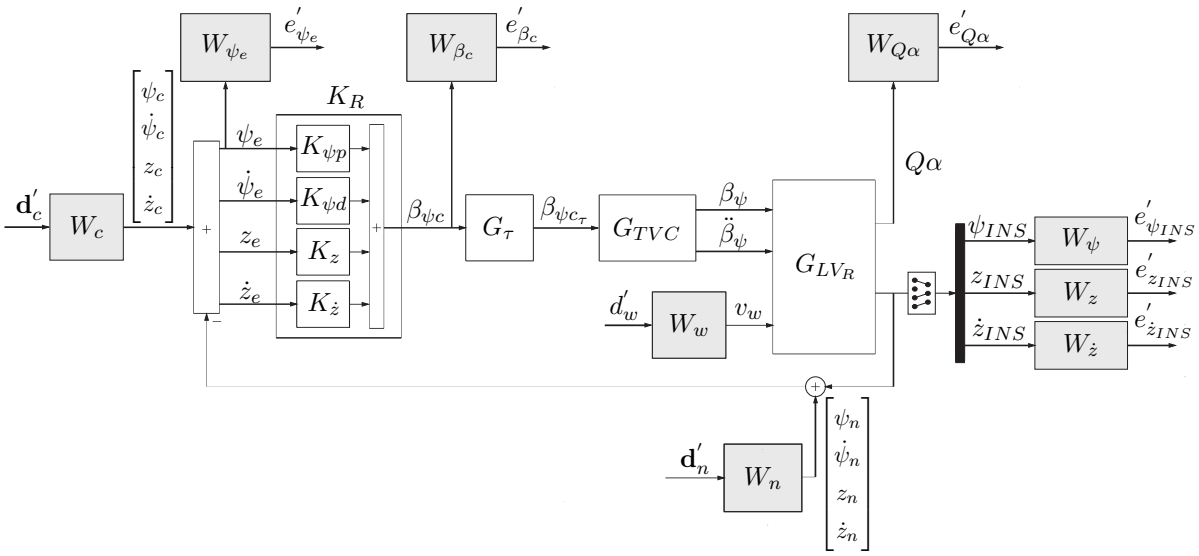

Figure 3.4: Closed-loop diagram for the VEGA launcher control legacy recovery

$G_\tau(s)$ and $G_{TVC}(s)$ are described in Sections 2.2.2.3 and 2.2.2.4, whereas the launch vehicle model $G_{LV_R}(s)$ is defined by the state-space representation given in Equation 3.8. Note that since the focus of the design is on the rigid-body controller, $G_{LV_R}(s)$ only accounts for the rigid-model contributions. The state-space matrices (A_R, B_R, C_R and D_R) and state, input and output vectors ($\mathbf{x_R}$, $\mathbf{u_{LV}}$ and $\mathbf{y_{LV}}$) are given in Section 2.2.1.5.

$$\underbrace{\begin{bmatrix} \dot{\mathbf{x_R}} \\ \mathbf{y_{LV}} \end{bmatrix} = \begin{bmatrix} A_R \\ C_R \end{bmatrix} \mathbf{x_R} + \begin{bmatrix} B_R \\ D_R \end{bmatrix} \mathbf{u_{LV}}}_{G_{LV_R}(s)} \tag{3.8}$$

It is important to highlight that the closed-loop diagram shown in Figure 3.4 differs from the real implementation of the VEGA TVC architecture (see Figure 2.4) where the attitude error rate signal $\dot{\psi}_e$ is obtained by processing ψ_e through a pseudo-derivative filter $H_2(s)$. The design model shown in Figure 3.4 explicitly adds an attitude rate channel by extracting $\dot{\psi}_{INS}$ directly from the launch vehicle model $G_{LV_R}(s)$. In practice, this additional measurement can be provided by VEGA's inertial measurement unit so there is no implementation restriction with the proposed architecture. This new design architecture not only simplifies the design interconnection while also allowing for a slight controller reduction order when using non-structured synthesis techniques (i.e. the pseudo-derivative filter $H_2(s)$ is no longer needed for design) but more critically allows for a transparent analysis by decoupling the inputs to the attitude rigid-body gains, i.e. $K_{\psi p}$ and $K_{\psi d}$.

The closed-loop system shown in Figure 3.4 can be formulated as a robust control problem using the augmented standard $\mathcal{H}_\infty$ interconnection shown in Figure 3.5. This representation gathers the main system dynamics, described by the generalised plant $P(s)$, and the design specifications represented by input and output weighting blocks (W_i and $W_o(s)$). The generalised plant $P(s)$ has a set of inputs formed by the commands, wind disturbance and sensor noise inputs $\big(\mathbf{d} = \begin{bmatrix}\mathbf{d}_c^T & d_w & \mathbf{d}_n^T\end{bmatrix}^T\big)$ and a set of outputs $\big(\mathbf{e} = \begin{bmatrix}e_{\psi_e} & e_{\psi_{INS}} & e_{z_{INS}} & e_{\dot{z}_{INS}} & e_{Q\alpha} & e_{\beta_c}\end{bmatrix}^T\big)$, which have been chosen to cope with all the atmospheric requirements presented in Table 2.1. In particular, the output vector $\mathbf{e}$ is formed by the attitude error ψ_e, the (attitude, drift and drift-rate) INS measurements at node location (ψ_{INS}, z_{INS} and $\dot{z}_{INS}$), the load performance requirement $Q\alpha$ and the commanded actuator deflection $\beta_{\psi c}$.

Also note in Figure 3.5 that the tunable controller K_R is pulled out of the generalised plant $P(s)$, with the scalar $u = \beta_{\psi c}$ representing the controller output and $\mathbf{y} = \begin{bmatrix}\psi_e & \dot{\psi}_e & z_e & \dot{z}_e\end{bmatrix}^T$ the controller input.

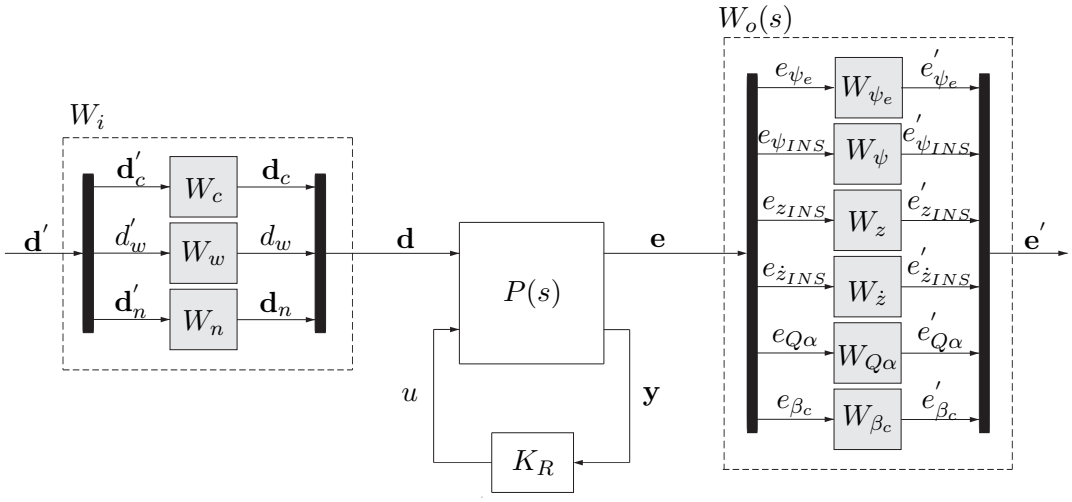

Figure 3.5: Augmented $\mathcal{H}_\infty$ interconnection for the VEGA launcher control legacy recovery

The control design specifications are imposed by scaling the input-output performance channel $\mathcal{T}_{ed}(s)$ using frequency-domain weighting functions (represented by shaded blocks in Figure 3.5). The selection of these weighting functions will be discussed later in Section 3.4.

The input weighting functions are tuned to scale the closed-loop dynamics at the input side with respect to their expected maximum variations, $W_i = diag\big(W_c, W_w, W_n\big)$. On the other hand, the output weighting functions are shaped to specify the desired closed-loop performance of the system in the frequency domain, $W_{out} = diag\big(W_{\psi_e}, W_\psi, W_z, W_{\dot{z}}, W_{Q\alpha}, W_{\beta_c}\big)$. Tracking objectives and stability requirements are set on the attitude channel by W_{ψ_e} and W_ψ. Similarly, W_z and $W_{\dot{z}}$ address the lateral control objectives while $W_{Q\alpha}$ adds constraints to satisfy the load requirements. Finally, the actuation performance is limited by W_{β_c}. It is worth noting that other requirements, such as actuation rate or angular acceleration, can also be considered in the design if necessary.

3.3 Analysis of the closed-loop transfer functions

In preparation for the subsequent weight design, all transfer functions between the exogenous inputs **d** and the regulated outputs **e** are analytically derived and analysed with the aim of identifying key design parameters and providing a more coherent and methodological approach to select the weighting functions. Since the structured $\mathcal{H}_\infty$ approach is a norm-based technique, the analysis of the transfer functions is rather focused on the magnitude information and specifically, on deriving asymptotic bounds that can be used to shape the weighting functions. In addition, this exercise provides very valuable insight on the constraints imposed by the controller structure.

First, the proposed analysis is presented for a rotational a_6/k_1 launch vehicle model in Section 3.3.1, and then extended for a full rigid-body model of the launcher in Section 3.3.2.

3.3.1 Simplified rotational rigid-body model

Consider the closed-loop diagram shown in Figure 3.6, where $G_{LV_{a_6/k_1}}(s)$ is the simplified rotational rigid-body launch vehicle model given in Equation 2.1 and the controller is defined as $K_\psi(s) = K_{\psi p} + K_{\psi d}s$. It is noted that neither the delay model nor the actuator model are considered for this analysis. The former does not affect this analysis because it has unity gain (recall Figure 2.16). Similarly, the latter can be approximated as unity gain for low frequencies.

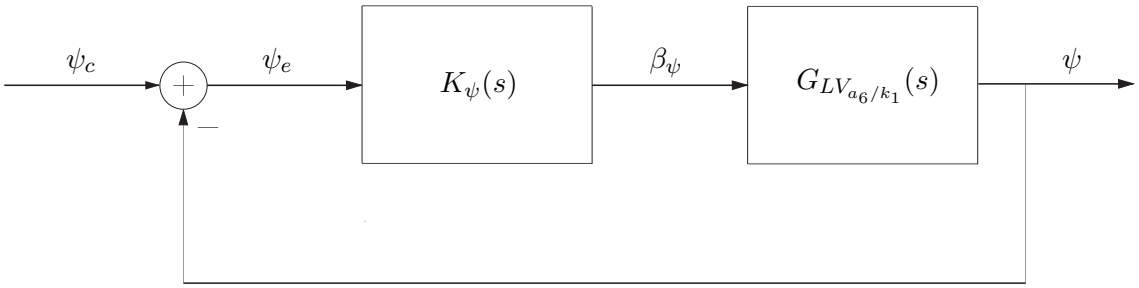

Figure 3.6: Simplified rotational launcher closed-loop diagram

A common way to study the robustness and performance of a system is to analyse the classical sensitivity and complementary sensitivity functions $\big($respectively $S_\psi(s)$ and $T_\psi(s)\big)$. The latter represents the transfer function from the attitude command ψ_c to the attitude output ψ, and is given by:

$$T_\psi(s) = \frac{\psi(s)}{\psi_c(s)} = \frac{G_{LV\,a_6/k_1}(s)K_\psi(s)}{1 + G_{LV\,a_6/k_1}(s)K_\psi(s)} = \frac{k_1K_{\psi d}s + k_1K_{\psi p}}{s^2 + k_1K_{\psi d}s + k_1K_{\psi p} - a_6} \tag{3.9}$$

It is easy to recognise that the above can be represented as an ideal second order system with an extra zero c_z and gain A:

$$T_\psi(s) = A(s + c_z)\frac{\omega_n^2}{s^2 + 2\zeta\omega_n s + \omega_n^2} = \frac{2\zeta\omega_n s + Ac_z\omega_n^2}{s^2 + 2\zeta\omega_n s + \omega_n^2} \tag{3.10}$$

Equating Equations 3.9 and 3.10, the controller gains can be expressed as a function of classical design parameters such as the natural frequency ω_n and the damping ratio ζ:

$$K_{\psi p} = \Big(1 + \frac{{\omega_n}^2}{a_6}\Big)\frac{a_6}{k_1} \tag{3.11}$$

$$K_{\psi d} = \frac{2\zeta\omega_n}{k_1} \tag{3.12}$$

The sensitivity function $S_\psi(s)$ represents the error between the attitude command and the output. Note that $S_\psi(s)$ and $T_\psi(s)$ are related by the well-known $S_\psi(s)+T_\psi(s) = 1$ relationship. Then, $S_\psi(s)$ is given as follows:

$$S_\psi(s) = 1 - T_\psi(s) = \frac{\psi_e(s)}{\psi_c(s)} = \frac{s^2 - a_6}{s^2 + 2\zeta\omega_n s + \omega_n^2} \tag{3.13}$$

Furthermore, the actuation channel is analysed by looking at the control sensitivity function $K_\psi S_\psi(s)$, which is given by:

$$K_\psi S_\psi(s) = \frac{\beta_\psi(s)}{\psi_c(s)} = \frac{1}{k_1}\frac{(2\zeta\omega_n s + a_6 + \omega_n^2)(s^2 - a_6)}{s^2 + 2\zeta\omega_n s + \omega_n^2} \tag{3.14}$$

In this context, the stability Gain Margin (GM) can also be derived as a function of a_6 and ω_n, as follows:

$$GM = 1 + \frac{{\omega_n}^2}{a_6} \tag{3.15}$$

All the previous transfer functions $\big($i.e. $T_\psi(s)$, $S_\psi(s)$ and $K_\psi S_\psi(s)\big)$ were subsequently analysed in terms of low-frequency asymptotes, see Table 3.1.

Table 3.1: Asymptotic analysis using an a_6/k_1 rigid-body launcher model

Transfer function	$\omega = 0$
$\lvert T_\psi(s)\rvert$	$1 + \frac{a_6}{\omega_n^2}$
$\lvert S_\psi(s)\rvert$	$\frac{a_6}{\omega_n^2}$
$\lvert K_\psi S_\psi(s)\rvert$	$\frac{a_6}{\lvert k_1\rvert}\big(1 + \frac{a_6}{\omega_n^2}\big)$

Looking at Equation 3.15 and Table 3.1, it is easily seen the dependency on the ratio a_6/ω_n^2. This term plays an important role for launchers since it can tune the stability gain margin and the low-frequency value of $S_\psi(s)$, which is an indicator of tracking performance (better tracking properties are achieved with lower values of $S_\psi(s)$ at low frequencies). In this regard, if ω_n is considered fixed, the most challenging design point (low gain margins and tracking performance) occurs over the high dynamic pressure region where a_6 is at its maximum value (around the flight instant t=55 s in Figure 2.2c), which is in agreement with standard launcher knowledge and experience.

Another relevant metric to assess the closed-loop robustness is the maximum peak of the sensitivity function $||S_\psi(s)||_\infty$. It is well known, see reference [22], that $||S_\psi(s)||_\infty$ directly yields a lower bound on the classical stability Gain Margin (GM) and Phase Margin (PM) through the Equations 3.16 and 3.17.

$$GM \geq \frac{||S_\psi(s)||_\infty}{||S_\psi(s)||_\infty - 1} \tag{3.16}$$

$$PM \geq 2\arcsin\Big(\frac{1}{2||S_\psi(s)||_\infty}\Big) \tag{3.17}$$

Figure 3.7 shows the evolution of $||S_\psi(s)||_\infty$ in terms of a_6/ω_n^2 and ζ variations. Notice from the figure that as expected the maximum gain of $S_\psi(s)$ increases as the damping ratio ζ reduces. It is also seen that it increases with increasing a_6/ω_n^2. Thus, it can be concluded that large peaks in the sensitivity function $S_\psi(s)$ imply poor tracking performance (large a_6/ω_n^2) as well as poor robustness (see Equations 3.16 and 3.17).

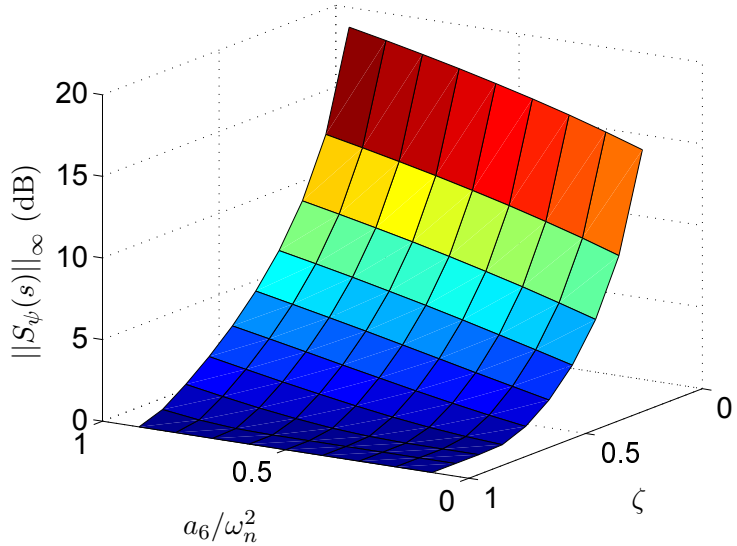

Figure 3.7: $||S_\psi(s)||_\infty$ evolution in terms of a_6/ω_n^2 and ζ variations

The previous analyses reconcile classical and robust control concepts by connecting classical metrics and requirements with those from the sensitivity functions. This provides an in-depth problem understanding that facilitates the selection of the weighting functions for the subsequent structured $\mathcal{H}_\infty$ optimisation. Indeed, the low-frequency asymptotes derived in Table 3.1 can be used to guide the formulation of the weighting functions. In this thesis, this process will be illustrated for a full rigid-body launch vehicle model case (i.e. rotational and translational dynamics) in Section 3.4 [2].

3.3.2 Full rigid-body model

In this subsection, the previous analysis is extended to a full rigid-body closed-loop system (see Figure 3.8). In this case, the launch vehicle model $G_{LV_R}(s)$ is the one given in Equation 3.8 (including full rigid-body rotational and translational dynamics) but note that only two inputs are considered (i.e. $\mathbf{u_{LV}} = [\beta_\psi \quad v_w]$). Furthermore, the controller K_R is defined within the controller space $\mathcal{K}_{\mathbf{VEGA_R}}$ previously described in Equation 3.7. Similarly as before, the delay and actuator models are not considered to simplify the analysis.

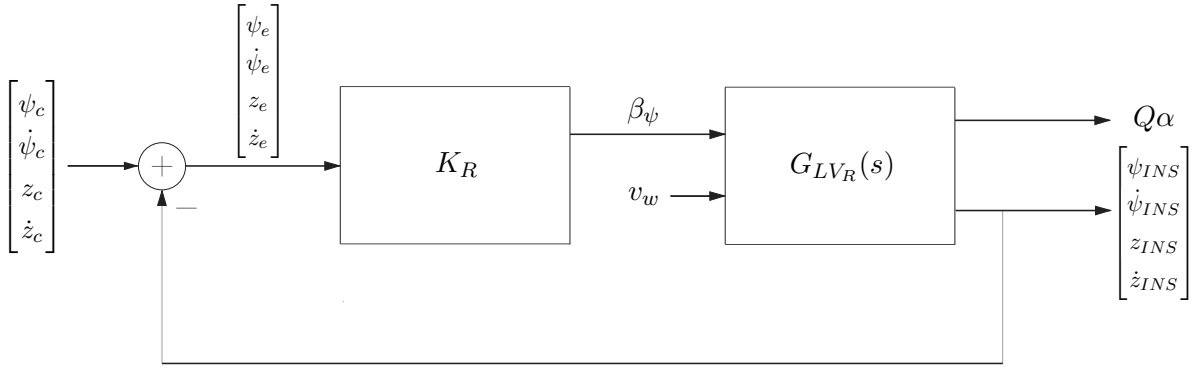

Figure 3.8: Simplified full rigid-body launcher closed-loop diagram

All the transfer functions of the closed-loop system in Figure 3.8 are also analytically derived. The main transfer functions of the attitude channel (complementary sensitivity, sensitivity and control sensitivity) are given as follows:

$$\frac{\psi_{INS}(s)}{\psi_c(s)} = K_{\psi p}\frac{s^2k_1 + sc_3}{C(s)} \tag{3.18}$$

$$\frac{\psi_e(s)}{\psi_c(s)} = \frac{s^4+s^3\left(K_{\psi d}k_1+K_{\dot{z}}c_4+c_1\right)+s^2\left(K_{\psi d}c_3+K_zc_4+K_{\dot{z}}c_5-a_6\right)+s\left(K_zc_5+K_{\dot{z}}c_6+c_2\right)+K_zc_6}{C(s)} \tag{3.19}$$

[2] Nonetheless, it is noted that this methodology to select the weights was also exemplified for the same closed-loop system defined in Figure 3.6 in reference [76]. In that reference, the weights were expressed in terms of system response parameters (ω_n and ζ) and launcher model parameters (a_6 and k_1) as well as identified key relations such as a_6/ω_n^2. The resulting weight setting was applied to recover the VEGA baseline rigid-body as previously defined (i.e. $K_\psi(s) = K_{\psi p} + K_{\psi d}s$) at two flight instants.

$$\frac{\beta_\psi(s)}{\psi_c(s)} = K_{\psi p}\frac{s^4 + s^3 c_1 - s^2 a_6 + s c_2}{C(s)} \tag{3.20}$$

where $C(s)$ is the characteristic equation described in Equation 3.21. Note that $C(s)$ is defined in terms of the rotational a_6 and k_1 parameters and the terms given in Equation 3.22, which are a combination of the launch vehicle parameters presented in Section 2.2.1.

$$\begin{aligned} C(s) = s^4 &+ s^3\big(K_{\psi d}k_1 + K_{\dot{z}}c_4 + c_1\big) + s^2\big(K_{\psi p}k_1 + K_{\psi d}c_3 + K_z c_4 + K_{\dot{z}}c_5 - a_6\big) \\ &+ s\big(K_{\psi p}c_3 + K_z c_5 + K_{\dot{z}}c_6 + c_2\big) + K_z c_6 \end{aligned} \tag{3.21}$$

$$\begin{aligned} &c_1 = -a_1 - a_5; && c_2 = a_1 a_6 - a_3 a_4; && c_3 = a_4 a_p - a_1 k_1; \\ &c_4 = a_p + l_{INS}k_1; && c_5 = a_2 k_1 - a_5 a_p + l_{INS}c_3; && c_6 = a_3 k_1 - a_6 a_p; \end{aligned} \tag{3.22}$$

The transfer functions of the other channels are similarly derived, see Appendix A. In this case, due to the high order of those transfer functions, it was not possible to perform the analysis based on classical design parameters (i.e. damping ratio ζ or natural frequency ω_n). Nevertheless, all transfer functions were analysed in terms of low- and high-frequency asymptotes.

Table 3.2 shows this asymptotic analysis for the most relevant transfer functions. It is observed that the low-frequency asymptote of the attitude sensitivity function is fixed to 1. This value is generally low for good tracking performance. However, in this case, due to the inclusion of the lateral control feedback in drift, the attitude error steady-state response is fixed to 1 and cannot be minimised or controlled with the current TVC architecture. Also note that some of the asymptotes depend exclusively on the rigid-body gains.

Table 3.2: Low- and high-frequency asymptote analysis

Transfer function	$\omega = 0$	$\omega = \infty$
ψ_e/ψ_c	1	1
z_{INS}/ψ_c	$K_{\psi p}/K_z$	0
$z_{INS}/\dot{\psi}_c$	$K_{\psi d}/K_z$	0
z_{INS}/z_c	1	0
$z_{INS}/\dot{z}_c$	$K_{\dot{z}}/K_z$	0
β_ψ/ψ_c	0	$K_{\psi p}$
$\beta_\psi/\dot{\psi}_c$	0	$K_{\psi d}$

The presented analysis shows that, in addition to the intrinsic physical limitations of the launch vehicle, the structure of the controller also introduces constraints to the system. This study is also very relevant because it gives information on how to shape the weights and it will be used later in Section 3.4 for the weighting function selection.

3.4 Weighting function selection

The selection of the weighting functions generally implies an iterative process with several heuristic steps to obtain an adequate set of weights. Nevertheless, in this section, some simple guidelines are provided to improve the understanding on how to express the design specifications in the frequency domain. Those guidelines are mainly based on physical properties of the launch vehicle and limitations imposed by the controller structure (see Table 3.2).

Alternatively, the weighting function selection for the control legacy-recovery process may also be performed based on the inverse of the closed-loop transfer functions using the baseline controller. This reverse-engineering process may result in a faster approach, but it does not provide any insight into the system limitations (physical and controller). Differently, the aim of the proposed approach is to show that the weighting function selection can be greatly eased by analytical analysis (i.e. low- and high-frequency asymptote analysis), as shown next in Sections 3.4.1 and 3.4.2. Nonetheless, note that the baseline closed-loop transfer functions were subsequently employed as reference to fine-tune the analytically-selected weighting functions in order to exactly recover the baseline controller.

In the standard $\mathcal{H}_\infty$ control problem, the order of the weighting functions is traditionally kept low to avoid high-order controllers. Recall that the order of the controller equals the order of the augmented standard $\mathcal{H}_\infty$ interconnection. However, using the structured $\mathcal{H}_\infty$ synthesis technique, this restriction is no longer applicable since the controller dimension is fixed by design. Nevertheless, for ease of tuning and simplicity, constant and first order weighting functions are used.

3.4.1 Input weighting functions

Proper scaling of the input channels is key for a good control design, particularly working with multivariable systems. It is also relevant the use of suitable units to balance the different channels (e.g. expressing angles in degrees instead of radians).

Firstly, the commanded input matrix W_c is described in Equation 3.23. In this thesis, W_{ψ_c} has been fixed to consider a maximum attitude angle command of 1 degree and $W_{\dot{\psi}_c}$ is tuned to balance the attitude and attitude rate channels so they have similar magnitude levels. Similarly, $W_{\dot{z}c}$ is kept fixed to 1 while W_{zc} is adjusted to balance both lateral feedback channels. Using the information from Table 3.2, a suitable scaling is achieved using the following relations: $W_{\dot{\psi}_c} \approx K_{\psi p}/K_{\psi d}$ and $W_{zc} \approx K_{\dot{z}}/K_z$.

$$W_c = \begin{bmatrix} \frac{\pi}{180} W_{\psi_c} & 0 & 0 & 0 \\ 0 & \frac{\pi}{180} W_{\dot{\psi}_c} & 0 & 0 \\ 0 & 0 & W_{zc} & 0 \\ 0 & 0 & 0 & W_{\dot{z}c} \end{bmatrix} \tag{3.23}$$

The input disturbance weight W_w aims to scale the wind channel with respect to the maximum expected wind speed. For the legacy recovery, this weight was chosen to balance the wind disturbance channel with respect to the other input channels at t=50 s (i.e. around maximum dynamic pressure), resulting in $W_w = 10$. Note that this value was kept fixed for the other flight instants throughout the atmospheric phase with the aim of reducing the tuning complexity of each linear design point.

Finally, the input noise weight W_n models the sensor noise of each feedback measurement (see Equation 3.24). The attitude and attitude rate noise levels from the INS sensor used by VEGA are 0.02 deg and 0.1 deg /s. For the lateral deviation measurements, the estimated errors provided by the guidance function are 0.01 m for the drift and 0.001 m/s for the drift-rate. Thus, $W_{\psi_n} = 0.02$, $W_{\dot{\psi}_n} = 0.1$, $W_{zn} = 0.01$ and $W_{\dot{z}n} = 0.001$. These values are fixed for all the designs throughout the atmospheric phase.

$$W_n = \begin{bmatrix} \frac{\pi}{180} W_{\psi_n} & 0 & 0 & 0 \\ 0 & \frac{\pi}{180} W_{\dot{\psi}_n} & 0 & 0 \\ 0 & 0 & W_{zn} & 0 \\ 0 & 0 & 0 & W_{\dot{z}n} \end{bmatrix} \tag{3.24}$$

3.4.2 Output weighting functions

The output weighting functions are shaped to specify the control design requirements on the regulated outputs of the generalised plant $P(s)$. Furthermore, they also scale the closed-loop dynamics at the output side (as before, all the output angle variables are expressed in degrees).

W_{ψ_e} and W_{ψ} enforce tracking and stability requirements. The inverse of both functions impose an upper bound on the classical sensitivity and complementary sensitivity functions of the attitude channel (respectively S_ψ and T_ψ).

Generally, ${W_{\psi_e}}^{-1}(s)$ is chosen as a high-pass filter, with a small low-frequency asymptote to keep low the steady-state tracking error. Nevertheless, as remarked in Section 3.3.2, the steady-state tracking error of the system is fixed to 1 due to the inclusion of the lateral control feedback, see Table 3.2. Thus, as shown in Equation 3.25, $S_\psi(s)$ is only limited by a constant weighting function to keep small the maximum peak of the sensitivity function and assure good stability margins. Recall from Equations 3.16 and 3.17 that $||S_\psi(s)||_\infty$ directly yields a lower bound on the classical stability margins. It is important to note that these relations do not explicitly incorporate stability margin design objectives, but it is an indirect way to bound the GM and PM margins at low frequency.

$$W_{\psi_e} = \frac{180}{\pi} \Big(||S_\psi(s)||_\infty \Big)^{-1} \tag{3.25}$$

${W_\psi}^{-1}(s)$ is shaped instead as a low-pass filter to limit the complementary sensitivity function $T_\psi(s)$, and is given by:

$$W_\psi(s) = \frac{180}{\pi}\left(\frac{h_\psi s + \omega_\psi}{s + \frac{\omega_\psi}{l_\psi}}\right)^{-1} \tag{3.26}$$

where l_ψ and h_ψ are the low- and high-frequency asymptotes of the low-pass filter and ω_ψ is the filter bandwidth. The latter should be sufficiently high to have an adequate attitude tracking but low enough to avoid interactions with the first bending mode. For the recovery of the baseline controller, ω_ψ has been fixed to 20 rad/s. Note that this value has been chosen much higher than the actual attitude control bandwidth to avoid over constraining the optimisation process. In addition, h_ψ is set to a gain of -60 dB to attenuate the control performance at high frequencies and minimise the noise contribution. Finally, in order to reduce the number of weight parameters to tune during the design process, the low-frequency asymptote l_ψ is set to the value corresponding to $||S_\psi(s)||_\infty$.

W_z and $W_{\dot{z}}$ specify the lateral control requirements on the design process. Both weights are defined as constants functions (see Equations 3.27 and 3.28). Their inverses must refer to the maximum drift and drift rate output expected values. Using the information from Table 3.2, note that the ratio $K_{\psi p}/K_z$ imposes a lower bound for ${W_z}^{-1}$.

$$W_z = \left(z_{max}\right)^{-1} \tag{3.27}$$

$$W_{\dot{z}} = \left(\dot{z}_{max}\right)^{-1} \tag{3.28}$$

The load requirement is set through the weighting function $W_{Q\alpha}$. In this case, ${W_{Q\alpha}}^{-1}$ bounds the maximum angle of attack as follows (where $Q\alpha_{max}$ is trajectory specific, and taken from the defined envelop limit):

$$W_{Q\alpha} = \frac{180}{\pi}\left(Q\alpha_{max}\right)^{-1} \tag{3.29}$$

Finally, $W_{\beta_c}(s)$ adds constraints on the actuation channel performance to avoid actuator saturation and reduce high-frequency actuation. ${W_{\beta_c}}^{-1}$ is shaped as a low-pass filter given by:

$$W_{\beta_c}(s) = \frac{180}{\pi}\left(\frac{h_u s + \omega_u}{s + \frac{\omega_u}{l_u}}\right)^{-1} \tag{3.30}$$

where l_u and h_u are the low- and high-frequency asymptotes and ω_u is the actuation bandwidth. The low-frequency asymptote l_u is tuned to be the maximum expected actuator deflection β_{max} at the design point and the actuation bandwidth has been fixed for all design points to $\omega_u = 30$ rad/s. Also note that the controller structure fixes the value of h_u to $K_{\psi p}$ (see Table 3.2).

3.5 Structured $\mathcal{H}_\infty$ linear design point

In this section, the proposed baseline controller recovery approach based on the structured $\mathcal{H}_\infty$ synthesis method is detailed. This approach was applied across several design points throughout the time range of interest, but it is only detailed next for the design point at t=50 s. This point is chosen for illustration purposes as it corresponds to the maximal dynamic pressure, and as such it is one of the most critical design points.

As discussed in Section 3.1, the structured $\mathcal{H}_\infty$ control problem consists of finding a stabilising sub-optimal controller K that minimises the $\mathcal{H}_\infty$ norm of the weighted design interconnection shown in Figure 3.5 as follows:

$$\min_{K} ||\mathcal{T}_{\mathbf{e'd'}}(s)||_\infty < \gamma; \qquad \text{subject to } K \in \mathcal{K}_{\mathbf{VEGA_R}} \tag{3.31}$$

For this legacy recovery exercise, the structured $\mathcal{H}_\infty$ optimisation is formulated using the *hinfstruct* function. Note that the four gains of the controller block K_R are defined as tunable parameters with no constraints on their allowable values. It is important to remark that the control problem was not initialised using the baseline knowledge (i.e. the baseline controller gains) in order not to influence the optimisation. Rather, it was configured to perform multiple optimisations from a set of 5 random starting points to mitigate the local-minima nature of the structured $\mathcal{H}_\infty$ optimisation.

The weighting functions were initially shaped following the guidelines presented in Section 3.4. Then, the analytically-selected weighting functions were subsequently fine-tuned using the baseline closed-loop transfer functions as reference. This fine-tuning process was necessary to successfully obtain the same rigid-body gains as the baseline controller employed in the VEGA VV05 mission. Specifically, the rigid-body gains obtained present less than 1% of error with respect to the baseline controller gains.

To validate the design, the bode plots of the system using the baseline controller (in solid black) and the structured $\mathcal{H}_\infty$ design (in dashed blue with square markers) are shown in Figure 3.9. This plot also illustrates in green the inverse of the final output weighting functions used for this design. It should be remarked that the frequency responses have been multiplied by the input weighting functions (for adequate scaling) and that only a subset of channels are shown for ease of visualisation.

Looking at Figure 3.9, it can be observed that the baseline controller is successfully recovered at t=50 s. This figure shows clearly the upper bound defined by the weighting functions.

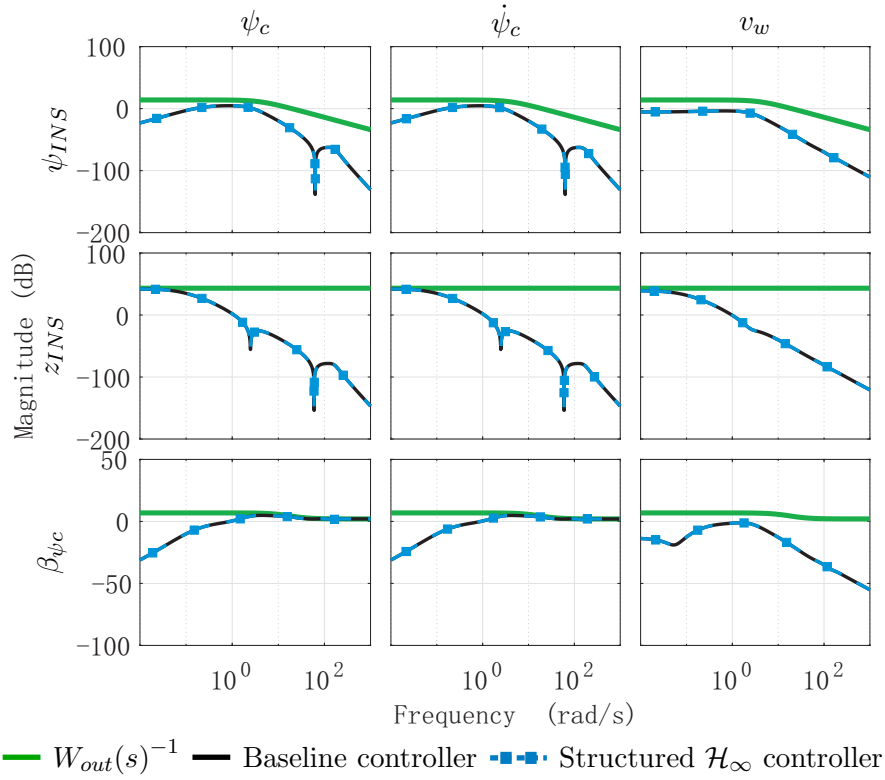

Figure 3.9: Bode plots comparison at t=50 s: baseline controller Vs structured $\mathcal{H}_\infty$ controller

The same design procedure is repeated for the rest of the linear design points along the atmospheric flight. In total, 9 structured $\mathcal{H}_\infty$ controllers have been synthesised starting at $t = 5s$ and then at every 10 seconds between the flight instants t=20 s and t=90 s. Due to the wide dynamic variation of the launch vehicle model, a different set of weighting functions is needed to recover the baseline controller at each grid design point (but note that the weights used for the design at t=50 s are employed as the basis for the weights in all the other points). Similarly, in all the design points, the rigid-body gains synthesised exhibit less than 1% of error with respect to the baseline controller gains.

3.6 Nonlinear verification

Finally, the global controller obtained by gain-scheduling the 9 synthesised rigid-body structured control designs is evaluated and compared with the baseline controller using the nonlinear, high-fidelity simulator described in Section 2.1.4.

Although not used in design process, the set of filters $H(s)$ of the VEGA TVC architecture are added to the synthesised rigid-body structured controllers before combining them into a full global legacy-recovery controller for the nonlinear verification stage. Therefore, both (the baseline and the global legacy-recovery) controllers exhibit the same implementation as shown in Figure 2.4. The only difference between them lies in the rigid-body controller gains (which as aforementioned are within 1% of their corresponding values).

Before the implementation in the simulator, the 9 linear structured $\mathcal{H}_\infty$ controllers (including the corresponding filters $H(s)$) are discretised and then gain scheduled in the same fashion as the actual baseline controller (i.e. using the non-gravitational velocity as scheduling parameter [3].

Figure 3.10 shows the load performance indicator $Q\alpha$ for nominal flight conditions (those encountered during the selected mission, i.e. VV05). It is important to highlight that although not used for the synthesis stage, the bending modes of the launch vehicle are also included for the nonlinear, time-domain simulations. Also note that the estimated wind from the VEGA VV05 mission is used in this analysis.

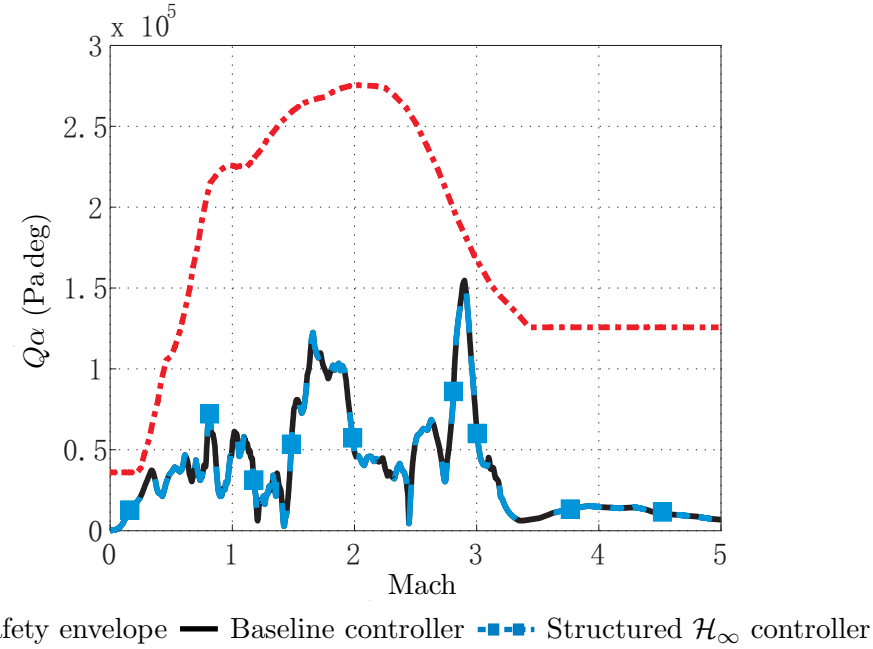

Figure 3.10: VEGA legacy recovery nonlinear validation

Figure 3.10 clearly illustrates that the control behaviour of the scheduled baseline controller for the VEGA atmospheric phase is successfully recovered using the structured $\mathcal{H}_\infty$ synthesis technique (again, no discernible difference is observed in the nonlinear responses – as expected from the previous frequency responses comparison of Figure 3.4).

3.7 Conclusions

This chapter describes a methodological robust control synthesis framework for the atmospheric control system design of a launch vehicle. The proposed synthesis framework is based on the recently-developed structured $\mathcal{H}_\infty$ optimisation approach, which allows to perform a systematic control tuning for a specified controller structure.

[3] In previous instances [77], time was employed as scheduling parameter for ease of simplicity. However, as discussed in reference [2], time is not recommended for interpolation purposes because is not linked to the trajectory (i.e. maximum dynamic pressure does not always happen at the same flight instance).

With the objective of building industrial confidence in this synthesis framework, it is shown that the structured $\mathcal{H}_\infty$ control problem can be formulated to recover the classically designed VEGA VV05 mission rigid-body baseline controller, but in a more methodological manner. It is highlighted that this legacy-recovery design process is not trivial and requires good understanding of the physics of the launch vehicle as well as of the constraints introduced by the controller structure into the system. With respect to the latter, it is highlighted that the PD structure used for the rigid-body gains derives from both, industrial legacy/experience as well as simplification of the tuning process (which currently for VEGA is performed in a classical manner, i.e. loop-at-a-time). This structure restricts the achievable performance and robustness, and raises the important question of whether there are other richer controller structures (this will be clearly demonstrated in subsequent chapters). At any rate, independently of the chosen controller structure, the closed-loop analysis performed in Section 3.3 will allow the designer in understanding the limits and capabilities of the structure. And this analysis will then drive the selection of the most appropriate frequency-dependent weights to optimise the trade-off between these two (robustness versus performance) competing objectives. This is especially important since it facilitates the weighting function selection process and facilitates the transfer of this technology to industrial control engineers with a more classical control background.

Nonetheless the difficulty, this successful demonstration greatly advances the case for the use of this more methodological robust design tools over the classical design approach (especially, or at least, for launcher TVC design). In addition, this robust framework is completely generic and can be used for any launcher with a specific controller structure, and for future launcher evolutions (e.g. VEGA C, VEGA E, Ariane 6 [4]).

[4]From references [97, 44] and also personal communications, it is known that the Ariane launcher family is also using structured $\mathcal{H}_\infty$ synthesis for the atmospheric TVC design.

CHAPTER 4

Control design augmentation

This chapter explores the potential for robustness and performance improvement offered by the structured $\mathcal{H}_\infty$ technique with respect to the traditional state-of-practice. In pursuit of these improvements the level of complexity of the design interconnection presented in the previous chapter is gradually increased towards enhancing the synthesis capabilities.

The chapter is organised in two main sections. The first part addresses the wind disturbance control problem by augmenting the design interconnection with a wind turbulence model prior to the controller synthesis. This wind model is based on a Dryden filter, which represents different statistical wind levels (light, moderate, severe) at different altitudes. It is shown via representative design examples, that the use of strong wind levels for design significantly contributes to improve the wind disturbance rejection performance of the system.

In the second section, the design framework is further augmented by considering parametric uncertainties explicitly in the design. This feature is quite relevant for uncertain control problems such as the launcher TVC problem. In essence, the optimisation is performed using a more realistic description of the launch vehicle, which also includes the expected dispersions of each parameter along the atmospheric flight. This robust augmented synthesis approach is also illustrated in a design example.

4.1 Wind generator augmentation

The effect of wind disturbance is a critical factor for any launcher atmospheric phase [98]. It generally produces a significant degradation in the global performance of the mission and it induces structural loads which can cause loss of vehicle.

In order to illustrate the impact of the wind disturbance on the system, the nominal VEGA VV05 mission data is simulated with (solid black line) and without (dashed blue line) wind effects using the nonlinear, high-fidelity simulator described in Section 2.1.4. Figure 4.1 compares the main performance metrics of the atmospheric flight for both cases. Note that both simulations were obtained using the VV05 mission baseline controller. It is easily seen that all the performance indicators are highly influenced by the wind disturbance – i.e. for the no-wind case, all the metrics are around the zero value. Unfortunately, a no-wind scenario is rather unrealistic as opposed to the presented wind case, which employs the estimated wind encountered during the VEGA VV05 mission. This wind-disturbance control problem is specially challenging since the wind characteristics change with every mission, and thus, the TVC system must be robust against a large range of wind profiles.

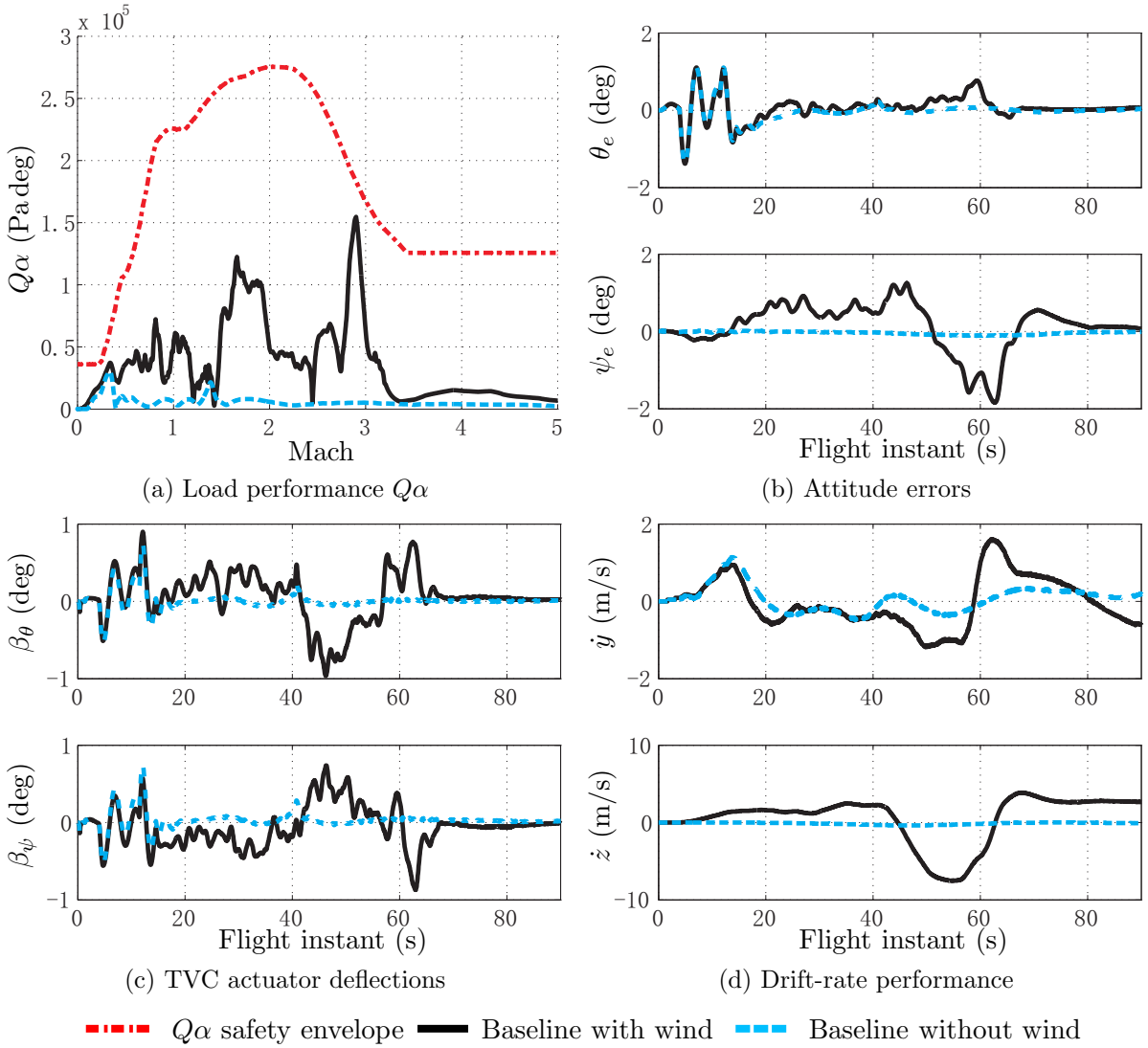

(a) Load performance $Q\alpha$

(b) Attitude errors

(c) TVC actuator deflections

(d) Drift-rate performance

Figure 4.1: Atmospheric nominal nonlinear flight responses with and without wind disturbances

In subsection 4.1.1, the wind channel transfer functions are analysed to provide better understanding on the controller capabilities to reduce the wind disturbance action. Then, in subsection 4.1.2, the structured $\mathcal{H}_\infty$ design framework presented in the previous chapter is augmented by incorporating a wind turbulence model, which accounts for real wind levels in the controller synthesis. Finally, in subsection 4.1.3, a nonlinear benchmark is presented to evaluate the influence of this proposed wind model.

4.1.1 Wind disturbance analysis

The design of the atmospheric TVC system of a launch vehicle is heavily influenced by the wind disturbance. Indeed, the main classical control design strategies considered in the literature for launcher control synthesis are directed to improve the wind disturbance rejection performance of the control system.

The classical approach to address this problem is based on the control design principles proposed in reference [15]. These control principles aim to minimise or cancel out the steady-state response of three different launcher performance metrics: attitude-error-minimum, drift-minimum and load-minimum. These control modes were employed for the design of the Saturn V's first stage control system [16, 17, 4], and subsequently, they have been extensively explored in the literature. Good examples are given in reference [7], where a load-relief control design for the H-IIA launch vehicle is presented and compared with other control modes, and in reference [99], where the Ares-I launcher control performance is further investigated using drift- and load-minimum controllers.

To evaluate the characteristics of the wind disturbance steady-state response of the VEGA launcher, the rigid-body transfer functions of the main performance outputs (i.e. ψ_{INS}, z_{INS}, $Q\alpha$ and $\beta_{\psi c}$) from the wind input v_w are analysed and their low-frequency asymptotes are given in Table 4.1. Recall that these transfer functions were derived and presented in Appendix A. It is critical to notice that only the steady-state value of the drift-wind channel, $z_{INS}(s)/v_w(s)$, can be minimised (by using a low gain ratio $K_{\psi p}/K_z$). Note that the minimum-drift condition can be achieved using $K_{\psi p} = -\frac{l_{CP}}{l_{CP}+l_{CG}}\frac{T-D}{T}$, but this choice leads to an unstable response. Differently, the other steady-state values only depend on physical parameters of the launch vehicle, and thus they cannot be set to zero or controlled in any way using the current TVC architecture of the VEGA launcher. This feature can only be enhanced by including new sensors and feedback loops to the TVC control system (for example, angle of attack), which implies changing the control law.

Despite the fact that most of the wind steady-state responses cannot be controlled for the VEGA launcher, the transient response also plays a significant role on the system and must be adequately considered in design. In this regard, it is very important to scale properly the wind channel with respect to the wind levels that the launcher will encounter in the real flight.

Table 4.1: Steady-state analysis of the wind disturbance channel.

Transfer function	$\omega = 0$
ψ_{INS}/v_w	$\frac{1}{V}\frac{Nl_{cpg}}{Nl_{cpg}+l_{CG}F_{TD}}$
z_{INS}/v_w	$\frac{1}{V}\frac{N}{T}\frac{K_{\psi p}Tl_{cpg}+l_{CP}F_{TD}}{K_z[Nl_{cpg}+l_{CG}F_{TD}]}$
$Q\alpha/v_w$	$-\frac{Q}{V}\frac{l_{CG}F_{TD}}{Nl_{cpg}+l_{CG}F_{TD}}$
$\beta_{\psi c}/v_w$	$-\frac{1}{V}\frac{N}{T}\frac{l_{CP}F_{TD}}{Nl_{cpg}+l_{CG}F_{TD}}$

Notes: $l_{cpg} = l_{CP} + l_{CG}$ and $F_{TD} = T - D$

Classical control design techniques generally do not implicitly consider any wind model during the design process. But as shown in Chapter 3, the robust control design framework can be augmented to include statistical wind models. This is quite relevant for design, since it can certainly guide the optimiser to obtain an overall better disturbance rejection performance. A method to do this is proposed in the next subsection.

4.1.2 Wind generator description

Following the criteria found in reference [100] and the model description from reference [71], the wind disturbance velocity v_w is modelled by colouring white noise n_w through a Dryden filter with the following transfer function:

$$G_w(s) = \frac{v_w(s)}{n_w(s)} = \frac{\sqrt{\frac{2}{\pi}\frac{V - v_{wp}(h)}{L_h}\sigma_h^2}}{s + \frac{V - v_{wp}(h)}{L_h}} \tag{4.1}$$

where L_h and σ_h are the turbulence length scale and the standard deviation versus altitude h. $v_{wp}(h)$ defines the vertical profile of wind velocity.

For the launcher problem, $v_{wp}(h)$ is characterised by the build-up wind speed profile envelope given in Equation 4.2 and illustrated in Figure 4.2. This altitude profile is defined by an exponential leading edge and a 1-cosine shape trailing edge for low and high altitudes respectively. For intermediate altitudes, the profile is described by a constant gust amplitude A. $v_{wp}(h)$ is described for the first 20 km of altitude ($H_f = 20\,000$ m), which is the altitude range where the wind disturbance plays the most significant role in the flight. The profile amplitude is set to $A = 14$ m/s and the thickness of the initial and final edges are given by $H_l = 2000$ m and $H_u = 2500$ m. It is highlighted that the previous values have been chosen to fit the wind model with the estimated wind encountered in the VEGA VV05 mission as indicated in reference [71].

$$v_{wp}(h) = \begin{cases} 10A[(\frac{h}{H_l})^{0.9} - 0.9\frac{h}{H_l}] & \text{for} \quad 0 \leq h < H_l \\ A & \text{for} \quad H_l \leq h \leq H_f - H_u \\ \frac{A}{2}[1 - cos(\frac{\pi}{H_u}(h - H_f))] & \text{for} \quad H_f - H_u < h \leq H_f \end{cases} \tag{4.2}$$

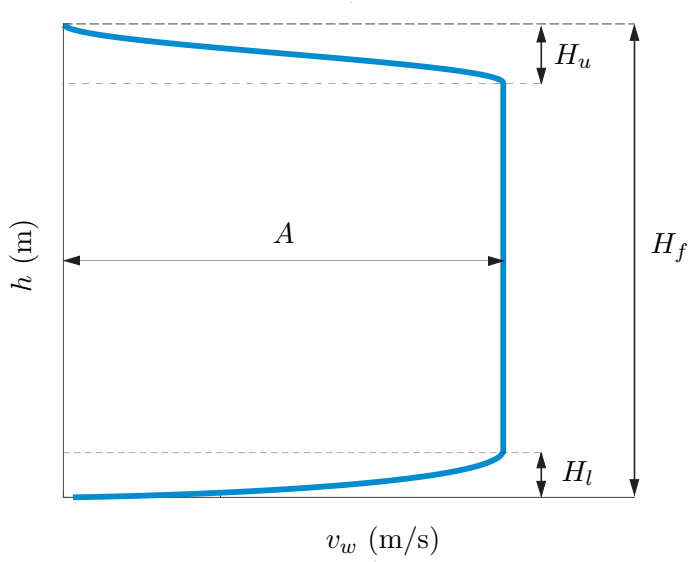

Figure 4.2: Planar wind steady-state profile $v_{wp}(h)$

The values of L_h and σ_h from Equation 4.1 can be found in tabular-form in reference [100] and are given in Table 4.2 for completeness. Note that the standard deviation of the wind turbulence is defined for light, moderate and severe turbulence levels.

Table 4.2: Turbulence length scale and wind standard deviation versus altitude.

Altitude	Turbulence length scale	Wind standard deviation σ_h (m/s)		
h (km)	L_h (m)	Light	Moderate	Severe
1	832	0.17	1.65	5.70
2	902	0.17	1.65	5.80
4	1040	0.20	2.04	6.24
6	1040	0.21	2.13	7.16
8	1040	0.22	2.15	7.59
10	1230	0.22	2.23	7.72
12	1800	0.25	2.47	7.89
14	2820	0.26	2.62	6.93
16	3400	0.24	2.44	5.00
18	5000	0.22	2.21	4.07
20	8640	0.23	2.26	3.85

As mentioned before, the vertical wind profile was selected to fit the wind model with the wind of the VEGA VV05 mission as indicated in reference [71]. The analysis shown in that reference is extended here to additional winds, see Figure 4.3. It can be seen that a set of 1000 random samples of this wind model (depicted in grey) envelopes the coverage of a range of different real wind data. Those wind profiles have been extracted from real measurements taken in French Guiana, the VEGA launch site, and were provided by ELV.

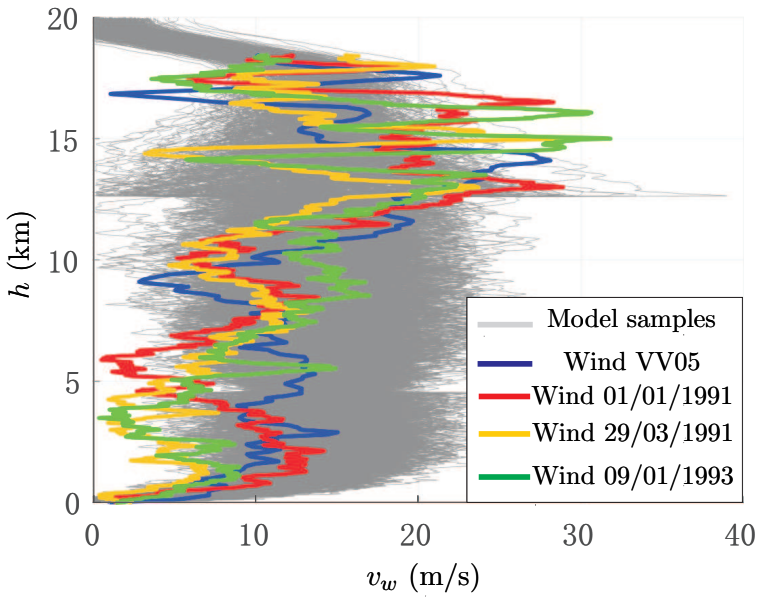

Figure 4.3: Wind profile analysis with real wind data

It is important to highlight that the wind model $G_w(s)$ has been successfully used for robust analysis of the VEGA launcher in reference [71]. The aim of this chapter is to demonstrate that the model can be used also for design, providing the optimiser information about the expected wind levels and also about the frequency content of the wind disturbance. The latter is very important in frequency-domain synthesis techniques such as the structured $\mathcal{H}_\infty$ technique.

4.1.3 Wind generator assessment

The wind model $G_w(s)$ is then used to augment the closed-loop design interconnection presented in Chapter 3. In particular, $G_w(s)$ is implemented at the wind disturbance input of the launch vehicle model, see the blue box in Figure 4.4. Using this configuration, the input disturbance weight W_w now scales the Gaussian process described by the Dryden filter $G_w(s)$. This input weighting function is defined as $W_w = \sigma_w$, where σ_w is the standard deviation of the unitary white noise input n_w. Note that σ_w is assumed to be 3 so that 99.7% of the wind levels are considered in design.

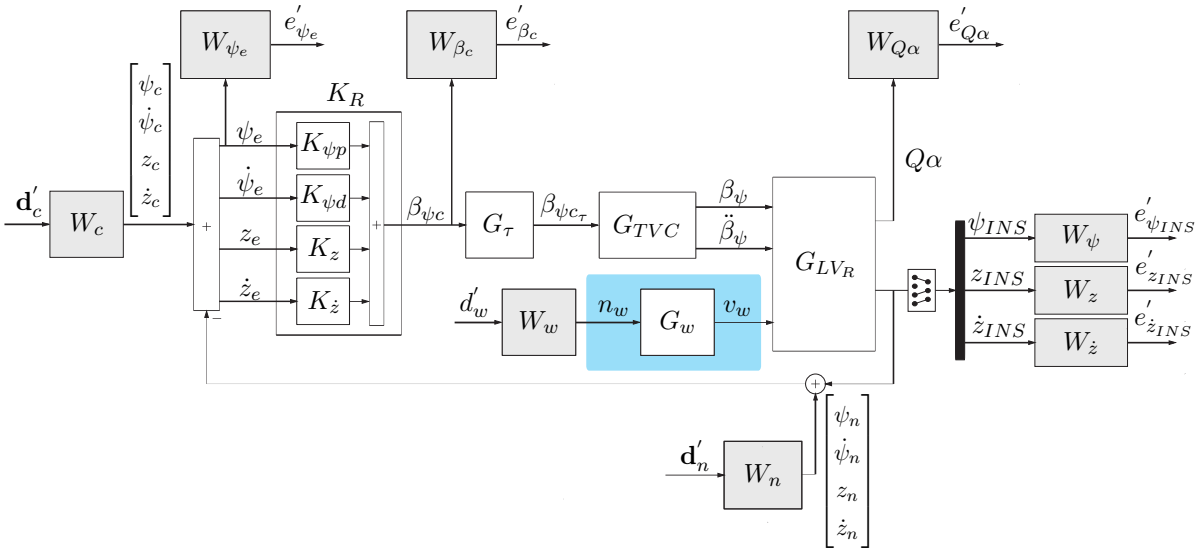

Figure 4.4: Closed-loop diagram for design with the wind generator model

To evaluate the influence of the wind model $G_w(s)$ on the design, two different controllers are synthesised using the structured $\mathcal{H}_\infty$ technique, one for moderate and the other for severe wind levels (using the values of σ_h given in Table 4.2). Both controller designs are performed using the same weighting functions (those used to recover the baseline controller in Chapter 3) at the same 9 operating points. Note that in these designs only the rigid-body gains are optimised, with the bending filters kept the same as the baseline controller when performing the verification campaigns.

The synthesised rigid-body gains are compared with those of the baseline in Figure 4.5. Note that the values in the y axis are not provided for confidentiality reasons. Looking at Figures 4.5a and 4.5b, it is observed that the attitude gains of the three designs present the same trend but with slightly different values (and that for the derivative gain, Figure 4.5b, both wind-based controllers have the same values across flight instance). It is also shown that the optimiser yields higher lateral feedback gains for the severe-wind design than for the other two cases (see Figure 4.5c and 4.5d). Also, note that the baseline and the moderate-wind controllers present almost the same rigid-body gain values across flight instance.

It is noted that the increase of $K_{\dot{z}}$ generally leads to a better drift-rate performance against wind disturbance, which in turn improves the wind disturbance rejection of the $Q\alpha$ channel as it will be shown later. This effect on $Q\alpha$ can be analytically ascertained by recalling from Equation 2.6 that the angle of attack depends directly on the drift-rate. Nevertheless, the increase of $K_{\dot{z}}$ must be handled with care since it deteriorates the rigid-body stability margins (specifically the high-frequency rigid-body gain margin).

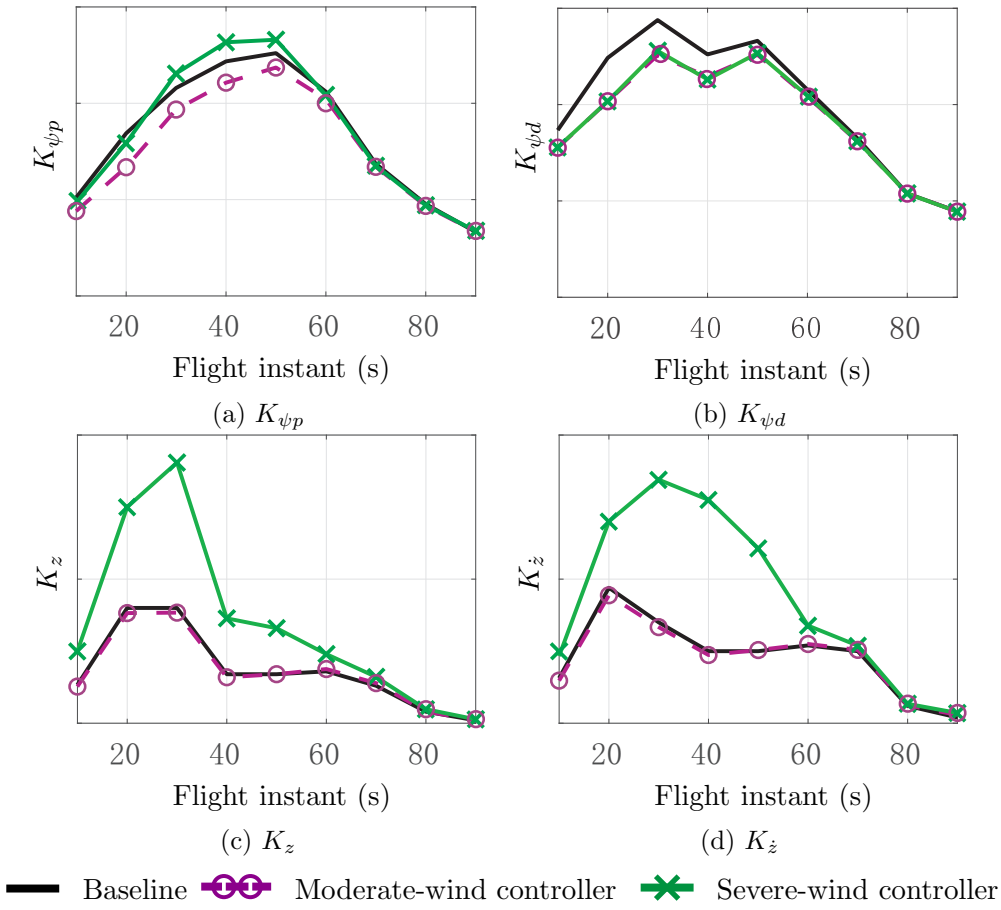

Figure 4.5: Time-evolution of the synthesised rigid-body gains

To confirm the above behaviour, the moderate-wind and severe-wind controllers are implemented in the nonlinear, high-fidelity simulator presented in Section 2.1.4. Figure 4.6 shows a comparison of the two augmented controllers (moderate-wind and severe-wind designs) versus the baseline controller using the simulation case defined by the VV05 nominal trajectory and wind data. It is interesting to see that in Figure 4.6, the baseline controller response (solid black line) and the moderate-wind controller (dashed magenta with circle markers) are almost coincident – hence, the need for the circle markers. This was expected since the moderate-wind controller roughly have the same rigid-body gains as the baseline controller, see Figure 4.5.

Furthermore, the severe-wind controller (in solid green with cross markers) reduces the aerodynamic loads (see Figure 4.6a). Particularly, the maximum $Q\alpha$ peak around Mach 3 is reduced by 13% with respect to the baseline controller. Moreover, the drift and drift-rate responses (see Figures 4.6b and 4.6c) are also significantly improved for the severe-wind controller resulting in less lateral deviations along the flight. It is highlighted that the same benchmarking was performed using different wind profiles, obtaining the same wind disturbance rejection capabilities shown in Figure 4.6.

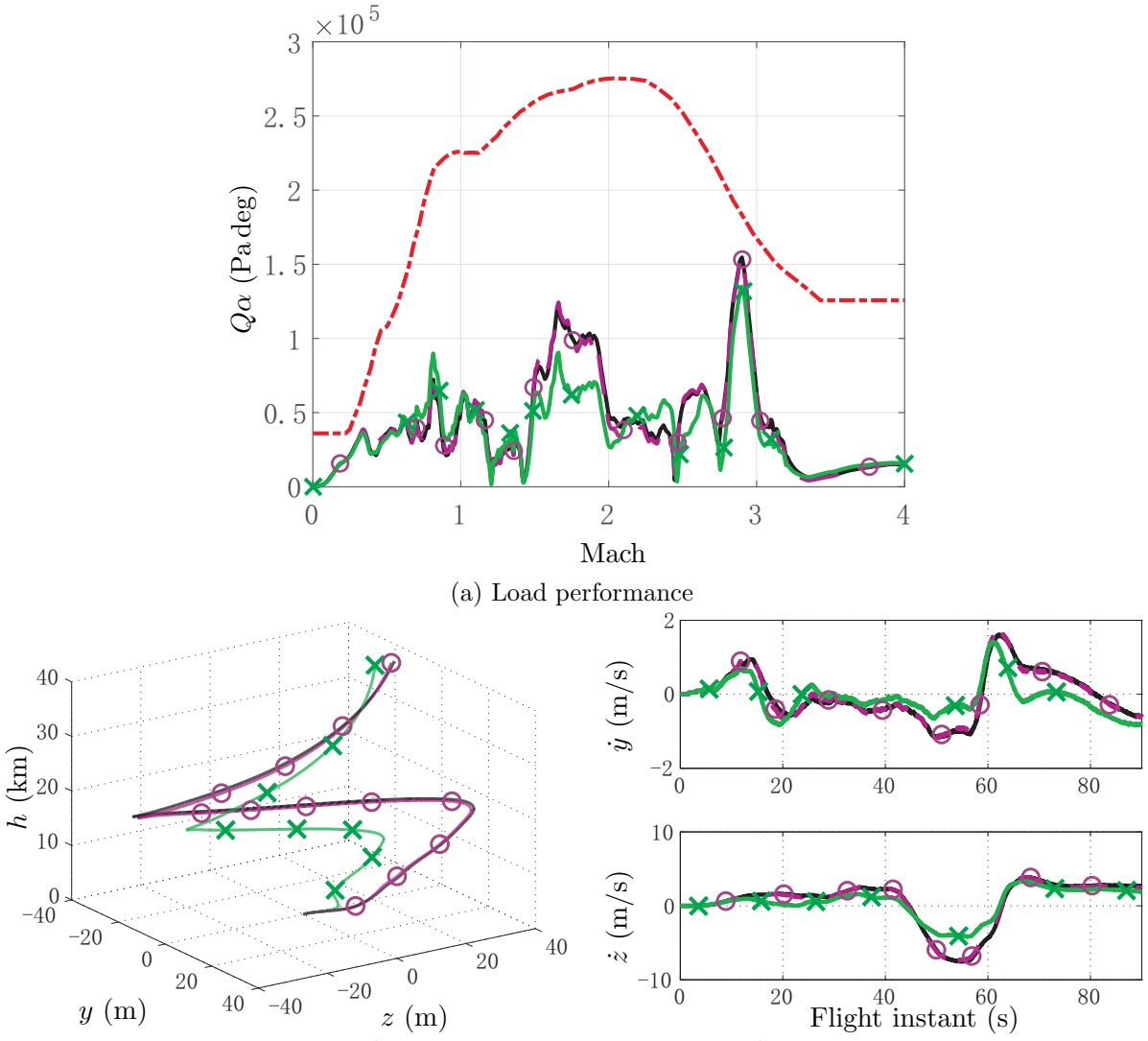

(a) Load performance

(b) Drift performance

(c) Drift rate performance

Figure 4.6: Nominal nonlinear flight responses for the moderate-wind and severe-wind controllers

To conclude, it is observed that the structured $\mathcal{H}_\infty$ optimisation results in better controllers (in terms of wind disturbance rejection) when stronger wind levels are employed in the design process. In addition, recall that the same weighting functions were used for the three controllers presented. For a finer synthesis, the weighting functions can be tailored according to the main controller objective at each linear design point.

4.2 Robust design augmentation

In this section, the VEGA rigid-body TVC system is formulated now in an explicit robust setting by augmenting the structured $\mathcal{H}_\infty$ design interconnection by means of LFT models for the main uncertain subsystems. The resulting controller is shown to provide a balanced performance but with higher robustness via linear and nonlinear analyses. For the former, classical stability margins as well as the structured singular value (which is also cursorily introduced in the section) are used, while for the latter the standard Monte Carlo (MC) approach is used.

4.2.1 Robust structured control problem formulation

The closed-loop design interconnection used in the previous section, see Figure 4.4, can be further augmented by including uncertainties in the design. As mentioned before in Section 3.1, the structured $\mathcal{H}_\infty$ optimisation can be performed accounting for real parametric uncertainties in the design [88]. To this end, the nominal LTI models of the TVC actuator, delay and rigid-body launch vehicle are replaced now by their LFT counterparts presented in Section 2.2.2. Note that the LFT model of the VEGA launcher only accounts for the rigid-model uncertainties Δ_{LV_R}. The resultant closed-loop diagram is shown in Figure 4.7 (as before, blue boxes are used to indicate the augmented components).

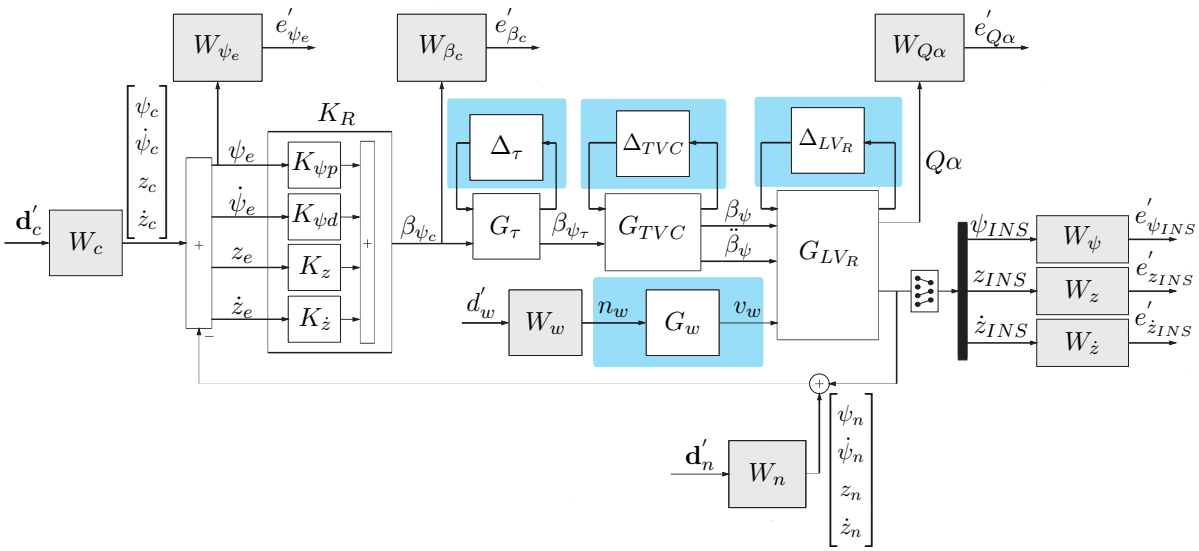

Figure 4.7: Closed-loop diagram for design with parametric uncertainties

In preparation for the subsequent structured $\mathcal{H}_\infty$ optimisation the weighted closed-loop diagram of Figure 4.7 is formulated as the robust standard $\mathcal{H}_\infty$ interconnection shown in Figure 4.8. In this generalised LFT design formulation the total uncertainty block Δ_R is pulled out of the generalised plant $P(s)$ and $\Delta_R \in \boldsymbol{\Delta_R}$ with $\boldsymbol{\Delta_R} = diag(\boldsymbol{\Delta_{LV_R}}, \boldsymbol{\Delta_\tau}, \boldsymbol{\Delta_{TVC}})$. The control problem consists of finding a stabilising sub-optimal controller K within the controller space $\mathcal{K}_{\mathbf{VEGA_R}}$ (which was defined in Equation 3.7) that minimises the cost function in Equation 4.3.

$$\min_{K} \max_{\Delta_R \in \mathbf{\Delta_R}} ||\mathcal{T}_{\mathbf{e'd'}}(s, \Delta_R)||_\infty < \gamma; \qquad \text{subject to } K \in \mathcal{K}_{\mathbf{VEGA_R}} \tag{4.3}$$

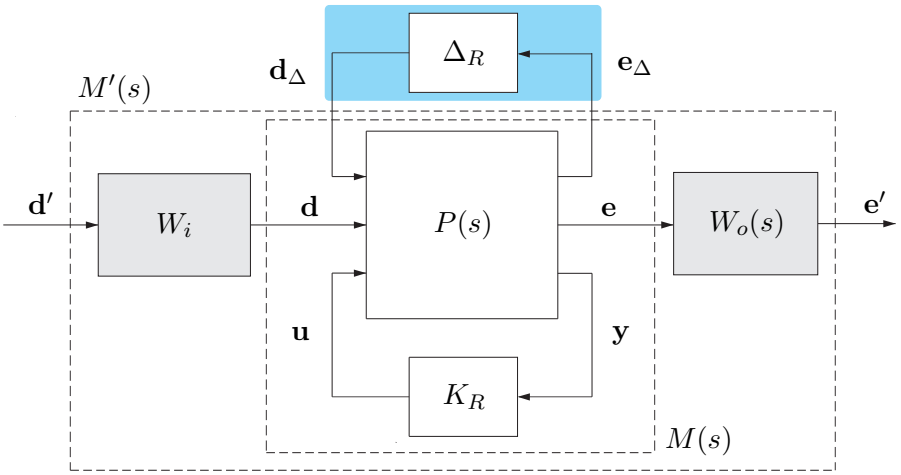

Figure 4.8: Augmented robust standard $\mathcal{H}_\infty$ interconnection

4.2.2 Robust structured $\mathcal{H}_\infty$ control design

The previous design configuration allows to synthesise a controller K that is robust against the expected variations of the main parameters of the system. To illustrate the capabilities of this design augmentation, the structured $\mathcal{H}_\infty$ synthesis approach is applied at 9 different linear operating points as before, i.e. at t=5 s and every 10 seconds between flight instants t=20 s and t=90 s.

For this robust design, an optimal control strategy is performed to achieve a trade-off balance for the best global performance. In particular, a load-relief control mode is employed about the maximum dynamic pressure region (t=[40, 50, 60]s). For the rest of the operating points, the design is focused on minimising the tracking error while keeping the lateral deviations bounded within specifications. In addition, it is highlighted that the wind model $G_w(s)$ is set to model severe turbulence levels for all the linear designs.

The weight setup follows the same rationale presented for the VEGA baseline recovery in Section 3.4, but differs in the value of the weights, which are selected in an iterative process to obtain a balanced performance while satisfying the stability requirements. Similarly, the values of the weighting functions are varied at each linear design point to cover the system variation along the atmospheric phase and also to tailor the different linear designs to the control strategies mentioned before. It is noted that that the values of the weights obtained now are slightly higher than the ones used to recover the baseline controller in Chapter 3 to account for the higher range of values of the transfer functions due to uncertainties.

To evaluate the performance of this new design, the frequency responses of the main output channels from the wind disturbance input n_w are shown in Figure 4.9 for the linear design point obtained at t=60 s (i.e. around maximum dynamic pressure). This plot compares the nominal responses (in dark solid lines) versus 500 dispersed random LFT samples (in lighter solid lines) for two controllers: the baseline controller (in black) and the new robust structured $\mathcal{H}_\infty$ design (in blue). In addition, the inverse of the corresponding output weighting functions are also illustrated (in solid green lines).

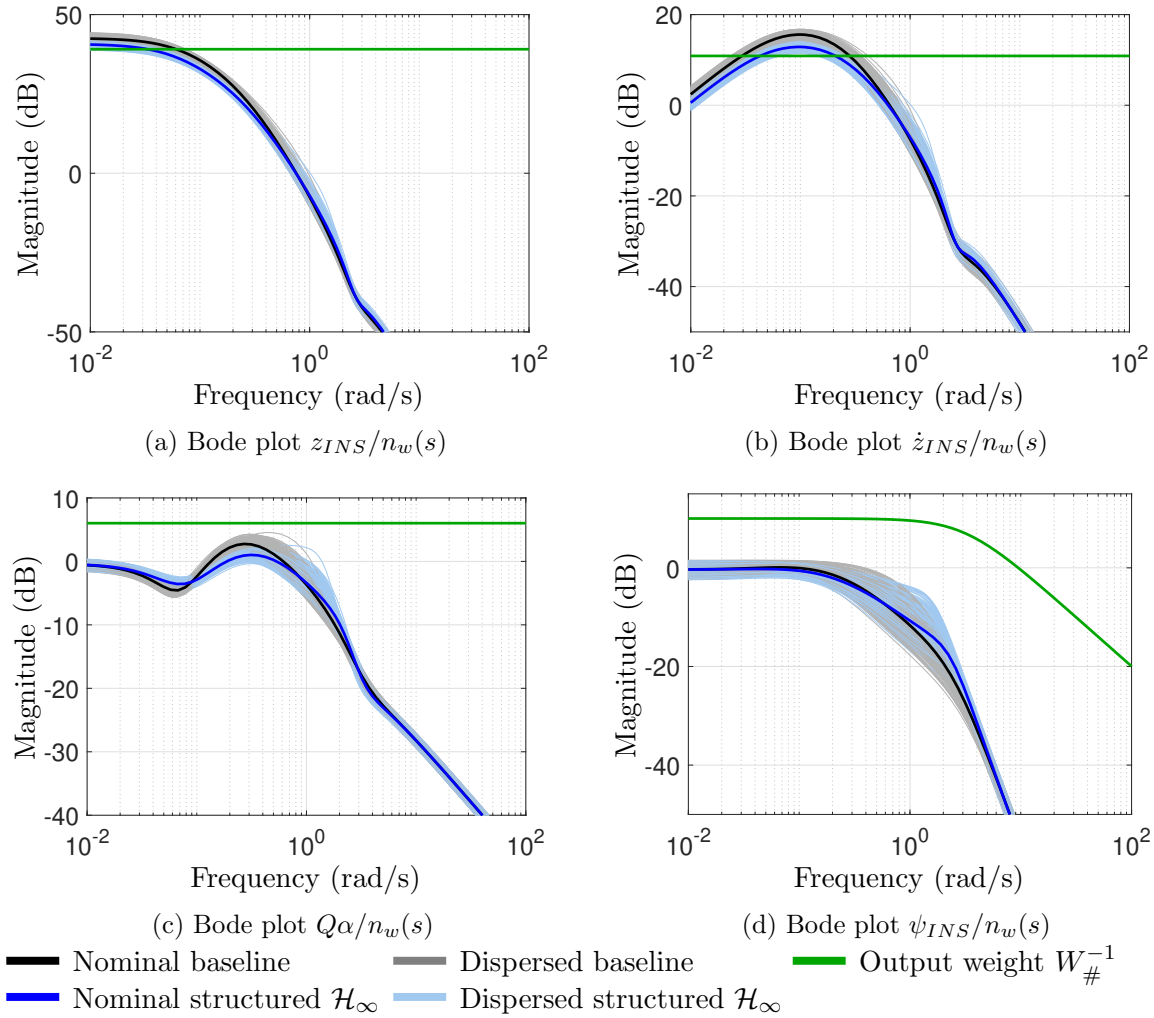

(a) Bode plot $z_{INS}/n_w(s)$

(b) Bode plot $\dot{z}_{INS}/n_w(s)$

(c) Bode plot $Q\alpha/n_w(s)$

(d) Bode plot $\psi_{INS}/n_w(s)$

Figure 4.9: Frequency responses of the main output channels from wind disturbance at t=60 s for the baseline controller and the augmented robust structured $\mathcal{H}_\infty$ controller

Looking at Figures 4.9a and 4.9b, it is noticeable that the augmented robust structured $\mathcal{H}_\infty$ controller reduces the wind disturbance contribution in both drift and drift-rate channels at low frequencies. In addition, Figure 4.9c demonstrate the ability of the robust structured $\mathcal{H}_\infty$ to reduce the transient energy of the $Q\alpha$ channel from the wind disturbance input (specially between 0.1 and 1 rad/s). This range is important as it is the frequency range where the wind disturbance has more impact.

4.2.3 Classical stability analysis

In this section, the stability of the VEGA launch vehicle using the robust structured $\mathcal{H}_\infty$ controller is assessed. The analysis is performed considering the full launch vehicle model (i.e. flexible-body dynamics are included) and using the full VEGA TVC architecture presented in Figure 2.4. This controller configuration uses the synthesised structured $\mathcal{H}_\infty$ rigid-body gains while the set of filters $H(s)$ are kept the same as the baseline controller.

The system stability is traditionally analysed through a set of gain and phase margins at different crossing frequencies (see Section 2.1.5). These stability margins are evaluated in the frequency domain through Nichols plots at different flight instants. To that end, the open-loop system (controller, actuator and launch vehicle model) is re-arranged and broken at the controller output in order to reduce the system to a SISO configuration.

The traditional design verification and validation for the VEGA launcher defines specifications for nominal and dispersed conditions. Firstly, the system stability using the robust structured $\mathcal{H}_\infty$ design is analysed in Figure 4.10 under nominal conditions at each linear design point. This plot shows that the structured $\mathcal{H}_\infty$ controller provides satisfactory margins throughout the flight satisfying the nominal stability specifications.

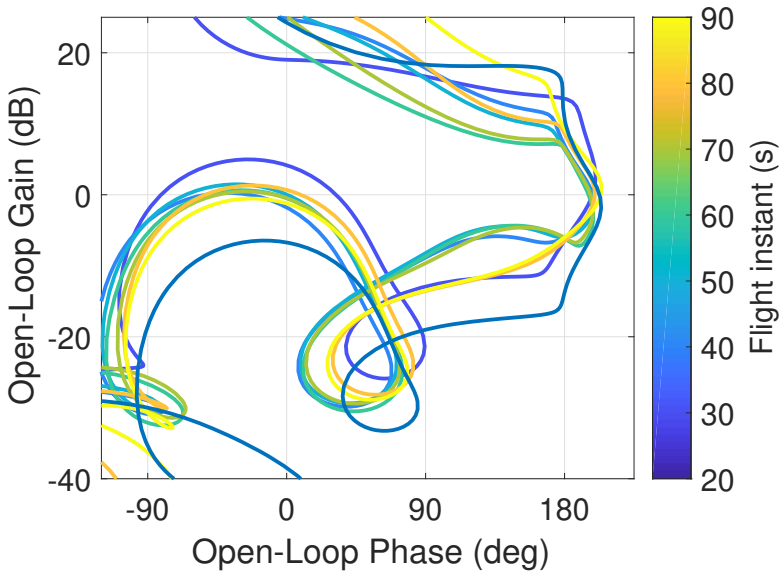

Figure 4.10: Nominal stability analysis of the robust structured $\mathcal{H}_\infty$ design

The analysis for scattered configurations is performed using a Monte Carlo (MC) approach with 1000 random samples (note that in this case the MC is performed on the LFT model uncertainty set Δ). Figure 4.11 illustrates the Nichols chart of the nominal system at t=60 s and 1000 MC random LFT samples (again using dark line for the former and lighter for the dispersed). This plot shows the stability degradation due to system uncertainties, which is still acceptable under the defined dispersed VEGA requirements.

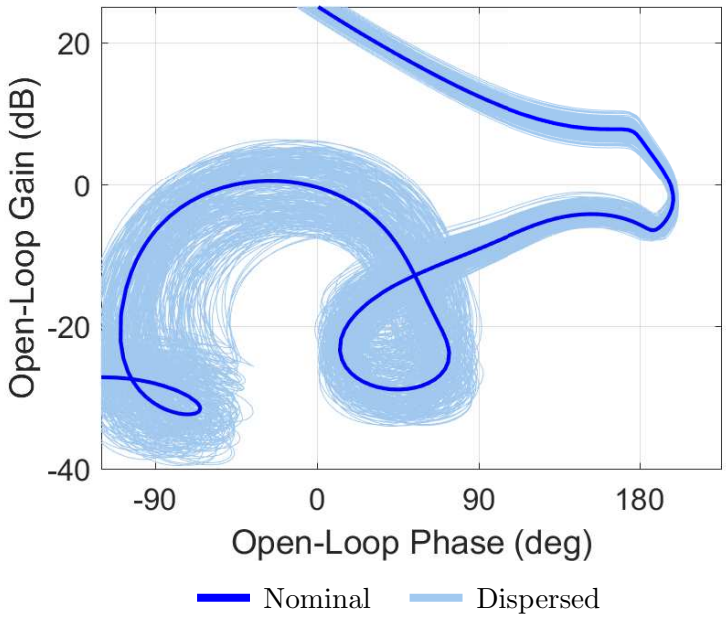

Figure 4.11: Dispersed stability analysis of the robust structured $\mathcal{H}_\infty$ design at t=60 s

To conclude this subsection, the main linear metrics from Table 2.1 are analysed for the new controller in Figure 4.12. This plot shows the stability margins along the different design points for the nominal LFT as well as for the LFT obtained using at each flight instance the "worst-case" among all the MC runs (these cases are referred to as "MC-based WC" in the plot). It is important to remark that all the stability specifications are fulfilled with the new robust design.

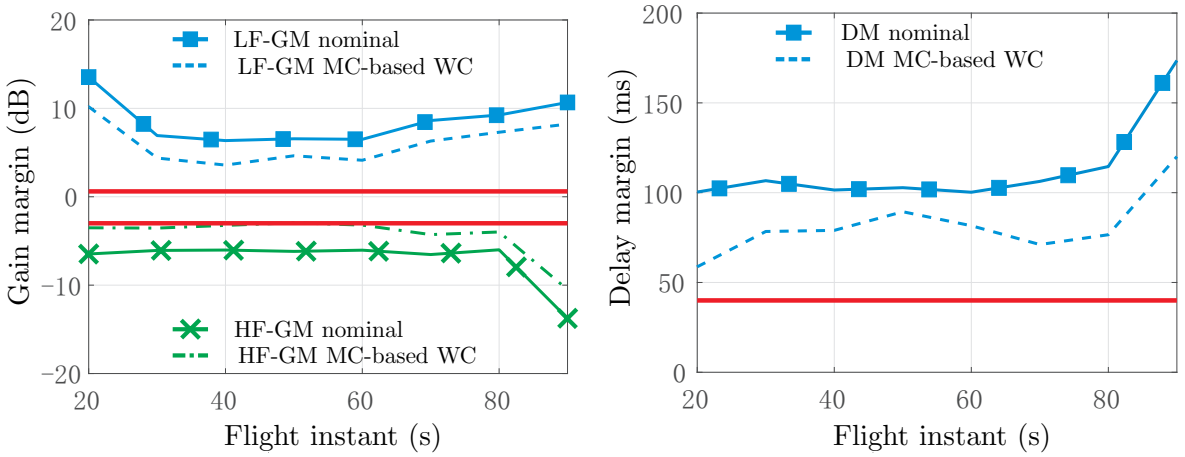

(a) Rigid-body gain margins

(b) Rigid-body delay margin

Stability margin requirements for dispersed conditions

Figure 4.12: Worst-case stability margin assessment

The traditional validation process further extends the previous nominal and MC-based analyses by using ad-hoc test cases to complete the coverage of the analysis, resulting in an expensive (in terms of both cost and time) procedure. Another practical limitation of the traditional approach is the lack of guarantees in finding the worst case. This can be overcome by complementing the MC approach by using worst-case tools such as the linear structured singular value μ, which can provide analytically guaranteed bounds on robust stability and performance. Next, this robust analysis technique is applied to the VEGA launcher.

4.2.4 Robust linear μ analysis

The structured singular value μ was first proposed in 1982 in reference [101]. This analysis approach allows to evaluate analytically the robustness of uncertain systems. The so-called μ analysis relies on systems defined by a LFT interconnection such as the one described in Figure 4.8. Basically, $\mu_{\Delta}\big(M(s)\big)$ represents a metric of the smallest structured uncertainty Δ that leads the system to instability. This provides very valuable insight on how the system stability is affected by uncertainties. In addition, the singular structured value can also be used to assess the performance degradation due to uncertainties.

The computation of μ was further developed by the original authors and subsequently included in 1993 in Matlab's *μ-analysis and Synthesis Toolbox* [33]. Since the appearance of this analysis tool, μ analysis has been used in many aerospace applications to evaluate the robust stability and performance of satellite missions [102] and also spacecrafts such as the European ATV [103]. Furthermore, the structured singular value has been applied on robust control analysis for the VEGA launcher in reference [71].

In this section, a cursory introduction of the singular structured value μ is presented. Then, this analysis approach is used to assess the robust stability and performance of the VEGA launcher using the robust structured $\mathcal{H}_{\infty}$ controller.

Structured singular value μ background

The robust stability of the VEGA launcher system, which is defined by $M(s)$ in Figure 4.8, can be assessed via the structured singular value μ [101], which is computed as follows:

$$\mu_{\Delta}(M_{11}) = \frac{1}{min_{\Delta}\{\overline{\sigma}(\Delta) : det(I - M_{11}\Delta) = 0\}} \quad \text{with } ||\Delta||_{\infty} < 1 \tag{4.4}$$

where $M_{11} = \mathcal{T}_{\mathbf{e}_{\Delta}\mathbf{d}_{\Delta}}$ represents the transfer function from the uncertainty channel $\mathbf{d}_{\Delta}$ to $\mathbf{e}_{\Delta}$.

In this context, the system $M(s)$ is then robustly stable if $M(s)$ is nominally stable and the following Robust Stability (RS) condition is satisfied over all frequencies:

$$\mu_{\Delta}\big(M_{11}(j\omega)\big) < 1, \quad \forall\, \omega \in \mathbb{R} \tag{4.5}$$

If robust stability is achieved, then there are analytical guarantees that there is no combination of uncertainties within the range defined by the LFT model which leads to instability.

It is important to mention that μ is computed using bounds because the structured singular value computation is a non-polynomial hard problem [104]. The Upper Bound (UB) provides the maximum size perturbation for which the RS condition given in Equation 4.5 is violated, whereas the Lower Bound (LB) provides the minimum size perturbation for which the RS condition is guaranteed.

In addition, the structured singular value can also be used for Robust Performance (RP) analysis, which verifies if the performance objectives defined by the weighting functions in Figure 4.8 are satisfied for all the plants in the uncertainty set defined by the LFT models.

In order to address the RP analysis, the robust interconnection of Figure 4.8 is closed using a fictitious full-complex perturbation matrix Δ_P, which does not represent any actual perturbation of the system. In this context, RP is guaranteed if $\mu_{\hat{\Delta}}\big(M'(s)\big) \leq 1$ over all frequencies, where $\hat{\Delta} = diag\big(\Delta, \Delta_P\big)$. Furthermore, it is well-known that RP values are directly related to RS and also to the maximum singular value, which represents Nominal Performance (NP), through Equation 4.6 [22].

$$\underbrace{\mu_{\hat{\Delta}}(M')}_{RP} \geq max\Big\{\underbrace{\mu_{\Delta}(M'_{11})}_{RS}, \underbrace{\overline{\sigma}(M'_{22})}_{NP}\Big\} \tag{4.6}$$

Robust stability analysis

In this section, the structured singular value μ is applied to analyse the RS provided by the augmented structured $\mathcal{H}_\infty$ controller. Note that for this analysis, the uncertainty matrix Δ_R has been modified to include a 1% complex uncertainty to one of the parametric uncertainties of the TVC model. It is well-known that a mixed real/complex uncertainty structure improves the accuracy of the μ computation (without affecting the actual analysis result in the majority of the cases) [75].

Figure 4.13 shows the upper and lower bounds of μ computed at the same time instance used for the previous linear analyses, t=60 s, for the baseline and the augmented robust structured design. Looking at the baseline μ bounds (in black), it is clear that the system is not robustly stable since there is a peak around 10 rad/s in which both upper and lower bounds are higher than 1. It is highlighted that μ does not only output a binary solution (either the system is robust stable or not), but also provides information in the frequency domain about how the system stability is degraded due to system uncertainties. For instance, it is identified that the peak above 1 is centered around the HF-GM frequencies. This information is quite valuable for synthesis, since it identifies stability problems before going for an extensive MC-based validation process.

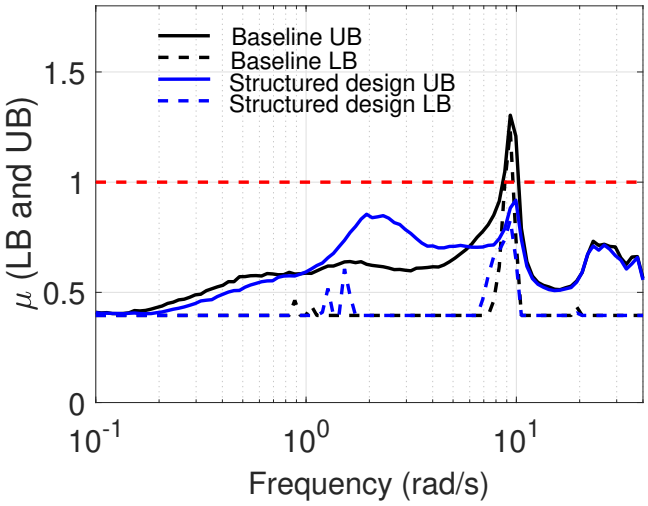

Figure 4.13: RS analysis of the robust structured $\mathcal{H}_\infty$ design and baseline controller at t=60 s (▬ RS condition)

In contrast, Figure 4.13 clearly shows that the RS condition is satisfied at all frequencies for the augmented robust structured $\mathcal{H}_\infty$ controller (at the analysed point of t=60 s). Looking at the upper bounds, this robust design slightly improves also the RS at low frequencies (below 1 rad/s) and critically much more at high frequencies particularly around the peak at 10 rad/s. These improvements come at the expense of larger upper bounds around 2 rad/s (this illustrates the so-called water-bed effect [22, 75]).

The same RS analysis is carried out at the other linear design points but only for the structured $\mathcal{H}_\infty$ design (see Figure 4.14). For ease of visualisation, only the upper bounds are shown. As before, this plot clearly shows that the system is robustly stable throughout the atmospheric phase.

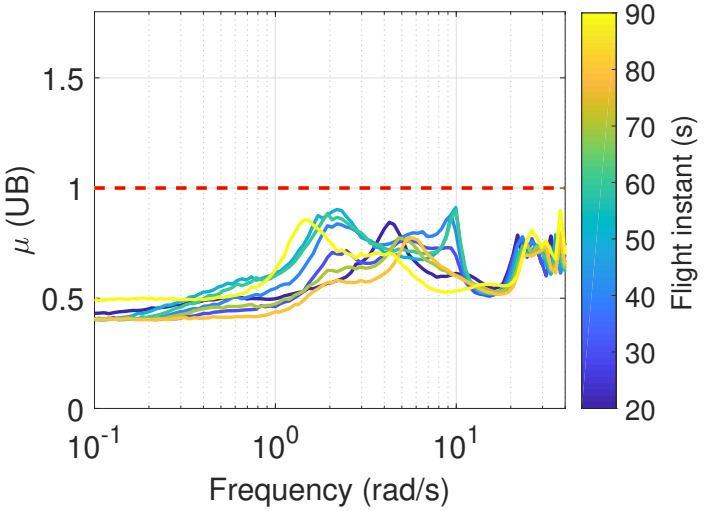

Figure 4.14: RS analysis of the robust structured $\mathcal{H}_\infty$ design over the atmospheric flight

Robust performance analysis

Figure 4.15 shows the RP analysis at t=60 s for two different performance indicators, tracking and drift-rate. Similarly, the baseline controller and the robust structured $\mathcal{H}_\infty$ design are compared. For each controller/metric, the upper bound of $\mu_{\hat{\Delta}}(M')$ and the maximum singular value $\overline{\sigma}(M'_{22})$ are shown. Note that the latter represents the NP when $\Delta = 0$. This comparison allows to observe the performance degradation due to uncertainties over the frequency axis.

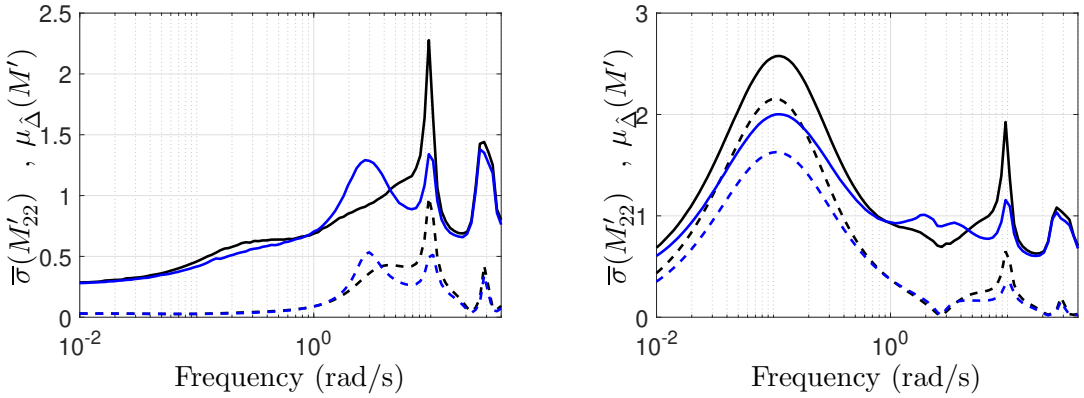

(a) RP analysis (tracking channel)

(b) RP analysis (drift-rate channel)

RP baseline NP baseline RP structured $\mathcal{H}_\infty$ NP structured $\mathcal{H}_\infty$

Figure 4.15: RP analysis of the robust structured $\mathcal{H}_\infty$ design and baseline controller at t=60 s

As mentioned before, Robust Performance (RP) is directly linked to Robust Stability (RS) and Nominal Performance (NP). Looking at Figure 4.15a, it is seen that the RP values for the tracking channel follows the same pattern seen in the RS analysis (e.g. lower upper bounds at low frequencies and at around 10 rad/s and higher values around 2 rad/s). Also, notice that RP values for the drift-rate channel (see right plot) are mainly influenced by NP at low frequencies.

It is important to highlight that these results are based on the specific weights used for the design of the augmented robust structured $\mathcal{H}_\infty$ controller. Thus, the fact that both controllers present RP upper bounds higher than one only means that the optimisation objectives were too demanding. This was already observed in Figures 4.9a and 4.9b, where it was seen that the frequency responses of both controllers take higher values than the corresponding weighting functions at low frequencies. Nonetheless, Figure 4.15 clearly illustrates that the structured $\mathcal{H}_\infty$ design generally improves the RP for both tracking and drift-rate channels with respect to the baseline controller.

The enhanced RP for both tracking and drift-rate channels also implies an improvement on the load performance requirement, since $Q\alpha$ directly depends on those two metrics (recall Equation 2.6). In this analysis framework, it is also possible to analyse the RP of a channel with respect to a certain input. For instance, Figure 4.16 shows the RP of the $Q\alpha$ channel from its main contributor which is the wind disturbance. It is seen that the augmented robust structured $\mathcal{H}_\infty$ design improves the $Q\alpha$ RP at low frequencies and also improves it with respect to high-frequency wind gusts (see around 10 rad/s).

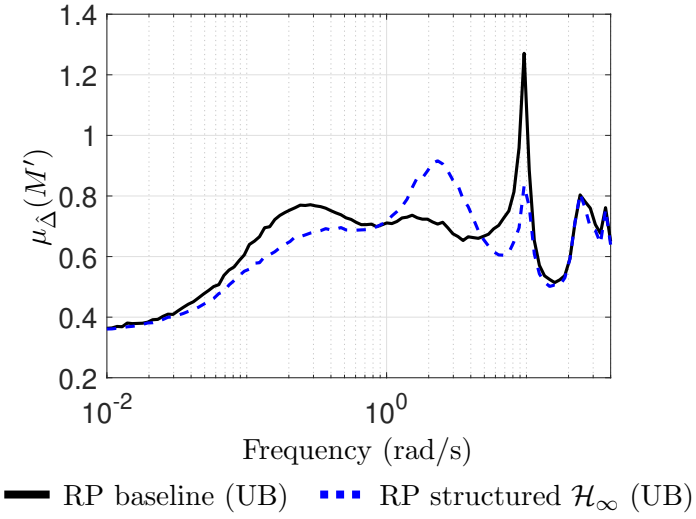

Figure 4.16: RP analysis of the $Q\alpha$ channel from wind disturbance input at t=60 s

Although not covered in this thesis, it is noted that the structured singular value also allows to perform sensitivity analysis and extract worst-case uncertainty combinations. References [71, 67] has shown that this analysis can be very efficient in finding demanding worst cases for the VEGA launcher.

4.2.5 Nonlinear analysis

Finally, all the 9 linear augmented robust structured $\mathcal{H}_\infty$ design-point controllers are scheduled, implemented and validated in the nonlinear, high-fidelity described in Section 2.1.4. To evaluate the performance and robustness of this global augmented robust design, four MC campaigns of 500 runs are performed. For each run, the same nominal VEGA VV05 flight trajectory is used but the system parameters are all sampled randomly. Each of the four MC campaign uses the same parameters' scattering but a different wind profile (among them, the estimated wind encountered in VEGA VV05 mission). Note that the four wind profiles have been extracted from real measurements taken at the VEGA launch site (French Guyana) and cover strong and moderate wind gusts at different altitudes. The same four MC set-ups are applied also to the VEGA VV05 baseline controller to allow comparing the improvements in robustness.

The outcomes of this MC campaign for both controllers are depicted side-by-side in Figure 4.17 (on the left for the baseline and on the right for the augmented robust structured design). For each, the total 2000 randomly sampled MC responses are shown for the aerodynamic load $Q\alpha$ (top plots) and the TVC actuator deflections (bottom plots). In order to have a reference, the nominal simulations using the VEGA VV05 mission wind are highlighted in darker lines. Looking at the $Q\alpha$ responses, it can be observed that the higher $Q\alpha$ peaks (around Mach 1.5, 2.5 and 2.9) are reduced for the augmented robust structured $\mathcal{H}_\infty$ design. As for the TVC actuation, although less visible, the responses using this controller require slightly less TVC deflections to handle the different strong wind gusts encountered.

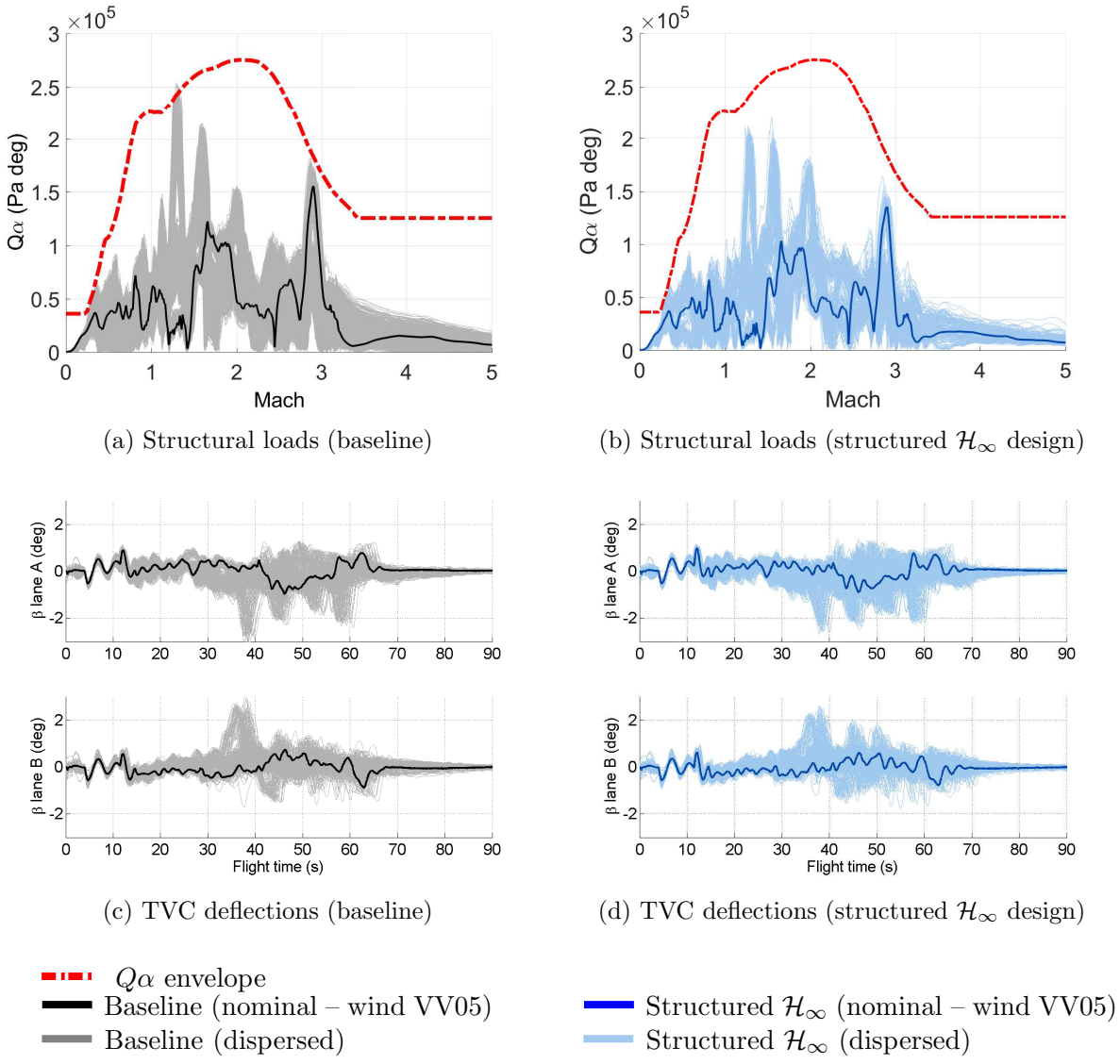

(a) Structural loads (baseline)

(b) Structural loads (structured $\mathcal{H}_\infty$ design)

(c) TVC deflections (baseline)

(d) TVC deflections (structured $\mathcal{H}_\infty$ design)

Figure 4.17: Nonlinear Monte Carlo responses

In order to quantitatively compare both designs, a set of performance indicators (such as actuation, attitude error, drift or aerodynamic load performance) are analysed. For each MC run and controller, two different metrics are computed for each indicator: the ∞-norm and the 2-norm. The former is equivalent to the maximum value taken by the assessed variable, whereas the latter accounts for the energy of the indicator. Then, for each controller and each indicator, the average of those two norms are computed with the aim of comparing the robustness of both controllers. Figure 4.18 shows the average obtained for each controller (for both ∞-norm and 2-norm) normalised with respect to the corresponding baseline controller values.

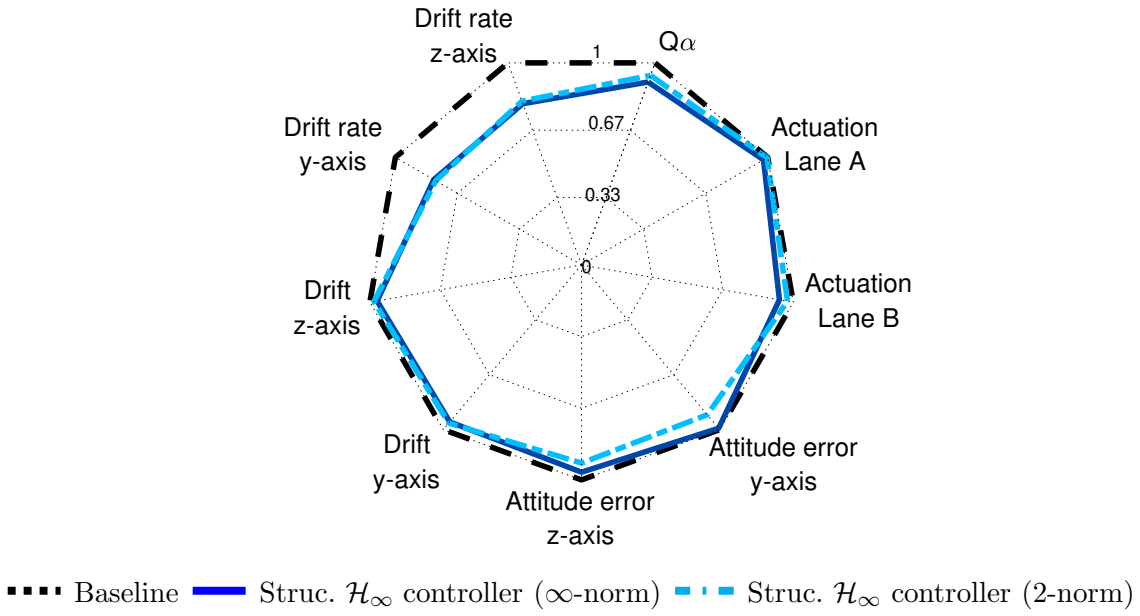

Figure 4.18: Monte Carlo quantitative assessment

Overall, it can be seen that the augmented robust structured $\mathcal{H}_\infty$ design improves the performance for all the indicator/norm pairs. It is interesting to observed that the linear RP results from the previous section are validated in this nonlinear analysis. This robust controller reduces the $Q\alpha$ peaks by 10%, the energy of the attitude error also by 10% in both axes and the drift-rate performance is significantly improved by 20% in both ∞- and 2-norms. Furthermore, the average TVC deflection peaks are reduced by 5%.

These results highlight that the augmented robust design is able to tackle different competing trade-off objectives at the same time and provides a balanced solution for a better global performance. Recall that this is achieved by only optimising the rigid-body controller gains (the bending filters are kept the same as the baseline). This design framework will be further augmented in the next chapter by including the bending filters' design in an integrated fashion.

4.3 Conclusions

This chapter demonstrates via LFT modeling, structured $\mathcal{H}_\infty$ optimisation, μ analysis and nonlinear MC simulations, how this robust control framework is suitable to address challenging and uncertain control problems such as launcher atmospheric TVC design.

With the aim to explore the potential for improvement over the traditional state-of-practice, the design interconnection was first augmented by including a wind turbulence Dryden filter and subsequently also uncertain LFT models. The former provides the control optimiser with information about the wind levels and the frequency content of the wind disturbance. In this regard, it is highlighted that the use of strong wind levels for design contributes to improve the wind disturbance rejection performance for this mission. Moreover, the latter augmentation allows to perform the design against the expected variations of the system parameters.

Using this augmented configuration, the linear structured $\mathcal{H}_\infty$ controllers are synthesised and then analysed in terms of the traditional verification and validation process based on stability margins and nonlinear MC simulations. The system has also been analysed using the structured singular value μ, which provides analytically guaranteed bounds on robust stability and robust performance. This analysis tool provides a direct connection to design, since it gives a good insight on the robustness of the system without applying an extensive MC validation process.

The final, scheduled (augmented robust structured $\mathcal{H}_\infty$) controller design provides robust stability throughout the flight envelope and improved robust performance with respect to the baseline controller, while keeping the classical VEGA TVC architecture and just using new values for the rigid-body gains. Furthermore, it is shown via μ analysis that the better robust performance mainly comes from the improved stability robustness. These results highlight the improvements that can be achieved by increasing the information provided to the control optimisation. In addition, they also show the capability of this synthesis framework to tackle the direct trade-off of robustness versus performance using a more comprehensive methodology.

CHAPTER 5

Joint design of VEGA's rigid-body controller and bending filter

In Chapter 3 the structured $\mathcal{H}_\infty$ technique was used to propose a legacy recovery approach that yielded the same rigid-body controller as that for the VEGA atmospheric TVC control system. This was followed in Chapter 4 with a control design augmentation approach that improved the performance and robustness of the rigid-body VEGA controller by introducing incrementally wind and uncertainty system knowledge. But the design of the full atmospheric control system for any launcher also requires careful consideration of its flexible dynamics. The elastic behaviour of launch vehicles are typically characterized by low-damping bending modes, which can create large oscillations and thus lead to instability if they are excited by the control system. To avoid these potential instabilities, the TVC system generally incorporates bending filters, which minimise these flexible-body structure interactions with the control system.

As mentioned in Section 1.2, the traditional design state-of-practice consists of several sequential and iterative steps [14], where the rigid-body controller and bending filters are designed separately. Then, both rigid-body controller and bending filters are manually tuned in an ad-hoc manual integration process until all the system requirements are met. Regardless the design approach used, the introduction of the bending filters generally results in degradation of the rigid-body stability margins and performance. This is particularly critical when the frequency of the first structural mode is close to the control system bandwidth.

In this chapter, the flexible dynamics of the launch vehicle are taken into account to also address the design of the bending filters. The significance of this chapter is that, unlike the state-of-practice, the rigid-body controller and bending filters are first parametrised and then optimized simultaneously using the structured $\mathcal{H}_\infty$ optimisation approach. The joint design of the rigid-body controller and the bending filters allows to optimise the rigid-body stability and performance while achieving a proper mode-stabilisation in one single step. Thus, this design scheme can significantly simplify the synthesis process and reduce the tuning effort prior to each launcher mission.

The layout of this chapter is as follows. Section 5.1 shows how to formulate the structured $\mathcal{H}_\infty$ optimisation to perform the joint design of VEGA's rigid-body controller and bending filters. The capabilities of this advanced synthesis framework are demonstrated, as in previous chapters, using as benchmark the VEGA 5^{th} mission data. Section 5.2 analyses the resulting structured $\mathcal{H}_\infty$ controller in terms of classical stability margins, μ analysis and nonlinear MC simulations. Finally, conclusions are presented in Section 5.3.

5.1 Joint rigid/flexible robust structured $\mathcal{H}_\infty$ synthesis

This section is dedicated to describe the joint synthesis of the rigid-body controller and bending filter for the atmospheric phase VEGA launcher. As in the previous chapters, the structured $\mathcal{H}_\infty$ optimisation is performed in continuous-time domain and applied at 9 several flight instants along the atmospheric phase (i.e. starting at t=5 s and then at 8 flight instants between t=20 s and t=90 s in intervals of 10 seconds).

First (subsections 5.1.1 and 5.1.2), the problem is formulated as a robust control problem and the controller structure parametrisation setup is described in detail. Then in subsection 5.1.3, the weighting functions used for design are introduced and finally (subsection 5.1.4), the synthesised rigid-body gains and bending filters are discussed.

5.1.1 Control problem formulation

The previous chapter's full augmented rigid-body design interconnection (with wind model and parametric uncertainties) is redefined to perform the already mentioned joint synthesis, see Figure 5.1 where the new blocks with respect to the previous interconnection are highlighted with a blue box.

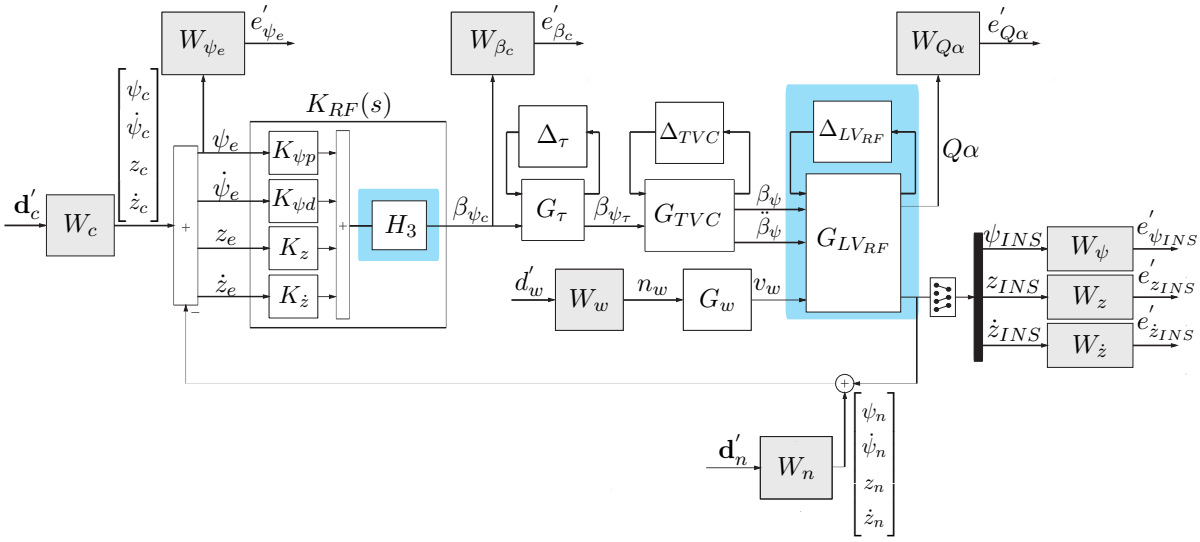

Figure 5.1: Closed-loop diagram for the joint design of VEGA's rigid-body controller and bending filters

Similarly as for the robust augmented design presented in Section 4.2, the wind model $G_w(s)$ is configured to model severe turbulence models. Also, notice that there are two main differences in this closed-loop diagram with respect to the one presented in the previous chapter. First, the launch vehicle model $G_{LV_{RF}}(s)$ also considers the flexible-body dynamics of the launcher accounting for the first bending mode (recall that the nominal representation is given by Equations 2.16–2.19). Accordingly, the VEGA LFT model is built using the uncertainty block $\Delta_{LV_{RF}}$, which includes rigid-body and flexible parametric uncertainties (see Section 2.2.2.2). And second, the controller architecture is augmented to incorporate the necessary structure to stabilise the bending modes.

5.1.2 Tunable controller structure

The architecture of the tunable controller $K_{RF}(s)$ is shown in Figure 5.1 and for clarity, as a single diagram in Figure 5.2. It is composed of a rigid-body controller and a bending filter $H_3(s)$. This structure is based on the actual VEGA TVC control system architecture (see Figure 2.4) [2], but differs in three main aspects. First, as in previous chapters, the attitude error rate signal $\dot{\psi}_e$ is assumed available for design. Second, in order to reduce the complexity of the controller structure and to simplify the optimisation process, the actual VEGA filters $H_1(s)$ and $H_4(s)$ are not implemented. And third, and most importantly, in order to apply the structured $\mathcal{H}_\infty$ optimisation, the filter $H_3(s)$ is parametrised based on the legacy information of the baseline bending filter.

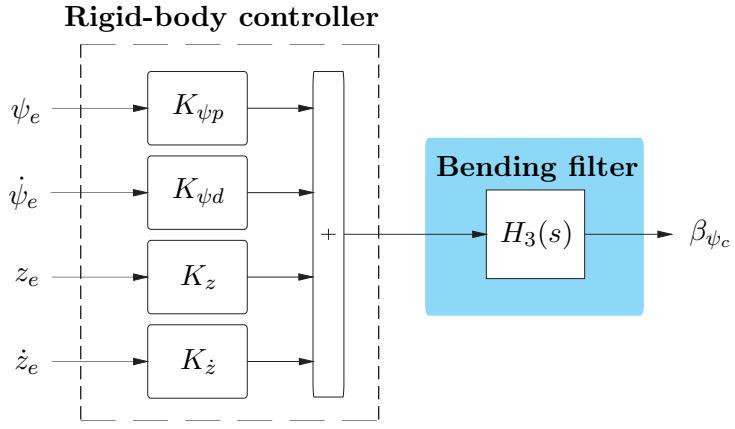

Figure 5.2: Block diagram of the tunable controller $K_{RF}(s)$

Tunable rigid-body controller

The rigid-body controller retains the PD controller architecture of the VEGA baseline controller ($K_{\psi p}$, $K_{\psi d}$, K_z and $K_{\dot{z}}$). As done before in previous chapters, those four gains are defined as tunable parameters with no constraints on their allowable values.

Tunable bending filter

The main objective of the filter $H_3(s)$ is to provide stabilisation against the flexible modes. In particular, the VEGA baseline $H_3(s)$ performs phase stabilisation for the first Bending Mode (BM) and gain stabilisation for the upper modes. Recall that phase stabilisation consists in shaping the phase of the bending mode so that the flexible phase stability margins are guaranteed, whereas gain stabilisation implies a filter design where the bending modes are attenuated to prevent any instability.

The design of the bending filter is a highly complex task due to the proximity of the rigid-body control bandwidth and the first bending filter. For this reason, this problem cannot be tackled by using a high-order, low-pass filter. That configuration would indeed provide a sharp cut-off transition to attenuate the first bending mode but at the expense of adding significant delay (i.e. phase) at low frequencies causing unacceptable degradation of the DM and HF-GM stability margins.

To overcome this problem, more complex structures are needed. For example, Figure 5.3 shows the frequency response of the VEGA baseline $H_3(s)$ (depicted in thick solid black) at the flight instant t=50 s. Note that the values in both x and y axes are not provided for confidentiality reasons. In preparation for the joint design, this baseline filter was analysed and factorised into several filters (see gray dashed-dot lines in Figure 5.3). It is important to highlight that the actual factorisation of the VEGA baseline filter $H_3(s)$ was not provided by the VEGA GNC team. The proposed factorisation was obtained based on an engineering and physical knowledge of filter theory and also on a thorough analysis of the actual shape of the baseline filter. Looking at Figure 5.3, it is recognised that the baseline bending filter can be factorised into 5 filters (4 notch filters and 1 low-pass filter) as described in Equation 5.1. The first three notch filters attenuate the first bending mode and provide phase stabilisation, whereas the other two filters (notch and low-pass) gain stabilise the upper modes.

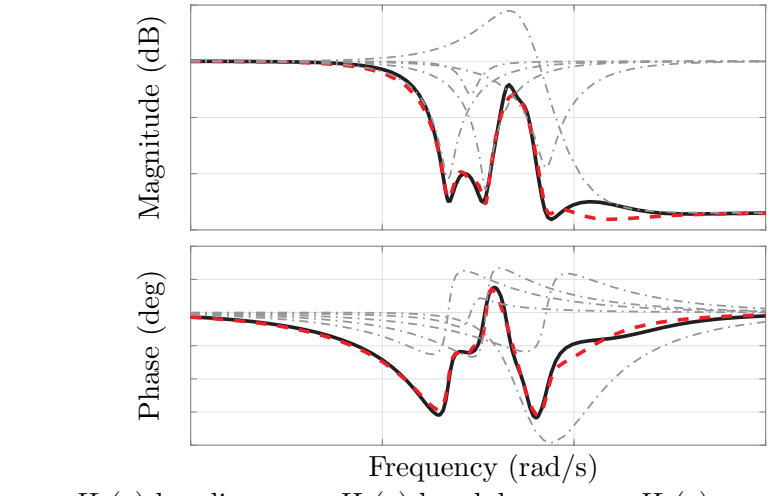

Figure 5.3: Baseline bending filter $H_3(s)$ factorization at t=50 s

The resulting factorised bending filter is depicted in thick red dashed line in Figure 5.3, where it is seen that the baseline filter $H_3(s)$ is roughly retrieved. Note that the main purpose of this factorisation analysis was not to recover exactly the baseline $H_3(s)$ as performed in Chapter 3 with the rigid-body controller, but to identify a clear modular structure to apply subsequently the structured $\mathcal{H}_\infty$ optimisation approach while respecting the legacy knowledge of the VEGA GNC team (i.e. alternative $H_3(s)$ parametrisations could be used but probably changing the design goal used by the team).

$$H_3(s) = \underbrace{\prod_{i=1}^{4} \frac{s^2 + \eta_i s + (\omega_i')^2}{s^2 + \eta_i/\epsilon_i s + (\omega_i')^2}}_{\text{Notch filters}} \cdot \underbrace{\left(\frac{\epsilon_{LP} s^2 + \eta_{LP} s + (0.6\omega_{q_2}')^2}{s^2 + \eta_{LP} s + (0.6\omega_{q_2}')^2} \right)^3}_{\text{Low-pass filter}} \tag{5.1}$$

$$\begin{aligned} \omega_1 &= \underline{\omega_{q_1}} \left[\min 1^{st} BM\right] \\ \omega_2 &= \omega_{q_1} \left[\text{nom} 1^{st} BM\right] \\ \omega_3 &= \overline{\omega_{q_1}} \left[\max 1^{st} BM\right] \\ \omega_4 &= \underline{\omega_{q_2}} \left[\min 2^{nd} BM\right] \end{aligned} \qquad \left[\text{Upper BMs attenuation}\right]$$

All filters in Equation 5.1 are parametrised as a function of the frequency values of the first two bending modes. The first and third notch filters are centred respectively at the minimum and maximum expected dispersed frequencies of the first bending mode due to uncertainties ($\underline{\omega_{q_1}}$ and $\overline{\omega_{q_1}}$), whereas the second notch filter is centred at the nominal frequency of the first bending mode (ω_{q_1}). Moreover, the fourth notch filter is centred at the minimum expected dispersed frequency of the second bending mode due to uncertainties ($\underline{\omega_{q_2}}$), and finally, the fifth filter is a 6^{th}-order low-pass filter which provides attenuation for the upper modes. Note that these frequency parameters are pre-warped before design using Equation 5.5 to reduce the impact of the discretisation process. This frequency mapping will be described at the end of this subsection.

Also note that all notch filters in Equation 5.1 are parametrised as a function of two parameters: η_i and ϵ_i (with $i = 1...4$), where η_i defines the width of the filter and ϵ_i the attenuation at the center frequency of the notch filter. Similarly, the low-pass filter is expressed as a function of ϵ_{LP} (which specifies the attenuation at high frequencies) and η_{LP} (which defines the quality factor of the filter). This parametrisation allows having a common structure for the bending filter design along the atmospheric phase and facilitates the subsequent scheduling process.

The $H_3(s)$ design configuration is defined as a function of fixed and tunable parameters for the structured $\mathcal{H}_\infty$ optimisation (see Table 5.1). The inclusion of fixed parameters simplifies the optimisation problem and allows to specify a common structure for all the different atmospheric-phase linear designs. For example, the low-pass filter parameter η_{LP} is fixed to ensure a certain filter selectivity (or quality factor) and ϵ_{LP} is also fixed to provide an attenuation of $-25\,\text{dB}$ to gain stabilise the higher bending modes along the flight envelope.

Table 5.1: Structured $\mathcal{H}_\infty$ configuration for tunable bending filter $H_3(s)$

	Fixed parameters		**Tunable parameters**		
Filter	*Parameter*	*Value*	*Parameter*	*min*	*max*
Notch filter 1	η_1	2	ϵ_1	$-25\,\text{dB}$	$-10\,\text{dB}$
Notch filter 2	η_2	5	ϵ_2	$-10\,\text{dB}$	$-4\,\text{dB}$
Notch filter 3	η_3	2	ϵ_3	$-25\,\text{dB}$	$-10\,\text{dB}$
Notch filter 4	η_4	12	ϵ_4	$-20\,\text{dB}$	$-15\,\text{dB}$
Low-pass filter	η_{LP}	40			
	ϵ_{LP}	$-25/3\,\text{dB}$			

With respect to the notch filters, their width (η_i) are also fixed whereas the attenuation at the center frequency (ϵ_i) are defined as tunable parameters. In order to restrict the range of attenuation of the latter, the allowable values of ϵ_i are limited in terms of minimum and maximum constraints. Those values have been selected to define the range covered by the different linear baseline bending filters along the first phase.

Figure 5.4 illustrates the allowable frequency responses of the tunable bending filter $H_3(s)$ described by Equation 5.1 and Table 5.1 by randomly sampling 200 times among the range of values. Notice, by comparing to Figure 5.3, that the proposed parameterisation is slightly different to the actual VEGA $H_3(s)$ filter. As mentioned before, this is done intentionally to favour subsequent scheduling across flight conditions.

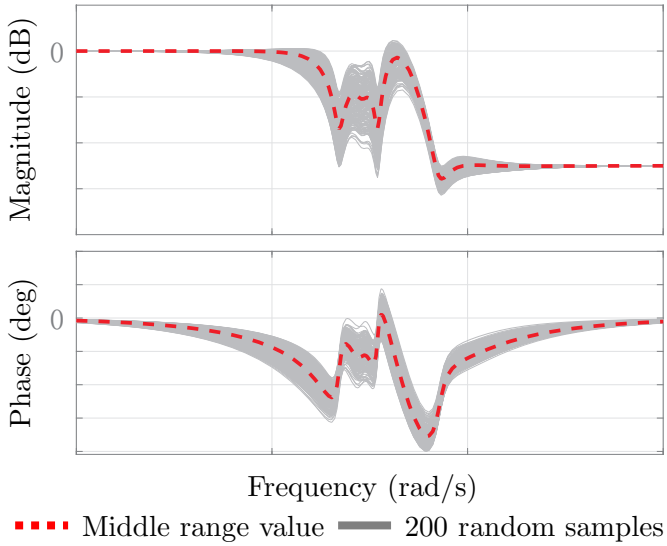

Figure 5.4: Allowable frequency responses for tunable bending filter $H_3(s)$

Remark on the discretisation process

After the synthesis stage, the designed continuous-time bending filter $H_3(s)$ must be converted to the discrete-time domain $H_3(\text{z})$ for its final implementation in the nonlinear,

high-fidelity simulator. Note that the notation z is not to be confused with the launcher drift z. Here, z is used to define the discrete z-plane ($\mathrm{z} = e^{sT_s}$ with T_s the sampling rate). This discretisation is generally performed using a bilinear transformation, also called Tustin's method, which is given by [105]:

$$s = \frac{2}{T_s}\frac{\mathrm{z}-1}{\mathrm{z}+1} \tag{5.2}$$

It is known that the Tustin's transformation causes a distortion in the frequency domain, which is described by Equation 5.3. In essence, a continuous-time frequency point ω_c is mapped to a discrete frequency ω_d. This distortion is very small at low frequencies (below 10 rad/s) but quite significant at high frequencies close to the Nyquist frequency ($\omega_{Nyquist} = \pi/T_s$).

$$\omega_d = \frac{2}{T_s}\tan^{-1}\Big(\omega_c\frac{T_s}{2}\Big) \tag{5.3}$$

In particular, due to industrial and heritage reasons, VEGA launcher's sampling rate T_s is too small to capture all the higher modes' dynamics ($\omega_{Nyquist}$ is barely higher than the nominal frequency of the second bending mode). This means that the distortion between the continuous- and discrete-time bending filters will be higher around the second bending mode frequency. Furthermore, this frequency deformation is specially critical when designing notch filters because the central frequency of the filter is shifted and thus, this effect must be taken into account from the design phase.

In order to address this problem, two main actions are taken. First, the discretisation is performed using Tustin's transformation with a pre-warping frequency ω_p, see Equation 5.4 [105]. This approach eliminates the scale distortion at frequency ω_p and alleviates the deformation at adjacent frequencies. For this design, the nominal first bending mode frequency is chosen as warping frequency (i.e. $\omega_p = \omega_{q_1}$). This selection is taken to specifically preserve the frequency region around the first bending mode, which is critical since it is generally very close to the rigid-body dynamics.

$$s = \frac{\omega_p}{\tan(\omega_p T_s/2)}\frac{\mathrm{z}-1}{\mathrm{z}+1} \tag{5.4}$$

Furthermore, all the frequency parameters in Equation 5.1 are pre-warped before design using the following frequency mapping:

$$\omega' = \frac{\omega_p}{\tan(\omega_p T_s/2)}\tan(\omega T_s/2) \tag{5.5}$$

Equation 5.5 actually describes the frequency distortion between a continuous-time frequency ω' and a discrete-time frequency ω when the transformation given in Equation 5.4 is applied. Therefore, using this equation in design allows to ensure that the notch filters will be centred at the intended frequencies after the discretisation process.

5.1.3 Weighting function selection

The proposed joint design uses the same weight setup (but not the values) presented in Section 3.4 for the VEGA control legacy recovery, except that the actuation weighting function $W_{\beta_c}(s)$ is modified to achieve the desired frequency response for the bending filter $H_3(s)$.

The input weighting functions used for this design are given in Equation 5.6. Recall that W_{ψ_c} and $W_{\dot{z}_c}$ are kept fixed throughout the different linear designs whereas $W_{\dot{\psi}_c}$ and W_{z_c} are varied to balance both attitude and drift channels. W_w is set to 3 to consider 99.7% of the wind levels defined by the wind disturbance model $G_w(s)$. Finally, W_n represents the sensor noise inputs according to the expected noise levels from VEGA's INS.

$$\begin{aligned} W_c &= diag\Big(\frac{\pi}{180}, [1-2.6]\frac{\pi}{180}, [5-30], 1\Big) \\ W_w &= 3 \\ W_n &= diag\Big(0.02\frac{\pi}{180}, 0.1\frac{\pi}{180}, 0.01, 0.001\Big) \end{aligned} \tag{5.6}$$

Similarly as for the robust structured $\mathcal{H}_\infty$ design presented in Section 4.2, two main control modes are employed. A load-relief control mode is used about the maximum dynamic pressure region whereas for the rest of operating points the focus is on minimising tracking error and lateral deviations. In this design, these two control modes are mainly accomplished by tuning the drift and drift-rate weights (W_z and $W_{\dot{z}}$), while the weighting functions W_{ψ_e}, W_ψ and $W_{Q\alpha}$ are kept fixed for all the design points. This strategy significantly reduces the tuning complexity of each linear design and offers sufficient design flexibility to achieve the desired performance. Furthermore, the bending filter specifications are implemented through the weight W_{β_c}, which is also tuned at each linear design point.

In particular, the inverse of W_{ψ_e} imposes an upper bound of 10 dB on the attitude sensitivity function, while the inverse of W_ψ is defined as a low-pass filter with a crossover frequency of 10 rad/s to limit the tracking bandwidth, a low-frequency gain of 10 dB to achieve good stability margins and a high-frequency gain of -40 dB to reduce the noise contribution.

$$\begin{aligned} W_{\psi_e} &= \frac{180}{\pi}\Big(3.16\Big)^{-1} \\ W_\psi(s) &= \frac{180}{\pi}\left(\frac{0.01s+10}{s+\frac{10}{3.16}}\right)^{-1} \end{aligned} \tag{5.7}$$

As previously mentioned, W_z and $W_{\dot{z}}$ are tuned to adjust the control mode at each linear design point. Both weights are defined as constant functions (see Equation 5.8, where it can be seen the range of values taken by both weights along the atmospheric phase). The load-relief control mode is achieved by setting low values for the inverses of W_z and $W_{\dot{z}}$. This approach directly reduces the wind disturbance effect on the drift-rate channel, and in turn, on the structural load $Q\alpha$ channel which is heavily impacted by the drift-rate contribution. On the other hand, the tracking control mode allows for lateral deviations (using higher values for the

inverse of both weights) to reduce the attitude deviations. Note that the maximum value of the inverse of W_z corresponds to the lateral control requirement for the atmospheric phase, see Table 2.1.

$$\begin{aligned} W_z &= \Big([30-500]\Big)^{-1} \\ W_{\dot{z}} &= \Big([2.5-6]\Big)^{-1} \end{aligned} \tag{5.8}$$

The structural load weighting function $W_{Q\alpha}$ is fixed throughout the atmospheric phase and imposes a maximum angle of attack of 3 degrees:

$$W_{Q\alpha} = \frac{180}{\pi}\Big(3Q\Big)^{-1} \tag{5.9}$$

Finally, the weighting function W_{β_c} enforces constraints to avoid actuator saturation and reduce high-frequency actuation. In addition, since W_{β_c} is located at the output of the bending filter, this weight is also shaped to achieve the desired frequency response for the bending filter $H_3(s)$. The inverse of W_{β_c} (see Equation 5.10) is expressed as a function of a low-frequency asymptote l_u and the bending filter $H_3(s)$ factorization given in Equation 5.1. Note that the notch filters' width parameters ($\eta_\#$) are kept fixed as described in Table 5.1. Thus, only the attenuation parameters ($\epsilon_\#$) are tuned for each linear design, including ϵ_{LP} which is adjusted considering that the high-frequency asymptote of the closed-loop channel $\mathcal{T}_{\beta_c\psi_c}$ equals $K_{p_\psi}\epsilon_{LP}$.

$$W_{\beta_c}(s) = \frac{180}{\pi}\Big(l_u H_3(s)\Big)^{-1} \tag{5.10}$$

5.1.4 Structured $\mathcal{H}_\infty$ linear point designs

For the application of the structured $\mathcal{H}_\infty$ approach, the closed-loop interconnection given in Figure 5.1 is formulated as a robust standard $\mathcal{H}_\infty$ interconnection, see Figure 4.8. In this LFT interconnection, the tunable controller $K_{RF}(s)$ described in Section 5.1.2 and the uncertainty block Δ_{RF} are pulled out of the generalised plant $P(s)$ in the same fashion as shown in Figure 4.8. In this case, Δ_{RF} belongs to the uncertainty set defined by $\boldsymbol{\Delta_{RF}} = diag(\boldsymbol{\Delta_{LV_{RF}}}, \boldsymbol{\Delta_\tau}, \boldsymbol{\Delta_{TVC}})$. In addition, the interconnection formed by $P(s)$, $K_{RF}(s)$ and Δ_{RF} is scaled by the input and output weighting functions described in Section 5.1.3. As discussed in Section 3.1, the structured $\mathcal{H}_\infty$ control problem consists of finding a stabilising sub-optimal controller $K(s)$ that minimises the $\mathcal{H}_\infty$ norm of the following cost function:

$$\min_{K(s)} \max_{\Delta_{RF}\in\boldsymbol{\Delta_{RF}}} ||\mathcal{T}_{\mathbf{e'd'}}(s,\Delta_{RF})||_\infty < \gamma; \qquad \text{subject to } K(s) \in \mathcal{K}_{\mathbf{VEGA}} \tag{5.11}$$

The controller space $\mathcal{K}_{\mathbf{VEGA}}$ represents all the controllers with the form described in Figure 5.2 and is formally defined as follows:

$$\mathcal{K}_{\mathbf{VEGA}} = \left\{ K(s) : K(s) = K_R \cdot H_3(s), \quad \text{with} \quad \begin{array}{c} K_R \in \mathcal{K}_{\mathbf{VEGA_R}} \\ H_3(s) \text{ defined by Equation 5.1} \end{array} \right\} \tag{5.12}$$

As aforementioned, the structured $\mathcal{H}_\infty$ optimisation is applied at 9 several flight instants along the atmospheric phase. Figure 5.5 shows the synthesised rigid-body gains of the joint structured $\mathcal{H}_\infty$ design as well as those for the baseline controller. The values in the y-axis are not shown for confidentiality reasons.

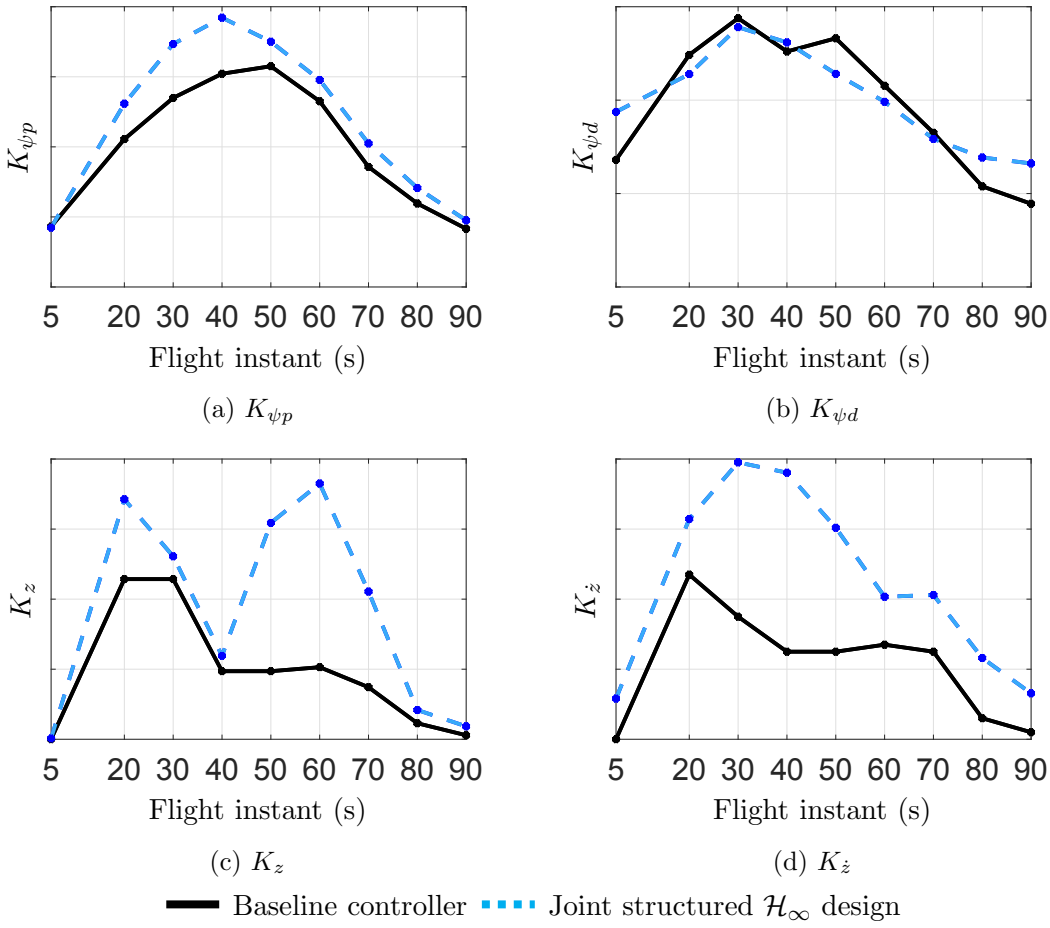

(a) $K_{\psi p}$ (b) $K_{\psi d}$

(c) K_z (d) $K_{\dot{z}}$

Figure 5.5: Comparison of rigid-body gains along the atmospheric phase

Looking at Figure 5.5, it is observed that the attitude gains (top plots) of the joint structured $\mathcal{H}_\infty$ design present the same behaviour with time but higher gains in the case of $K_{\psi p}$ and slightly lower gains for $K_{\psi d}$. Furthermore, it is seen that the structured $\mathcal{H}_\infty$ controller exhibits higher drift gains K_z (see Figure 5.5c), especially about the maximum dynamic pressure. Similarly, the drift-rate gains $K_{\dot{z}}$ are also higher along the atmospheric flight for the new design favouring the reduction of wind-induced structural loads.

With respect to the 9 synthesized continuous-time bending filters, their frequency responses are illustrated in Figure 5.6. It is worth noticing that all the filters present the same structure but with different attenuation levels for the first bending mode and also shifted by the time-evolving bending mode frequencies. Indeed, note that the frequency of the bending modes increases with time. In addition, it can be seen that all the filters provide attenuation at high frequencies to gain stabilise the upper bending modes.

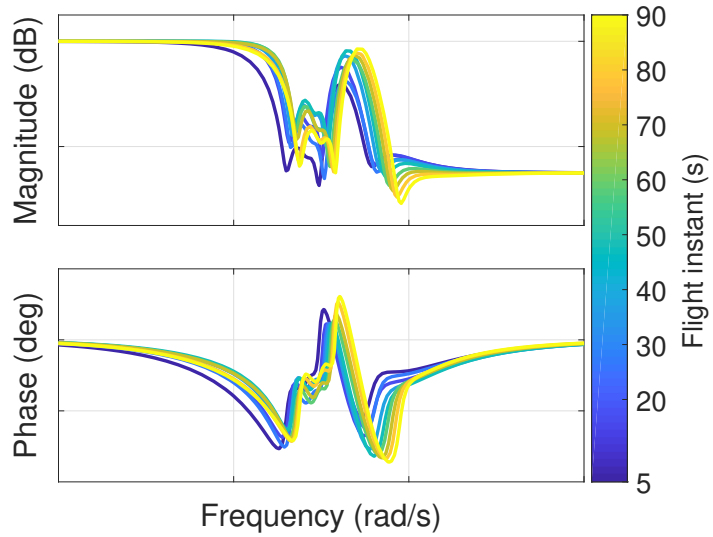

Figure 5.6: Bode plots of the 9 designed bending filter $H_3(s)$ along the atmospheric phase

In order to provide further insight, the frequency responses of the baseline and the structured $\mathcal{H}_\infty$ bending filters $H_3(s)$ at the flight instant t=50 s are compared in Figure 5.7. In this case, the filters are illustrated in the discrete-time domain, which is limited in frequency range by the Nyquist frequency. It is highlighted that the structured $\mathcal{H}_\infty$ bending filter provides a sharper cut-off transition in magnitude and introduces less delay at low frequencies. This strategy significantly reduces the interaction between the first bending mode and the rigid-body dynamics. Indeed, the structured $\mathcal{H}_\infty$ bending filter minimises the degradation of the rigid-body stability margins and improves the decoupling between the rigid-body controller and the bending filter action.

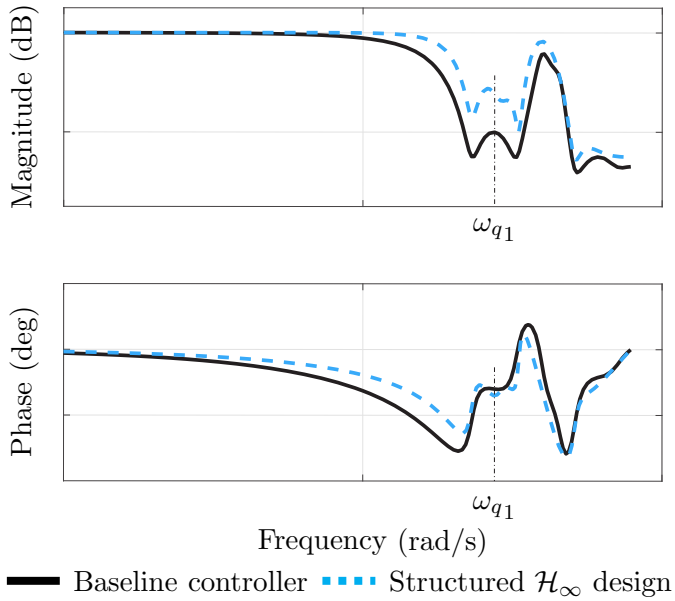

Figure 5.7: Bode plot of the designed discrete-time bending filter $H_3(s)$ at t=50 s

The previous two advantages come at the expense of presenting less attenuation for the first bending mode (very noticeable in the magnitude plot around the ω_{q_1} frequency). Nevertheless, since the first bending mode is phase stabilised, the gain attenuation of this mode is not critical for the design task. Looking at the phase plot, it can be seen that both bending filters add approximately the same phase around the first bending mode frequencies. Furthermore, as it will be shown in Section 5.2.1, the structured $\mathcal{H}_\infty$ design successfully achieves phase stabilisation providing sufficient margins with respect to the instability points. Finally, it is also observed that the structured $H_3(s)$ filter roughly recovers the roll-off and attenuation level for the upper modes.

5.2 Simulation results

In this section, the structured $\mathcal{H}_\infty$ controller designed in Section 5.1 is analysed in terms of linear stability (Section 5.2.1) and nonlinear performance (Section 5.2.2).

5.2.1 Linear stability analysis

The stability of the joint robust structured $\mathcal{H}_\infty$ controller is first analysed in terms of the classical (gain and phase) stability margins. For ease of visualisation, only the Nichols chart at the maximum dynamic pressure region (t=50 s) is shown in Figure 5.8 (but similar results were achieved at all the other points). This plot shows that the structured $\mathcal{H}_\infty$ controller presents adequate rigid-body margins, it phase stabilises the first bending mode and provides enough attenuation to gain stabilise the upper modes. Furthermore, it is highlighted that all the 9 synthesised linear structured $\mathcal{H}_\infty$ controllers satisfy the atmospheric stability requirements (see Table 2.1) under nominal and dispersed conditions.

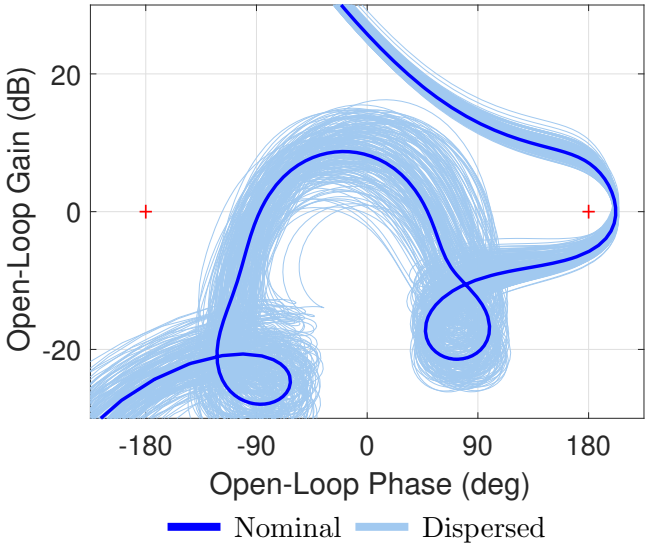

Figure 5.8: Nichols chart of the joint robust structured $\mathcal{H}_\infty$ controller at t=50 s

In addition to the previous classical analysis, the stability of the structured $\mathcal{H}_\infty$ design is also analysed using the structured singular value μ (see Section 4.2.4 for details about this robust analysis technique). Figure 5.9 shows the upper bounds of μ for the structured $\mathcal{H}_\infty$ controller at the different linear design points. This plot clearly illustrates that the system is robustly stable for all the design points since the RS condition is satisfied at all frequencies.

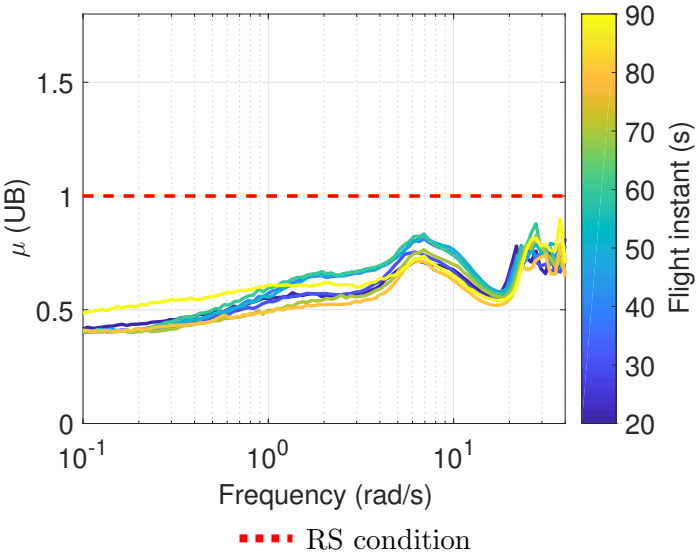

Figure 5.9: Robust stability analysis of the joint robust structured $\mathcal{H}_\infty$ controller

5.2.2 Nonlinear performance analysis

Finally, the performance of the synthesised joint rigid/flexible structured $\mathcal{H}_\infty$ controller is evaluated and compared with that of the baseline VEGA controller using the nonlinear, high-fidelity simulator described in Section 2.1.4.

Remarks on the controllers implementation

Before the implementation in the nonlinear simulator, the 9 synthesised linear structured $\mathcal{H}_\infty$ controllers are first discretised using the Tustin's transformation with the first bending mode frequency as warping frequency, see Equation 5.4. Then, the individual discrete-domain controllers are gain-scheduled in the same fashion as the actual baseline controller (i.e. using the non-gravitational velocity in a linear manner as scheduling parameter).

The implementation of the baseline controller is as shown in Figure 2.4. As for the joint robust structured $\mathcal{H}_\infty$ controller, the TVC architecture shown in Figure 5.2 is adjusted for the final implementation to compute the attitude rate error signal $\dot{\psi}_e$ from ψ_e. In this case, instead of using the baseline filter $H_2(s)$, the fixed (non-scheduled) first-order pseudo-derivative filter $H_d(s)$ presented in Equation 5.13 is employed. This configuration further simplifies the tuning effort, since the same filter is used for the whole atmospheric flight, and reduces the controller complexity (1 order versus 4). Note that $H_d(s)$ is also discretised before implementation in the simulator.

$$H_d(s) = \frac{s}{0.02s + 1} \tag{5.13}$$

Including the filter $H_d(s)$, the final implementation of the joint robust structured $\mathcal{H}_\infty$ controller has 15 states, in contrast to the 26 states of the baseline controller.

Monte-Carlo campaign

This nonlinear analysis is based on the same 4 Monte-Carlo campaigns (2000 runs in total using 4 different wind profiles) described in Section 4.2.5. This MC setup allows to analyse the controllers against different strong wind gusts at different altitudes.

Figure 5.10 shows the 2000 nonlinear MC responses of the load performance indicator $Q\alpha$ versus Mach for both controllers. It is worth noticing that the structured joint $\mathcal{H}_\infty$ design globally reduces the different $Q\alpha$ peaks throughout the atmospheric flight, particularly around the maximum dynamic pressure region (i.e. Mach 1.25-3).

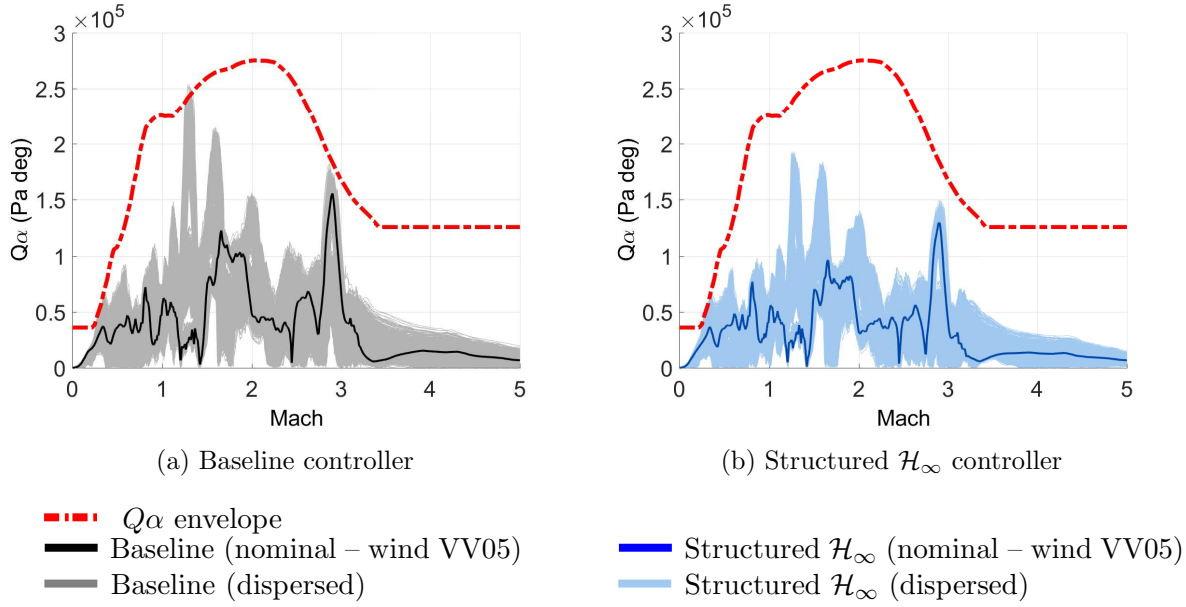

(a) Baseline controller

(b) Structured $\mathcal{H}_\infty$ controller

Figure 5.10: MC nonlinear $Q\alpha$ analysis

In addition, other atmospheric performance indicators such as TVC consumption (integrated TVC angle $< 250\,\text{deg}$) and lateral control requirements (lateral position $< 500\,\text{m}$ and lateral velocity $< 15\,\text{m/s}$) are compared among the two controllers in Figure 5.11. This plot shows the Gaussian distribution of the values of those indicators before the tail-off phase at t=90 s, which is the last linear design point for the structured $\mathcal{H}_\infty$ controller.

Looking at Figures 5.11a-b, it is observed that the TVC actuation performance is improved by the structured $\mathcal{H}_\infty$ design at both lanes, presenting less TVC consumption (mean value) and also less variation. Furthermore, the structured $\mathcal{H}_\infty$ controller provides significantly better (i.e. similar mean but much tighter variations) lateral robust performance in both Y and Z axes as shown in Figures 5.11c-f. These results give a good statistical insight of the design robustness.

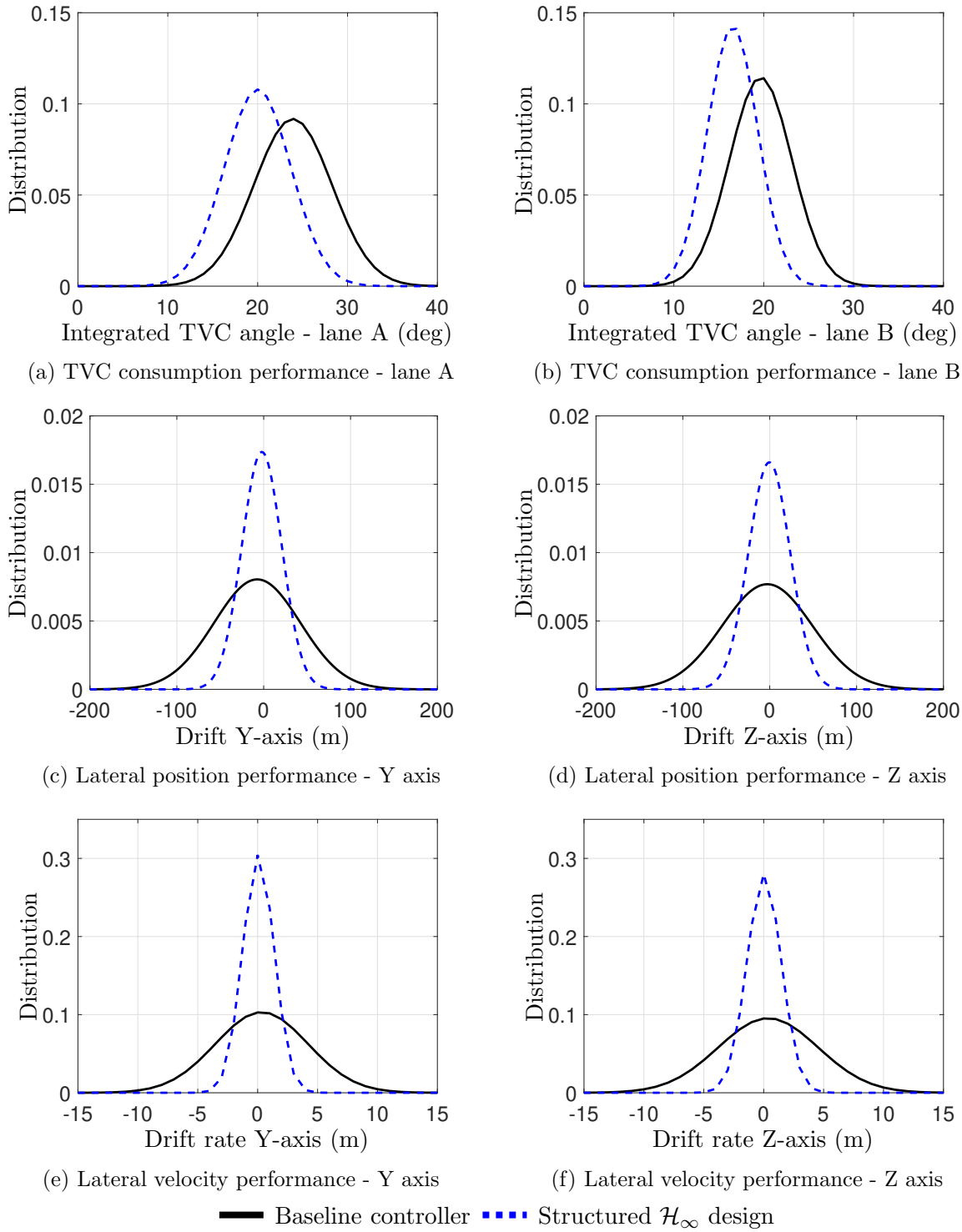

(a) TVC consumption performance - lane A

(b) TVC consumption performance - lane B

(c) Lateral position performance - Y axis

(d) Lateral position performance - Z axis

(e) Lateral velocity performance - Y axis

(f) Lateral velocity performance - Z axis

Figure 5.11: MC statistical analysis of TVC consumption and lateral control performance

5.3 Conclusions

This chapter presents a joint rigid-flexible controller design of a robust atmospheric control system for the VEGA launcher. The control formulation is based on the structured $\mathcal{H}_\infty$ optimisation and makes use of the augmenting capabilities presented in Chapter 4 (wind model and parametric uncertainties).

It is shown how the legacy information from the classically-designed baseline controller can be used to guide the tunable controller parametrisation. Furthermore, it is highlighted that the proposed formulation allows to perform the design of the rigid-body controller and bending filter in one single design procedure. This joint design scheme can significantly simplify the industrial state-of-the-practice for TVC design while improving the performance and robustness objectives in a more methodological manner.

The results show that the structured $\mathcal{H}_\infty$ synthesis technique, and proposed methodology, improve the performance and robustness of the launcher, while keeping and further simplifying the classical VEGA TVC architecture. This represents a paradigm change in terms of the control design process followed by VEGA but not in terms of the objectives and accumulated flight experience heritage by the actual VEGA GNC team.

Part II

From full-order control design to structured design

CHAPTER 6

Linear parameter varying control design

This chapter presents the design of the atmospheric control system of a launch vehicle using the LPV synthesis technique. The LPV framework can be considered as an augmentation of the standard $\mathcal{H}_\infty$ approach, which is based on LTI models, but capturing the time-varying behaviour of the system (over a defined performance envelope using a measurable set of scheduling parameters). This time-varying information is used by the LPV design process to generate in a single step a scheduled controller on the chosen parameters.

The LPV control synthesis problem is also formulated using the same design framework as in previous chapters (i.e. conceptually the same frequency-based weighted interconnection as that used for the previous structured $\mathcal{H}_\infty$ optimization designs –although with important differences as detailed in the chapter). This is quite valuable, since it allows to build up the confidence on the weighting function selection and also to apply the augmenting capabilities presented in Chapters 4-5. For example, the proposed LPV design framework makes use of the wind model presented in Chapter 4 to account for statistical wind levels in design. In addition, as it was performed in Chapter 5, the design of the rigid-body controller and bending filters is unified in the same design process. In this case, since the approach used for LPV design does not allow defining a specific controller structure, the joint rigid-flexible design is performed by a different choice of weighting functions.

The layout of this chapter is as follows. Section 6.1 provides a brief cursory introduction of the LPV modelling and synthesis approaches. Section 6.2 describes the LPV modelling approach for the VEGA launch vehicle. The resulting VEGA LPV model is employed in Section 6.3 to design an LPV controller for the VEGA VV05 mission. Then, this LPV design is analysed and validated through MC nonlinear simulations in Section 6.4. Finally, conclusions are given in Section 6.5.

6.1 LPV background

The foundations of LPV theory were first introduced in reference [106], which represented a paradigm shift for analysis and control design. In this reference it was shown that the LPV framework extends the capabilities of the Gain Scheduling (GS) approach. As mentioned in Section 1.2.1, the main issue of the GS methodology is that the stability and performance robustness achieved at the linear design points are no longer guaranteed for the flight instants between two design points.

The LPV synthesis offers several advantages over the more widespread gain-scheduling approach: i) performance and robustness are guaranteed along the flight envelope for the LPV model; ii) the controller design and scheduling are incorporated into a single design procedure; and iii) it uses the same design framework as the $\mathcal{H}_\infty$ synthesis approach, so requirements are also expressed in terms of weighting functions.

LPV synthesis has been applied to numerous works in aerospace applications [107, 108, 109, 110] and also including launch vehicle control design [46]. References [10, 111, 112, 113] are good survey articles on LPV applications. Furthermore, LPV control is receiving increased attention in the past few years thanks to the development of LPV software tools shuch as *LPVTools* [47]. The introduction of this Matlab toolbox has resulted in some recent studies on different applications such as aeroservoelastic aircraft control [114], flutter suppression [48] and load reduction of wind turbines [49].

In this section, a brief introduction to LPV modelling and synthesis is provided.

6.1.1 LPV modelling

As the name indicates, LPV systems are linear systems which are dependent on a vector of time-varying parameters $\boldsymbol{\rho}(t) = \left[\rho_1(t), \ldots, \rho_{n_\rho}(t)\right]^T$ that belongs to the compact set $\mathcal{P} \subseteq \mathbb{R}^{n_\rho}$. A general LPV state-space description is formulated as follows:

$$\begin{bmatrix} \dot{\mathbf{x}}(t) \\ \mathbf{y}(t) \end{bmatrix} = \begin{bmatrix} A\big(\boldsymbol{\rho}(t)\big) & B\big(\boldsymbol{\rho}(t)\big) \\ C\big(\boldsymbol{\rho}(t)\big) & D\big(\boldsymbol{\rho}(t)\big) \end{bmatrix} \begin{bmatrix} \mathbf{x}(t) \\ \mathbf{u}(t) \end{bmatrix}, \qquad \text{with} \quad \begin{matrix} \boldsymbol{\rho} \in \mathcal{P} \\ \underline{\boldsymbol{\nu}} \leq \dot{\boldsymbol{\rho}} \leq \overline{\boldsymbol{\nu}} \end{matrix} \tag{6.1}$$

where $A : \mathcal{P} \to \mathbb{R}^{n_x \times n_x}$, $B : \mathcal{P} \to \mathbb{R}^{n_x \times n_u}$, $C : \mathcal{P} \to \mathbb{R}^{n_y \times n_x}$ and $D : \mathcal{P} \to \mathbb{R}^{n_y \times n_u}$ are the continuous state-space matrices, $\mathbf{x} \in \mathbb{R}^{n_x}$ is the state vector, $\mathbf{u} \in \mathbb{R}^{n_u}$ is the input vector and $\mathbf{y} \in \mathbb{R}^{n_y}$ represent outputs of the system.

Note that this model characterisation defines a set of admissible trajectories for the scheduling vector, in which $\boldsymbol{\rho}$ can take values within the region $\mathcal{P}$ and may have bounds on the rate variation defined by $\underline{\boldsymbol{\nu}} \in \mathbb{R}^{n_\rho}$ and $\overline{\boldsymbol{\nu}} \in \mathbb{R}^{n_\rho}$. In addition, it is important to highlight that for LPV systems the variation of $\boldsymbol{\rho}$ is assumed to be unknown but measurable in real time (i.e. causal). In essence, this is the main difference with respect to Linear Time Varying (LTV) systems, which are defined for a priori known specific trajectory on the scheduling vector.

Several modelling approaches have been proposed in the literature to derive LPV models. Reference [115] offers a good overview of LPV modelling methods and presents a comparison between three different approaches (Jacobian linearisation, state transformation and function substitution) to model the longitudinal motion of an aircraft. More recently, reference [113] presents a survey on LPV control applications based on three different LPV modelling approaches: polytopic, LFT-based and grid-based. Polytopic LPV models are represented using an affine parameter dependence on $\boldsymbol{\rho}$ (i.e. the state-space matrices A, B, C and D depend affinely on the scheduling parameters $\boldsymbol{\rho}$) [116, 117]. On the other hand, the LFT-based modelling method makes use of LFT theory to capture the time-varying behaviour of the system [118, 119]. And finally, a grid-based LPV model is obtained using a family of LTI models extracted at different linear operating points throughout the performance envelope [120]. It is noted that last two modelling methods (LFT-based and grid-based) are implemented in the recently developed Matlab toolbox *LPVTools* [47].

In this thesis, the grid-based approach is used to derive the LPV model of the VEGA launcher, see Section 6.2. This modelling method provides a straightforward yet effective way to derive LPV models.

6.1.2 LPV synthesis

As before with the structured $\mathcal{H}_\infty$ problem, the LPV control design approach also relies on the standard $\mathcal{H}_\infty$ interconnection shown again in Figure 6.1 (but indicating the dependency of the systems on the scheduling vector ρ). In this case, the generalised plant $P(\boldsymbol{\rho})$ is an LPV model as shown in Equation 6.2. Note that the dependence on t is dropped for clarity.

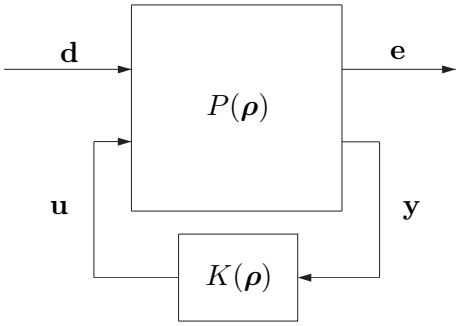

Figure 6.1: LPV control problem formulation

$$\begin{bmatrix} \dot{\mathbf{x}} \\ \mathbf{e} \\ \mathbf{y} \end{bmatrix} = \underbrace{\begin{bmatrix} A(\boldsymbol{\rho}) & B_1(\boldsymbol{\rho}) & B_2(\boldsymbol{\rho}) \\ C_1(\boldsymbol{\rho}) & D_{11}(\boldsymbol{\rho}) & D_{12}(\boldsymbol{\rho}) \\ C_2(\boldsymbol{\rho}) & D_{21}(\boldsymbol{\rho}) & D_{22}(\boldsymbol{\rho}) \end{bmatrix}}_{P(\boldsymbol{\rho})} \begin{bmatrix} \mathbf{x} \\ \mathbf{d} \\ \mathbf{u} \end{bmatrix} \tag{6.2}$$

where $\mathbf{x} \in \mathbb{R}^{n_x}$, $\mathbf{u} \in \mathbb{R}^{n_u}$, $\mathbf{y} \in \mathbb{R}^{n_y}$, $\mathbf{d} \in \mathbb{R}^{n_d}$, $\mathbf{e} \in \mathbb{R}^{n_e}$ and the state-space matrices present the appropriate dimensions. In addition, the time-varying parameters hold that $\boldsymbol{\rho} \in \mathcal{P}$ and $\underline{\boldsymbol{\nu}} \leq \dot{\boldsymbol{\rho}} \leq \overline{\boldsymbol{\nu}}$.

Furthermore, the n_x-state controller $K(\boldsymbol{\rho})$ can be written as:

$$\begin{bmatrix} \dot{\mathbf{x}}_\mathbf{K} \\ \mathbf{u} \end{bmatrix} = \underbrace{\begin{bmatrix} A_K(\boldsymbol{\rho}) & B_K(\boldsymbol{\rho}) \\ C_K(\boldsymbol{\rho}) & D_K(\boldsymbol{\rho}) \end{bmatrix}}_{K(\boldsymbol{\rho})} \begin{bmatrix} \mathbf{x}_\mathbf{K} \\ \mathbf{y} \end{bmatrix} \tag{6.3}$$

Then, using the above LPV models, the closed-loop system $\mathcal{T}_{ed}(\boldsymbol{\rho})$ can be represented as follows:

$$\begin{bmatrix} \dot{\mathbf{x}}_\mathbf{clp} \\ \mathbf{e} \end{bmatrix} = \underbrace{\begin{bmatrix} A_{clp}(\boldsymbol{\rho}) & B_{clp}(\boldsymbol{\rho}) \\ C_{clp}(\boldsymbol{\rho}) & D_{clp}(\boldsymbol{\rho}) \end{bmatrix}}_{\mathcal{T}_{ed}(\boldsymbol{\rho}) = \mathcal{F}_l\left(P(\boldsymbol{\rho}), K(\boldsymbol{\rho})\right)} \begin{bmatrix} \mathbf{x}_\mathbf{clp} \\ \mathbf{d} \end{bmatrix} \tag{6.4}$$

In this framework, the LPV synthesis optimisation consists of finding an stabilising controller $K(\boldsymbol{\rho})$ which minimises the induced $\mathcal{L}_2$ norm of the cost function given in Equation 6.5 for all the admissible time-varying parameter trajectories.

$$\min_{K(\boldsymbol{\rho})} ||\mathcal{T}_{ed}(\boldsymbol{\rho})||_{\mathcal{L}_2 \to \mathcal{L}_2}; \qquad \text{subject to} \quad \begin{matrix} \boldsymbol{\rho} \in \mathcal{P} \\ \underline{\boldsymbol{\nu}} \leq \dot{\boldsymbol{\rho}} \leq \overline{\boldsymbol{\nu}} \end{matrix} \tag{6.5}$$

The induced $\mathcal{L}_2$ norm is the generalisation of the $\mathcal{H}_\infty$ norm for LPV systems [120]. Indeed, the induced $\mathcal{L}_2$ norm is a performance measure that represents the maximum amplification of energy from inputs $\mathbf{d}$ to outputs $\mathbf{e}$ within the admissible set of scheduling parameters:

$$||\mathcal{T}_{ed}(\boldsymbol{\rho})||_{\mathcal{L}_2 \to \mathcal{L}_2} = \begin{matrix} \sup \\ \boldsymbol{\rho} \in \mathcal{P} \\ \underline{\boldsymbol{\nu}} \leq \dot{\boldsymbol{\rho}} \leq \overline{\boldsymbol{\nu}} \end{matrix} \quad \begin{matrix} \sup \\ \mathbf{d} \in \mathcal{L}_2 \\ ||\mathbf{d}||_{\mathcal{L}_2} \neq 0 \end{matrix} \quad \frac{||\mathbf{e}||_{\mathcal{L}_2}}{||\mathbf{d}||_{\mathcal{L}_2}} \tag{6.6}$$

The control problem given in Equation 6.5 can be formulated as a set of LMI optimisation problems. If the trajectory is rate unbounded (i.e. $\underline{\nu_i} = -\infty$ and $\overline{\nu_i} = \infty$ with $i = 1, \ldots, n_\rho$), the synthesis is performed using a single quadratic Lyapunov function [116]. In essence, the optimisation consists in finding a parameter-dependent controller such that theorem 1 is satisfied over the performance envelope. This is the simplest LPV design approach, although it may result in conservative designs.

Theorem 1 *[116] Consider the closed-loop LPV system given by Equation 6.4, where $\boldsymbol{\rho} \in \mathcal{P}$, and $\underline{\nu_i} = -\infty$ and $\overline{\nu_i} = \infty$ with $i = 1, \ldots, n_\rho$. Then, the LPV control problem is solvable if there exist a controller of the form given in Equation 6.3, and a continuously differentiable matrix function $X \in \mathbb{R}^{2n_x \times 2n_x}$, such that $X = X^T > 0$ and*

$$\begin{bmatrix} A_{clp}^T(\boldsymbol{\rho})X + XA_{clp}(\boldsymbol{\rho}) & XB_{clp}(\boldsymbol{\rho}) & \gamma^{-1}C_{clp}^T(\boldsymbol{\rho}) \\ B_{clp}^T(\boldsymbol{\rho})X & -I & \gamma^{-1}D_{clp}^T(\boldsymbol{\rho}) \\ \gamma^{-1}C_{clp}(\boldsymbol{\rho}) & \gamma^{-1}D_{clp}(\boldsymbol{\rho}) & -I \end{bmatrix} < 0 \tag{6.7}$$

A more general case is defined when the time time-varying parameters are rate bounded. This approach allows reducing the conservatism in the design but results in a more complex and more computationally demanding optimisation. In this case, parameter-dependent Lyapunov functions are employed to find a parameter-dependent controller such that theorem 2 is satisfied over the performance envelope [120, 121].

Theorem 2 *[120, 121] Consider the closed-loop LPV system given by Equation 6.4, where $\boldsymbol{\rho} \in \mathcal{P}$, and $\underline{\boldsymbol{\nu}} \leq \dot{\boldsymbol{\rho}} \leq \overline{\boldsymbol{\nu}}$. Then, the LPV control problem is solvable if there exist a continuously differentiable matrix function X, such that for all $X = X^T > 0$ and*

$$\begin{bmatrix} A_{clp}^T(\boldsymbol{\rho})X(\boldsymbol{\rho}) + X(\boldsymbol{\rho})A_{clp}(\boldsymbol{\rho}) + \sum_{i=1}^{n_\rho}\left(\overline{\nu_i}\frac{\partial X}{\partial \rho_i}\right) & X(\boldsymbol{\rho})B_{clp}(\boldsymbol{\rho}) & \gamma^{-1}C_{clp}^T(\boldsymbol{\rho}) \\ B_{clp}^T(\boldsymbol{\rho})X(\boldsymbol{\rho}) & -I & \gamma^{-1}D_{clp}^T(\boldsymbol{\rho}) \\ \gamma^{-1}C_{clp}(\boldsymbol{\rho}) & \gamma^{-1}D_{clp}(\boldsymbol{\rho}) & -I \end{bmatrix} < 0 \tag{6.8}$$

$$\begin{bmatrix} A_{clp}^T(\boldsymbol{\rho})X(\boldsymbol{\rho}) + X(\boldsymbol{\rho})A_{clp}(\boldsymbol{\rho}) + \sum_{i=1}^{n_\rho}\left(\underline{\nu_i}\frac{\partial X}{\partial \rho_i}\right) & X(\boldsymbol{\rho})B_{clp}(\boldsymbol{\rho}) & \gamma^{-1}C_{clp}^T(\boldsymbol{\rho}) \\ B_{clp}^T(\boldsymbol{\rho})X(\boldsymbol{\rho}) & -I & \gamma^{-1}D_{clp}^T(\boldsymbol{\rho}) \\ \gamma^{-1}C_{clp}(\boldsymbol{\rho}) & \gamma^{-1}D_{clp}(\boldsymbol{\rho}) & -I \end{bmatrix} < 0 \tag{6.9}$$

Both LPV synthesis approaches (non-rate and rate bounded) are implemented in the Matlab toolbox *LPVTools* through the function *lpvsyn* [47].

The LPV framework also allows to take system uncertainties into account for analysis and design [122]. In this case, the uncertainties are described by integral quadratic constraints [123] and the robust control is formulated using an iterative design procedure similar to the D-K iteration employed for μ synthesis. This robust LPV design process alternates LPV design and IQC analysis steps. Furthermore, the IQC formulation can also include nonlinearities of the system. Note that this robust LPV synthesis approach is not yet available in the aforementioned *LPVTools* toolbox, but it has recently been discussed in reference [124].

6.2 LPV modelling for the VEGA launcher

In order to support the LPV control design, first an LPV model of the VEGA launcher is formulated by expressing the system as a function of a set of time-varying scheduling parameters $\boldsymbol{\rho}(t)$.

In a first step, time was chosen as a scheduling parameter [1] (i.e. $\rho = t$) and a rigid-body non-rate bounded LPV design (Theorem 1) was performed, see reference [125] –for readability, this preliminary design is not shown in this thesis but rather a more advanced, final design will be presented. As shown in the aforementioned reference, the performance results were promising and showed improvement with respect to the (rigid-motion) baseline and structured $\mathcal{H}_\infty$ designs.

In this chapter, the LPV model used for design was derived including the rigid/flexible launcher dynamics and using the same scheduling parameter as that for the VEGA controller, i.e. the Non-Gravitational Velocity (NGV). Initially, the non-rate bounded LPV synthesis approach was also tried but in this case it did not yield overall good designs. Thus, the rate-bounded approach of Theorem 2 was followed using the NGV as a time-varying parameter and the Non-Gravitational Acceleration (NGA) to bound the NGV rate variation (i.e. $\rho = NGV$ and $\underline{\nu_{NGA}} \leq \dot{\rho} \leq \overline{\nu_{NGA}}$). It is important to mention that both parameters can be computed on-board, and thus, they are available to schedule the controller along the flight. Figure 6.2 shows the time evolution of these two variables (NGV and NGA) for the VEGA VV05 mission.

In this thesis, the VEGA LPV model is built using the recently developed MATLAB toolbox LPVTools [47]. In particular, a grid-based approach is employed using a set of 6 linearised plants throughout the atmospheric phase (at NGV = [433 818 1029 1286 1599 2345]m/s which corresponds to t = [20 40 50 60 70 90]s). It is important to remark that this LPV modelling approach requires model consistency, which means that all the LTI models on the grid must have the same inputs, outputs and states.

[1] Although it is recognised that formally this yields an LTV model, this formulation was preferred initially for ease of simplicity (and under the consideration of time being a measured and bounded parameter within the ascent flight).

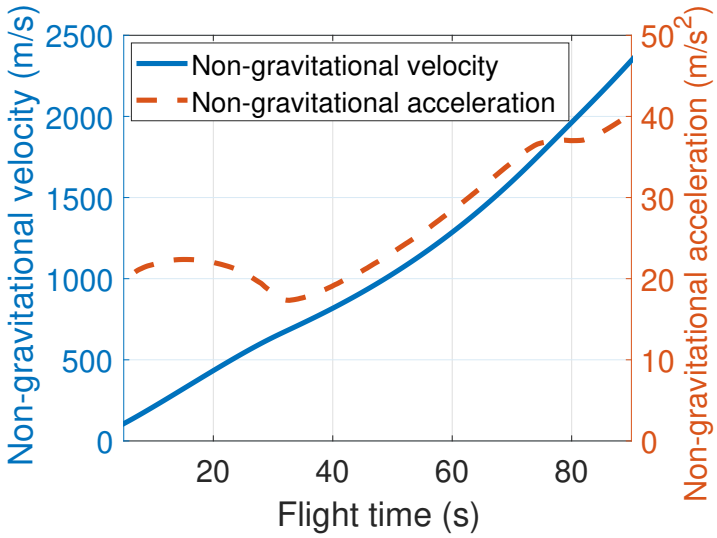

Figure 6.2: Non-gravitational velocity and acceleration for VEGA VV05 flight

Based on the values from Figure 6.2, the admissible time-varying parameter trajectories are defined for $\rho \in \mathcal{P}_{NGV}$, where $\mathcal{P}_{NGV} \in \mathbb{R}$ is the region defined by 6 grid points within the range $\rho = [433 - 2345]$ m/s, and the following rate constraint $\underline{\nu_{NGA}} < \dot{\rho} < \overline{\nu_{NGA}}$, with $\underline{\nu_{NGA}}$ =17 m/s^2 and $\overline{\nu_{NGA}}$ =40 m/s^2.

The resulting LPV model is given in Equation 6.10. At each grid point, the LPV model is described by the respective LTI model at that point. However, at flight instants between the given grid points, the LPV system is defined by linear interpolation.

$$\begin{bmatrix} \dot{\mathbf{x}}_{\mathbf{LV}} \\ \mathbf{u}_{\mathbf{LV}} \end{bmatrix} = \underbrace{\begin{bmatrix} A_{LV}(\rho) & B_{LV}(\rho) \\ C_{LV}(\rho) & D_{LV}(\rho) \end{bmatrix}}_{G_{LV_{RF}}(\rho)} \begin{bmatrix} \mathbf{x}_{\mathbf{LV}} \\ \mathbf{y}_{\mathbf{LV}} \end{bmatrix}; \qquad \text{with} \quad \begin{matrix} \rho \in \mathcal{P}_{NGV} \\ \underline{\nu_{NGA}} < \dot{\rho} < \overline{\nu_{NGA}} \end{matrix} \tag{6.10}$$

where $\mathbf{x_{LV}} = \begin{bmatrix} \mathbf{x_R} & \mathbf{x_F} \end{bmatrix}^T$, with the (same, as in previous chapters) four rigid-body states $\mathbf{x_R} \in \mathbb{R}^4$ and two flexible states $\mathbf{x_F} \in \mathbb{R}^2$ (accounting for the second order first bending mode dynamics) as described in Section 2.2.1.5. Similarly, the description of the 6 LTI launch vehicle models $\left(G_{LV_{RF}}(\rho_i) \text{ with } i = [1, 2, 3, 4, 5, 6]\right)$, the input vector $\mathbf{u_{LV}} \in \mathbb{R}^3$ and the output vector $\mathbf{y_{LV}} \in \mathbb{R}^5$ can be found in Section 2.2.1.5.

LPV model validation

In order to ensure that the LPV model captures the main launcher dynamics, the frequency responses of the LPV model (frozen at specific scheduling parameter instances) and the corresponding LTI models at those instances are compared in Figure 6.3. This plot shows the validation for two different flight instants (located between grid points): t=35 s and t=55 s. In both cases, some small differences can be seen but are considered negligible.

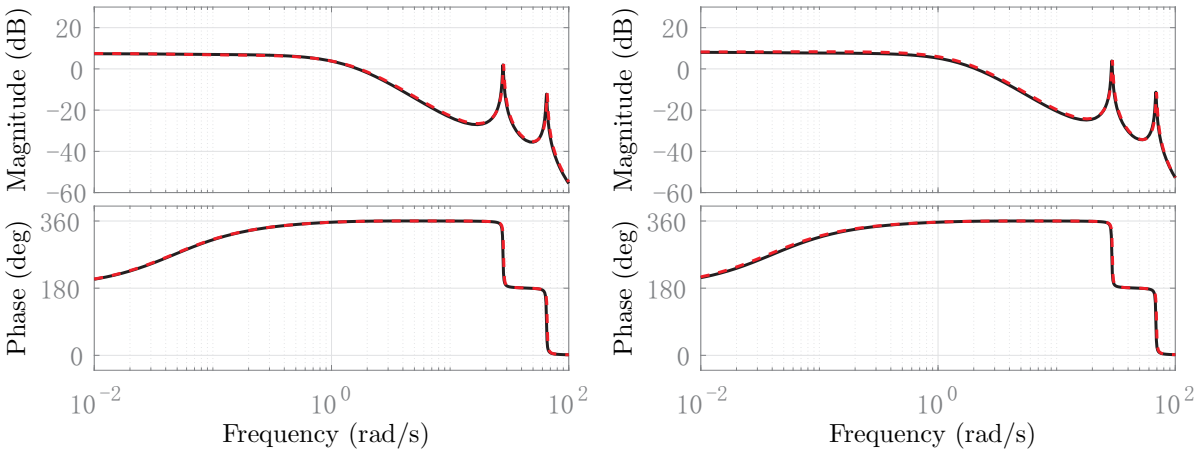

(a) Bode plot $\psi_{INS}/\beta_{\psi}(s)$ at t=35 s

(b) Bode plot $\psi_{INS}/\beta_{\psi}(s)$ at t=55 s

Figure 6.3: VEGA LPV model validation

6.3 LPV synthesis for the VEGA launcher

This section describes the design of the VEGA atmospheric phase control system using the LPV synthesis technique of Theorem 2. As already mentioned, designs using Theorem 1 (i.e. assuming a non-rate bounded approach) provided poor performance and did not yield the desired robustness.

6.3.1 LPV control problem formulation

The control design problem is formulated as the augmented closed-loop system shown in Figure 6.4. LPV control design, like $\mathcal{H}_\infty$ theory, relies on frequency-domain weighting functions to impose the desired requirements over the system (see gray-shaded blocks in Figure 6.4). Its selection will be discussed in Section 6.3.2.

The main difference with respect to the closed-loop systems presented in the previous chapters is that the launch vehicle model $G_{LV_{RF}}(\rho)$, the wind generator $G_w(\rho)$ and the controller $K(\rho)$ are described by LPV representations (see these blocks highlighted in blue). Note that $G_{LV_{RF}}(\rho)$ corresponds to the LPV model given in Equation 6.10 (that is, including rigid/flexible effects and parametrised based on NGV) whereas $G_w(\rho)$ is derived using the same grid-based approach used for the launcher model in Section 6.2.

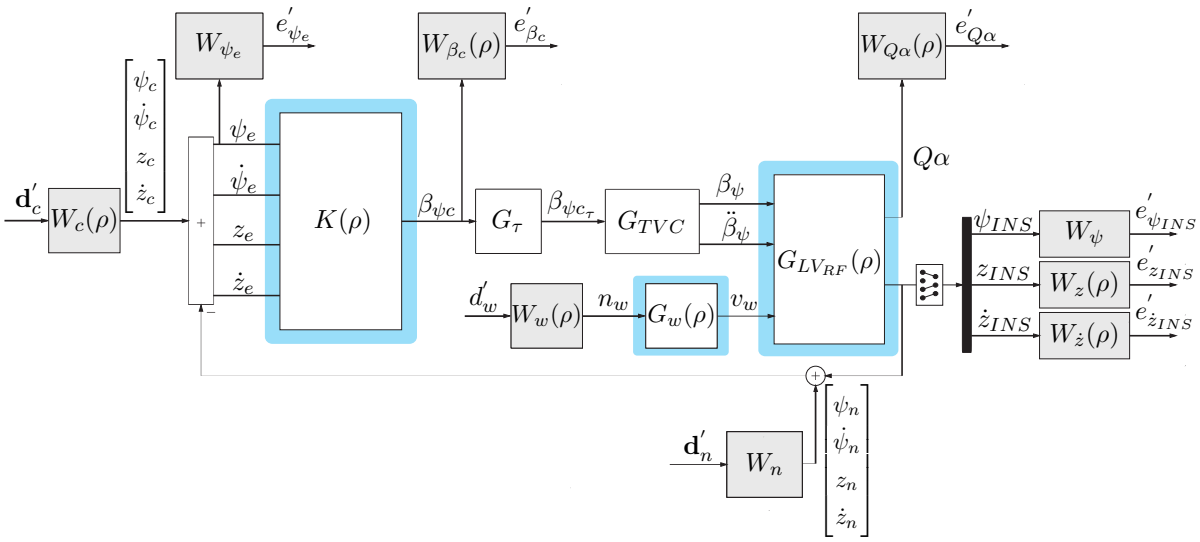

Figure 6.4: Closed-loop diagram for the VEGA LPV control design

6.3.2 Weighting function selection

As seen in the interconnection shown in Figure 6.4, the same weighting function layout, but different values, as for the structured $\mathcal{H}_\infty$ designs from previous chapters is used here. But note that some of the input and output weighting functions are represented by LPV models also dependent on $\rho = \text{NGV}$. Each of these parameter-varying weights were obtained using the LPV modelling approach described in Section 6.2 and the set of 6 weight values obtained from an initial linear, standard (non-structured) $\mathcal{H}_\infty$ design at each of the grid points.

Although it may seem a doubling of efforts to design these 6 linear $\mathcal{H}_\infty$ designs prior to the LPV design, this step is recommended due to the following two reasons. First, these designs serve as an initial starting point to select the weighting functions for the subsequent LPV optimisation and it provides a reference level on the possibly (best) performance/robustness at each of these points (the $\mathcal{H}_\infty$-norm obtained by these linear designs were in the range between 1.18 and 1.84). And second, due to the higher computational demand of the rate-bounded LPV synthesis it is more efficient to ascertain in the LTI domain the local performance/robustness objectives using a sparse, but representative, set of grid points (if necessary the number of points can be increased).

Using the LTI and LPV weights derived directly from the 6 initial LTI $\mathcal{H}_\infty$ designs, and the interconnection from Figure 6.4, the resulting LPV controller turned out to be unstable and with high-frequency poles, although it achieved global closed-loop stability and the desired performance/robustness. For safety reasons, it is not desirable to implement unstable controllers and similarly, practical implementation aspects recommend not having high-frequency poles. Thus, further tuning of the weighting functions was necessary to obtain a stable controller that could be implemented in the nonlinear, high-fidelity simulator.

After this tuning process, the range of values taken by the input and output weighting functions are given in Equations 6.11 and 6.12.

$$\begin{aligned} W_c(\rho) &= diag\Big(\frac{\pi}{180}, [1.8-2.6]\frac{\pi}{180}, [3-4], [0.5-1]\Big) \\ W_w(\rho) &= [2-3] \\ W_n &= diag\Big(0.02\frac{\pi}{180}, 0.1\frac{\pi}{180}, 0.01, 0.001\Big) \end{aligned} \tag{6.11}$$

$$\begin{aligned} W_{\psi_e} &= \frac{180}{\pi}\Big(5.62\Big)^{-1} \\ W_{\psi}(s) &= \frac{180}{\pi}\left(\frac{0.0316s+15}{s+\frac{15}{3.16}}\right)^{-1} \\ W_z(\rho) &= \Big([100-130]\Big)^{-1} \\ W_{\dot{z}}(\rho) &= \Big([1-3]\Big)^{-1} \\ W_{Q\alpha}(\rho) &= \frac{180}{\pi}\Big(3Q\Big)^{-1} \end{aligned} \tag{6.12}$$

As for the actuation weighting function $W_{\beta_c}(\rho)$, a different configuration is used with the aim to reduce the tuning effort and the total size of the controller. Recall from Equation 5.10 that this weight was defined as a function of the actual shape of the baseline filter $H_3(s)$, which resulted in a weight of 14 states dimension. For the proposed LPV design, a simpler weight with only 6 states was used including only a low-pass filter and two notch filters, see Equation 6.13, whose selection is decribed next. The inverse of this weight is illustrated in Figure 6.5 for a single grid point. As it can be seen, W_u^{-1} is composed of two notch filters centered at the minimum and maximum expected dispersion of the 1^{st} bending mode frequency due to uncertainties ($\omega_{q1} = [\underline{\omega_{q1}}, \overline{\omega_{q1}}]$), plus a second order low-pass filter $F(\rho)$, which imposes an actuation bound at low-frequencies and also provides an attenuation of $-30\,\text{dB}$ at high frequencies for the upper bending modes. This double-notch filter configuration offers a good trade-off between attenuation and phase response and provides the necessary design flexibility to attenuate the 1^{st} bending mode while not degrading too much the rigid-body margins due to the phase delay.

$$W_{\beta_c}(\rho) = \left(\underbrace{\frac{s^2+0.5s+\big(\underline{\omega_{q1}}(\rho)\big)^2}{s^2+70s+\big(\underline{\omega_{q1}}(\rho)\big)^2}}_{\text{Notch 1}} \underbrace{\frac{s^2+0.5s+\big(\overline{\omega_{q1}}(\rho)\big)^2}{s^2+70s+\big(\overline{\omega_{q1}}(\rho)\big)^2}}_{\text{Notch 2}} \underbrace{F(\rho)}_{\text{Low-pass filter}} \right)^{-1} \tag{6.13}$$

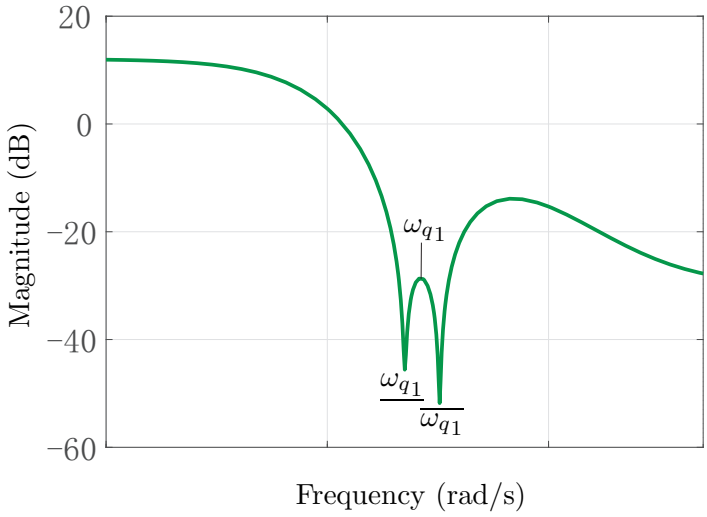

Figure 6.5: Bode magnitude plot of $W_u^{-1}(\rho)$

6.3.3 LPV design

Similarly as for the structured $\mathcal{H}_\infty$ approach, the LPV control design is formulated using the augmented standard $\mathcal{H}_\infty$ representation given in Figure 6.6, where it can be seen that all blocks depend on the time-varying parameter ρ.

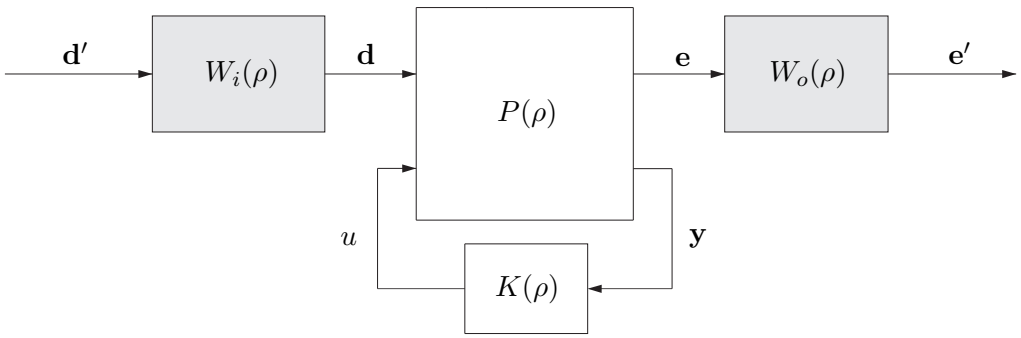

Figure 6.6: Standard $\mathcal{H}_\infty$ interconnection for LPV synthesis

Then, using the interconnection and weighting functions previously presented, a rate bounded LPV design is performed using NGV as time-varying parameter with the parameter grid described in Section 6.2. The LPV synthesis consists of finding a stabilising controller $K(\rho)$ which minimises the induced $\mathcal{L}_2$ norm of the cost function given in Equation 6.14 for all the admissible time-varying parameter trajectories.

$$\min_{K(\rho)} ||\mathcal{T}_{e'd'}(\rho)||_{\mathcal{L}_2 \to \mathcal{L}_2}; \qquad \text{subject to} \quad \begin{matrix} \rho \in \mathcal{P}_{NGV} \\ \underline{\nu_{NGA}} < \dot{\rho} < \overline{\nu_{NGA}} \end{matrix} \tag{6.14}$$

The previous control problem is performed using the Matlab toolbox *LPVTools* [47] through the command *lpvsyn*. As described in Section 6.1.2, the optimisation is formulated as a set of LMI problems, which must be solved to generate a controller. The constraints on the rate variation of $\rho(t)$ are included via basis functions X_ρ and Y_ρ. This design is performed using quadratic basis functions: $X_\rho = X_0 + X_1\rho + X_2\rho^2$ and $Y_\rho = Y_0 + Y_1\rho + Y_2\rho^2$. This configuration yields a good compromise between performance and complexity. For example, constant and linear dependent basis functions were initially employed but they provided very poor performance. On the other hand, more complex basis functions resulted in a very costly computational process, also due to the high order of the design plant. In addition, the use of a quadratic dependence on NGV parallels the physical insight on the system since dynamic pressure is a critical physical parameter for launchers (and it depends on the square of the velocity).

Like the standard (i.e. non-structured) $\mathcal{H}_\infty$ control design approach, the applied LPV synthesis does not allow defining a specific controller structure and the resulting controller has as many states as those used in the design interconnection, which results in a 22^{th} order controller. The induced $\mathcal{L}_2$ norm of the LPV controller is 2.13 (which is only a 15% increase with respect to the highest linear $\mathcal{H}_\infty$ design norm).

6.4 Analysis

This section analyses first the LPV design in terms of classical linear stability margins (Subsection 6.4.1), and then the LPV controller is compared with the VEGA baseline controller by means of a Monte Carlo campaign using VEGA's nonlinear, high-fidelity benchmark (Subsection 6.4.2).

6.4.1 Linear stability analysis

As in previous chapters, the closed-loop stability is analysed in terms of the classical (gain and phase) stability margins. Figure 6.7 shows the Nichols chart of the system at distinct flight instants. To perform this analysis, a set of frozen-parameter controllers, i.e. each then an LTI system, are extracted from the LPV controller at every 10 seconds in the range t=[20,90]s (this range covers the grid points used for design as well as additional in-between points). It is noted that this LTI extraction is performed using for the scheduling parameter and its rate the corresponding values of NGV and NGA taken from the nominal trajectory at the selected times. Looking at Figure 6.7, it is highlighted that the LPV design provides satisfactory rigid-body margins while it yields gain stabilisation for the first and upper bending modes.

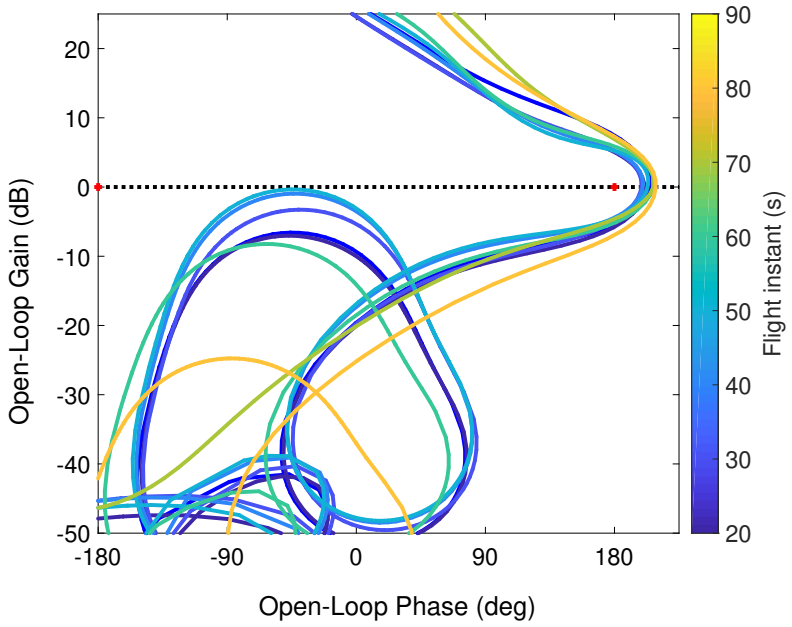

Figure 6.7: Nichols charts using the LPV design using $\dot{\rho}(t) = NGA(t)$

Although not shown here, the stability margins are also evaluated at the minimum and maximum rate of change ($\dot{\rho} = \underline{\nu_{NGA}}$ and $\dot{\rho} = \overline{\nu_{NGA}}$) with NGV taken as before from the nominal trajectory. It is observed that the variation of the margins are less than 1% with respect to the case shown above $\left(\dot{\rho} = NGA\right)$, except at t=20 s and t=90 s where the differences are below 5%.

6.4.2 Nonlinear analysis

Before presenting the results of the Monte Carlo campaign using the VEGA benchmark, a brief comment on the implementation of the LPV controller in the benchmark is given.

Remarks on the LPV controller implementation

The final VEGA LPV control structure is shown in Figure 6.8. This architecture is composed of the synthesised full-order controller $K(\rho)$ (22 states, which includes the rigid-body controller and bending filter functionalities) and the first order pseudo-derivative filter $H_d(s)$ used previously in Chapter 5, see Equation 5.13, which computes the attitude error signal $\dot{\psi}_e$ from ψ_e. Thus, the final implementation of the LPV controller has 23 states, in contrast to the 26 states of the baseline controller.

$K(\rho)$ is implemented using a Simulink block provided in the Matlab toolbox *LPVTools* [47]. Note that this block performs a multidimensional linear interpolation to evaluate the state-space matrices of the controller at the measured scheduling parameter ρ.

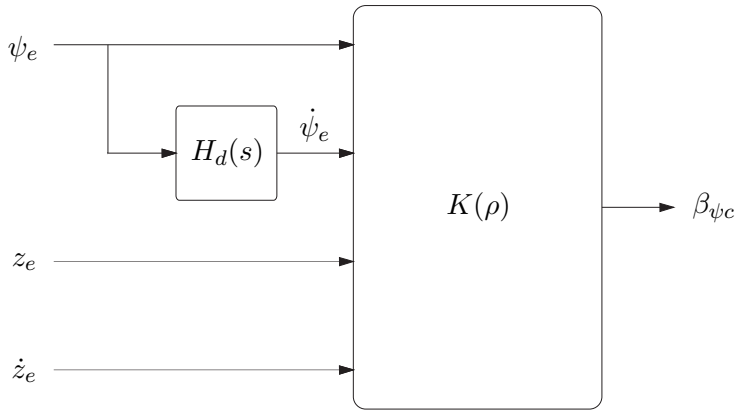

Figure 6.8: Nonlinear TVC implementation for the LPV controller

Monte-Carlo campaign

To evaluate the performance and robustness of the LPV design, the same 4 MC campaigns performed in previous chapters (described in Section 4.2.5) are performed (i.e. 500 runs each, all using the same scattered parameters and VV05 flight but a different wind).

Figure 6.9 shows the 2000 MC responses for the aerodynamic load performance indicator $Q\alpha$ versus Mach for the baseline VEGA controller and the designed LPV controller. In darker lines, the corresponding nominal simulations using the estimated wind from the actual VEGA VV05 mission are depicted for each controller to serve as reference.

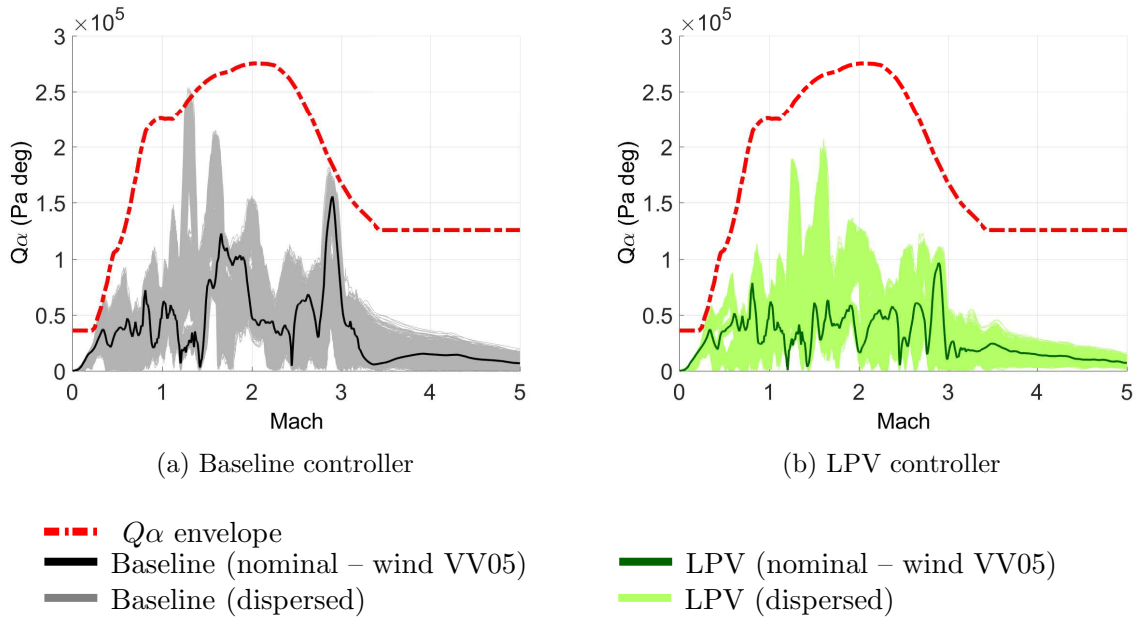

(a) Baseline controller

(b) LPV controller

Figure 6.9: MC nonlinear $Q\alpha$ analysis: baseline versus LPV controller

Comparing both plots, it can be seen that the LPV controller reduces significantly the aerodynamic loads with respect to the baseline $Q\alpha$ performance. Note that using the baseline controller there are several cases that violate the $Q\alpha$ safety envelope (around Mach 1.25), while the LPV design manages to reduce this performance indicator for that Mach point and throughout the flight envelope. It is highlighted that this is not only achieved on a unique wind, but using the four different wind profiles –including the real wind from the flown VEGA VV05 mission.

In addition to the above $Q\alpha$-vs-Mach comparison, the main performance indicators of the atmospheric phase (attitude error, drift, actuation and aerodynamic load) are evaluated using the same quantitative assessment presented in Section 4.2.5. Recall that for each MC run, the ∞-norm and 2-norm are computed for each indicator. Figure 6.10 illustrates the average of those two norms normalised with respect to the values obtained for the baseline controller.

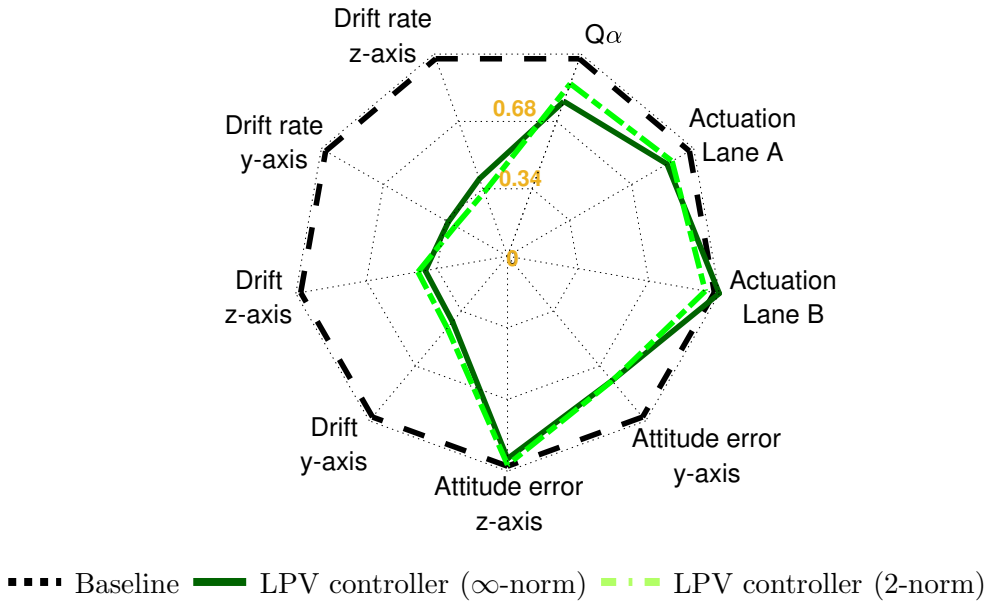

Figure 6.10: Monte Carlo quantitative assessment for the LPV controller

From the spider plot of Figure 6.10, it is easily seen that the LPV controller offers improved performance for all the indicator/norm pairs, except for the ∞-norm of the actuation actuation (i.e. maximum deflection) at lane B, which is degraded but only about 2% with respect to the baseline. Nonetheless, the LPV controller provides a reduction on the TVC overall consumption (measured by the 2-norm of the actuation, which shows a reduction of 10% at lane A and 5% at lane B). As for the $Q\alpha$ performance, as it was already observed in Figure 6.9, the maximum peaks of the LPV controller are reduced by 22%. Simlarly, the tracking performance is also improved, particularly over the y-axis. And finally, the drift and drift-rate performance are significantly improved as it can be seen at the left-side of Figure 6.10.

6.5 Conclusions

This chapter presents an LPV control design for the VEGA atmospheric-phase control system. The design is performed using NGV, which is the actual VEGA scheduling parameter, as the scheduling time-varying parameter. In addition, information about its rate variation (non-gravitational acceleration) is also considered in the design process.

A grid-based approach is used to obtain an LPV model of VEGA launcher. The control problem is formulated as a robust control design problem, where the requirements are expressed in terms of weighting functions. The weighting functions are also defined as grid-based LPV models. This allows to cope with the large dynamical system variations and tackle different design strategies at each design grid point. In order to address the bending mode attenuation, the control effort is weighted by a double notch-filter, which results to be very effective providing gain stabilisation for the first and upper bending modes. Finally, note that the proposed design framework uses an LPV representation of the wind turbulence Dryden filter presented in Section 4.1, to reduce the performance degradation caused by the wind disturbance.

The LPV controller provides satisfactory linear stability margins throughout the flight envelope. Furthermore, the Monte-Carlo simulations exhibit that the LPV controller provides further improved robust performance with respect to the baseline controller. The same conclusion is obtained using four different wind profiles, giving a measure of the wind disturbance rejection capabilities of this design. Also note that the final implementation of the LPV controller has 23 states, while the baseline controller has 26 states.

It is also important to highlight that as for the joint design presented in Chapter 5, this synthesis approach allows to design the rigid-body controller and the flexible bending filters in one single procedure. This can be used to reduce the tuning and design effort required for each mission.

CHAPTER 7

Reconciling full-order designs and augmented structured $\mathcal{H}_\infty$ design via internal model principle

Wind disturbance rejection is one of the main factors that must be addressed by the ascent-flight control system of any launch vehicle. For adequate disturbance rejection, the control system must contain the necessary structure to encapsulate a model of the disturbance dynamics. This idea is formally known as the Internal Model Principle (IMP) [126]. In particular, the actual VEGA TVC architecture does not satisfy this principle because it does not have any dynamics at low frequencies which is the frequency range where the wind disturbance has more impact. This chapter aims to reconcile the current VEGA control system architecture with the IMP.

The IMP can be managed via the classical Internal Model Control (IMC) [127], which consists of parametrising the controller to include an explicit model of the process to be controlled (tracking reference, plant, disturbance) and also by including a wind disturbance observer in the closed-loop system [128]. This Internal Model (IM) structure is created implicitly when using full-order robust control synthesis techniques such as the standard (i.e. non-structured) $\mathcal{H}_\infty$, μ or LPV. Nevertheless, as already mentioned, these methods result in high-order designs and do not allow to explicitly define a structure for the controller. This is an important limitation in aerospace applications where a good understanding of the controller structure is appreciated.

In this chapter, the IMP is tackled by using the structured $\mathcal{H}_\infty$ technique as it enables to explicitly embed a wind IM structure to the current VEGA TVC architecture to get further wind disturbance rejection. The aim of this chapter is also to show how to characterise such an IM model for the atmospheric ascent phase of the VEGA launcher, and also to show how to effectively use it within the VEGA TVC design. The process followed leverages the knowledge from the full-order LPV control design presented in Chapter 6 and the joint robust structured $\mathcal{H}_\infty$ design from Chapter 5.

The layout of the chapter is as follows. Section 7.1 describes the process followed to characterise a wind/gust rejection internal model. Then, a structured $\mathcal{H}_\infty$ design including the characterised IM architecture is performed in Section 7.2. Section 7.3 analyses the robust stability and performance of this new design using the structured singular value technique. Finally, Section 7.5 presents the conclusions.

7.1 Wind internal model identification

In this section, the structure of the LPV design from Chapter 6 is examined and compared with the baseline controller used for the actual VEGA VV05 mission and the joint rigid/flexible structured $\mathcal{H}_\infty$ controller presented in Chapter 5. This comparison is carried out using magnitude Bode plots obtained at flight time t=50 s as shown in Figure 7.1. The figure shows the transfer functions from the controller inputs (i.e. from top-to-bottom in the left the attitude and drift errors, ψ_e and z_e, and in the right their corresponding rates, $\dot{\psi}_e$ and $\dot{z}_e$) to the controller output $\beta_{\psi c}$ (i.e. the commanded actuator deflection).

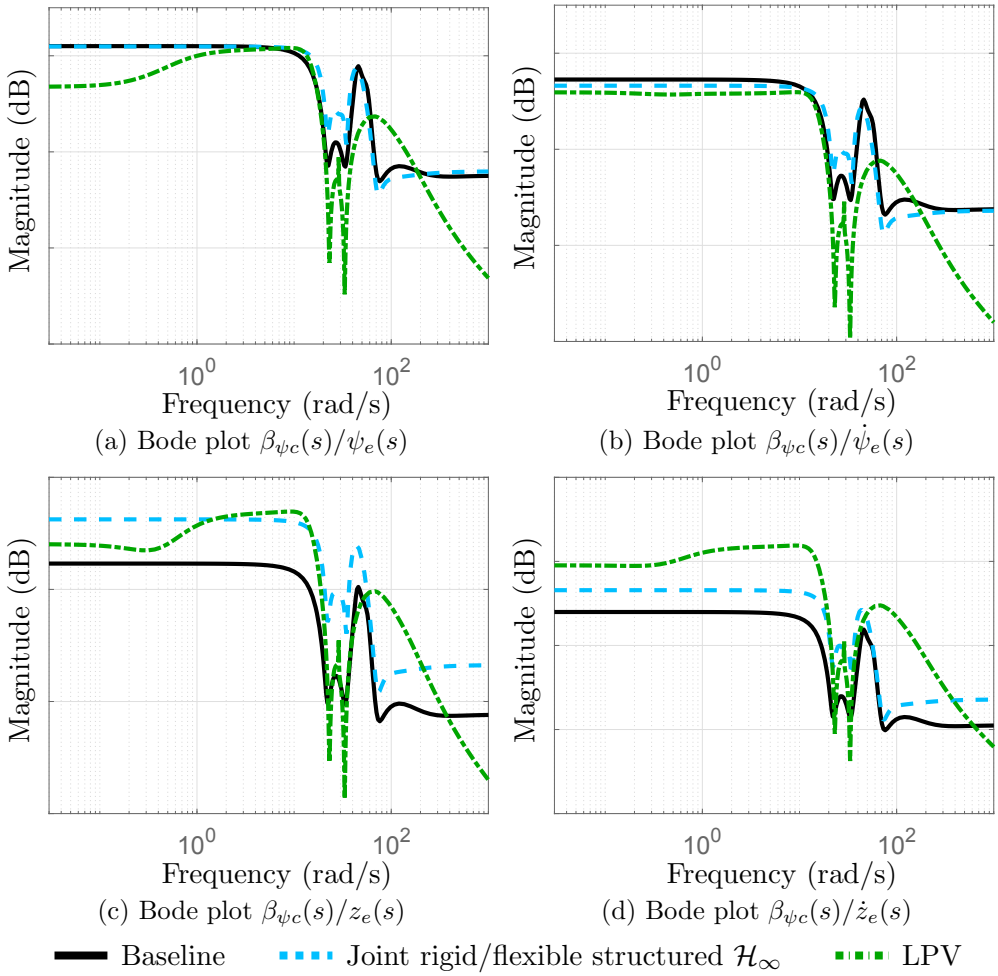

Figure 7.1: Bode plot comparison of baseline, joint structured and LPV controllers at t=50 s

When comparing the frequency responses shown in Figure 7.1, it becomes clear that the LPV design has an extra structure at low frequencies that is missing in the other two. Specifically, the LPV design performs a derivative action at low frequencies in all the controller channels excepts for the attitude rate error (i.e. top-right plot) where the derivative response is minimal. This extra structure can be interpreted as a wind disturbance IM since it occurs in the frequency range where the wind disturbance input has a major effect. Recall that full-order control synthesis techniques implicitly encapsulate the IM in the resultant controller as they absorb all the dynamics used for the design, in this case, the wind disturbance dynamics which are predominantly low frequency.

Figure 7.1 also shows a different behaviour at high frequencies (above 1 rad/s) between the LPV design and the other two controllers. This is ascribed to the bending filter functionalities of the LPV controller, whose high-frequency response is determined by the particular actuation weighting function $W_{\beta c}(\rho)$ (Equation 6.13) employed for the LPV synthesis. Indeed, the high-frequency behaviour of the LPV controller matches with the shape of the aforementioned weight $W_{\beta c}(\rho)$ shown in Figure 6.5. Among these differences, it is observed that the LPV controller provides more attenuation for the first bending mode in the attitude channels (see the double-notch filters in Figures 7.1a and 7.1b) as well as the additional high-frequency roll-off seen for the LPV in all channels.

In addition, it is notable that the LPV design presents higher drift-rate gains than the other controllers, see Figure 7.1d. As shown in Section 6.4, this feature leads to a better drift-rate performance against wind disturbance, which in turn improves the wind rejection performance of the $Q\alpha$ channel (recall that the angle of attack α depends directly on the drift-rate). This wind rejection performance will be further analysed in the next section.

Focusing on the derivative action at the low-frequency region, and taking advantage of the easily augmenting capabilities of the structured $\mathcal{H}_\infty$ approach, it was decided to characterise the aforementioned wind IM and then assess its re-usability for the redesign of the joint rigid/flexible structured $\mathcal{H}_\infty$ controller (the latter will be presented in the next section). The observed IM structure can be roughly approximated as a first-order high-pass filter at low frequencies with the following expression:

$$H_{IM}(s) = \frac{s + z_{IM}}{s + p_{IM}} \tag{7.1}$$

where z_{IM} and p_{IM} are respectively the zero and the pole of $H_{IM}(s)$.

In preparation for the subsequent structured $\mathcal{H}_\infty$ optimisation, z_{IM} and p_{IM} are configured as tunable parameters, whose values are constrained to limit the action of the internal model $H_{IM}(s)$ to low frequencies as shown in Figure 7.2. This plot shows the allowable frequency responses of $H_{IM}(s)$ by randomly sampling 100 times among the defined range of values. This range is chosen based on the low-frequency behaviour of the LPV controller at different flight times.

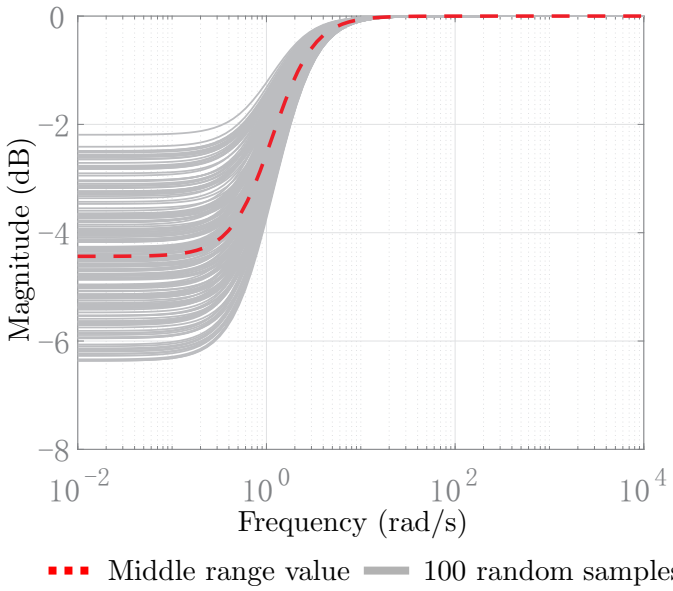

Figure 7.2: Allowable frequency responses for the internal model $H_{IM}(s)$

7.2 Augmented structured $\mathcal{H}_\infty$ design

In this section, the joint robust structured $\mathcal{H}_\infty$ controller from Chapter 5 is re-designed but incorporating the identified wind internal model.

7.2.1 Problem formulation

The control problem is formulated in the same manner as in Chapter 5 (with wind model and rigid/flexible parametric uncertainties), see Figure 7.3. As in previous chapters, the new block with respect to the previous interconnection is highlighted with a blue box.

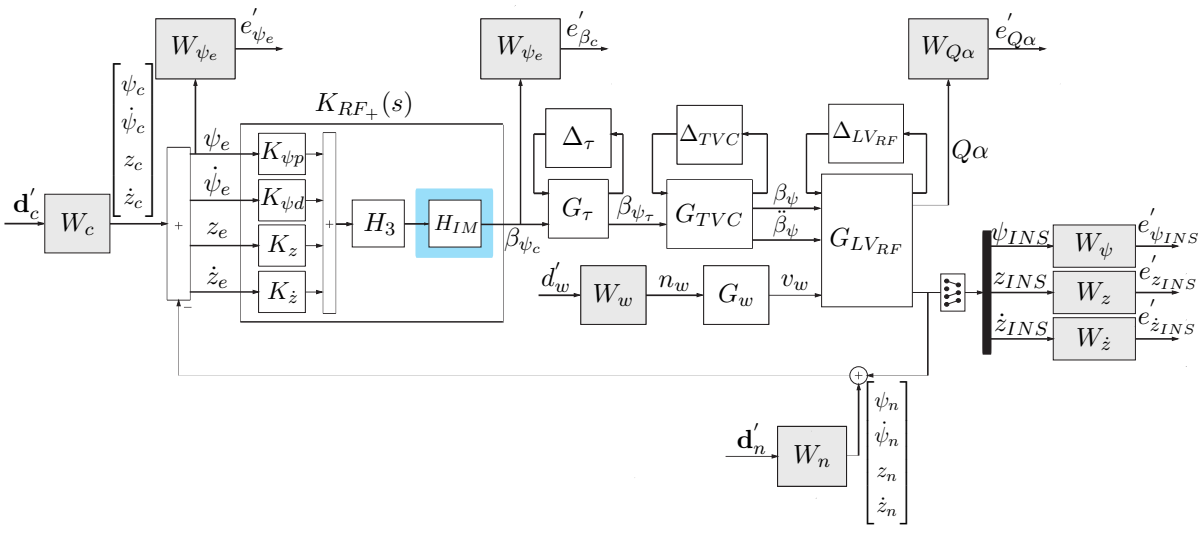

Figure 7.3: Closed-loop diagram for the IM-based structured $\mathcal{H}_\infty$ design

The structure of the controller $K_{RF_+}(s)$ is shown in Figure 7.3 and for clarity, is also given in Figure 7.4 as a single diagram. $K_{RF_+}(s)$ is composed of the same rigid-body controller K_R and bending filter $H_3(s)$ proposed in Chapter 5 (recall Figure 5.2) and the internal model $H_{IM}(s)$ characterised in the previous section. This results in a controller of 15 states. Notice that using this configuration, the derivative action of $H_{IM}(s)$ is applied to all the controller channels, as opposed to the full-order LPV design (see Figure 7.1). This scheme is chosen to reduce the complexity of the controller structure as well as of the optimisation process.

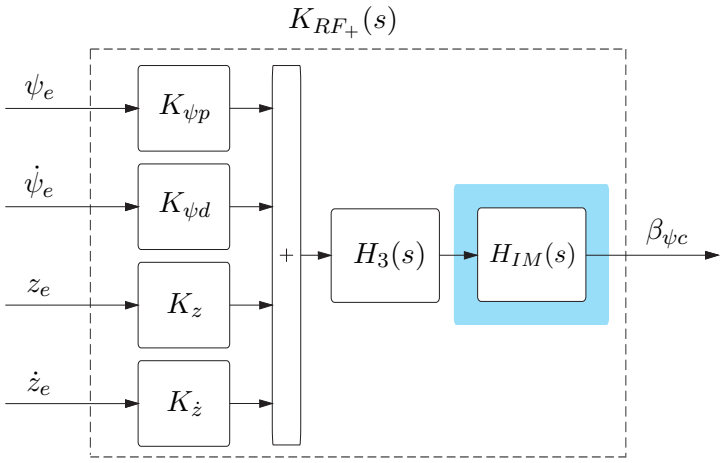

Figure 7.4: TVC structure for the IM-based structured $\mathcal{H}_\infty$ design

The above controller architecture defines the following controller space:

$$\mathcal{K}_{\mathbf{VEGA}_+} = \left\{ K(s) : K(s) = K_R \cdot H_3(s) \cdot H_{IM}(s), \text{ with } \begin{array}{r} K_R \in \mathcal{K}_{\mathbf{VEGA_R}} \\ H_3(s) \text{ defined by Equation 5.1} \\ H_{IM}(s) \text{ defined by Equation 7.1} \end{array} \right\} \quad (7.2)$$

For the structured $\mathcal{H}_\infty$ design, the rigid-body controller K_R and bending filter $H_3(s)$ of Equation 7.2 are defined as in previous chapters (i.e. four rigid-body tunable parameters with no constraints on their allowable values and four flexible-body tunable parameters as indicated in Table 5.1), whereas $H_{IM}(s)$ is defined as presented in the previous section via two tunable parameters. Therefore, the tunable controller $K_{RF_+}(s)$ is characterised by a total of 10 tunable parameters.

As in previous chapters, the closed-loop interconnection of Figure 7.3 is re-arranged into a robust standard $\mathcal{H}_\infty$ interconnection (recall Figure 4.8). The control problem is then formulated as the optimisation given as follows:

$$\min_{K(s)} \max_{\Delta_{RF} \in \mathbf{\Delta_{RF}}} ||\mathcal{T}_{\mathbf{e'd'}}(s, \Delta_{RF})||_\infty < \gamma; \qquad \text{subject to } K(s) \in \mathcal{K}_{\mathbf{VEGA}_+} \quad (7.3)$$

To illustrate the capabilities offered by the internal model $H_{IM}(s)$, the above structured $\mathcal{H}_\infty$ optimisation is applied at the same 9 flight instants used in Part I for design. Note also that, the same weight setup (and values) as the ones presented in Section 5.1.3 is employed for these 9 designs. Only the output drift and drift-rate requirements are set tighter (i.e. lower values for W_z and $W_{\dot{z}}$) at the design points t=[40, 50, 60]s with the aim to emulate the $Q\alpha$ wind rejection performance of the LPV controller.

7.2.2 Controllers comparison

Figure 7.5 compares the Bode plots of the new IM-based design with the three controllers previously analysed at t=50 s. Looking at the IM-based frequency responses (in red with square markers), it is worth noticing that, as for the LPV design, the new design shows now also the high-pass action at low frequencies, which is the result of including the internal model $H_{IM}(s)$. Note also that, the bending filter structure of the IM-based controller is the one given in Equation 5.1. Thus, the new design does not exhibit the deep double-notch filtering and high-frequency roll-off characteristics of the LPV controller.

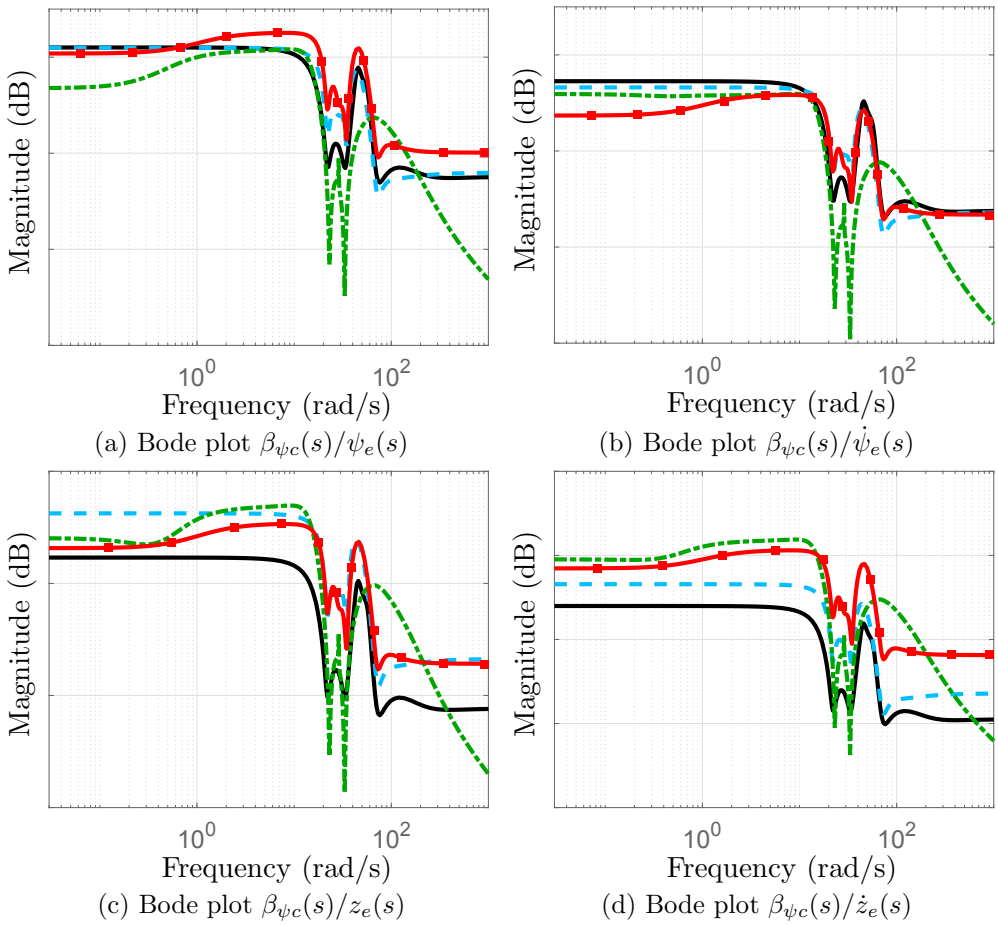

(a) Bode plot $\beta_{\psi c}(s)/\psi_e(s)$ (b) Bode plot $\beta_{\psi c}(s)/\dot{\psi}_e(s)$

(c) Bode plot $\beta_{\psi c}(s)/z_e(s)$ (d) Bode plot $\beta_{\psi c}(s)/\dot{z}_e(s)$

Figure 7.5: Bode plot controller comparison at t=50 s (with IM-based struct. $\mathcal{H}_\infty$ controller)

Furthermore, it is also observed that the IM-based controller presents similar drift-rate gains as the LPV controller, see Figure 7.5d. As mentioned before, this feature generally results in an improved $Q\alpha$ wind rejection performance. To support this analysis, the frequency responses of the $Q\alpha$ channel from the wind disturbance input are shown for all the analysed controllers in Figure 7.6. This plot shows that the structured IM-based and LPV designs (respectively red and green responses) achieve a significant reduction of the $Q\alpha$ transient energy between 0.1 and 1 rad/s, which is precisely the range of action of the internal model $H_{IM}(s)$. In order to ensure that the improvement in wind disturbance in the [0.1-1.0] rad/s range does not result in unacceptable degradation of performance for very low- and high-frequency wind gusts, a campaign of simulations using the nonlinear, high-fidelity launcher simulation model with different wind profiles is performed (this will be presented later in Section 7.4). The results indicate that the $Q\alpha$ deterioration at those frequencies is not critical.

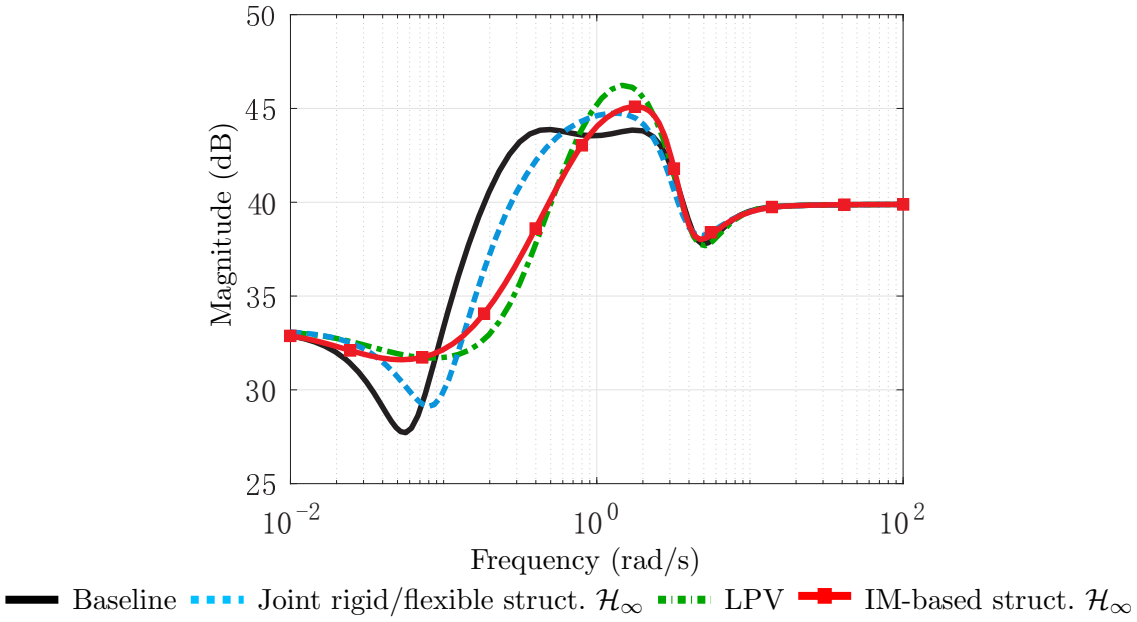

Figure 7.6: Bode plots of the $Q\alpha$ channel from wind input at t=50 s

7.3 Robustness analysis

This section analyses the robust stability of the internal-model-based structured $\mathcal{H}_\infty$ design with respect to the joint rigid/flexible structured $\mathcal{H}_\infty$ controller from Chapter 5 and the LPV controller from Chapter 6. These three controllers are analysed using the structured singular value μ technique (see Section 4.2.4).

Figure 7.7 shows the upper bound of μ computed at t=50 s for the three controllers mentioned above. Note that for this analysis, an LTI system is extracted from the LPV controller in the same manner as explained in Section 6.4.1 (i.e. using the corresponding values of NGV and its rate NGA from the nominal trajectory at the selected time).

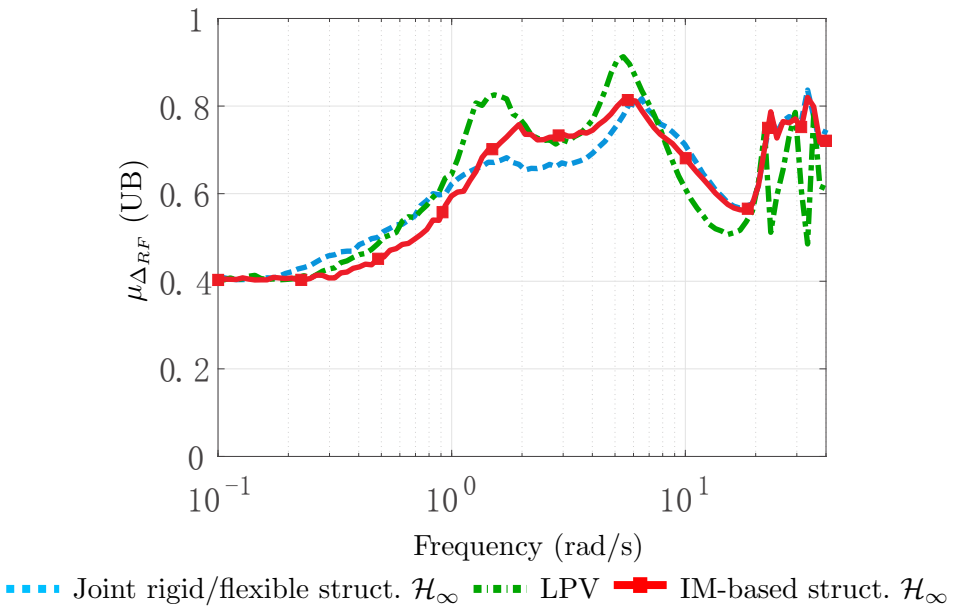

Figure 7.7: Robust stability analysis at t=50 s

It is interesting to observe that all the designs in Figure 7.7 satisfy the RS condition (recall from Equation 4.5, $\mu_{\Delta_{RF}} < 1$) across all frequencies. Thus, they are robustly stable at the analysed flight instant for the considered parametric uncertainties defined by Δ_{RF}. It is also seen that the LPV controller presents higher peaks at mid frequencies than the two structured $\mathcal{H}_\infty$ designs. This can be ascribed to the better RS (i.e. lower values of μ) of the LPV design at frequencies above 10 rad/s (which is in turn mainly caused by the higher attenuation of the LPV bending double-notch filtering). In addition, recall that the LPV controller was designed using nominal conditions, whereas both structured $\mathcal{H}_\infty$ controllers were synthesised considering parametric uncertainties in the design process.

Note, by comparing both structured $\mathcal{H}_\infty$ designs (dash cyan versus red with square markers), that the IM-based controller achieves an improvement in RS at low frequencies (below 0.1 rad/s) with respect to the joint rigid/flexible design. It is worth noticing that this improvement occurs in the frequency range where the internal model $H_{IM}(s)$ performs the high-pass action. It is also observed that the aforementioned improvement comes at the expense of slightly increasing μ at mid frequencies where the wind contribution is much smaller.

7.4 Nonlinear analysis

In this section, the IM-based structured $\mathcal{H}_\infty$ is evaluated in the nonlinear, high-fidelity simulator and compared to the other controllers analysed before (baseline, joint rigid/flexible structured $\mathcal{H}_\infty$ and LPV).

The implementation in the nonlinear simulator is carried out as described in Section 5.2.2, that is including the first-order pseudo-derivative filter $H_d(s)$ given in Equation 5.13. As a consequence, the final implementation of $K_{RF_+}(s)$ has 16 states. The individual 9 linear IM-based structured $\mathcal{H}_\infty$ controllers are first discretised using the Tustin's transformation with the first bending mode frequency as warping frequency. Then, the 9 discrete-domain controllers are linearly gain-scheduled using the non-gravitational velocity as scheduling parameter.

The same 4 Monte Carlo campaigns described in Section 4.2.5 (2000 runs in total using 4 different wind profiles) were carried out for the scheduled global IM-based structured $\mathcal{H}_\infty$ controller. Figure 7.8 compares the 2000 nonlinear $Q\alpha$ responses for the aforementioned controllers.

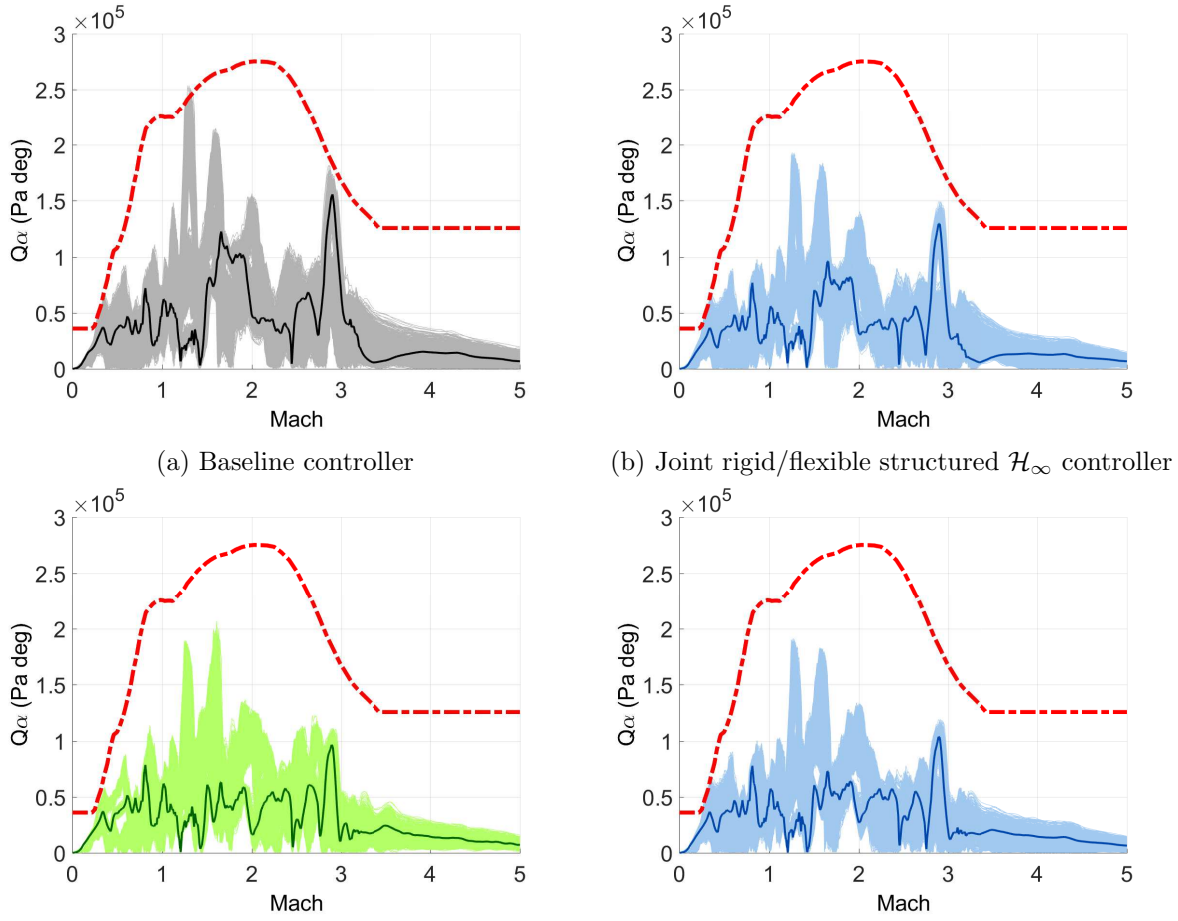

(a) Baseline controller

(b) Joint rigid/flexible structured $\mathcal{H}_\infty$ controller

(c) LPV controller

(d) IM-based structured $\mathcal{H}_\infty$ controller

Figure 7.8: Monte Carlo nonlinear $Q\alpha$ analysis

Comparing the responses for the two structured $\mathcal{H}_\infty$ controllers (see Figures 7.8b and 7.8d), it is observed that the introduction of the internal model $H_{IM}(s)$ results in a further improved structural load performance. This is clearly seen by looking at the $Q\alpha$ peak around Mach 3 (which is caused by the actual estimated wind from the VEGA VV05 mission). Focusing on the nominal responses (in darker lines), the maximum value of this peak is approximately 1.3 Pa deg for the joint rigid/flexible structured $\mathcal{H}_\infty$ controller (top-right plot) whereas using the IM-based structured $\mathcal{H}_\infty$ design this peak is around 1 Pa deg (bottom-right plot). This improvement is even more significant when compared to the baseline nominal response (Figure 7.8a), which exhibits a peak of approximately 1.5 Pa deg around Mach 3.

It is also important to note that the IM-based design (16 states) achieves a similar $Q\alpha$ performance to that shown by the LPV controller in Figure 7.8c, despite the latter having a richer structure, i.e. higher number of states with 23.

7.5 Conclusions

In this chapter, the internal model principle is applied to the design of the atmospheric control system of the VEGA launcher. The main idea of this principle is that the controller must have the necessary structure to perform adequate wind disturbance rejection control.

A wind disturbance internal model is identified by comparing the control architecture of the current VEGA TVC controller with the full-order LPV design from Chapter 6, which encapsulates this model implicitly by design. From this comparison, the internal model is parametrised as a first-order transfer function, whose tunable pole and zero parameters are configured to perform a high-pass action at low frequencies. In order to study the effect of this extra structure, the structured $\mathcal{H}_\infty$ approach is used again to re-design the controller at a linear operating point but now incorporating in its structure the internal model. In this case, the structured $\mathcal{H}_\infty$ control problem is formulated to simultaneously design the rigid-body controller, bending filter and internal model in one single procedure.

Using robust μ analysis it is shown that the robustness characteristics of the new design are improved. The results show that the introduction of the internal model achieves a better robust stability at low frequencies, which is the frequency range where the wind disturbance has more impact. Indeed, this coincides with the identified internal model bandwidth. Furthermore, the nonlinear Monte-Carlo simulations exhibit that the internal model enhances the nominal and robust $Q\alpha$ wind rejection performance capabilities of the current VEGA control system architecture.

These results highlight that the overall performance of the TVC system can be improved by adding a first-order structure to the actual VEGA TVC architecture, which explicitly embeds a model of the wind disturbance in the controller to achieve better wind disturbance rejection. This also emphasises the importance of satisfying the internal model principle when applying structured synthesis techniques.

Part III

Adaptive control design

CHAPTER 8

Adaptive control design

This chapter presents the design and evaluation of an adaptive controller for the atmospheric phase VEGA launcher. The main goal of this chapter is first, to explore adaptive features for the VEGA control system and second, to evaluate its performance and robustness properties.

The proposed adaptive controller is obtained by integrating the structured $\mathcal{H}_\infty$ controller presented in Chapter 5 with an adaptive control structure. This approach is also known as adaptive augmenting control, and has been shown to provide minimal adaptation under nominal conditions, but to improve robustness to launch vehicle failures and to provide extended safety envelope capabilities [51].

The layout of this chapter is as follows. Section 8.1 describes the adaptive control architecture as well as the control law tuning. Then in Section 8.2, the resulting adaptive controller is analysed and compared with respect to the controllers presented in Chapters 5 and 6 (i.e. joint rigid/flexible structured $\mathcal{H}_\infty$ and LPV controllers). The analysis is carried out using the high-fidelity, nonlinear simulator of the VEGA launcher in two test cases for nominal and extreme off-nominal conditions. Next, in Section 8.3, the main performance indicators for the atmospheric phase are also evaluated through a Monte Carlo campaign. Finally, Section 8.4 presents the conclusions.

8.1 Adaptive control design for the VEGA launcher

In this section, the proposed adaptive control scheme is first described (Section 8.1.1) and then the design tuning process is presented (Section 8.1.2).

8.1.1 Adaptive control structure

The adaptive control strategy used in this thesis is based on the NASA's Space Launch System (SLS) presented in reference [51] (see Figure 8.1). It should be noted that the SLS algorithm has evolved and there are currently more modern versions of the adaptive control

law [53]. Nonetheless, the adaptive architecture presented here still represents a good benchmark scenario to study adaptive augmentation control functionalities.

The adaptive augmentation relies on a controller which is designed to operate under nominal conditions. This controller is then integrated with an adaptive control law which has the following main objectives: 1) adapt minimally in nominal conditions; 2) increase performance and command tracking in dispersed conditions and when disturbances produce large errors; 3) prevent loss of vehicle (LoV) in extreme off nominal conditions.

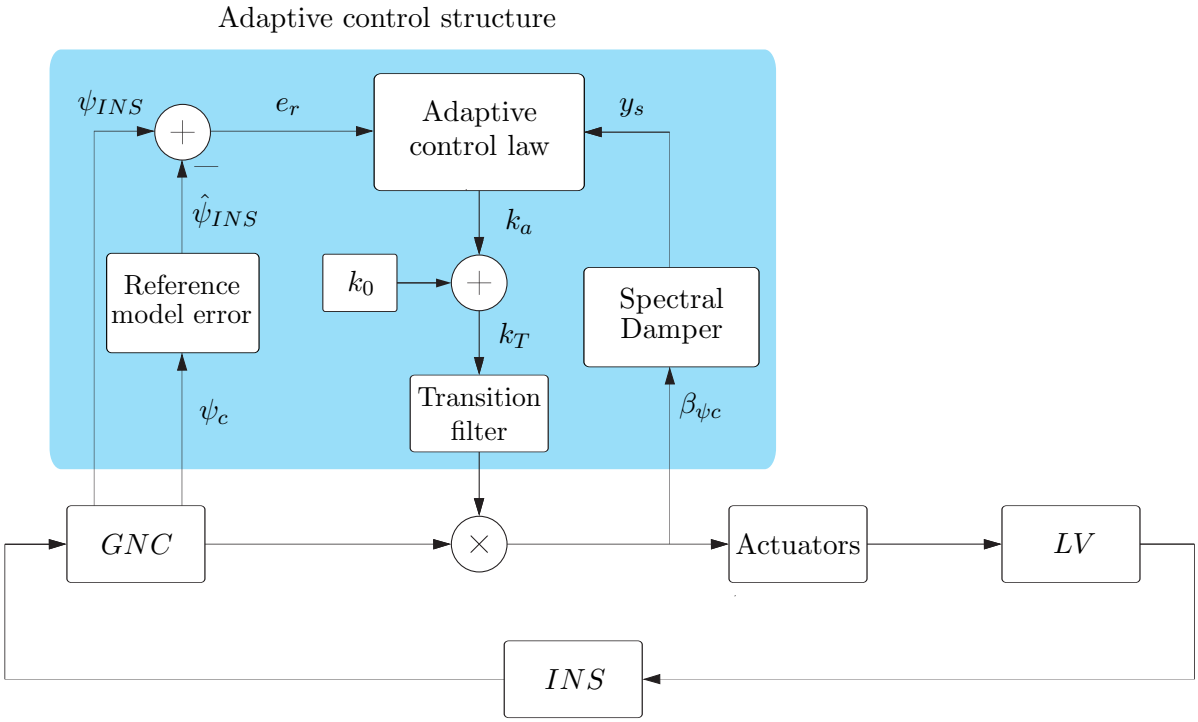

Figure 8.1: Nonlinear simulator with adaptive control structure

The SLS adaptive augmenting control system is based on a multiplicative law. As it can be seen in Figure 8.1, the actual actuators commands are computed by multiplying the controller output by the total loop gain k_T, which is defined in Equation 8.1. This gain is composed of two terms: a fixed gain k_0, which establishes a lower bound for k_T and the adaptive gain k_a, which is the output of the adaptive control law block.

$$\underbrace{k_T}_{\text{Total loop gain}} = \underbrace{k_0}_{\text{Minimum total loop gain}} + \underbrace{k_a}_{\text{Adaptive gain}} \tag{8.1}$$

In this configuration, the adaptive action should be minimal under nominal conditions ($k_T \approx 1$). On the other hand, under dispersed conditions, k_T will increase or decrease the loop gain according to the adaptive control law (i.e. variations in k_a).

The allowable values for k_T are defined based on the nominal stability gain margins of the system. For instance, assuming a nominal low-frequency gain margin of 6 dB, the lower bound for k_T is defined as $k_{T\,min} = k_0 = 0.5$. For the maximum allowable k_T, a high-frequency gain margin of $-6\,\mathrm{dB}$ corresponds to a magnitude of 2, and thus, $k_{T\,max} = 2$. This approach to set upper and lower gain limits based on linear stability margins may result in conservatism since it can potentially over-constrain the actual capabilities of the adaptive approach due to differences between the LTI models and the actual nonlinear system. As it will be seen later in the nonlinear test cases analysed in Section 8.2, the upper limit does not influence the performance of the adaptive scheme. On the contrary, the adaptive action is clearly bounded in the test case shown in Section 8.2.4 due to the lower limit $k_{T\,min} = 0.5$. To avoid this source of conservatism, other approaches to establish this gain limits based on nonlinear analyses can be considered, and are advised as a topic for future research. Nevertheless, it should be mentioned that the performance of the adaptive scheme relies more on the adaptive control law presented in Equation 8.2, which offers different mechanisms to limit the adaptation as well as to increase the robustness of the system as it will be explained later. The rate of variation of the adaptive gain k_a is described by the following first-order ordinary differential equation:

$$\dot{k}_a = \underbrace{H^e_{LP} k_e {e_r}^2}_{\text{Adaptive error}} - \underbrace{\frac{k_a}{k_{a\,max}} H^e_{LP} k_e {e_r}^2}_{\text{Logistic damper}} - \underbrace{k_{sd} k_a y_s}_{\text{Spectral damper}} - \underbrace{k_\beta (k_T - 1)}_{\text{Leakage}} \tag{8.2}$$

The adaptive control law is initialised by a starting value $k_a(0) = 0.5$ so the total loop gain is k_T equals 1 when the adaptive control is activated. In this regard, the adaptive control structure is only activated at t=15 s to avoid the vertical flight phase and the start of the pitch over manoeuvre (i.e. $k_T = 1$ for t<15 s).

It should be remarked that there are three main differences between the adaptive control law presented in this thesis and the one described in reference [51]. The first one is that the total loop gain k_T is passed through a transition filter (see Figure 8.1). Initial transients on the adaptive control law terms (Equation 8.2) were observed when the adaptive action is activated at t=15 s. Thus, in order to provide a smoother transition, instead of using a binary switch between the initial $k_T = 1$ and the output from the adaptive control law, a simple second order interpolation between both is implemented.

The second difference is the use of the filter H^e_{LP} in the adaptive error and the logistic damper terms, see Equation 8.2. The reason to include this low-pass filter is to smooth the evolution of both adaptive terms, which were found to exhibit very high-frequency fluctuations. And third, in reference [51] the adaptive control law is analysed using a high-fidelity linearised pitch dynamics simulator, whereas in this thesis a more realistic set-up is employed. The adaptive control structure is implemented and evaluated using the high-fidelity, nonlinear 6 DoF nonlinear simulator presented in Section 2.1.4. Note that the same adaptive control law (Equation 8.2) is employed for pitch and yaw axes under the assumption that they are decoupled.

Next, the different terms of Equation 8.2 are explained in detail.

Adaptive error

The adaptive error term increases the adaptive gain driven by the reference model error e_r, which is defined as $e_r = \psi_{INS} - \hat{\psi}_{INS}$ (see Figure 8.1). In reference [51], the estimated attitude angle $\hat{\psi}_{INS}$ is computed using a simple second order model with a time-varying natural frequency ω_r. Inspired by the approach used in that reference, the same transfer function is employed here, but implemented as an LPV model given by:

$$\frac{\hat{\psi}_{INS}}{\psi_c} = \frac{2\zeta_r(\rho)\omega_r(\rho)s + {\omega_r}^2(\rho)}{s^2 + 2\zeta_r(\rho)\omega_r(\rho)s + {\omega_r}^2(\rho)} \tag{8.3}$$

The above LPV model is built using the same grid-based approach described in Section 6.2 with the non-gravitational velocity (NGV) as scheduling parameter ρ. In this case, 9 different grid points are used to cover the atmospheric flight (at NGV = [108 433 639 818 1029 1286 1599 1963 2345]m/s which corresponds to t = [5 20 30 40 50 60 70 80 90]s). Note also that, $\zeta_r(\rho)$ and $\omega_r(\rho)$ are chosen to approximate the linear closed-loop dynamics at every grid point along the ascent trajectory.

The signal error e_r is multiplied by the adaptive error gain k_e, which scales the contribution of the adaptive error term in the adaptive control law. The adaptive error signal is then passed through a low-pass filter H^e_{LP} to avoid high-frequency fluctuations on the adaptive gain.

Logistic damper

The logistic damper term is computed by scaling the adaptive error term by a ratio between the adaptive gain k_a and its maximum value k_{amax}. Using this configuration, the rate of variation of k_a is decreased as k_a approaches its maximum value k_{amax}, imposing an upper bound for the adaptive gain k_a.

Spectral damper

The spectral damper term reduces the adaptive gain to suppress the effect of undesired high-frequency dynamics in the actuators commands. This term is based on the spectral damper signal y_s which is computed as follows:

$$\begin{aligned} y_{HP} &= H^{sd}_{HP}\beta_{\psi c} \\ y_s &= H^{sd}_{LP}(y_{HP})^2 \end{aligned} \tag{8.4}$$

The actual actuator command $\beta_{\psi c}$ is filtered through a high-pass (HP) filter H^{sd}_{HP}, which captures undesired dynamics at frequencies higher than the rigid-body dynamics of the launch vehicle. This filtered signal y_{HP} is then squared and smoothed through another low-pass (LP) filter H^{sd}_{LP}, which in turn removes high-frequency fluctuations on y_s and thus on the total loop gain k_T.

Finally, the spectral damper signal y_s is multiplied by the adaptive gain k_a as well as by the spectral damping gain k_{sd}, which also scales the contribution of the spectral damper term in the adaptive control law.

Leakage

The leakage term is a compensation model which attempts to lead k_T towards unity. This term is tuned through a leakage gain k_β, which is chosen to achieve minimal adaptation for nominal conditions.

8.1.2 Adaptive control law tuning

This subsection presents the tuning of the adaptive controller. As aforementioned, the proposed adaptive controller is formed by integrating the joint rigid/flexible structured $\mathcal{H}_\infty$ controller from Chapter 5 with the adaptive control structure presented in the previous subsection. This integration is carried out and implemented in the nonlinear simulator of the VEGA launcher (see Section 2.1.4) as shown in Figure 8.1.

The upper and lower limits of the total loop gain k_T are determined first. As mentioned before, these bounds are chosen based on the nominal stability gain margins of the system (without adaptation). In this regard, the joint rigid/flexible structured $\mathcal{H}_\infty$ controller globally achieves $\pm 6\,\text{dB}$ nominal rigid-body margins along the atmospheric phase. Thus, to preserve the robustness characteristics of the system, $k_{Tmin} = 0.5$ and $k_{Tmax} = 2$, which in turn leads to the following gains: $k_0 = 0.5$ and $k_{amax} = 1.5$.

Unlike the other techniques presented in this thesis (structured $\mathcal{H}_\infty$ and LPV), there is no systematic approach to tune the other gains of Equation 8.2 (i.e. k_e, k_{sd} and k_β). In this case, they are selected in a heuristic manner in two steps. Starting with the values given in reference [51] (i.e. $k_e = 500$, $k_{sd} = 50000$ and $k_\beta = 0.05$), the aforementioned three gains are first tuned using a nonlinear nominal test case without wind disturbance. The tuning objective for this test case is to achieve minimal adaptation (recall that one of the main goals of the presented adaptive approach is to adapt minimally under nominal conditions). In a second step, the obtained gains are re-tuned using the same nonlinear nominal test case but with the estimated wind from the actual VEGA VV05 mission. In this case, the gains are adjusted to balance the contribution of the adaptive error with respect to the spectral damper and leakage terms. Note that no other test cases were considered for this tuning to avoid tailoring the design for a specific off-nominal mission scenario. The final set of parameters is shown in Table 8.1 [1].

Table 8.1: Adaptive control law gains

Gain	Value
k_0	0.5
k_{amax}	1.5
k_e	200
k_{sd}	5000
k_β	0.25

[1] It should be noted that the final set of tuned parameters given in Table 8.1 was subsequently evaluated using other wind profiles, and the same behaviour was achieved.

Figure 8.2 shows the Bode plots of the adaptive error and spectral damper filters, which are also designed empirically. The former (i.e. H^e_{LP} in Figure 8.2a) is a fourth-order low-pass filter, whose bandwidth is selected to smooth and remove the high-frequency components of the adaptive error signal e_r. On the other hand, see Figure 8.2b, H^{sd}_{HP} is designed to capture high-frequency components above the launcher rigid-body bandwidth and H^{sd}_{LP} is tuned to smooth the spectral damper signal y_s. Note that all those filters are discretised for the final implementation in the nonlinear, high-fidelity simulator using the Tustin's transformation.

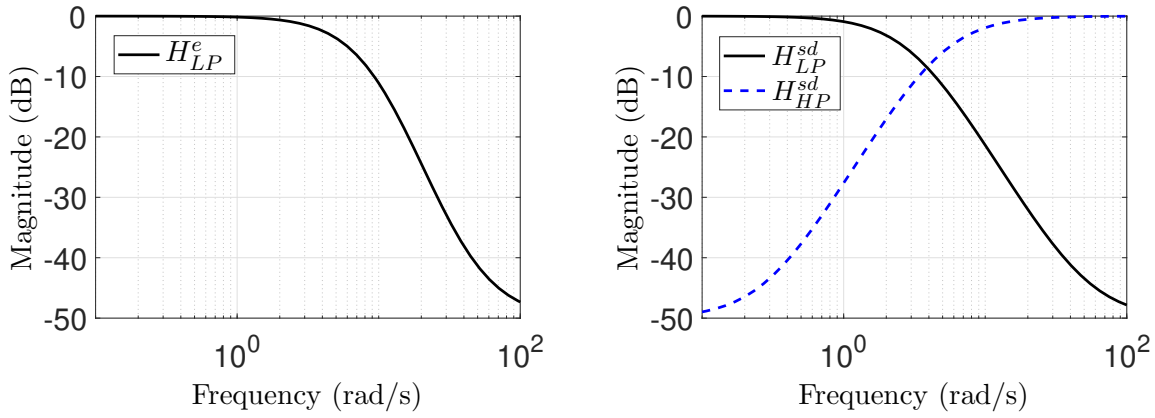

(a) Adaptive error filter

(b) Spectral damper filters

Figure 8.2: Bode plots of the adaptive control law filters

8.2 Nonlinear test cases

This section analyses and compares the performance of the adaptive controller with respect to the non-adapted joint rigid/flexible structured $\mathcal{H}_\infty$ controller from Chapter 5 and the LPV design presented in Chapter 6. Unlike reference [51] where only the pitch axis is considered, in this thesis, the adaptive controller is implemented and analysed in pitch and yaw axes under the assumption that both axes are decoupled (i.e. roll rate is considered negligible).

The aforementioned three controllers are evaluated using the following 4 test cases:

***Test case 1**: nominal VV05 flight*

***Test case 2**: nominal VV05 flight + VV05 wind*

***Test case 3**: dispersed VV05 flight + VV05 wind (all uncertainties ± 100%)*

***Test case 4**: dispersed VV05 flight + VV05 wind (all uncertainties ± 135%)*

Note that the first two test cases are the ones used for the tuning process described in Section 8.1.2. The other two aim to analyse the effect of the adaptive control structure in two dispersed, off-nominal scenarios: *test case 3* sets all the simulator uncertainties at the limits of the mission uncertainty range (i.e. 100%) and *test case 4* increases the level of uncertainties beyond the operation range of the specific VEGA VV05 mission.

It is noted that the above nonlinear test cases do not consider ad-hoc scenarios where specific effects are triggered (i.e. excessive aerodynamic instability or bending instability [51]), yet they define a representative benchmark to analyse and stress the selected controllers.

8.2.1 Test case 1: nominal VV05 flight

This test case aims to verify that the adaptive control structure provides minimal adaptation under nominal conditions (those encountered during the selected VEGA VV05 mission). For this simulation, all the nonlinear simulator flags are set to 0 (i.e. zero uncertainty) and the wind disturbance is disabled.

Figure 8.3 shows the adaptive total loop gain k_T for the pitch and yaw axis (see top plots). It is observed that $k_T \approx 1$ for both axes along the atmospheric phase and thus, the adaptive action is negligible in this case. In addition, it is noted that k_T presents a small transient in the pitch axis (Figure 8.3a). To better visualise this effect, the contribution of each of the adaptive control law terms from Equation 8.2 is also given in Figure 8.3 (see bottom plots). It is seen that the rate of k_a in the pitch axis (bottom-left plot) presents a transient which is caused by the adaptive control activation at t=15 s. This initial transient occurs because the launch vehicle is still following the pitch over manoeuvre and that creates an initial adaptive error contribution (in blue), which is rapidly counteracted by the logistic damper and leakage terms.

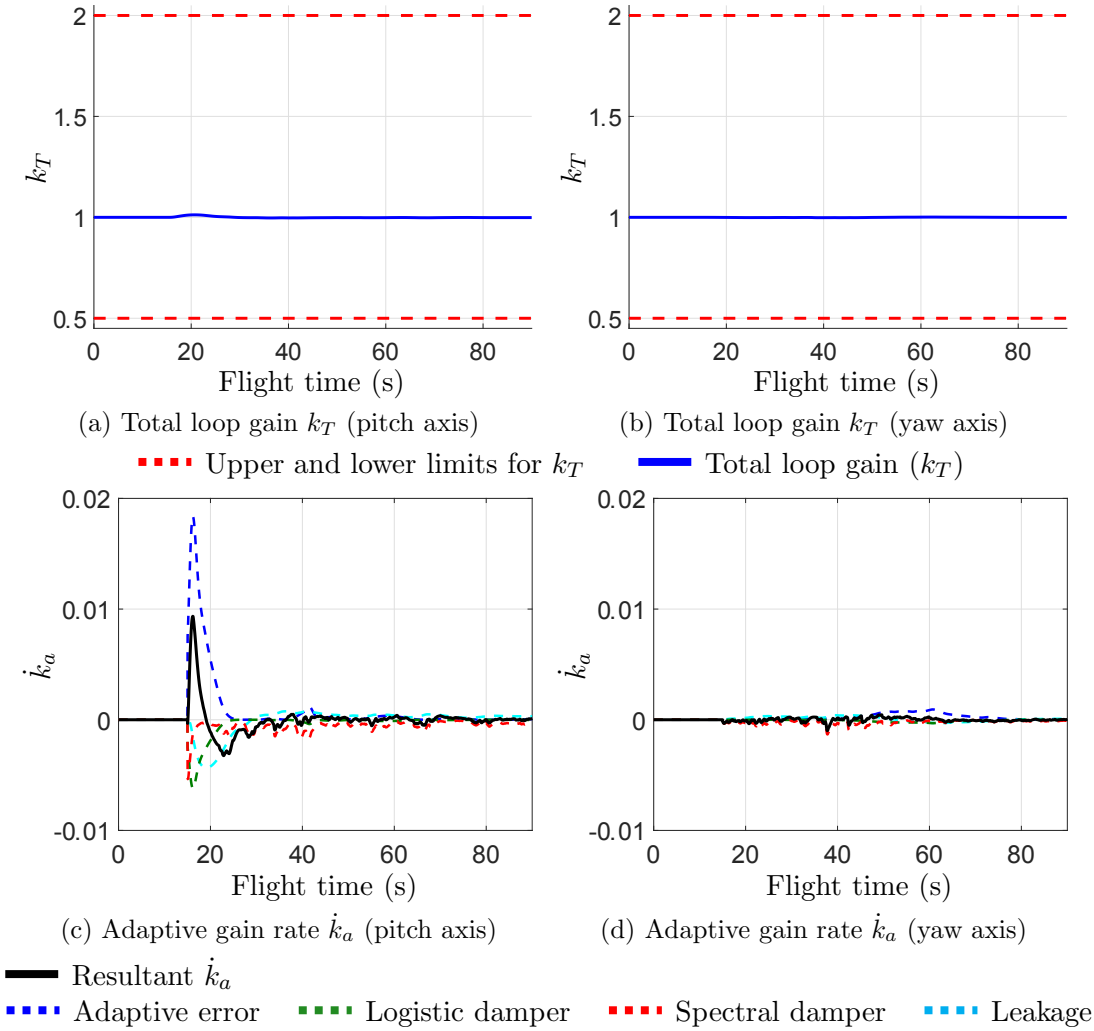

(a) Total loop gain k_T (pitch axis)

(b) Total loop gain k_T (yaw axis)

(c) Adaptive gain rate $\dot{k}_a$ (pitch axis)

(d) Adaptive gain rate $\dot{k}_a$ (yaw axis)

Figure 8.3: Adaptive test case 1: k_T and $\dot{k}_a$ analysis

8.2.2 Test case 2: nominal VV05 flight + VV05 wind

In this test case, all the nonlinear simulator flags are set to 0 as before, but the wind disturbance is enabled (the estimated wind from the VEGA VV05 mission is employed).

Figure 8.4 illustrates the total loop gain k_T and the rate of the adaptive gain $\dot{k}_a$. The first important observation is that there is more adaptive action in the yaw axis than in pitch (see top plots). This is mainly due to the characteristics of the wind profile used here, which affects more the yaw axis. The internal mechanism of the adaptive control law can be analysed by looking at Figure 8.4d. It is observed that the adaptive error term (in dash blue) exhibits several peaks along the atmospheric flight, which are caused because differences between the reference model error and the actual attitude angle are detected due to the wind disturbance. Actually, these peaks correspond to wind gusts of the VV05 wind profile mainly around the maximum dynamic pressure at t=45 s and t=60 s. This is a very interesting aspect because these wind gusts are easily recognised in the $Q\alpha$ responses shown in this thesis, since they cause the high-$Q\alpha$ peaks around Mach 1.8 and 3 respectively (see for example Figure 3.10). Indeed, these results provide an indication of the validity of the adaptive control law tuning.

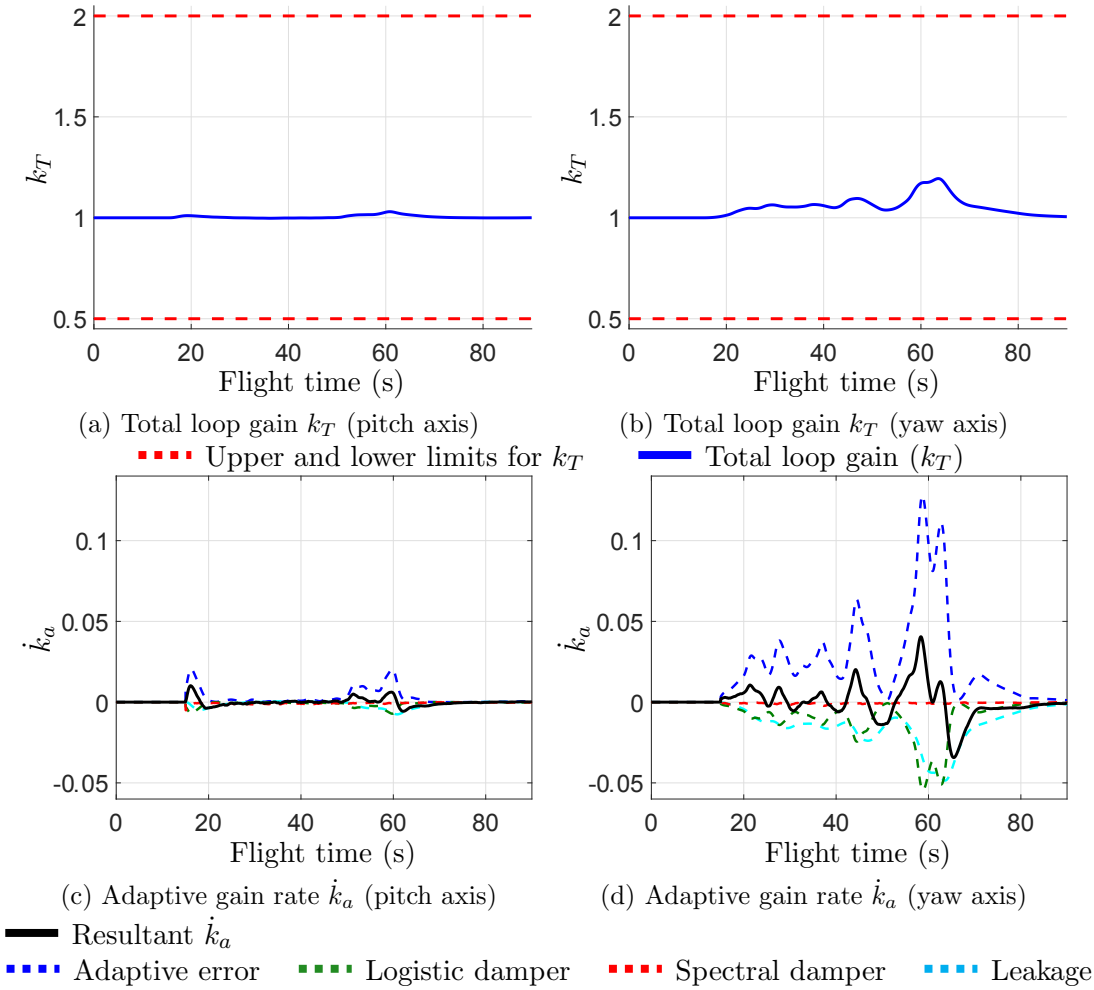

(a) Total loop gain k_T (pitch axis)

(b) Total loop gain k_T (yaw axis)

(c) Adaptive gain rate $\dot{k}_a$ (pitch axis)

(d) Adaptive gain rate $\dot{k}_a$ (yaw axis)

Figure 8.4: Adaptive test case 2: k_T and $\dot{k}_a$ analysis

8.2.3 Test case 3: dispersed VV05 flight + VV05 wind (uncertainties 100%)

This simulation analyses the adaptive controller action at the limits of the mission uncertainty range. In this test case, all uncertainty flags are set to 1, which corresponds to a level of uncertainty of 100%. As before, the estimated wind from the VEGA VV05 mission is employed.

Figure 8.4 illustrates the total loop gain k_T and the rate of the adaptive gain $\dot{k}_a$. Looking at Figures 8.5a and 8.5b, it is observed that the adaptive action is more noticeable here (i.e. higher values of k_T) than in the previous test case (particularly in the pitch axis). The same conclusion can be extracted from the adaptive gain rate $\dot{k}_a$ analysis in Figure 8.4 (see bottom plots). It is noted that the adaptive error term (in dashed blue) takes higher values. This was expected since the differences between the reference model error and the actual system response are higher not only due to the wind disturbance but also to a severe uncertainty configuration (i.e. 100%).

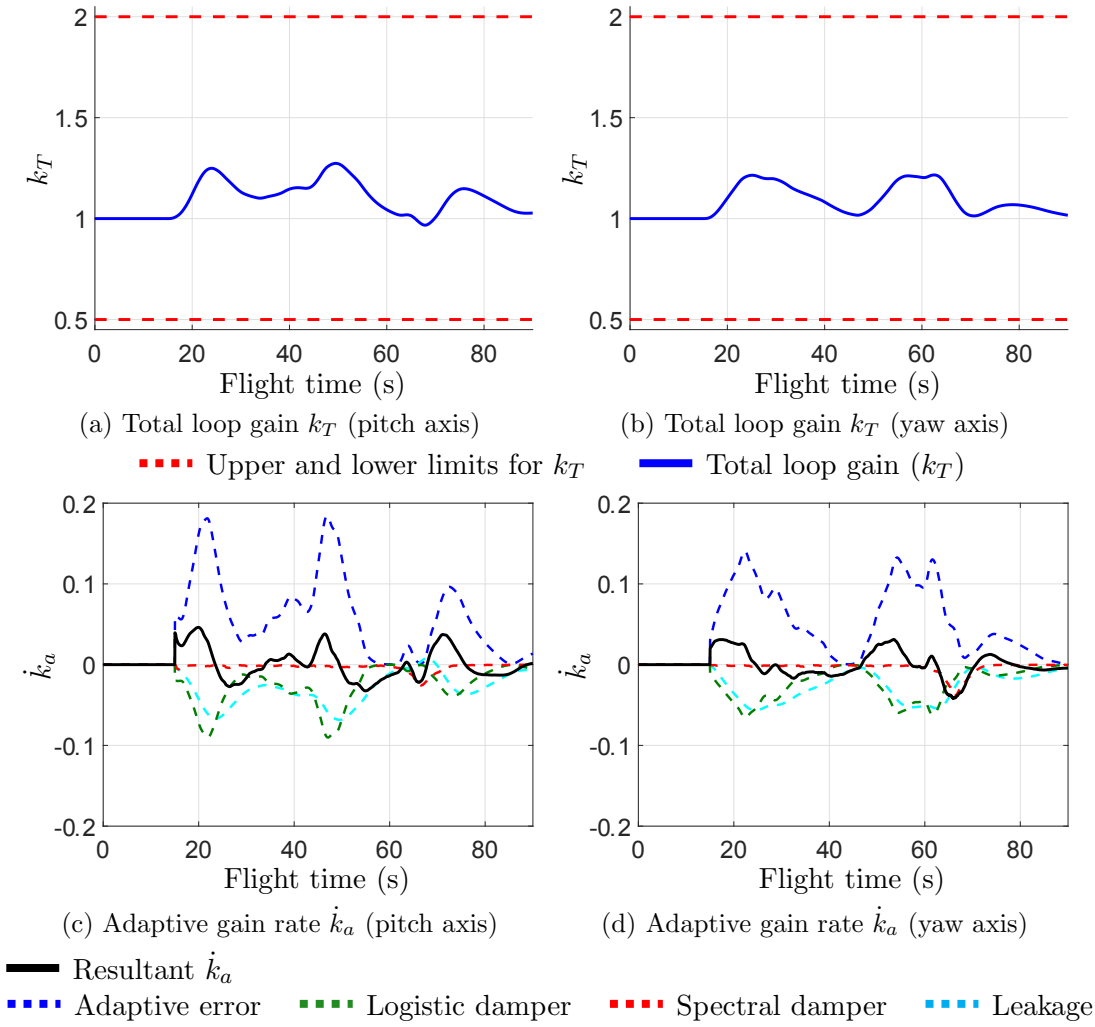

(a) Total loop gain k_T (pitch axis)

(b) Total loop gain k_T (yaw axis)

(c) Adaptive gain rate $\dot{k}_a$ (pitch axis)

(d) Adaptive gain rate $\dot{k}_a$ (yaw axis)

Figure 8.5: Adaptive test case 3: k_T and $\dot{k}_a$ analysis

Figure 8.6 shows the nonlinear $Q\alpha$ responses for the three analysed controllers. It is observed that the adaptive controller improves the structural loads performance throughout the atmospheric with respect to the non-adapted structured $\mathcal{H}_\infty$ controller, but only minimally (as shown in the zoom box area given in Figure 8.6). Also note that the rate-bounded LPV design improves the performance under the same conditions.

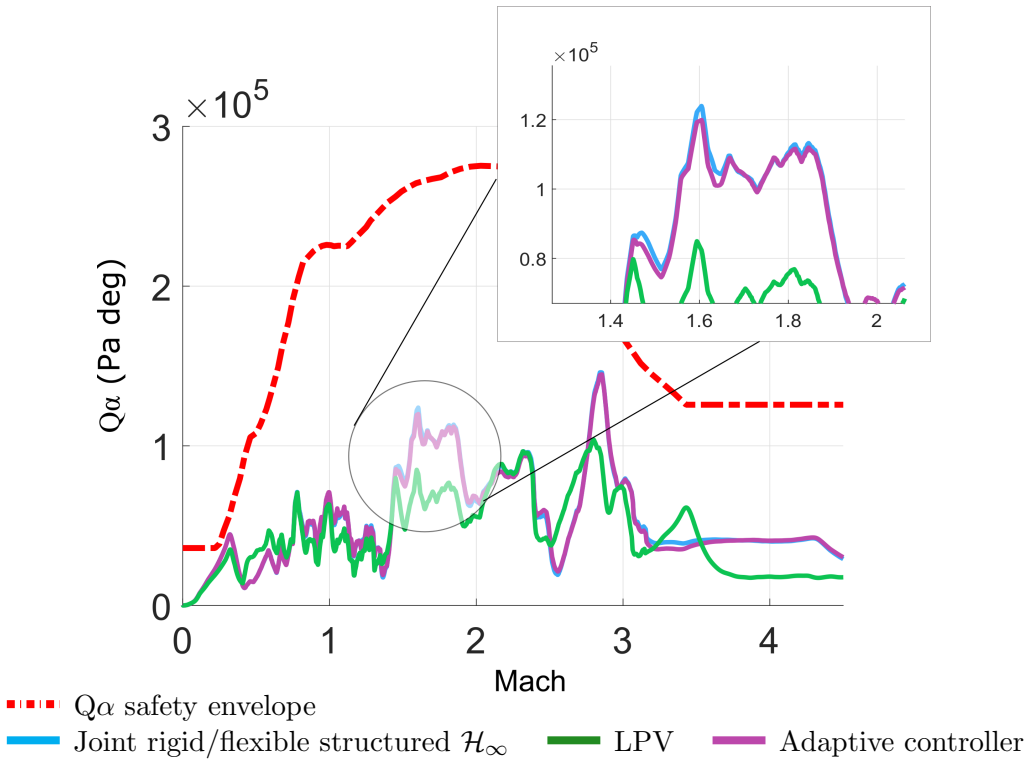

Figure 8.6: Adaptive test case 3: $Q\alpha$ analysis

The results confirm that the adaptive controller satisfies the first two objectives of the adaptive augmentation approach (i.e. adapt minimally under nominal conditions and increase performance in dispersed conditions and when disturbance produce large errors). Next, the third main objective of this adaptive approach, which is to prevent loss of vehicle under extreme off-nominal conditions, will be assessed.

8.2.4 Test case 4: dispersed VV05 flight + VV05 wind (uncertainties 135%)

This test explores the extended safety envelope capabilities that the adaptive scheme can provide by increasing the level of uncertainties beyond the range defined for the specific mission (i.e. VEGA VV05). Specifically, all the nonlinear simulator uncertainty flags are set to 1.35, which means a level of uncertainty of 135%.

Figure 8.7 shows the nonlinear responses of three key performance metrics (attitude errors, actuator deflections and structural loads) for the three analysed controllers. Note that a severe launch vehicle failure is observed for the joint rigid/flexible structured $\mathcal{H}_\infty$ controller (in cyan) around the maximum dynamic pressure region (t=50-60 s) finally causing a Loss of Vehicle (LoV) at t=60 s. This failure was expected since this test is a very critical scenario and also because the controller was designed only considering a 100% level of uncertainty.

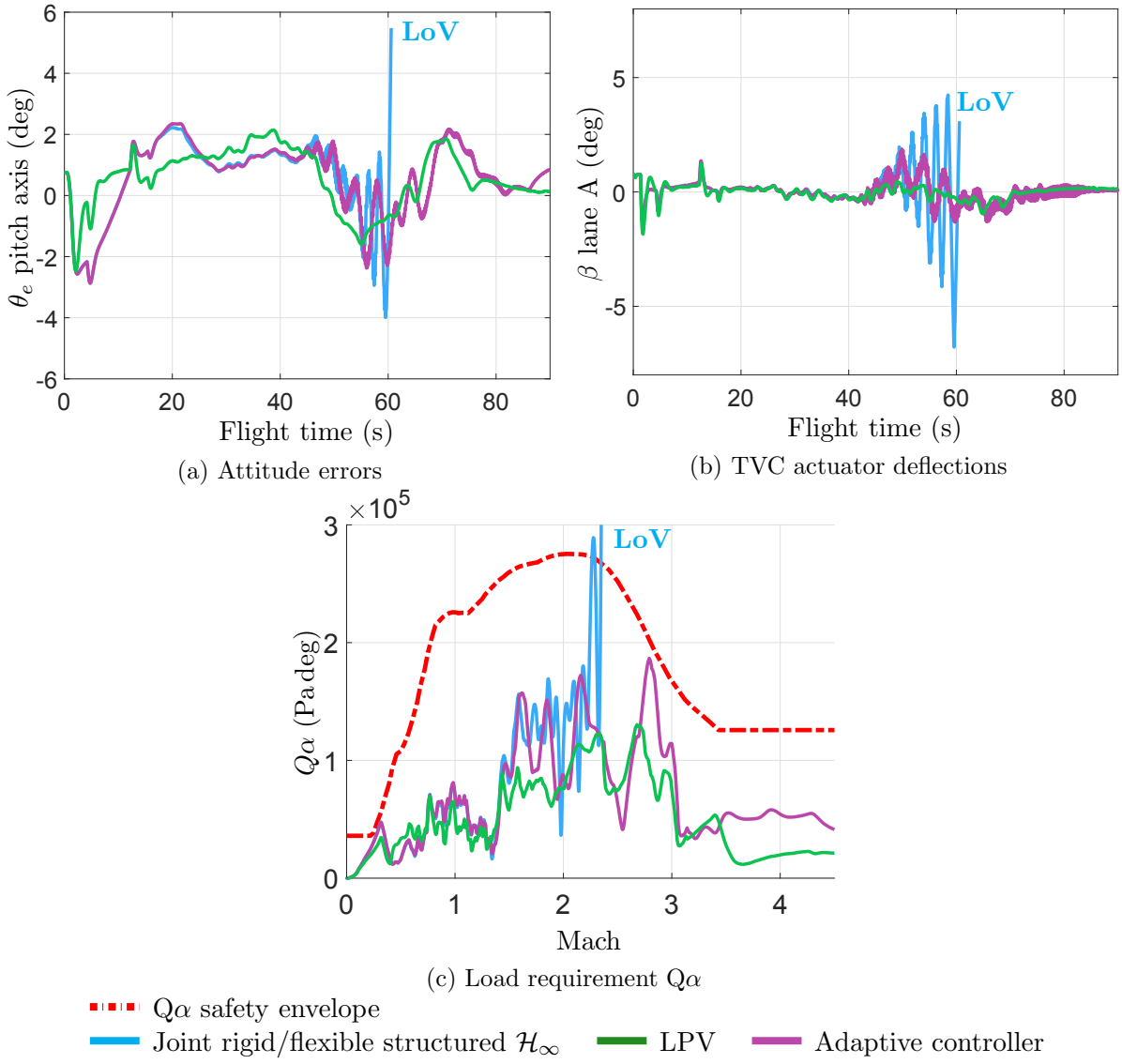

(a) Attitude errors

(b) TVC actuator deflections

(c) Load requirement Qα

Figure 8.7: Adaptive test case 4: nonlinear dispersed flight responses

On the other hand, it is interesting to observe that the adaptive controller (in purple) manages to control the instability and prevents the loss of vehicle (see Figure 8.7). To illustrate the effect of the adaptive control structure, the total loop gain k_T and the rate of the adaptive gain $\dot{k}_a$ are shown in Figure 8.8. It is worth noticing that the contribution of the spectral damper term is increased at t=45 s (see dash-red lines in Figures 8.8c and 8.8d). As seen before, this is actually the flight instant when the responses of the non-adapted structured $\mathcal{H}_\infty$ controller start to oscillate. Indeed, this high-frequency action is detected by the adaptive control law (through the spectral damper term), leading to an immediate reduction of the total loop gain k_T in both axes (see Figures 8.8a and 8.8b) which, in turn, allows to maintain the stability of the system as shown in Figure 8.7 (see purple lines).

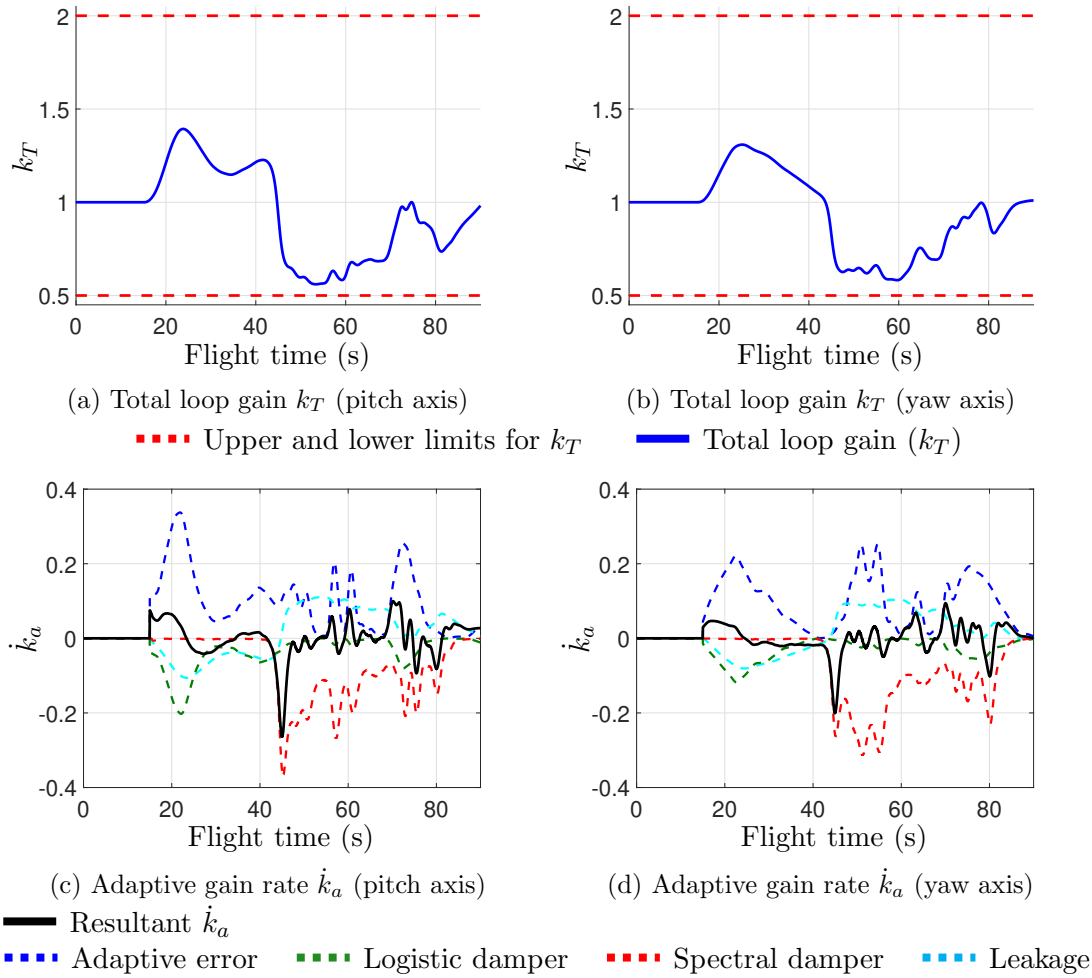

(a) Total loop gain k_T (pitch axis)

(b) Total loop gain k_T (yaw axis)

(c) Adaptive gain rate $\dot{k}_a$ (pitch axis)

(d) Adaptive gain rate $\dot{k}_a$ (yaw axis)

Figure 8.8: Adaptive test case 4: k_T and $\dot{k}_a$ analysis

Furthermore, Figure 8.7 shows that the LPV controller (green lines) also prevents the loss of vehicle under such extreme flight conditions. Indeed, it is observed that the LPV controller improves the overall performance with respect to the adaptive controller. It significantly reduces the $Q\alpha$ peak at Mach 2.8 (see Figure 8.7c) and although less noticeable in Figure 8.7b, it does not exhibit high-frequency components in the actuation channel as the adaptive controller.

8.3 Nonlinear Monte Carlo analysis

To evaluate the performance and robustness of the adaptive design with respect to the other two designs (i.e. joint rigid/flexible structured $\mathcal{H}_\infty$ controller without adaptive component and the LPV controller), a MC campaign of 500 runs is performed. For each run, the same nominal VEGA VV05 flight trajectory (with the measured wind from VV05 mission) is used but the operational parameters are all dispersed randomly. In this case, the uncertainty flags of the nonlinear simulator are allowed to vary in the interval [-1.3, 1.3], which corresponds a level of uncertainty of 130%. Note that since the nonlinear *test case 4* presented in Section 8.2.4 represented a very critical case for the structured $\mathcal{H}_\infty$ controller, in here, it was decided to use a smaller (i.e. 5%) uncertainty range.

Figure 8.9 shows the 500 MC time-domain responses of the TVC actuator deflections (in lane B) for the three controllers. In darker lines, the corresponding simulations under nominal dispersions.

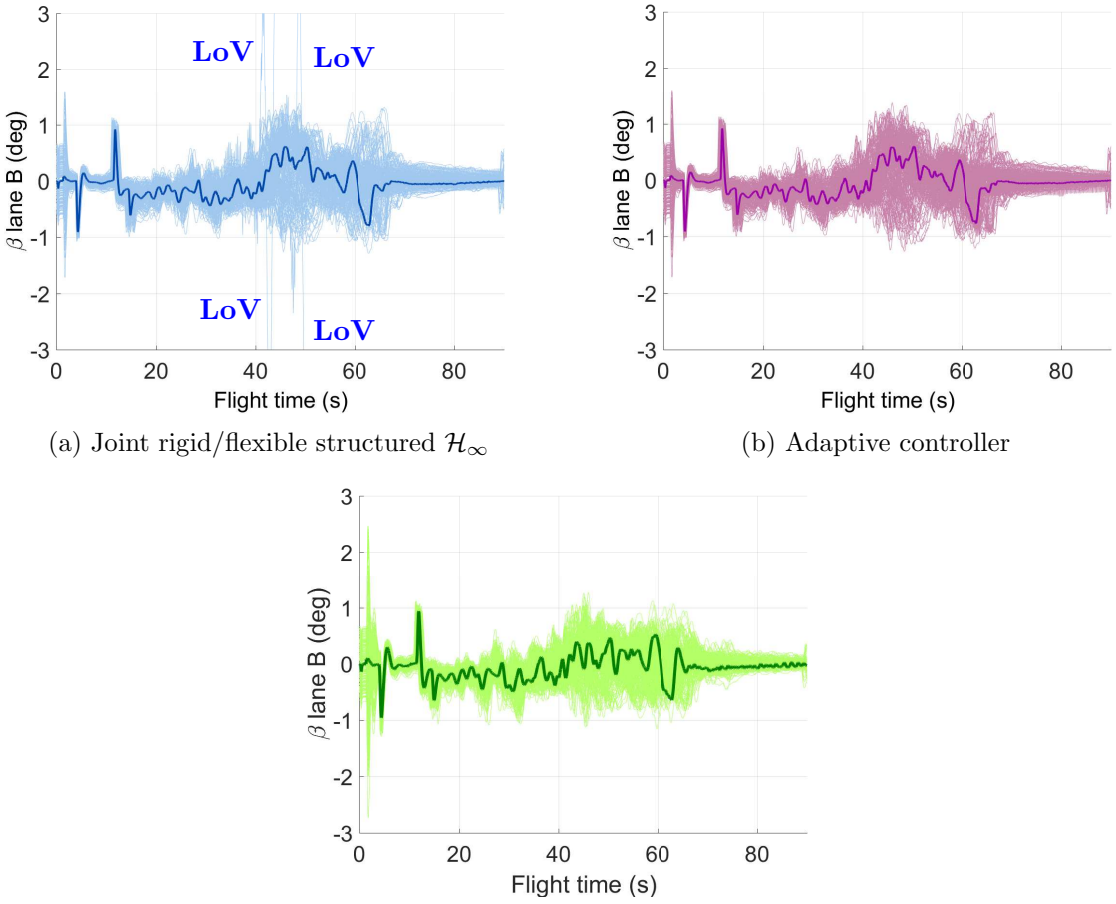

(a) Joint rigid/flexible structured $\mathcal{H}_\infty$

(b) Adaptive controller

(c) LPV controller

Figure 8.9: Extended Monte Carlo: TVC actuator command responses

By looking at Figure 8.9, it is observed that there are some critical launch vehicle failures for the structured $\mathcal{H}_\infty$ controller (see top-left plot), while the adaptive and LPV controllers manage to prevent the loss of vehicle. An inspection of the failure cases shows that they are caused by a significant reduction ($\approx 26\%$) on the nominal first bending mode frequency. This causes interactions between the rigid-body and the bending modes leading to instability.

The same behaviour can be observed in Figure 8.10, where the aerodynamic load performance indicator $Q\alpha$ is shown for the three controllers. The adaptive controller manages to keep the structural loads under the $Q\alpha$ safety envelope for all the cases. In addition, it can be seen that the LPV controller not only achieves this but also reduces noticeably the aerodynamic loads with respect to the other two cases.

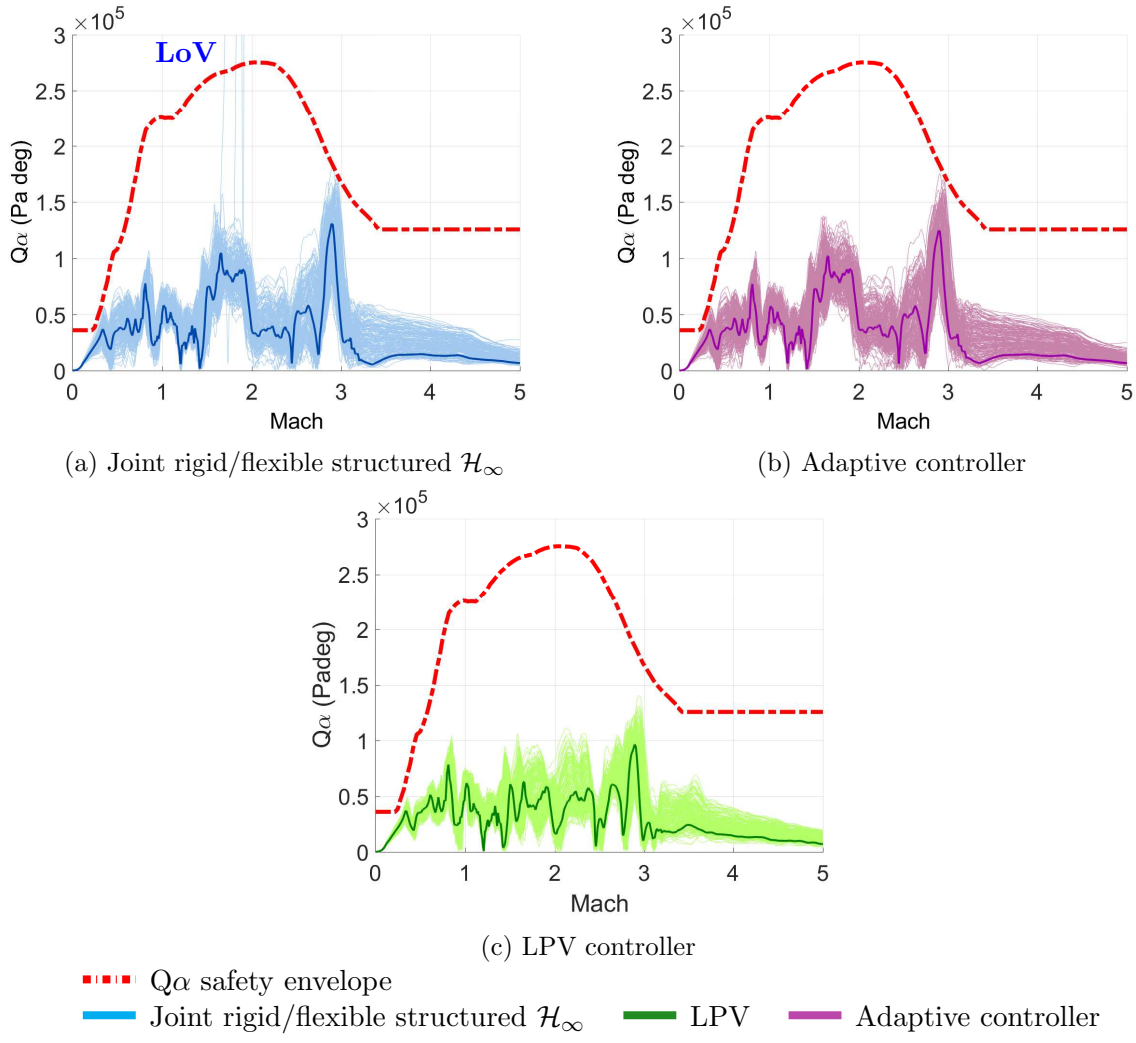

Figure 8.10: Extended Monte Carlo: $Q\alpha$ responses

The results confirm the behaviour shown in Section 8.2. That is, the adaptive controller is able to prevent a major launch vehicle failure under extreme off-nominal conditions as expected, but that the LPV design is equally capable and in addition shows better performance.

Finally, a quantitative assessment of the MC results for the three controllers is provided based on a set of performance indicators (such as attitude error, drift, or aerodynamic load performance). For each of the previous MC runs, two different metrics are computed for each indicator: the ∞-norm, which is equivalent to the maximum value taken by the indicator, and the 2-norm, which accounts for its energy. Figure 8.11 shows the average of those two norms normalised with respect to the joint rigid/flexible structured $\mathcal{H}_\infty$ controller (cyan dashed line).

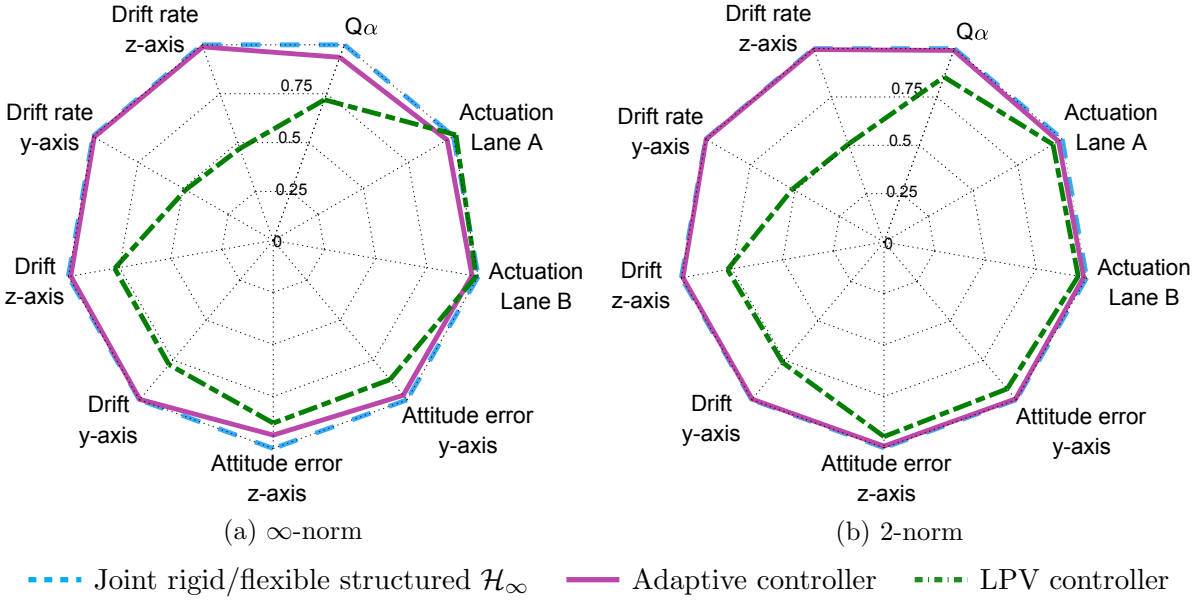

(a) ∞-norm (b) 2-norm

Figure 8.11: Extended Monte-Carlo: analysis in terms of ∞-norm and 2-norm

Looking at Figure 8.11, it can be seen that the adaptive controller not only can prevent the loss of vehicle in several cases but also slightly improves the performance of the non-adapted structured $\mathcal{H}_\infty$ controller. Particularly with respect to the ∞-norm of $Q\alpha$, which is reduced by 8%, and the the ∞-norm of actuation and attitude error indicators, which are reduced by approximately 5%. It is recognised that a more aggressive adaptive control tuning might improve these metrics, but that would generate a more intrusive adaptive controller strategy, causing more impact on the nominal performance of the system. Furthermore, it is now clear that the LPV design shows an overall superior performance with respect to the baseline and adaptive controllers. For example, the LPV controller achieves a reduction on average $Q\alpha$ peaks by approximately 30% (see Figure 8.11a), which confirms the results shown before in Figure 8.10.

8.4 Conclusions

This chapter illustrates the design of an adaptive controller for the VEGA launcher based on NASA's SLS adaptive augmenting control algorithm. This design relies on the joint rigid/flexible structured $\mathcal{H}_\infty$ design presented in Chapter 5, which is integrated with an adaptive control structure to extend safety envelope capabilities and increase performance under extreme off-nominal conditions.

The adaptive design is compared with the joint rigid/flexible $\mathcal{H}_\infty$ controller (without adaptation) as well as with the LPV design presented in Chapter 6. The three controllers are analysed using a set of nonlinear test cases with different uncertainty configurations and also via a Monte Carlo campaign using an extended uncertainty range. The results show that the adaptive control law can successfully prevent severe failures such as loss of vehicle and slightly improve the performance of the TVC system under uncertainty levels beyond the mission range.

Nevertheless, the LPV controller is also capable of preventing such failures while improving performance and robustness with respect the adaptive scheme. Furthermore, this is achieved using a more methodological synthesis approach versus the tuning complexity of the adaptive law and the lack of adaptive analysis tools.

Part IV

Conclusions

CHAPTER 9

Conclusions of the thesis

9.1 Thesis summary and main achievements

This thesis presents a methodological robust control framework for the design of the atmospheric control system of the VEGA launcher. The atmospheric flight is the most challenging phase of a launch vehicle mission from a control point of view. Indeed, this control problem is a highly time-consuming task, which requires to address multiple competing system requirements while also considering external perturbations such as wind gusts and parameter dispersions.

Part I - Structured $\mathcal{H}_\infty$ control design

In a first step, the proposed synthesis framework is based on the recently-developed structured $\mathcal{H}_\infty$ optimisation approach, which allows to perform a systematic control tuning for a specified controller structure. Special emphasis is placed on facilitating the transfer of this technology to the Space industry, starting with the recovery of the legacy behaviour of the baseline controller and gradually building up the design model towards further enhancing the synthesis capabilities (i.e. statistical wind models, parametric uncertainties and joint design of the rigid-body controller and bending filters).

As mentioned before, the structured $\mathcal{H}_\infty$ control problem is first formulated to recover the classically-designed VEGA VV05 mission rigid-body baseline controller, but in a more methodological manner. One of the novelties of the proposed methodology is that an asymptote analysis is included to reconcile the closed-loop transfer functions with the frequency-dependent weighting functions and to provide a good understanding of the constraints introduced by the controller structure. This legacy recovery exercise is paramount since it greatly facilitates the transfer of this technology to industrial control engineers with a more classical control background.

Another main contribution of this thesis is the use of a wind turbulence model in the controller synthesis. Although this is critically important, especially for launchers, only a few instances in the aerospace domain can be found where this is directly employed in the design process. This wind model is based on a Dryden filter, which represents different statistical wind levels (light, moderate, severe) at different altitudes. The main aim here is to provide the optimiser with the frequency behaviour of the wind disturbance. This characteristic is very important in frequency-domain synthesis techniques such as the structured $\mathcal{H}_\infty$ technique. In this regard, this thesis shows, via several representative design examples, that the use of strong wind levels for design significantly contributes to improve the wind disturbance rejection performance of the system.

In a subsequent design exercise, the synthesis framework is also augmented by considering parametric uncertainties in design via LFT modelling. This design feature is quite relevant for uncertain control problems such as the launcher TVC system. In essence, the optimisation is performed using a more realistic description of the launch vehicle, which also includes the expected dispersions of each parameter along the atmospheric flight. It is shown that this formulation provides improved robust stability and robust performance with respect to the baseline controller, while keeping the classical VEGA TVC architecture.

Based on the previous rigid-body synthesis framework, the structured $\mathcal{H}_\infty$ control problem is further reformulated to simultaneously perform the design of the rigid-body controller and of a bending filter in one single procedure (as opposed to the industrial state-of-practice where the design of the rigid-body controller and bending filters is performed separately in a sequential and iterative fashion). This rigid/flexible formulation is an important contribution of this thesis since it represents a paradigm shift in launcher TVC design. This joint optimisation allows to optimise rigid-body stability and performance while achieving a proper mode-stabilisation in one single design step. The effectiveness of this formulation is validated through a design example. It is shown how the legacy information from the classically-designed VEGA baseline controller can be used to guide the tunable controller parametrisation. The results show that the proposed methodology improves the performance and robustness of the launcher, while keeping and further simplifying the classical VEGA TVC architecture.

Overall, this research work demonstrates via LFT modelling, structured $\mathcal{H}_\infty$ optimisation, μ analysis and nonlinear Monte-Carlo simulations, how this robust control framework is suitable to address challenging and uncertain control problems such as launcher TVC design. In addition, it is highlighted that the proposed structured $\mathcal{H}_\infty$ synthesis framework is completely generic and can be used for any launcher with a specific controller structure, and for future launcher evolutions (e.g. VEGA C, VEGA E, Ariane 6).

Part II - From full-order control design to structured design

In this second part of the thesis, the limitations in performance of the current VEGA TVC architecture are assessed by comparing the current VEGA baseline controller and the joint rigid/flexible structured $\mathcal{H}_\infty$ design presented in Chapter 5 to a full-order controller.

To that end, the LPV synthesis approach is applied to the design of the full (rigid/flexible) VEGA TVC system. The relevance of the proposed LPV methodology is that it considers the full rigid-body dynamics (rotational and translational) as well as the flexible-body dynamics of the launch vehicle, as opposed to the previous works found in the literature where simpler rotational a_6/k_1 models were employed. The LPV modelling and synthesis steps are performed using a grid-based approach based on the non-gravitational velocity as scheduling time-varying parameter and the non-gravitational acceleration to bound its rate of variation. It is shown that the resulting LPV controller achieves a significant reduction in the aerodynamic loads (maximum peaks are reduced approx 22%) with respect to the baseline controller while also providing an overall improved performance for all the main atmospheric performance indicators.

In a second phase, the role of the internal model principle is discussed with respect to the actual VEGA TVC architecture. The full-order LPV design is compared with the current VEGA baseline controller and it is shown that the former incorporates an extra internal model structure that is missing in the other. In particular, this internal model is characterised as a high-pass filter action at low frequencies, which is the frequency range where the wind disturbance input has a major effect. In order to evaluate the effect of this wind-disturbance internal model, the structured $\mathcal{H}_\infty$ is used again to re-design the controller but now incorporating in its structure the characterised internal model. The results show that the introduction of this extra structure (consisting of a simple 1^{st} order function with two tunable parameters) enhances the nominal and robust wind rejection performance capabilities of the current VEGA control system architecture and bridges the gap between the capabilities offered by the full-order technique and the current control structure.

Part III - Adaptive control design

In the third part of the thesis, the design and evaluation of an adaptive controller for the atmospheric phase VEGA launcher is presented. The proposed adaptive approach relies on an adaptive control law that augments a robust-based baseline controller, specifically the robust joint rigid/flexible structured $\mathcal{H}_\infty$ controller presented in Chapter 5. Unlike the structured $\mathcal{H}_\infty$ and LPV techniques, which were designed in a methodological robust design framework via weighting functions, the adaptive controller must be tuned manually using nonlinear simulations. It is shown via extreme off-nominal nonlinear test cases and an extended Monte Carlo campaign (using an uncertainty range of 130%) that the resulting adaptive controller can successfully prevent severe failures such as loss of vehicle and slightly improve the performance of the baseline controller.

To conclude the work performed for this thesis, the adaptive controller from Chapter 8 is compared with the LPV design presented in Chapter 6. The results show that the LPV controller is also capable of preventing such failures while improving performance and robustness with respect the adaptive scheme. Furthermore, this is achieved using a more methodological synthesis approach versus the tuning complexity of the adaptive law and the lack of adaptive analysis tools. These results indicate that at least for the studied case of the VEGA launcher, LPV approaches are more advantageous.

9.2 Future work

In this section, a number of possible improvements for this thesis work and some suggestions for future research are given.

Robust control validation with Hardware-In-the-Loop

A clear follow-up of this research work would be to implement the controllers presented in this thesis in the VEGA flight-code hardware and subsequently validate them with software-in-the-loop and hardware-in-the-loop campaigns.

Robust design in presence of roll

All designs and results presented in this thesis are based on the assumption that the roll rate is negligible. Recall that this assumption allows to consider pitch and yaw axes decoupled. As stated in Section 2.1.2, the existing coupling between both axes due to roll rate is typically considered as a disturbance and examined ad hoc after design.

Motivated by the above observation and following the work found in references [43, 129], the structured $\mathcal{H}_\infty$ control optimisation could be extended to a MIMO problem to account for an specific roll rate in design. The control problem would be formulated to design simultaneously pitch and yaw controllers, which in this case will have different gains.

Robust design of the atmospheric tail-off controller

Future research can potentially address the design and analysis of different controllers for the whole atmospheric phase.

The current thesis only focused on the design of the atmospheric phase TVC system until the beginning of the tail-off phase (i.e. t=90 s), which is when the thrust is rapidly cut down and the vehicle starts preparing the stage separation. During this phase, the tail-off controller takes control using an scheduling versus longitudinal acceleration [2]. Future research can potentially address the design and analysis of the different controllers for the whole atmospheric phase (i.e. lift-off, atmospheric controller and tail-off), also taking into account the transition between them.

TVC control design across missions

In this thesis, all the designs and analyses are performed using the actual VEGA VV05 mission data. Despite there are large differences between missions (i.e. payload, trajectory, mass-center-inertia properties), there is also commonality between them. In this regard, it could be possible to research how to take into account shared features among missions to create a common design framework for the entire set of VEGA missions based on the design methodology presented in this thesis.

Further research on LPV (uncertainties and structured design)

Motivated by reference [124], future research might investigate the use of a robust LPV synthesis technique taking into account uncertainties in design. As stated in Section 6.1.2, this robust LPV formulation alternates LPV design and IQC analysis steps in an iterative design procedure similar to the D-K iteration employed for μ synthesis.

Furthermore, it would also be interesting to explore the LPV methodology presented in reference [50], where the LPV optimisation is performed using structured $\mathcal{H}_\infty$ tools in order to obtain low-order structured LPV controllers.

Further research on joint rigid/flexible design

Two different approaches, one using the structured $\mathcal{H}_\infty$ method and the other for LPV design, have been proposed in this thesis for the joint design of rigid/flexible TVC controllers. A research venue will be to examine if the solutions presented are valid for other launchers (with only changes in the values of the free parameters) or if other alternative architectures could be more applicable.

Bibliography

[1] Arianespace, "VEGA user's manual," April 2014, http://www.arianespace.com/vehicle/vega/.

[2] C. Roux and I. Cruciani, "Scheduling schemes and control law robustness in atmospheric flight of VEGA launcher," in *Proceedings of the* 7^{th} *ESA International Conference on Spacecraft Guidance, Navigation and Control Systems*, June 2008.

[3] T. Benson, "Brief history of rockets," June 2014, https://www.grc.nasa.gov/www/k-12/TRC/Rockets/history_of_rockets.html.

[4] J. A. Frosch and D. P. Vallely, "Saturn AS-501/S-IC flight control system design," *Journal of Spacecraft and Rockets*, vol. 4, no. 8, pp. 1003–1009, August 1967.

[5] W. Haeussermann, *Description and performance of the Saturn launch vehicle's navigation, guidance and control system.* NASA Technical Note, NASA TN D-5869, July 1970.

[6] L. D. Edinger, "The Space Shuttle ascent flight control system," in *AIAA 76-1942 Guidance and Control Conference.* American Institute of Aeronautics and Astronautics, August 1976, pp. 225–235.

[7] H. Suzuki, "Load relief control of H-IIA launch vehicle," in *Proceedings of the* 16^{th} *IFAC Symposium on Automatic Control in Aerospace*, June 2004, pp. 985–990.

[8] J. Jang, A. Alaniz, R. Hall, N. Bedrossian, C. Hall, S. Ryan, and M. Jackson, "Ares I flight control system design," in *Proceedings of the AIAA Guidance, Navigation, and Control Conference*, August 2010.

[9] W. C. Leite Filho, "Control system of brazilian launcher," in *Proceedings of the* 4^{th} *ESA International Conference on Spacecraft Guidance, Navigation and Control Systems*, October 1999, pp. 401–405.

[10] D. J. Leith and W. E. Leithead, "Survey of gain-scheduling analysis and design," *International Journal of Control*, vol. 73, no. 11, pp. 1001–1025, 2000.

[11] A. Marcos, C. Roux, M. Rotunno, H. Joos, S. Bennani, L. F. Peñín, and A. Caramagno, "The V&V problematic for launchers: current practice and potential advantages on the

application of modern analysis techniques," in *Proceedings of the* 8^{th} *International ESA Conference on Guidance, Navigation and Control Systems*, June 2011.

[12] C. Roux, V. Mantini, A. Marcos, L. Peñín, and S. Bennani, "Robust flight control system design verification & validation for launchers," in *AIAA Guidance, Navigation, and Control Conference*. American Institute of Aeronautics and Astronautics, August 2012.

[13] A. L. Greensite, *Analysis and Design of Space Vehicle Flight Control Systems. Volume VII - Attitude Control During Launch*. NASA Contractor Report CR-826, 1967.

[14] NASA Space Vehicle Design Criteria (Guidance and Control), *Effects of Structural Flexibility on Launch Vehicle Control Systems*. NASA Technical Report, NASA SP-8036, February 1970.

[15] R. F. Hoelker, *Theory of Artificial Stabilization of Missiles and Space Vehicles with Exposition of Four Control Principles*. NASA Technical Note, NASA TN D-555, June 1961.

[16] R. J. Harris, *Trajectory Simulation Applicable to Stability and Control Studies of Large Multi-Engine Vehicles*. NASA Technical Note, NASA TN D-1838, August 1963.

[17] M. H. Rheinfurth, *The Alleviation of Aerodynamic Loads on Rigid Space Vehicles*. NASA Technical Memorandum, NASA TM X-53397, February 1966.

[18] A. Brito, W. Leite Filho, and F. Ramos, "Approach comparison for controller design of a launcher," in *Proceedings of* 6^{th} *ESA International Conference on Spacecraft Guidance, Navigation and Control Systems*, October 2005.

[19] H. Klotz, "Ariane 5 dynamics and control," in *Proceedings of the* 12^{th} *IFAC Symposium on Automatic Control in Aerospace*, September 1992, pp. 227–233.

[20] A. Dhabale, R. N. Banavar, and M. V. Dhekane, "LQG controller designs from reduced order models for a launch vehicle," *Sadhana*, vol. 33, no. 1, pp. 1–14, February 2008.

[21] J. C. Doyle, "Guaranteed margins for LQG regulators," *IEEE Transactions on Automatic Control*, vol. 23, no. 4, pp. 756–757, August 1978.

[22] S. Skogestad and I. Postlethwaite, *Multivariable Feedback Control: Analysis and Design*. John Wiley & Sons, 2005.

[23] G. Zames, "Feedback and optimal sensitivity: Model reference transformations, multiplicative seminorms, and approximate inverses," *IEEE Transactions on Automatic Control*, vol. 26, no. 2, pp. 301–320, April 1981.

[24] K. Glover and J. C. Doyle, "State-space formulae for all stabilizing controller that satisfy an $\mathcal{H}_\infty$ norm bound and relations to risk sensitivity," *Systems and Control Letters*, vol. 11, pp. 167–172, 1988.

[25] J. C. Doyle, K. Glover, P. P. Khargonekar, and B. A. Francis, "State-space solutions to standard $\mathcal{H}_2$ and $\mathcal{H}_\infty$ control problems," *IEEE Transactions on Automatic Control*, vol. 34, no. 8, pp. 831–847, 1989.

[26] M. deVirgilio and D. Kamimoto, "Practical applications of modern controls for booster autopilot design," in *Proceedings of the AIAA/IEEE Digital Avionics Systems Conference*. IEEE, October 1993.

[27] S. Mauffrey, F. Chabert, and M. Ganet-Schoeller, "$\mathcal{H}_\infty$ method applied to launcher control during atmospheric flight," in *Proceedings of the* 3^{rd} *ESA International Conference on Spacecraft Guidance, Navigation and Control Systems*, November 1996, pp. 349–354.

[28] E. Iriarte, B. Lu, and E. Besnard, "Robust control design for a nanosat launch vehicle," in *Volume 4: Dynamics, Control and Uncertainty, Parts A and B.* ASME, November 2012.

[29] S. Mauffrey, P. Meunier, F. Seillier, M. Ganet-Schoeller, and I. Rongier, "$\mathcal{H}_\infty$ control for Ariane 5 Plus launcher: the industrialisation of a new technology," in *Proceedings of the* 5^{th} *International Conference on Launcher Technogoly*, November 2003.

[30] Y. Morita and J. Kawaguchi, "Attitude control design of the M-V rocket," *Philosophical Transactions: Mathematical, Physical and Engineering Sciences*, vol. 359, no. 1788, pp. 2287–2303, 2001.

[31] Y. Morita, T. Imoto, S. Tokodume, and H. Ohtsuka, "First launch in months: Japan's Epsilon launcher and its evolution," *Aerospace Technology Japan*, vol. 12, no. 29, pp. 21–28, 2014.

[32] Y. Morita and S. Goto, "Design for robustness using the μ-synthesis applied to launcher attitude and vibration control," *Acta Astronautica*, vol. 62, no. 1, pp. 1–8, 2008.

[33] G. J. Balas, J. C. Doyle, K. Glover, A. Packard, and R. Smith, *μ-Analysis and Synthesis Toolbox*. The Mathworks, Inc., 1993.

[34] D. F. Enns, "Rocket stabilization as a structured singular value synthesis design example," *IEEE Control Systems*, vol. 11, no. 4, pp. 67–73, June 1991.

[35] E. Gadea, "Design of a robust controller for the VEGA TVC using the μ-synthesis technique," Master's thesis, Universitat Politècnica de Catalunya, Barcelona, Spain, 2011.

[36] J. V. Burke, D. Henrion, A. S. Lewis, and M. L. Overton, "HIFOO - A MATLAB package for fixed-order controller design and $\mathcal{H}_\infty$ optimization," in *Proceedings of the* 5^{th} *IFAC Symposium on Robust Control Design*, 2006.

[37] P. Gahinet and P. Apkarian, "Structured $\mathcal{H}_\infty$ synthesis in MATLAB," in *Proceedings of the* 18^{th} *World Congress of the International Federation of Automatic Control (IFAC)*, vol. 18, August 2011, pp. 1435–1440.

[38] A. Falcoz, C. Pittet, S. Bennani, A. Guignard, C. Bayart, and B. Frapard, "Systematic design methods of robust and structured controllers for satellites," *CEAS Space Journal*, vol. 7, no. 3, pp. 319–334, 2015.

[39] C. Pittet and P. Prieur, *Structured Accelero-Stellar Estimator for Microscope Drag-Free Mission*. Springer International Publishing, 2015, pp. 591–604.

[40] A. Marcos and M. Sato, "Flight testing of an structured $\mathcal{H}_\infty$ controller: an EU-Japan collaborative experience," in *Proceedings of the* 1^{st} *IEEE Conference on Control Technology and Applications*, August 2017, pp. 1590–1595.

[41] M. Knoblauch, D. Saussié, and C. Bérard, "Structured H_∞ control for a launch vehicle," in *Proceedings of the American Control Conference*, June 2012, pp. 967–972.

[42] D. Saussié, Q. Barbès, and C. Bérard, "Self-scheduled and structured $\mathcal{H}_\infty$ synthesis : a launch vehicle application," in *Proceedings of the American Control Conference*, June 2013, pp. 1590–1595.

[43] D. S. de la Llana, "Design of H-infinity controllers for ill-conditioned plants in presence of disturbances," Ph.D. dissertation, Universidad Nacional de Educación a Distancia, Spain, 2015.

[44] M. Ganet-Schoeller, J. Desmariaux, and C. Combier, "Structured control for future european launchers," *AerospaceLab Journal*, no. 13, pp. 1–10, September 2017.

[45] O. Voinot, P. Apkarian, and D. Alazard, "Gain-scheduling $\mathcal{H}_\infty$ of the launcher in atmospheric flight via linear-parameter varying techniques," in *Proceedings of the AIAA Guidance, Navigation, and Control Conference and Exhibit*. American Institute of Aeronautics and Astronautics, August 2002.

[46] M. Ganet-Schoeller and M. Ducamp, "LPV control for flexible launcher," in *Proceedings of the AIAA Guidance, Navigation, and Control Conference*, August 2010.

[47] A. Hjartarson, P. Seiler, and A. Packard, "LPVTools: A toolbox for modeling, analysis, and synthesis of parameter varying control systems," *IFAC-PapersOnLine*, vol. 48, no. 26, pp. 139–145, 2015.

[48] B. Patartics, T. Luspay, T. Péni, B. Takarics, B. Vanek, and T. Kier, "Parameter varying flutter suppression control for the BAH jet transport wing," in *Proceedings of the* 20^{th} *IFAC World Congress*, July 2017.

[49] D. Ossmann, J. Theis, and P. Seiler, "Load reduction on a clipper liberty wind turbine with linear parameter-varying individual blade pitch control," *Wind Energy*, vol. 20, no. 10, pp. 1771–1786, June 2017.

[50] V. Preda, J. Cieslak, D. Henry, S. Bennani, and A. Falcoz, "Robust microvibration mitigation and pointing performance analysis for high stability spacecraft," *International Journal of Robust and Nonlinear Control*, vol. 28, pp. 5688–5716, October 2018.

[51] J. S. Orr and T. S. VanZwieten, "Robust, practical adaptive control for launch vehicles," in *Proceedings of the AIAA Guidance, Navigation, and Control Conference*. American Institute of Aeronautics and Astronautics, August 2012.

[52] J. S. Orr, J. H. Wall, T. S. VanZwieten, and C. E. Hall, *Space Launch System Ascent Flight Control System*. NASA AAS 14-038, 2014.

[53] J. H. Wall, J. S. Orr, and T. S. VanZwieten, *Space Launch System Implementation of Adaptive Augmenting Control*. NASA AAS 14-051, 2014.

[54] T. S. VanZwieten, E. T. Gilligan, and J. H. Wall, *Adaptive Augmenting Control Flight Characterization Experiment on an F/A-18*. NASA AAS 17-126, 2017.

[55] A. Hodel, M. Whorton, and J. Jim Zhu, "Stability metrics for simulation and flight-software assessment and monitoring of adaptive control assist compensators," in *Proceedings of the AIAA Guidance, Navigation and Control Conference and Exhibit*, August 2008.

[56] K. Clements and J. H. Wall, *Time Domain Stability Margin Assessment of the NASA Space Launch System GN%C Design for Exploration Mission One*. NASA AAS 17-126, 2017.

[57] T. S. VanZwieten, M. R. Hannan, and J. H. Wall, "Evaluating the stability of NASA's space launch system with adaptive augmenting control," in *Proceedings of the* 10^{th} *International ESA Conference on Guidance, Navigation and Control Systems*, May 2017.

[58] J.-W. Jang, R. Hall, N. Bedrossian, and C. Hall, "Ares-I bending filter design using a constrained optimization approach," in *Proceedings of the AIAA Guidance, Navigation and Control Conference and Exhibit*, August 2008.

[59] N. Bedrossian, J.-W. Jang, A. Alaniz, M. Johnson, K. Sebelius, and Y. Mesfin, "International space station US GN&C attitude hold controller design for orbiter repair

maneuver," in *Proceedings of the AIAA Guidance, Navigation and Control Conference and Exhibit*, August 2005.

[60] J. S. Orr, *Optimal Recursive Digital Filters for Active Bending Stabilization.* NASA AAS 13-054, 2013.

[61] A. Brito, S. França, and W. L. Filho, "Varying-time notch filter for bending modes active suppression in aerospace systems," in *Proceedings of the* 7^{th} *ESA International Conference on Spacecraft Guidance, Navigation and Control Systems*, June 2008.

[62] C.-S. Oh and H. Bang, "Attitude control of flexible launch vehicle using adaptive notch filter," in *Proceedings of the* 16^{th} *IFAC World Congress*, July 2005.

[63] T. Vanthuyne, "An electrical thrust vector control system for the VEGA launcher," in *Proceedings of the* 13^{th} *European Space Mechanisms and Tribology Symposium*, September 2009.

[64] Arianespace, "VEGA flight VV05," June 2015, http://www.arianespace.com/mission/vega-flight-vv05/.

[65] C. Roux and I. Cruciani, "Roll coupling effects on the stability margins for VEGA launcher," in *Proceedings of the AIAA Atmospheric Flight Mechanics Conference and Exhibit*, August 2007.

[66] M. Valli, D. Spallotta, C. Roux, A. Marcos, A. Mujumdar, P. P. Menon, and S. Bennani, "Thrust vector control validation results for performance and stability robustness assessments," in *Proceedings of the* 3^{rd} *CEAS Conference on Guidance, Navigation and Control*, April 2015.

[67] A. Marcos, P. Rosa, C. Roux, M. Bartolini, and S. Bennani, "An overview of the RFCS project V&V framework: Optimization-based and linear tools for worst-case search," *CEAS Space Journal*, vol. 7, no. 2, pp. 303–318, 2015.

[68] A. L. Greensite, *Analysis and Design of Space Vehicle Flight Control Systems. Volume I - Short Period Dynamics.* NASA Contractor Report CR-820, 1967.

[69] J. Orr, M. Johnson, J. Wetherbee, and J. McDuffie, "State space implementation of linear perturbation dynamics equations for flexible launch vehicles," in *Proceedings of the AIAA Guidance, Navigation, and Control Conference*, August 2009.

[70] M. Bernard, "VEGA missionization and post flight analyses," Ph.D. dissertation, Sapienza Università di Roma, Italy, 2009.

[71] P. Simplício, S. Bennani, A. Marcos, C. Roux, and X. Lefort, "Structured singular-value analysis of the VEGA launcher in atmospheric flight," *Journal of Guidance, Control, and Dynamics*, vol. 39, no. 6, pp. 1342–1355, 2016.

[72] J. C. Doyle, A. Packard, and K. Zhou, "Review of LFTs, LMIs, and μ," in *Proceedings of the* 30^{th} *IEEE Conference on Decision and Control*, December 1991, pp. 1227–1232.

[73] K. Zhou, J. C. Doyle, and K. Glover, *Robust and Optimal Control*. Upper Saddle River, NJ, USA: Prentice-Hall, Inc., 1996.

[74] A. Marcos, S. Bennani, C. Roux, and M. Valli, "LPV modeling and LFT uncertainty identification for robust analysis: application to the VEGA launcher during atmospheric phase," in *Proceedings of the* 1^{st} *IFAC Workshop on Linear Parameter Varying Systems*, October 2015.

[75] G. J. Balas, R. Chiang, A. Packard, and M. G. Safonov, *Robust Control Toolbox*. The MathWorks, Inc., 2005.

[76] D. Navarro-Tapia, A. Marcos, S. Bennani, and C. Roux, "Structured $\mathcal{H}_\infty$ control based on classical control parameters for the VEGA launch vehicle," in *Proceedings of the IEEE Multi-Conference on Systems and Control*, September 2016.

[77] ——, "Structured H_∞ control design for the VEGA launch vehicle: Recovery of the legacy control behaviour," in *Proceedings of the* 10^{th} *International ESA Conference on Guidance, Navigation and Control Systems*, May 2017.

[78] P. Apkarian and D. Noll, "The $\mathcal{H}_\infty$ control problem is solved," *AerospaceLab Journal*, no. 13, pp. 1–11, September 2017.

[79] P. Gahinet and P. Apkarian, "A linear matrix inequality approach to $\mathcal{H}_\infty$ control," *International Journal of Robust and Nonlinear Control*, vol. 4, no. 4, pp. 421–448, 1994.

[80] P. Apkarian and D. Noll, "Nonsmooth $\mathcal{H}_\infty$ synthesis," *IEEE Transactions on Automatic Control*, vol. 51, no. 1, pp. 71–86, 2006.

[81] ——, "Nonsmooth optimization for multidisk $\mathcal{H}_\infty$ synthesis," *European Journal of Control*, vol. 12, no. 3, pp. 229–244, February 2006.

[82] P. Gahinet and P. Apkarian, "Automated tuning of gain-scheduled control systems," in *Proceedings of the* 52^{nd} *IEEE Conference on Decision and Control*, December 2013.

[83] H. Lhachemi, D. Saussié, and G. Zhu, "A robust and self-scheduled longitudinal flight control system: a multi-model and structured $\mathcal{H}_\infty$ approach," in *Proceedings of the AIAA Guidance, Navigation and Control Conference*, January 2014.

[84] P. Apkarian, "Tuning controllers against multiple design requirements," in *Proceedings of the American Control Conference*, June 2013, pp. 3888–3893.

[85] P. Apkarian, D. Noll, and A. Rondepierre, "Nonsmooth optimization algorithm for mixed $\mathcal{H}_2/\mathcal{H}_\infty$ synthesis," in *Proceedings of the* 46^{th} *IEEE Conference on Decision and Control*, December 2007.

[86] ——, "Mixed $\mathcal{H}_2/\mathcal{H}_\infty$ control via nonsmooth optimization," in *Proceedings of the* 48^{th} *IEEE Conference on Decision and Control*, December 2009.

[87] P. Apkarian, L. Ravanbod-Hosseini, and D. Noll, "Time domain constrained $\mathcal{H}_\infty$-synthesis," *International Journal of Robust and Nonlinear Control*, vol. 21, no. 2, pp. 197–217, July 2011.

[88] P. Apkarian, M. N. Dao, and D. Noll, "Parametric robust structured control design," *IEEE Transactions on Automatic Control*, vol. 60, no. 7, pp. 1857–1869, 2015.

[89] R. S. da Silva de Aguiar, P. Apkarian, and D. Noll, "Structured robust control against mixed uncertainty," *IEEE Transactions on Control Systems Technology*, vol. 26, no. 5, pp. 1771–1781, September 2018.

[90] P. Simplício, A. Marcos, E. Joffre, M. Zamaro, and N. Silva, "Synthesis and analysis of robust control compensators for space descent & landing," *International Journal of Robust and Nonlinear Control*, pp. 1–22, March 2018.

[91] M. Řezáč and Z. Hurák, "Structured MIMO design for dual-stage inertial stabilization: Case study for HIFOO and hinfstruct solvers," *Mechatronics*, vol. 23, no. 8, pp. 1084–1093, December 2013.

[92] P. Loiseau, P. Chevrel, M. Yagoubi, and J.-M. Duffal, "A robust feedback control design for broadband noise attenuation in a car cabin," in *Proceedings of the* 20^{th} *IFAC World Congress*, July 2017.

[93] J. Biannic and P. Apkarian, "Anti-windup design via nonsmooth multi-objective $\mathcal{H}_\infty$ optimization," in *Proceedings of the American Control Conference*, June 2011, pp. 4457–4462.

[94] J.-M. Biannic and C. Roos, "Flare control law design via multi-channel $\mathcal{H}_\infty$ synthesis: Illustration on a freely available nonlinear aircraft benchmark," in *Proceedings of the American Control Conference*, 2015.

[95] D. Navarro-Tapia, P. Simplício, A. Iannelli, and A. Marcos, "Robust flare control design using structured $\mathcal{H}_\infty$ synthesis: a civilian aircraft landing challenge," in *Proceedings of the* 20^{th} *IFAC World Congress*, July 2017.

[96] P. Simplício, D. Navarro-Tapia, A. Iannelli, and A. Marcos, "From standard to strutured robust control design: Application to aircraft automatic glide-slope approach," in *Proceedings of the Joint* 9^{th} *IFAC Symposium on Robust Control Design and* 2^{nd} *IFAC Workshop on Linear Parameter Varying Systems*, September 2018.

[97] M. Ganet-Schoeller, "Towards structured $\mathcal{H}_\infty$ synthesis for flexible launcher," in *Proceedings of the* 3^{rd} *CEAS Conference on Guidance, Navigation and Control*, April 2015.

[98] G. F. McDonough, W. D. Murphree, J. C. Blair, J. R. Scoggins, T. G. Reed, E. L. Linsley, V. S. Verderaime, J. A. Lovingood, M. H. Rheinfurth, and R. S. Ryan, *Wind Effects on Launch Vehicles*. Technivision Services, 1970.

[99] B. Wie, W. Du, and M. Whorton, "Analysis and design of launch vehicle flight control systems," in *Proceedings of the AIAA Guidance, Navigation and Control Conference and Exhibit*, August 2008.

[100] D. L. Johnson, *Terrestrial Environment (Climatic) Criteria Guidelines for Use in Aerospace Vehicle Development*. NASA Technical Memorandum, NASA TM 4511, August 1993.

[101] J. C. Doyle, "Analysis of feedback systems with structured uncertainties," *IEE Proceedings D - Control Theory and Applications*, vol. 129, no. 6, pp. 242–250, November 1982.

[102] C. Charbonnel, "$\mathcal{H}_\infty$ controller design and μ-analysis: powerful tools for flexible satellite attitude control," in *Proceedings of the AIAA Guidance, Navigation, and Control Conference*, August 2010.

[103] M. Ganet-Schoeller, J. Bourdon, and G. Gelly, "Non linear and robust stability analysis for ATV rendezvous control," in *Proceedings of the AIAA Guidance, Navigation, and Control Conference*, August 2009.

[104] A. Packard and J. C. Doyle, "The complex structured singular value," *Automatica*, vol. 29, no. 1, pp. 71–109, January 1993.

[105] K. J. Aström and B. Wittemark, *Computer-Controlled Systems: Theory and Design*. Prentice Hall, 2001.

[106] J. S. Shamma, "Analysis and design of gain scheduled control systems," Ph.D. dissertation, Massachusetts Institute of Technology, 1988.

[107] G. J. Balas, J. Mueller, and J. Barker, "Application of gain-scheduled, multivariable control techniques to the f/a-18 system research aircraft," in *Guidance, Navigation, and*

Control Conference and Exhibit. American Institute of Aeronautics and Astronautics, August 1999.

[108] G. J. Balas, "Linear, parameter-varying control and its application to a turbofan engine," *International Journal of Robust and Nonlinear Control*, vol. 12, no. 9, pp. 763–796, 2002.

[109] A. Marcos and S. Bennani, "LPV modeling, analysis and design in space systems: Rationale, objectives and limitations," in *Proceedings of the AIAA Guidance, Navigation, and Control Conference*, August 2009.

[110] ——, *A Linear Parameter Varying Controller for a Re-entry Vehicle Benchmark*. Berlin, Heidelberg: Springer Berlin Heidelberg, 2011, pp. 15–27.

[111] W. J. Rugh and J. S. Shamma, "Research on gain scheduling," *Automatica*, vol. 36, no. 10, pp. 1401–1425, 2000.

[112] J. S. Shamma, "An overview of LPV systems," in *Control of Linear Parameter Varying Systems with Applications*. Springer, 2012, pp. 3–26.

[113] C. Hoffmann and H. Werner, "A survey of linear parameter-varying control applications validated by experiments or high-fidelity simulations," *IEEE Transactions on Control Systems Technology*, vol. 23, no. 2, pp. 416–433, March 2015.

[114] A. Hjartarson, P. J. Seiler, and G. J. Balas, "LPV aeroservoelastic control using the LPVTools toolbox," in *AIAA Atmospheric Flight Mechanics (AFM) Conference*. American Institute of Aeronautics and Astronautics, August 2013.

[115] A. Marcos and G. J. Balas, "Development of linear-parameter-varying models for aircraft," *Journal of Guidance, Control, and Dynamics*, vol. 27, no. 2, pp. 218–228, March 2004.

[116] G. Becker and A. Packard, "Robust performance of linear parametrically varying systems using parametrically-dependent linear feedback," *Systems & Control Letters*, vol. 23, no. 3, pp. 205–215, September 1994.

[117] P. Apkarian, P. Gahinet, and G. Becker, "Self-scheduled $\mathcal{H}_\infty$ control of linear parameter-varying systems: a design example," *Automatica*, vol. 31, no. 9, pp. 1251–1261, September 1995.

[118] A. Packard, "Gain scheduling via linear fractional transformations," *Systems & Control Letters*, vol. 22, no. 2, pp. 79–92, February 1994.

[119] P. Apkarian and P. Gahinet, "A convex characterization of gain-scheduled $\mathcal{H}_\infty$ controllers," *IEEE Transactions on Automatic Control*, vol. 40, no. 5, pp. 853–864, May 1995.

[120] F. Wu, "Control of linear parameter varying systems," Ph.D. dissertation, University of California at Berkeley, 1995.

[121] F. Wu, X. H. Yang, A. Packard, and G. Becker, "Induced $\mathcal{L}_2$-norm control for lpv systems with bounded parameter variation rates," *International Journal of Robust and Nonlinear Control*, vol. 6, no. 9–10, pp. 983–998, November 2000.

[122] J. Veenman and C. W. Scherer, "IQC-synthesis with general dynamic multipliers," *International Journal of Robust and Nonlinear Control*, vol. 24, no. 17, pp. 3027–3056, 2014.

[123] A. Megretski and A. Rantzer, "System analysis via integral quadratic constraints," *IEEE Transactions on Automatic Control*, vol. 42, no. 6, pp. 819–830, June 1997.

[124] S. Wang, H. Pfifer, and P. J. Seiler, "Robust synthesis for linear parameter varying systems using integral quadratic constraints," *Automatica*, vol. 68, pp. 111–118, June 2016.

[125] D. Navarro-Tapia, A. Marcos, S. Bennani, and C. Roux, "Structured $\mathcal{H}_\infty$ and linear parameter varying control design for the VEGA launch vehicle," in *Proceedings of the* 7^{th} *European Conference for Aeronautics and Aerospace Sciences*, July 2017.

[126] B. A. Francis and W. M. Wonham, "The internal model principle of control theory," *Automatica*, vol. 12, no. 5, pp. 457–465, 1976.

[127] M. Morari and E. Zafiriou, *Robust Process Control*. Prentice-Hall, 1989.

[128] H. Shim, G. Park, Y. Joo, J. Back, and N. H. Jo, "Yet another tutorial of disturbance observer: robust stabilization and recovery of nominal performance," *Control Theory and Technology*, vol. 14, no. 3, pp. 237–249, August 2016.

[129] D. S. de la Llana, S. Bennani, I. Cruciani, and J. Aranda, "H-infinity control of the VEGA launch vehicle first stage in presence of roll," in *Proceedings of the* 19^{th} *IFAC Symposium on Automatic Control in Aerospace*, vol. 46, no. 19, September 2013, pp. 54–59.

APPENDIX A

Analysis of TVC closed-loop transfer functions

In this appendix, the open-loop transfer functions of the rigid-body launch vehicle model are given. Then, the main transfer functions of the rigid-body closed-loop interconnection used for TVC system design are analytically derived and analysed. As indicated in Chapter 3, this closed-loop analysis facilitates the selection of the weighting functions to formulate the structured $\mathcal{H}_\infty$ control optimisation and also provides valuable information on the limits and capabilities of the control system.

A.1 Launch vehicle transfer functions

Consider the rigid-body launch vehicle model shown in Figure A.1. This model is described in a state-space formulation in Equation A.1, where the state-space matrices (A_R, B_R, C_R and D_R) and state, input and output vectors ($\mathbf{x_R}$, $\mathbf{u_{LV}}$ and $\mathbf{y_{LV}}$) are given in Section 2.2.1.5.

$$\begin{bmatrix} \dot{\mathbf{x_R}} \\ \mathbf{y_{LV}} \end{bmatrix} = \begin{bmatrix} A_R & B_R \\ C_R & D_R \end{bmatrix} \begin{bmatrix} \mathbf{x_R} \\ \mathbf{u_{LV}} \end{bmatrix} \tag{A.1}$$

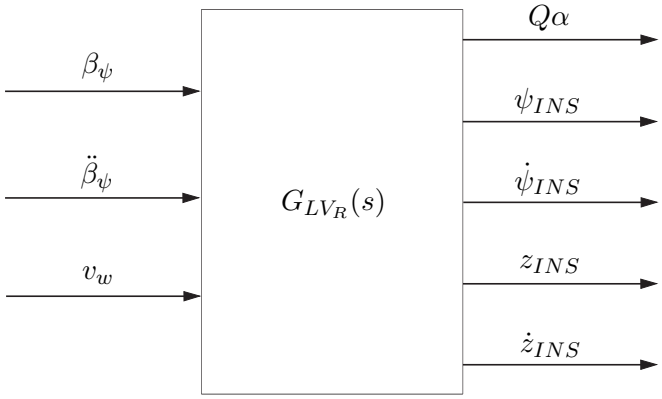

Figure A.1: Rigid-body launcher model diagram

Next, all the transfer functions from $\mathbf{u_{LV}}$ to $\mathbf{y_{LV}}$ are derived and expressed in terms of the rigid-body matrix coefficients defined in Equation 2.18.

A.1.1 Attitude channels

The transfer functions from the launch vehicle inputs to the attitude measurements at INS location are given by:

$$\frac{\psi_{INS}(s)}{\beta_\psi(s)} = \frac{sk_1 + c_3}{s^3 + s^2c_1 - sa_6 + c_2} \tag{A.2}$$

$$\frac{\psi_{INS}(s)}{\ddot{\beta}_\psi(s)} = \frac{sk_3 + \big(a_4k_2 - a_1k_3\big)}{s^3 + s^2c_1 - sa_6 + c_2} \tag{A.3}$$

$$\frac{\psi_{INS}(s)}{v_w(s)} = \frac{-sa_4}{s^3 + s^2c_1 - sa_6 + c_2} \tag{A.4}$$

where $c_1 = -a_1 - a_5$, $c_2 = a_1a_6 - a_3a_4$ and $c_3 = a_4a_p - a_1k_1$.

From the above equations, it is now trivial to derive the transfer functions to the attitude rate $\dot{\psi}_{INS}$, as follows:

$$\frac{\dot{\psi}_{INS}(s)}{\beta_\psi(s)} = \frac{s^2k_1 + sc_3}{s^3 + s^2c_1 - sa_6 + c_2} \tag{A.5}$$

$$\frac{\dot{\psi}_{INS}(s)}{\ddot{\beta}_\psi(s)} = \frac{s^2k_3 + s\big(a_4k_2 - a_1k_3\big)}{s^3 + s^2c_1 - sa_6 + c_2} \tag{A.6}$$

$$\frac{\dot{\psi}_{INS}(s)}{v_w(s)} = \frac{-s^2a_4}{s^3 + s^2c_1 - sa_6 + c_2} \tag{A.7}$$

A.1.2 Drift channels

The transfer functions from $\mathbf{u_{LV}}$ to the drift measured at INS location are given by:

$$\frac{z_{INS}(s)}{\beta_\psi(s)} = \frac{1}{s}\frac{s^2c_4 + sc_5 + c_6}{s^3 + s^2c_1 - sa_6 + c_2} \tag{A.8}$$

$$\frac{z_{INS}(s)}{\ddot{\beta}_\psi(s)} = \frac{1}{s}\frac{s^2\big(k_2 + l_{INS}k_3\big) + s\big(a_2k_3 - a_5k_2 + l_{INS}(a_4k_2 - a_1k_3)\big) + \big(a_3k_3 - a_6k_2\big)}{s^3 + s^2c_1 - sa_6 + c_2} \tag{A.9}$$

$$\frac{z_{INS}(s)}{v_w(s)} = \frac{1}{s}\frac{-s^2\big(a_1 + l_{INS}a_4\big) + c_2}{s^3 + s^2c_1 - sa_6 + c_2} \tag{A.10}$$

where $c_4 = a_p + l_{INS}k_1$, $c_5 = a_2k_1 - a_5a_p + l_{INS}c_3$ and $c_6 = a_3k_1 - a_6a_p$.

Similarly, the transfer functions to the drift-rate $\dot{z}_{INS}$ can be expressed as follows:

$$\frac{\dot{z}_{INS}(s)}{\beta_\psi(s)} = \frac{s^2 c_4 + s c_5 + c_6}{s^3 + s^2 c_1 - s a_6 + c_2} \tag{A.11}$$

$$\frac{\dot{z}_{INS}(s)}{\ddot{\beta}_\psi(s)} = \frac{s^2\big(k_2 + l_{INS} k_3\big) + s\big(a_2 k_3 - a_5 k_2 + l_{INS}(a_4 k_2 - a_1 k_3)\big) + \big(a_3 k_3 - a_6 k_2\big)}{s^3 + s^2 c_1 - s a_6 + c_2} \tag{A.12}$$

$$\frac{\dot{z}_{INS}(s)}{v_w(s)} = \frac{-s^2\big(a_1 + l_{INS} a_4\big) + c_2}{s^3 + s^2 c_1 - s a_6 + c_2} \tag{A.13}$$

A.1.3 $Q\alpha$ channel

Finally, all the transfer functions from the inputs to the structural load indicator $Q\alpha$ are given by:

$$\frac{Q\alpha(s)}{\beta_\psi(s)} = Q\frac{1}{V}\frac{s^2 a_p + s\big(k_1(V + a_2) - a_5 a_p\big) + \big(c_3 V + c_6\big)}{s^3 + s^2 c_1 - s a_6 + c_2} \tag{A.14}$$

$$\frac{Q\alpha(s)}{\ddot{\beta}_\psi(s)} = Q\frac{1}{V}\frac{s^2 k_2 + s\big(k_3(V + a_2) - a_5 k_2\big) + \big((a_4 k_2 - a_1 k_3)V + a_3 k_3 - a_6 k_2\big)}{s^3 + s^2 c_1 - s a_6 + c_2} \tag{A.15}$$

$$\frac{Q\alpha(s)}{v_w(s)} = Q\frac{1}{V}\frac{-s^3 + s^2 a_5}{s^3 + s^2 c_1 - s a_6 + c_2} \tag{A.16}$$

A.2 Rigid-body closed-loop transfer functions

In this section, the closed-loop diagram shown in Figure A.2 is analytically analysed. The transfer functions from each of the inputs (i.e. commands and wind disturbance) to the main outputs of the system are derived and analysed in terms of low- and high-frequency asymptotes. Note that the delay and actuator models are not included in the actuation channel to simplify the analysis. As mentioned in Section 3.3, this simplification does not affect the asymptotic analysis because both models present unity gain at low frequencies. Also note that the launch vehicle model $G_{LV_R}(s)$ presents now only two inputs $\mathbf{u_{LV}} = [\beta_\psi \quad v_w]$.

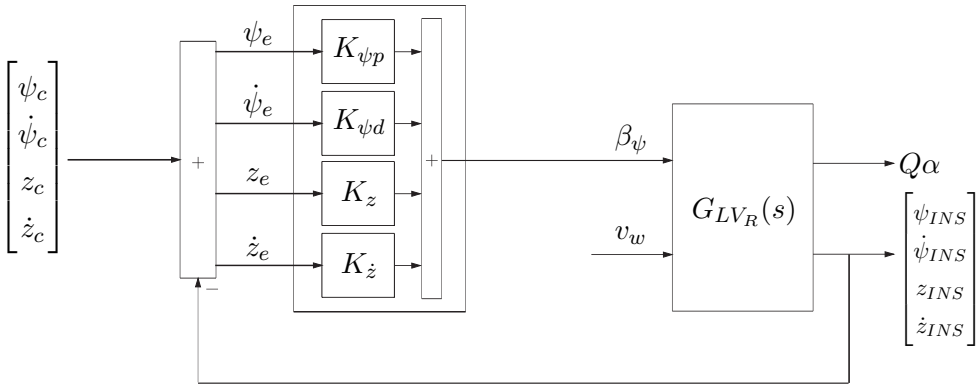

Figure A.2: TVC closed-loop diagram for analysis

Next, the transfer functions from commands and wind disturbance input to the most relevant performance channels (e.g. attitude, drift, drift-rate, $Q\alpha$ and actuation) are presented.

A.2.1 Attitude channel

The attitude complementary sensitivity function from the attitude command ψ_c can be derived as follows:

$$\frac{\psi_{INS}(s)}{\psi_c(s)} = \frac{K_{\psi p}\frac{\psi_{INS}(s)}{\beta_\psi(s)}}{1 + K_{\psi p}\frac{\psi_{INS}(s)}{\beta_\psi(s)} + K_{\psi d}\frac{\dot{\psi}_{INS}(s)}{\beta_\psi(s)} + K_z\frac{z_{INS}(s)}{\beta_\psi(s)} + K_{\dot{z}}\frac{\dot{z}_{INS}(s)}{\beta_\psi(s)}} \tag{A.17}$$

Using the launch vehicle transfer functions presented in Section A.1 and after some manipulation, the following expression is obtained:

$$\frac{\psi_{INS}(s)}{\psi_c(s)} = K_{\psi p}\frac{s^2k_1 + sc_3}{C(s)} \tag{A.18}$$

where $C(s)$ is the characteristic equation given in Equation A.19.

$$\begin{aligned} C(s) = s^4 &+ s^3\big(K_{\psi d}k_1 + K_{\dot{z}}c_4 + c_1\big) + s^2\big(K_{\psi p}k_1 + K_{\psi d}c_3 + K_z c_4 + K_{\dot{z}}c_5 - a_6\big) \\ &+ s\big(K_{\psi p}c_3 + K_z c_5 + K_{\dot{z}}c_6 + c_2\big) + K_z c_6 \end{aligned} \tag{A.19}$$

Similarly, the transfer functions from the other inputs can be derived following the same formulation as before:

$$\frac{\psi_{INS}(s)}{\dot{\psi}_c(s)} = K_{\psi d}\frac{s^2k_1 + sc_3}{C(s)} \tag{A.20}$$

$$\frac{\psi_{INS}(s)}{z_c(s)} = K_z\frac{s^2k_1 + sc_3}{C(s)} \tag{A.21}$$

$$\frac{\psi_{INS}(s)}{\dot{z}_c(s)} = K_{\dot{z}}\frac{s^2k_1 + sc_3}{C(s)} \tag{A.22}$$

$$\frac{\psi_{INS}(s)}{v_w(s)} = -\frac{s^2a_4 + s\big(K_{\dot{z}}c_3\big) + K_z c_3}{C(s)} \tag{A.23}$$

Furthermore, using the attitude complementary sensitivity function given in Equation A.18, it is easy to obtain the attitude sensitivity function through the relation $\psi_{INS}/\psi_c + \psi_e/\psi_c = 1$:

$$\frac{\psi_e(s)}{\psi_c(s)} = \frac{s^4 + s^3\Big(K_{\psi d}k_1 + K_{\dot{z}}c_4 + c_1\Big) + s^2\Big(K_{\psi d}c_3 + K_z c_4 + K_{\dot{z}}c_5 - a_6\Big) + s\Big(K_z c_5 + K_{\dot{z}}c_6 + c_2\Big) + K_z c_6}{C(s)} \tag{A.24}$$

All previous transfer functions are analysed in terms of low- and high-frequency asymptotes as shown in Table A.1. It is observed that as expected the sensitivity function (ψ_e/ψ_c) equals one at high frequencies while the asymptote of the complementary sensitivity function (ψ_{INS}/ψ_c) is zero. At low frequencies, this trend is generally the opposite (i.e. the low-frequency asymptote of ψ_e/ψ_c is normally low to achieve good tracking performance). However, it is noted that due to the inclusion of the lateral control feedback, the steady-state tracking error of the system is fixed to 1 (see ψ_e/ψ_c when $\omega = 0$ in Table A.1).

Table A.1: Rigid-body asymptotic analysis for the attitude channel

Transfer function	$\omega = 0$	$\omega = \infty$
ψ_{INS}/ψ_c	0	0
ψ_e/ψ_c	1	1
$\psi_{INS}/\dot{\psi}_c$	0	0
ψ_{INS}/z_c	0	0
$\psi_{INS}/\dot{z}_c$	0	0
ψ_{INS}/v_w	-c_3/c_6	0

In addition, it is also observed that the low-frequency asymptote of the transfer function from the wind input v_w to ψ_{INS} only depends on physical parameters of the launch vehicle. Therefore, the attitude steady-state response from the wind disturbance cannot be minimised or controlled in any way with the current TVC architecture.

A.2.2 Drift channel

Similarly as before, the transfer functions from the closed-loop system inputs to the drift measured at INS location are given by:

$$\frac{z_{INS}(s)}{\psi_c(s)} = K_{\psi p}\frac{s^2c_4 + sc_5 + c_6}{C(s)} \tag{A.25}$$

$$\frac{z_{INS}(s)}{\dot{\psi}_c(s)} = K_{\psi d}\frac{s^2c_4 + sc_5 + c_6}{C(s)} \tag{A.26}$$

$$\frac{z_{INS}(s)}{z_c(s)} = K_z\frac{s^2c_4 + sc_5 + c_6}{C(s)} \tag{A.27}$$

$$\frac{z_{INS}(s)}{\dot{z}_c(s)} = K_{\dot{z}}\frac{s^2c_4 + sc_5 + c_6}{C(s)} \tag{A.28}$$

$$\frac{z_{INS}(s)}{v_w(s)} = \frac{-s^2\big(a_1 + l_{INS}a_4\big) + s\big(K_{\psi d}c_3\big) + \big(K_{\psi p}c_3 + c_2\big)}{C(s)} \tag{A.29}$$

Table A.2 shows the low- and high-frequency asymptotes of the above transfer functions. In this case, it is interesting to observe that the drift steady-state response can be cancelled out by an appropriate choice of $K_{\psi p}$. In addition, note that the low-frequency asymptotes from the commands (except z_{INS}/z_c the drift complementary sensitivity function) depend exclusively on a ratio of rigid-body gains.

Table A.2: Rigid-body asymptotic analysis for the drift channel

Transfer function	$\omega = 0$	$\omega = \infty$
z_{INS}/ψ_c	$K_{\psi p}/K_z$	0
$z_{INS}/\dot{\psi}_c$	$K_{\psi d}/K_z$	0
z_{INS}/z_c	1	0
$z_{INS}/\dot{z}_c$	$K_{\dot{z}}/K_z$	0
z_{INS}/v_w	$-\big(K_{\psi p}c_3 + c_2\big)/\big(K_z c_6\big)$	0

A.2.3 Drift-rate channel

From the drift transfer functions presented in Section A.2.2, it is now trivial to derive the closed-loop transfer functions for the drift-rate channel as follows:

$$\frac{\dot{z}_{INS}(s)}{\psi_c(s)} = K_{\psi p}\frac{s^3c_4 + s^2c_5 + sc_6}{C(s)} \tag{A.30}$$

$$\frac{\dot{z}_{INS}(s)}{\dot{\psi}_c(s)} = K_{\psi d}\frac{s^3c_4 + s^2c_5 + sc_6}{C(s)} \tag{A.31}$$

$$\frac{\dot{z}_{INS}(s)}{z_c(s)} = K_z\frac{s^3c_4 + s^2c_5 + sc_6}{C(s)} \tag{A.32}$$

$$\frac{\dot{z}_{INS}(s)}{\dot{z}_c(s)} = K_{\dot{z}}\frac{s^3c_4 + s^2c_5 + sc_6}{C(s)} \tag{A.33}$$

$$\frac{\dot{z}_{INS}(s)}{v_w(s)} = \frac{-s^3\big(a_1 + l_{INS}a_4\big) + s^2\big(K_{\psi d}c_3\big) + s\big(K_{\psi p}c_3 + c_2\big)}{C(s)} \tag{A.34}$$

The asymptotic analysis for the drift-rate transfer functions is presented in Table A.3, although in this case this analysis does not provide functional information to be used on the weighting function selection.

Table A.3: Rigid-body asymptotic analysis for the drift-rate channel

Transfer function	$\omega = 0$	$\omega = \infty$
$\dot{z}_{INS}/\psi_c$	0	0
$\dot{z}_{INS}/\dot{\psi}_c$	0	0
$\dot{z}_{INS}/z_c$	0	0
$\dot{z}_{INS}/\dot{z}_c$	0	0
$\dot{z}_{INS}/v_w$	0	0

A.2.4 $Q\alpha$ channel

The transfer functions from each of the inputs to the structural load performance indicator $Q\alpha$ are derived using the following relation:

$$Q\alpha = Q\big(\psi + \frac{\dot{z}}{V} - \frac{v_w}{V}\big) \tag{A.35}$$

Using the above relation and the equations of the attitude and drift-rate channels presented in Sections A.2.1 and A.2.3, the transfer functions to $Q\alpha$ are obtained after some manipulation and given by:

$$\frac{Q\alpha(s)}{\psi_c(s)} = Q\frac{1}{V}K_{\psi p}\frac{s^3a_p + s^2\big(k_1(V+a_2) - a_5a_p\big) + s\big(c_3V + c_6\big)}{C(s)} \tag{A.36}$$

$$\frac{Q\alpha(s)}{\dot{\psi}_c(s)} = Q\frac{1}{V}K_{\psi d}\frac{s^3a_p + s^2\big(k_1(V+a_2) - a_5a_p\big) + s\big(c_3V + c_6\big)}{C(s)} \tag{A.37}$$

$$\frac{Q\alpha(s)}{z_c(s)} = Q\frac{1}{V}K_{z}\frac{s^3a_p + s^2\big(k_1(V+a_2) - a_5a_p\big) + s\big(c_3V + c_6\big)}{C(s)} \tag{A.38}$$

$$\frac{Q\alpha(s)}{\dot{z}_c(s)} = Q\frac{1}{V}K_{\dot{z}}\frac{s^3a_p + s^2\big(k_1(V+a_2) - a_5a_p\big) + s\big(c_3V + c_6\big)}{C(s)} \tag{A.39}$$

$$\frac{Q\alpha(s)}{v_w(s)} = -Q\frac{1}{V}\frac{s^4+s^3\big(K_{\psi d}k_1+K_{\dot{z}}c_4-a_5\big)+s^2\big(K_{\psi p}k_1+K_zc_4+K_{\dot{z}}c_5\big)+s\big(K_zc_5+K_{\dot{z}}(c_3V+c_6)\big)+K_z(c_3V+c_6)}{C(s)} \tag{A.40}$$

Similarly, the above transfer functions are analysed and their low- and high-frequency asymptotes are obtained and shown in Table A.4. In this case, as for the attitude and drift-rate channels, the steady-state response from the wind disturbance only depends on physical parameters of the launch vehicle and thus, it cannot be minimised with the current TVC architecture.

Table A.4: Rigid-body asymptotic analysis for the $Q\alpha$ channel

Transfer function	$\omega = 0$	$\omega = \infty$
$Q\alpha/\psi_c$	0	0
$Q\alpha/\dot{\psi}_c$	0	0
$Q\alpha/z_c$	0	0
$Q\alpha/\dot{z}_c$	0	0
$Q\alpha/v_w$	$-Q/V\big(1 + Vc_3/c_6\big)$	$-Q/V$

A.2.5 Actuation channel

Finally, the transfer functions of the actuation channel are also derived and analysed. As an example, the transfer function from the attitude angle command ψ_c to β_ψ can be expressed as the sum of the sensitivity functions multiplied by the corresponding rigid-body gain as follows:

$$\frac{\beta_\psi(s)}{\psi_c(s)} = K_{\psi p}\frac{\psi_e(s)}{\psi_c(s)} + K_{\psi d}\frac{\dot{\psi}_e(s)}{\psi_c(s)} + K_z\frac{z_e(s)}{\psi_c(s)} + K_{\dot{z}}\frac{\dot{z}_e(s)}{\psi_c(s)} \tag{A.41}$$

The above equation can also be expressed in terms of the complementary sensitivity functions which have been previously presented and then the following expression is obtained:

$$\frac{\beta_\psi(s)}{\psi_c(s)} = K_{\psi p}\frac{s^4 + s^3c_1 - s^2a_6 + sc_2}{C(s)} \tag{A.42}$$

The transfer functions from the other inputs of the closed-loop system in Figure A.2 can be derived using the same procedure as before:

$$\frac{\beta_\psi(s)}{\dot{\psi}_c(s)} = K_{\psi d}\frac{s^4 + s^3c_1 - s^2a_6 + sc_2}{C(s)} \tag{A.43}$$

$$\frac{\beta_\psi(s)}{z_c(s)} = K_z\frac{s^4 + s^3c_1 - s^2a_6 + sc_2}{C(s)} \tag{A.44}$$

$$\frac{\beta_\psi(s)}{\dot{z}_c(s)} = K_{\dot{z}}\frac{s^4 + s^3c_1 - s^2a_6 + sc_2}{C(s)} \tag{A.45}$$

$$\frac{\beta_\psi(s)}{v_w(s)} = \frac{s^3\big(K_{\psi d}a_4 + K_{\dot{z}}(a_1 + l_{INS}a_4)\big) + s^2\big(K_{\psi p}a_4 + K_z(a_1 + l_{INS}a_4)\big) - s\big(K_{\dot{z}}c_2\big) - K_zc_2}{C(s)} \tag{A.46}$$

Table A.5 shows the asymptotic analysis of the above transfer functions. It is observed the high-frequency asymptote from commands to the controller output equals the corresponding rigid-body gain of each channel. As mentioned in Section 3.4, this feature is quite interesting since it gives a direct connection between the controller gains and the weighting function selection. It is also noted that the actuation steady-state response from wind disturbance also depends only on physical parameters of the launch vehicle model.

Table A.5: Rigid-body asymptotic analysis for the actuation channel

Transfer function	$\omega = 0$	$\omega = \infty$
β_ψ/ψ_c	0	$K_{\psi p}$
$\beta_\psi/\dot{\psi}_c$	0	$K_{\psi d}$
β_ψ/z_c	0	K_z
$\beta_\psi/\dot{z}_c$	0	$K_{\dot{z}}$
β_ψ/v_w	$-c_2/c_6$	0